

JET-P(93)63

W.W. Heidbrink, G. Sadler

The Behaviour of Fast Ions in Tokamak Experiments

“This document contains JET information in a form not yet suitable for publication. The report has been prepared primarily for discussion and information within the JET Project and the Associations. It must not be quoted in publications or in Abstract Journals. External distribution requires approval from the Publications Officer, JET Joint Undertaking, Abingdon, Oxon, OX14 3EA, UK”.

“Enquiries about Copyright and reproduction should be addressed to the Publications Officer, EFDA, Culham Science Centre, Abingdon, Oxon, OX14 3DB, UK.”

The contents of this preprint and all other JET EFDA Preprints and Conference Papers are available to view online free at www.iop.org/Jet. This site has full search facilities and e-mail alert options. The diagrams contained within the PDFs on this site are hyperlinked from the year 1996 onwards.

The Behaviour of Fast Ions in Tokamak Experiments

W.W. Heidbrink¹, G. Sadler

JET-Joint Undertaking, Culham Science Centre, OX14 3DB, Abingdon, UK

¹*University of California, Irvine, California, USA.*

Preprint of a paper to be submitted for publication in Nuclear Fusion
August 1993

The Behaviour of Fast Ions in Tokamak Experiments

W W Heidbrink¹, G Sadler.

JET Joint Undertaking, Abingdon, Oxon, OX14 3EA, UK.

¹ University of California, Irvine, California, USA.

Preprint of a paper to be submitted for publication in Nuclear Fusion

August 1993

Abstract

Fast ions with energies significantly larger than the bulk ion temperature are used to heat most tokamak plasmas. Fast-ion populations created by fusion reactions, by neutral-beam injection, and by radio-frequency (rf) heating are usually concentrated in the center of the plasma. The velocity distribution of these fast-ion populations is determined primarily by Coulomb scattering; during wave heating, perpendicular acceleration by the rf waves is also important. Transport of fast ions is typically much slower than thermal transport except during MHD events. Intense fast-ion populations drive collective instabilities. Implications for the behavior of alphas in future devices are discussed.

CONTENTS. 1. INTRODUCTION: 1.1. Scope of the review; 1.2. Fast-ion diagnostics; 2. THE ORIGIN OF FAST IONS: 2.1. Fusion reactions; 2.2. Neutral beam injection; 2.3. Radio frequency heating: 2.3.1. Ion cyclotron range of frequencies; 2.3.2. Lower hybrid; 3. VELOCITY DISTRIBUTION: 3.1. Coulomb scattering: 3.1.1. Deceleration; 3.1.2. Pitch-angle scattering; 3.1.3. Energy diffusion; 3.2. Acceleration: 3.2.1. Low frequency electric fields; 3.2.2. ICRF; 3.2.3. Lower hybrid; 3.3. Loss terms; 4. CONFINEMENT: 4.1. Drift orbit; 4.2. Toroidal field ripple; 4.3. Fluctuation-induced transport; 4.4. Resonant losses; 4.5. Transport by nonresonant MHD instabilities; 5. COLLECTIVE EFFECTS: 5.1. Internal kink modes; 5.2. Alfvén waves and ballooning modes; 5.3. Ion cyclotron and lower hybrid instabilities; 6. CONCLUSIONS; ACKNOWLEDGEMENTS; LIST OF SYMBOLS AND ACRONYMS; REFERENCES.

1. Introduction

1.1. Scope of the review

Tritium experiments in tokamaks have begun [1]. In the next few years, large alpha particle populations produced in deuterium-tritium (d-t) fusion reactions are expected in JET and TFTR. How will these alpha particles behave? Will they thermalize classically? Will they create hot spots on the vacuum vessel walls? Will they drive collective instabilities?

Although definitive answers to these questions must await d-t experiments, much is already known about the likely behavior of the alpha particles. Alpha particles are a type of *fast ion*. A typical tokamak contains electrons, ions of various species and charge states, and neutrals. Except near the edge of the plasma, the velocity distribution function of most of these particles is described by a shifted Maxwellian distribution function characterized by a rotation velocity \vec{V}_j , a temperature T_j , and a density n_j . In general, the parameters \vec{V}_j , T_j , and n_j depend on the species j of the particle and upon position. In addition to thermal particles, most tokamaks contain a population of ions that have energies much larger than the thermal ion temperature and whose velocities do not conform to a Maxwellian distribution. These “fast” ions execute orbits that are much larger than thermal particles (Fig. 1); quantitatively, the fast ion gyroradius ρ_f is much larger than the thermal ion or electron gyroradii: $\rho_f \gg \rho_i \gg \rho_e$. The speed v_f of fast ions is usually intermediate between the thermal electron and ion speeds, $v_e \gg v_f \gg v_i$. Because of the large excursions of their orbits and their high speeds, fast ions interact differently with the plasma and with electromagnetic fields than thermal particles. A goal of fast-ion studies is to understand the effect of these interactions on the fast-ion distribution function $f(\vec{v}, \vec{r}, t)$ and, in turn, to understand the effect of the fast-ion population upon the background plasma.

Experimental studies of fast ions in tokamaks span a period of more than two decades. In this review, we attempt to reference all measurements published in archival journals between 1970 and 1992 that relate to the physics of fast ions in tokamaks. Many laboratory reports and papers that appear in conference proceedings are also cited. Approximately 200 papers are based upon fusion product measurements, approximately 150 upon neutral particle analysis, and the remainder of the papers (~ 80) rely upon various other diagnostic techniques. Papers that discuss instabilities that are excited by the fast ions are referenced, but other effects of the fast-ion population on the background

plasma are not included.

The review is primarily descriptive. Quoted accuracies are usually the ones assigned by the original authors. Unfortunately, many papers contain no error analysis. For some of these works, we have estimated the random error from the published data.

Briefer reviews of aspects of the subject include papers on alpha particle physics by Thomas [2] and Furth *et al.* [3], a 1977 review of neutral-beam-driven tokamak fusion reactors by Jassby [4], and a paper on fast-ion stabilization of the sawtooth instability by Porcelli [5]. Although our review of the physics of fast-ion experiments is comprehensive, our treatments of theoretical work and of diagnostics are cursory. Theoretical work is only cited when it elucidates the observations. Theoretical reviews include the 1980 paper by Kolesnichenko [6] and portions of the 1989 textbook by White [7]. Reviews of tokamak diagnostics include the book by Hutchinson [8], the paper by Olinskij and Magyar [9], and the article by Stott [10]. For the reader unfamiliar with tokamaks, Wesson's book [11] gives a concise introduction.

The review is organized as follows. Section 1.2 is a brief introduction to the principal diagnostic techniques for readers unfamiliar with the field. In Sec. 2, the principal methods of generating fast ions are presented: fusion reactions (Sec. 2.1), neutral-beam injection (Sec. 2.2), and radio-frequency (rf) heating (Sec. 2.3). This section includes phenomenological descriptions of the various fast-ion populations. The velocity distribution of fast ions is determined by the competition between Coulomb scattering (Sec. 3.1) and various acceleration (Sec. 3.2) and loss (Sec. 3.3) mechanisms. Next, the effect of the plasma upon the confinement of fast ions is considered (Sec. 4). In Sec. 5, the effect of intense fast-ion populations upon plasma stability is discussed. In the final section (Sec. 6), the implications of the results for future alpha-particle experiments are discussed and suggestions for future work are given.

1.2. *Fast-ion Diagnostics*

Particles emitted from the plasma in reactions with fast ions constitute the basis of the principal fast-ion diagnostics.

If a fast ion collides with a neutral it may undergo a charge-exchange reaction and escape from the plasma as a fast neutral. Escaping neutrals are reionized in gas cells or stripping foils and deflected by electric and magnetic fields to determine their energy and mass. These neutral particle analyzers (NPA) are generally collimated to measure the velocity distribution of neutrals that escape in a particular direction. The *sightline* of the analyzer determines the angles between the velocity vector of the escaping neutrals and the magnetic field. For analyzers that view the plasma in the horizontal midplane, the sightline is specified by the minimum major radius of the sightline, or the *tangency radius* R_{tan} . With several sightlines, the velocity distribution of escaping neutrals can be determined.

Relating the measured flux to a particular location in the plasma can be complicated, however. In general, an NPA measures neutrals created anywhere in its sightline. The background neutral density n_o peaks strongly at the edge of the plasma, while the fast-ion density n_f usually peaks near the center of the plasma; since the probability of a charge-exchange reaction depends upon the product $n_o n_f$ the spatial origin of the flux is often uncertain. Measurements that employ the background neutral density are called *passive* measurements. In *active* measurements, a neutral beam provides a localized,

modulated, source of neutrals in the interior of the plasma, so that the spatial origin of the signal is accurately known. There is an additional complication, however: neutrals can reionize before they escape from the plasma. The probability of a reionization event is greatest for low energy ($\lesssim 20$ keV) neutrals in dense, large ($n_e \gtrsim 10^{19} \text{ m}^{-3}$) plasmas. If reionization is likely, little useful information is available from the neutral spectrum.

A readable introduction to the principles of charge-exchange analysis can be found in Hutchinson's book [8]. A 1965 survey of analyzer designs and detectors appears in Osher's article [12]. Alternatively, the instruments paper by Davis *et al.* [13] describes a particular analyzer in detail and provides a succinct introduction to neutral particle analysis.

Neutral-particle analysis yields the velocity distribution in particular regions of phase space. In contrast, most fusion-product measurements effectively integrate over velocity space. The weight function for the integration is determined by the reaction cross section σ ; in most cases, the signal is weighted toward the fastest part of the distribution function.

The fusion emissivity s (reactions per second per unit volume) is given by

$$s(\vec{r}) = n_1(\vec{r})n_2(\vec{r}) \int \int f_1(\vec{v}_1; \vec{r})f_2(\vec{v}_2; \vec{r})\sigma v d\vec{v}_1 d\vec{v}_2, \quad (1)$$

where n_1 , n_2 , f_1 , and f_2 are the densities and velocity distribution functions of the reacting particles, and the fusion reactivity σv is a function of the relative velocity $v \equiv |\vec{v}_2 - \vec{v}_1|$. Three types of reactions are distinguished. If the distribution functions of both reactants are Maxwellian, the reactions are called *thermonuclear*. In this case the reactivity [14] is only a function of temperature. If a fast-ion population interacts with a thermal distribution, the reactions are termed *beam-plasma*. If the energy of the fast ions is much greater than the plasma temperature, the reactivity depends rather weakly upon the ion temperature. If both reactants are non-Maxwellian, the reactions are termed *beam-beam*. For this case the full integral (Eq. 1) must be evaluated numerically.

For beam-plasma reactions, the fusion-product emission is proportional to the density of fast ions n_f . For this case, Eq. 1 simplifies to

$$s = n_f n_p \langle \sigma v \rangle, \quad (2)$$

where n_p is the density of the target reactants and $\langle \sigma v \rangle$ is the beam-plasma reactivity. (The brackets indicate the average over the distribution functions, $\langle \sigma v \rangle = \int \int \sigma v f_1 f_2 d\vec{v}_1 d\vec{v}_2$.) If the target density and velocity distribution are known, measurement of the fusion emissivity yields the density of fast ions n_f . An important special case occurs when the density of the fast ions n_f peaks much more sharply than the target density n_p . For this case, the volume-integrated fusion source strength S is approximately

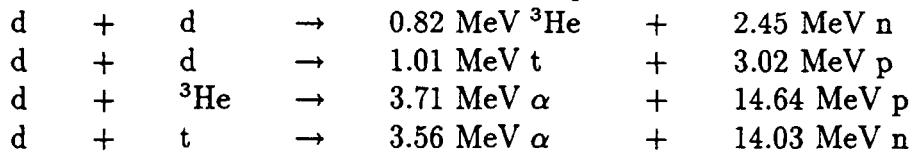
$$S = N_f \hat{n}_p \langle \sigma v \rangle, \quad (3)$$

where N_f is the total number of fast ions in the plasma and \hat{n}_p is the central target density. If $\langle \sigma v \rangle$ can be evaluated, measurement of the fusion source strength yields the number of fast ions in the plasma N_f .

For fast-ion studies, it is often desirable to distinguish thermonuclear reactions from the beam-plasma and beam-beam reactions produced by fast ions, but this is difficult in practice. Sometimes deconvolution of the spectrum of fusion products allows separation

of the various contributions to the reaction rate [15]. Injection of a deuterium pellet into the plasma allows separation of the beam-plasma component [16,17], but this technique is seldom employed. Often the thermonuclear emission is negligible but, in some of the most interesting plasmas, uncertainty in the magnitude of the thermonuclear emission complicates interpretation of the measurements.

The four main fusion reactions in tokamak plasmas are:



(4)

The more compact nuclear physics notation 2(1,3)4, where particles 1,2,3,4 are the projectile, target, and products, respectively, is often employed. The cross sections for these reactions are illustrated in Fig. 2. Improved fits to the measured cross-section data were recently published [14].

Most of the fusion products in Eq. 4 have been used for fast-ion diagnostics. An advantage of neutron diagnostics is that neutrons travel on straight trajectories; however, neutrons are more difficult to collimate than other reaction products. Charged fusion products are easily collimated but their trajectories are affected by the magnetic field, so determination of their spatial origin can be complex. For large MeV ion populations, fusion gamma measurements are useful but the relatively small branching ratio [18,19] restricts their utility at lower densities and energies.

In plasmas with large d-d reaction rates, “burnup” measurements of the $\text{d}(\text{t},\text{n})\alpha$ and $\text{d}(^3\text{He},\text{p})\alpha$ reactions are frequently used to study the confinement of fusion products [20]. The technique is illustrated in Fig. 2. Measurements of 2.5 MeV neutrons monitor the creation rate of 0.8 MeV ^3He ions and 1.0 MeV tritons. (The branching ratio of the d-d reaction is close to unity [14].) If they are confined in the plasma, the tritons and ^3He ions can undergo a secondary fusion reaction as they slow down through the peak of the $\text{d}(\text{t},\text{n})\alpha$ or $\text{d}(^3\text{He},\text{p})\alpha$ cross section. The number of secondary reactions depends upon the slowing-down time and confinement of the tritons and ^3He ions and upon the deuterium density. Measurements of these reaction rates are used to study both the thermalization and the confinement of fusion products.

For further information on fusion-product detectors and basic nuclear techniques consult the textbook by Knoll [21]. Introductions to fusion-product diagnostics in tokamaks can be found in Refs. [8] and [9]. More detailed accounts appear in Refs. [22–25].

2. On the Origin of Fast Ions

In tokamaks, fast ions are generated by fusion reactions, by injection of neutral beams, and by rf acceleration. This section summarizes the observed properties of each of these sources. Fast ions created in nuclear or atomic reactions have a well-defined initial energy (or “birth” energy), while fast ions generated by rf heating do not. For fast ions with a birth energy, this section focuses on the initial velocity distribution; the subsequent development of the velocity distribution function is discussed in Sec. 3. For fast ions generated by rf, phenomenological descriptions of the various sources are given. The physics of rf heating is discussed in Sec. 3.2.

The three main sources of fast ions are compared qualitatively in Table 1.

2.1. Fusion reactions

The four main nuclear reactions that produce fast ions in tokamaks are listed in Eq. 4. The reaction rates depend upon the density and velocity distributions of the reactants and upon the nuclear cross sections. In principle, tokamak measurements could test nuclear theory but, in practice, the nuclear cross sections are assumed valid and fusion product measurements are used to infer the properties of the reactants. In this section, the predictions of nuclear theory are summarized and compared qualitatively with the measurements.

It is customary to distinguish between three types of fusion reactions: thermonuclear, beam-plasma, and beam-beam. The thermonuclear emissivity equals $n_1 n_2 \langle \sigma v \rangle$, where the reactivity $\langle \sigma v \rangle$ is a strong function of temperature.

The total thermonuclear 2.5 MeV neutron emission from the $d(d,n)^3\text{He}$ reaction is found by integrating Eq. 1,¹

$$S = \int \frac{1}{2} n_d^2 \langle \sigma v \rangle d\vec{r}, \quad (5)$$

where n_d is the deuterium density. Measurements of the thermonuclear neutron emission have been performed on most tokamaks. Many studies of the scaling of the emission with plasma parameters have been reported [26–32]. The effect of the sawtooth instability on the total thermonuclear emission was studied by many authors [33–37], with the most complete study being the one by Lovberg *et al.* [36]. The most common use of thermonuclear neutron measurements is to infer the ion temperature through the dependence of $\langle \sigma v \rangle$ upon T_i ; comparisons of this diagnostic technique with other measurements of T_i for many devices are reported in Ref. [38]. Alternatively, when T_i is measured by other diagnostics, measurements of the total thermonuclear emission are used to infer the deuterium density n_d [39–41].

Since both the density and temperature usually peak on axis, the radial profile of thermonuclear reactions peaks very strongly on axis. This expectation was first confirmed on PLT during hydrogen beam injection into a deuterium plasma ($\text{H}^0 \rightarrow \text{D}^+$) [42]. The measured profile (Fig. 3) shows that virtually all the fusion reactions occur in the inner half of the plasma. Subsequent measurements on PLT using 3 MeV protons [from the $d(d,p)t$ branch] also found very steep gradients in the emission profile [43–45].

¹For reactions between particles of the same population, Eq. 1 needs to be multiplied by $\frac{1}{2}$ in order to avoid double counting of the particles in the integrals. Also, care must be taken to use the cross section for the $d(d,n)^3\text{He}$ branch alone in evaluating $\langle \sigma v \rangle$ (some compilations report the total d-d reactivity).

On JET, horizontal and vertical neutron cameras permit two dimensional reconstructions of the emissivity profile [46–50]. The full-width half-maximum (FWHM) of the profile is 0.7–1.1 m in ohmically heated discharges [48], which is much smaller than the horizontal plasma diameter of ~ 2.5 m.

The birth energies of fusion products listed in Eq. 4 are only nominal values. For a reaction 2(1,3)4 where particles 1,2,3,4 are the projectile, target, and products, respectively, the energy of particle 3 using non-relativistic kinematics² is

$$E_3 = \frac{m_4}{m_3 + m_4}(Q + K) + V \cos \varphi \sqrt{\frac{2m_3m_4}{m_3 + m_4}(Q + K)} + \frac{1}{2}m_3V^2, \quad (6)$$

where Q is the energy released by the fusion reaction, $K = \frac{1}{2}m_1m_2v^2/(m_1 + m_2)$ is the relative kinetic energy of the reactants, $\vec{v} = \vec{v}_1 - \vec{v}_2$ is the relative velocity, $\vec{V} = (m_1\vec{v}_1 + m_2\vec{v}_2)/(m_1 + m_2)$ is the center-of-mass velocity, and φ is the angle between \vec{V} and the center-of-mass velocity of particle 3. The first term in Eq. 6, $m_4Q/(m_3 + m_4)$, is the nominal birth energy. Generally, the energy released in the reaction Q is much larger than the initial kinetic energy of the reactants K but, because the second term in Eq. 6 is proportional to \sqrt{KQ} , large shifts in the nominal birth energies are possible, particularly for beam-beam and beam-plasma reactions. For thermonuclear reactions, the Doppler shifts and broadenings are more modest; for this case, the energy spread (FWHM) of the fusion reaction products is approximately proportional to $\sqrt{T_i}$ [51].

The energy spectrum of 2.5 MeV neutrons produced in thermonuclear reactions has been measured on many tokamaks [15,29,52–58]. Figure 4 shows a representative thermonuclear spectrum from JET. As expected, the Doppler broadening is greater in plasmas with beam-plasma reactions than in plasmas with thermonuclear reactions alone (Fig. 4). Thermonuclear energy spectra of 15 MeV protons [59,60] and of 1 MeV tritons and 3 MeV protons [61–63] have also been measured. Beam-plasma neutron spectra have been measured during deuterium beam injection in ORMAK [64], PLT [53], and JET [65,15,58]. The spectrum of 15 MeV protons during $D^o \rightarrow {}^3\text{He}$ heating is also rather broad [66,67] and the FWHM of 15 MeV protons produced by burnup of 0.8 MeV ${}^3\text{He}$ ions is 2.5 MeV [60]. Significant Doppler broadenings are also observed in the spectra of escaping 3 MeV protons during lower hybrid heating [68,69,62]. The largest energy distortions are observed during ion cyclotron heating [66,67,70,59,71]. In PLT, energy broadenings as large as ~ 1 MeV were observed (Fig. 5); up and down shifts of ~ 1.5 MeV are observed in JET [71]. Examination of Eq. 6 indicates that the Doppler shift is nearly the same for both reaction products. Thus, the “3.7 MeV alphas” produced in $d({}^3\text{He},\alpha)p$ reactions during rf heating can have energies that range from 2–5 MeV [72].

Another complication introduced by Doppler broadening (Eq. 6) is that the fusion product distribution function need not be isotropic if the reactants are anisotropic (Fig. 5). The d-t and d- ${}^3\text{He}$ reactions are isotropic in the center-of-mass frame, so deviations from isotropy appear in order $\sqrt{K/Q}$. The d-d reactions are anisotropic in the center-of-mass frame [73–76], so even greater distortions are possible for the d-d reaction products.

Bulk rotation of the plasma has two effects on the creation of fusion products. One effect, which was observed on ASDEX [77,57], is a Doppler shift in the birth energy.

²For 15 MeV protons (which are the fastest fusion products), $(v/c)^2 = O(0.01)$. Of course, for reactions involving gamma rays, the full relativistic expression is needed.

A second effect, observed during tangential neutral beam injection [78,79,57,80], is a reduction in the beam-plasma reaction rate because the relative velocity between beam ions and thermal ions is reduced.³

The profile of fusion products created in beam-plasma and beam-beam reactions depends upon the spatial distribution of beam and rf-accelerated ions and is discussed in the next two subsections.

2.2. Neutral Beam Injection

By undergoing a charge exchange or electron impact ionization reaction, an injected fast atom can ionize and become confined by the magnetic field. The probability of ionization depends upon the temperature, density, and composition of the plasma and upon the energy and species of the atom.

Hydrogenic beam injectors accelerate monotonic, diatomic, and triatomic hydrogen ions, resulting in an injected beam that has three energy components (known as the *full-energy*, the *half-energy* and the *third-energy* components). Because little energy is exchanged in charge-transfer or electron-impact reactions, beam ions are created with three distinct energies E_b , $E_b/2$, and $E_b/3$, where E_b is the injector acceleration voltage. The fraction of ions in each component depends upon the properties of the particular source.⁴

Ionization cross sections and rates are compiled in Ref. [81]. Recent studies [82,83] have reexamined various atomic cross sections and reported results which deviate from older measurements [84–86]. The cross section can also be effectively enhanced by multi-step ionization processes [87–89]. In practice, the deposition profile of the injected neutrals is calculated numerically with a computer code such as TRANSP [90,91].

The injected neutral beam is attenuated by ionization events. Measurements of the fraction of the beam that “shines through” the plasma test the validity of the deposition calculations. Calorimeters mounted on the wall opposite one of the beam lines measured this beam *shinethrough* in TFR [39,92]. The results are shown in Fig. 6. The experimental shinethrough is 15% less than predicted using the older cross-section measurements [85,86] but 20% larger than predicted with the multi-step cross sections.

Measurements of a 30 keV helium beam on JT-60 found that the measured shinethrough is $\sim 20\%$ less than expected [93].

On TFTR [94], measurements of the central density rise immediately following beam injection allowed an accurate test of beam deposition physics (Fig. 7). The data agree well with the calculations based upon the older cross-section measurements [84–86], although the authors conclude [94] that the new tabulations including multi-step processes would also agree well.

A different way to study beam deposition is to measure the Doppler-shifted H_α light emitted by the neutral beams. Measurements of ~ 75 keV hydrogen neutrals with a multichordal spectrometer in DIII-D [95] found better agreement with the data when multi-step ionization processes [88] were incorporated in the calculation. Data from JET agreed to within $\sim 15\%$ with attenuation calculations that include multistep processes [96–98].

³The beam-plasma reactivity of trapped ions is enhanced by plasma rotation [78], however.

⁴Helium beams, of course, have only a full-energy component.

Another test of beam deposition physics utilizes measurement of the profile of beam-plasma fusion reactions following a short beam pulse. For a sufficiently short neutral beam pulse, created beam ions do not have time to thermalize or diffuse, so the fusion profile (Eq. 1) only depends upon the nuclear cross section σv , upon the deuterium density profile $n_d(\vec{r})$, and upon the beam deposition profile $n_b(\vec{r})$. The measured TFTR profile and the profile calculated by TRANSP (using the old cross-section formulations [84–86]) agree to within $\sim 20\%$ (Fig. 8).

During steady-state neutral-beam injection, the profile of fusion reactions is affected by beam-ion thermalization and diffusion as well as the deposition profile. Nevertheless, the measured and the computed profiles are consistent in all reported cases except one [99], including the d-d neutron profile in PLT [42], JET [65] and TFTR [99], the d-d proton profile in PLT [69], the d-t neutron profile in JET [1], and the d- ^3He proton profile in TFTR [100].

In summary, multi-step calculations of beam deposition are accurate to within $\sim 20\%$.

2.3. Radio Frequency Heating

Fast ions are created by radio waves in two frequency bands: the ion cyclotron range of frequencies (ICRF) and the lower hybrid (LH) band. In this section, the characteristics of the fast-ion populations observed during ICRF (Sec. 2.3.1) and LH (Sec. 2.3.2) heating are described; detailed discussion of the mechanisms responsible for fast-ion acceleration is deferred to Sec. 3.2. An overview of rf heating in tokamaks appears in the book by Golant and Fedorov [101].

2.3.1. Ion Cyclotron Range of Frequencies

The most energetic and most intense fast-ion populations created by wave heating occur during ICRF heating of a plasma that contains a majority species (often deuterium) and a minority species (often hydrogen or ^3He). The toroidal magnetic field is adjusted so that the frequency of the fast wave launched by the ICRF antenna resonates with the cyclotron frequency of the minority ions near the center of the plasma. (Because of the $1/R$ dependence of the tokamak toroidal field, the minority ions resonate with the wave at a particular major radius known as the *resonance layer*.) The waves are launched from the low-field side so that they encounter the resonance layer before they reach a mode conversion layer. In this heating regime, strong acceleration of the minority ions is observed.

Fast-ion populations during hydrogen minority heating were first observed on T-4 using a mass-resolving charge-exchange diagnostic [102–104]. At low energies, the perpendicular hydrogen distribution function was approximately a Boltzmann distribution but, at higher energies, there was a non-Maxwellian tail (Fig. 9). Proton tails during hydrogen minority heating have been observed by neutral-particle analyzers on many tokamaks, including PLT [105–107], JIPP T-II [108], JFT-2 [109], TFR [110,111], ASDEX [112,113], JET [114,115], Alcator C [116], and TORE SUPRA [117].

On JET, measurements of gamma rays produced in fusion reactions between energetic protons and oxygen impurity ions demonstrate the presence of protons with energies in excess of 7.5 MeV [71]. Fusion gammas produced in the $d(p,\gamma)^3\text{He}$ reaction

[118] and in reactions with carbon [71,65] and beryllium [71] are also observed. The prominent 4.4 MeV line produced by reactions between energetic protons and carbon impurities is shown in Fig. 10. The data imply that about 1.5% of the protons inside the 0.5 m radius have energies above 5 MeV [65].

Although early measurements at relatively low power suggested that the hydrogen tail was isotropic [102–105], later work conclusively demonstrated that the distribution is anisotropic. Measurements of the angular distribution of the passive charge-exchange flux in PLT [106] found strong peaking of the distribution at a particular analyzer orientation (Fig. 11). The peak in the signal was produced by banana-trapped protons that have their turning point in the resonance layer; presumably, these protons gain perpendicular energy in the resonance layer. Further support for this interpretation was obtained using a calorimeter probe at the plasma edge [119,120]. The probe signal increased with increasing power and decreasing proton concentration and peaked at the angle that corresponds to trapped ions with turning points in the resonance layer.

Additional evidence that the energetic protons have their turning points near the resonance layer was obtained by scanning the resonance layer across the line of sight of a vertically viewing analyzer in TFTR. The passive charge exchange signal of 100 keV protons dropped two orders of magnitude when the layer was shifted ~ 20 cm away from the analyzer sightline [121]. The passive charge exchange data from a poloidal array of analyzers on JET show the largest tail for the chord that views through the magnetic axis [114], suggesting that the hydrogen tail is concentrated in the plasma center for central ICRF heating.

The most convincing demonstration of the anisotropy of the proton distribution function is from comparisons of the perpendicular stored energy (from the plasma diamagnetism) and the equilibrium stored energy (from the vertical field). Measurements on JET [122–124] and TEXTOR [125] show that most of the energy in the hydrogen tail distribution is in the perpendicular direction.

Very energetic perpendicular tails are also observed when ^3He is employed as the minority species. Most experiments employ deuterium as the majority species but, by using ^4He majority plasmas, Hammett *et al.* were able to measure an energetic ^3He tail (up to 150 keV) with passive charge exchange in PLT [126] and Petrov *et al.* observed a ~ 1 MeV tail on JET [127]. With deuterium as the majority species, $\text{d-}^3\text{He}$ fusion reactions occur in large numbers, as first demonstrated in PLT through detection of 15 MeV protons [128,120]. The data imply ^3He tail energies of 100–400 keV [66]. Spectroscopic measurements demonstrate [67] that the reacting ^3He tail ions are strongly anisotropic (Fig. 5). The spatial distribution of the $\text{d-}^3\text{He}$ reactions was measured in PLT through detection of 3.7 MeV alphas [129]. The data show that most of the reactions occur within 8 cm of the resonance layer (Fig. 12), which implies that the energetic ^3He tail ions that produce the reactions are also strongly concentrated in the plasma center.

Fusion reaction measurements of the ^3He tail have been extended to higher tail energies on JET. Both the 15 MeV proton [59,71] and the 16.6 MeV gamma from the weak $\text{d}(^3\text{He},\gamma)^5\text{Li}$ branch [130–134,71,135,136] are observed. The data suggest ^3He tail temperatures in the range of 1 MeV [133,136] and a total fast energy content of ^3He ions in excess of 1.4 MJ [71,136]. Measurements of the 15 MeV proton spectrum [71,59] and of gamma rays produced in reactions with beryllium impurities [136] also indicate a very energetic ^3He distribution. The depth profile of ^3He embedded in wall samples implies energies in excess of ~ 3 MeV [137].

When the resonance layer is moved 10 cm away from the line-of-sight of the vertically viewing JET fusion gamma detector, the observed gamma ray intensity falls by a factor of 2.5 [132], which is consistent with the idea that most of the reactions are produced by ^3He ions on trapped orbits which turn at the resonance layer.

On TFTR, the ^3He tail is studied through detection of the $d\text{-}^3\text{He}$ alpha particle with scintillators at the plasma edge [72]. The gyroradius distribution of the escaping alphas suggests a ^3He tail temperature in the range of 0.4-0.8 MeV. The pitch-angle distribution of the escaping alphas is consistent with a peaked $d\text{-}^3\text{He}$ reaction rate profile.

Comparison of the stored energy derived from diamagnetic loop data and the stored energy implied by the plasma equilibrium indicates that the ^3He tail population is strongly anisotropic in JET [131,133,124].

In summary, when fast waves are launched from the low-field side in a plasma with a resonant minority species (either hydrogen or ^3He), all of the available measurements indicate that an energetic population of trapped ions is created within 10 cm of the resonance layer.

Although the largest tails are created during minority heating, fast-ion tails are also observed with other ICRF heating schemes. Fast waves launched from the high-field side (inside) of the tokamak created perpendicular fast-ion tails (measured with passive charge-exchange) in JFT-2 [138,139], ST [140], and JIPP T-IIU [141]. On JFT-2, the deuterium majority distribution function was distorted when the hydrogen concentration was 2-4% [139], while on JIPP T-IIU a weak hydrogen tail was observed in the mode conversion regime (hydrogen concentration $\simeq 30\%$) [141].

As well as damping on a minority species at the fundamental frequency, fast waves launched from the low-field (outside) of the tokamak can damp at the second harmonic of the cyclotron frequency. A distorted distribution function during second-harmonic heating was first reported on PLT [142,120], and was subsequently measured on JFT-2 [109], ASDEX [113], and JT-60 [143,144]. The PLT studies employed active and passive charge exchange measurements in both the perpendicular and parallel directions [142] and 3 MeV proton measurements from the $d(d,p)t$ fusion reaction [68]; the measurements showed that the fast ions were more energetic in the perpendicular direction and were concentrated in the plasma center. On JT-60, proton energies up to 140 keV have been measured during second-harmonic heating [143] (Fig. 13). Second harmonic heating is observed even in the presence of strong minority damping [109,145], when the resonant particles are the minority [143], during combined fundamental and second-harmonic heating [146], and in plasmas with comparable concentrations of hydrogen and deuterium [145].

Fast-wave second-harmonic heating from the low-field side can also accelerate beam ions above the injection energy, as shown with charge-exchange diagnostics for hydrogen beam ions in JT-60 [144,147,148] and for deuterium beam ions in PLT [120], ASDEX [149], JET [150,151], and TFTR [152]. Active charge-exchange measurements show that the energetic particles are concentrated near the center of the plasma [148]. In JET, fusion gamma ray measurements indicate deuterium energies in excess of 1.7 MeV during second harmonic heating of deuterium beam ions [65].⁵ Gamma ray spectra for hydrogen minority heating with and without beam injection are shown in Fig. 10. During beam injection, second-harmonic heating of deuterium is increased and fundamental heating

⁵Broadening of the spectrum is also observed at higher ICRF powers without neutral beam injection; in this case, background ions from a hotter plasma may be accelerated.

of hydrogen is reduced, causing the gamma spectrum to shift from hydrogen lines to deuterium lines (Fig. 10). During second harmonic heating of hydrogen in ASDEX without a Faraday shield a deuterium tail was accelerated in the plasma edge [153].

A few experiments have created fast ions with higher harmonic fast-wave heating. On JT-60, beam-ion acceleration during combined hydrogen beam injection and third-harmonic ICRF heating was observed with perpendicular active charge-exchange diagnostics [154,147,155]. Second, third, and fourth harmonic acceleration of hydrogen was observed on Tokapole II [156]. Fourth harmonic deuterium beam acceleration was seen on JET [157]. On JIPP T-IIU, acceleration at the fifth or sixth harmonic of the deuterium majority was observed, perhaps due to mode conversion to an ion Bernstein wave [158]. On CCT, passive charge exchange data suggested a fast-ion tail for $\omega \gg \Omega$ [159].

In contrast to the fast-wave results, launching the slow wave does not generally produce a fast-ion population [160–163], although an anisotropic majority population and a tail in the minority distribution function was seen during ion Bernstein wave heating on JIPP T-IIU [164–166]. On DIII-D, formation of a tail in the plasma edge was correlated with parametric decay of the ion Bernstein waves [167].

2.3.2. Lower hybrid

All tokamak lower hybrid experiments exhibit a characteristic dependence upon plasma density.

- Below a certain critical density the waves damp on electrons and (if directional waves are employed) current is driven.
- As the density approaches the critical density for current drive a fast-ion population is formed.
- If the density is raised still further, fast-ion tail formation ceases and both heating and current drive are ineffective.

The critical density depends upon the frequency of the lower hybrid waves ω and usually occurs when $\omega/\omega_{LH} \lesssim 2$, where the lower-hybrid frequency ω_{LH} is a function of density. Neutron data from Alcator A [168,169] illustrate this behavior (Fig. 14). For densities below about $1.5 \times 10^{14} \text{ cm}^{-3}$, the neutron emission does not increase during the lower hybrid pulse but, above this density, a large enhancement in $d(d,n)^3\text{He}$ reactions occurs due to formation of a deuterium tail. Above $\sim 2.2 \times 10^{14} \text{ cm}^{-3}$, application of the lower hybrid pulse has no effect on the neutron rate.

Formation of a fast-ion population near the critical density has been reported on Petula [170], Petula-B [171], JFT-2 [172–174], PLT [68,69], WEGA [175], JIPP T-II [176], ASDEX [177,178,149,179,62,180,181], Alcator C [182], and FT-2 [183]. The fast-ion distribution function measured with charge exchange appears bi-Maxwellian, with relatively modest ($\sim 10 \text{ keV}$) tail temperatures typically observed [68,178] and a fairly isotropic angular distribution [68]. Spectral measurements of 3 MeV protons [68,69,179,62] and 1 MeV tritons [179,62] produced in $d(d,p)t$ fusion reactions indicate that the mean energy of the reactants is roughly 20 keV, which is consistent with the charge-exchange spectra. The bi-Maxwellian distribution function is the result of an abrupt energy threshold for acceleration by the waves. Just above this minimum energy E_{min} , the charge-exchange flux increases rapidly when the lower hybrid is applied, as

expected for direct heating [183] (Fig. 15). Just below E_{min} , the flux increases gradually on a collisional timescale (Fig. 15). This threshold energy is typically ten times larger than the central ion temperature T_{i0} (Table 2), scales with T_{i0} [183], and is independent of the rf power [171,183]. Comparison of different parallel wavelength spectra in WEGA found a lower value of E_{min} and a more intense tail for higher values of $n_{||}$ [175]. The critical density for tail formation depends only weakly upon toroidal field. In terms of the ion plasma frequency ω_{pi} , tail formation occurs for $\omega \sim \omega_{pi}$ (Table 2). In tokamaks with both hydrogen and deuterium, the proton tail is much larger than the deuterium tail [184]. (In Table 2, the mass of the experimentally observed fast ions is employed in the calculation of ω_{pi} .)

The spatial location of the fast-ion tail seems to depend upon the density profile (Table 2). On FT-2, passive charge-exchange profiles suggested that the tail moves from the edge to the center with increasing density [183]. Both edge and central profiles have been observed on other tokamaks, but the density dependence was not reported. The d-d neutron profile from Alcator A (Fig. 16) [169] indicates that the tail ions are located near the center of the plasma. On PLT, measurements with an array of 3 MeV proton detectors found evidence of fast ions both in the plasma center and in the plasma edge, but implied that the density of fast ions was largest in the plasma interior [69]. The time evolution of the neutron and proton signals also suggest a central tail [185]. In JFT-2 [173], the rate of decay of the tangential charge-exchange signal indicated a central tail. In contrast, d-d proton [179] and active charge-exchange [178] data from ASDEX suggest that the tail ions are concentrated in the edge (Fig. 17). The rapid decay of the charge-exchange signal following the lower hybrid pulse and the weak effect of the lower hybrid on the neutron emission suggest that the ion tail in Alcator C was at the plasma edge [182]. As indicated in Table 2, these differences appear to correlate with the ratio of the central density to the line-average density, n_{e0}/\bar{n}_e . For peaked profiles ($n_{e0}/\bar{n}_e \gtrsim 1.5$), central tail formation is observed but, for broad profiles ($n_{e0}/\bar{n}_e \lesssim 1.3$), the fast ions are created near the plasma periphery. The physical mechanisms responsible for tail formation are discussed in Sec. 3.2.3.

Acceleration of beam ions during combined neutral beam injection and lower hybrid heating is also observed [186,176,187,188,147,189]. In ATC, passive charge exchange measurements at four different pitch angles indicated that injected 26 keV hydrogen beam ions are accelerated in the perpendicular direction [186]. In JT-60, perpendicular charge-exchange measurements indicate that injected 70 keV protons are accelerated up to 200 keV, with a tail temperature of ~ 60 keV [188]. Both passive channels and an analyzer with a crossed-beam geometry observe beam acceleration [187], which implies that at least some of the energetic ions are located near the plasma center. The long decay time of the accelerated ions (~ 200 ms) supports this conclusion as well [188]. Modelling of the data suggests that the largest concentration of accelerated beam ions is at $r/a \simeq 0.5$ [188]. Variation of the frequency of the lower hybrid waves shows that beam acceleration occurs at higher densities for higher frequencies [189,147], as shown in Fig. 18. When the beam injection energy is reduced to 40 keV, the critical density at which acceleration occurs increases $\sim 40\%$ [189].

Experimentally, changes in the polarization of the launched wave have little effect on ion-tail formation. Perpendicular charge-exchange measurements on JIPP T-IIU [190] and neutron and charge-exchange measurements on PLT [191] indicate that a fast-ion tail forms at nearly the same density for fast-wave antennas as for slow-wave antennas.

In the PLT experiment, the passive charge-exchange signal decayed quickly when the fast-wave pulse turned off [191], indicating that at least some of the fast ions were located in the edge region.

3. Velocity Distribution

The velocity distribution function of a fast-ion population changes when fast ions are created or destroyed (through reactions or losses from the plasma) and through interactions with the electromagnetic fields. In principle, a complete theoretical treatment of the evolution of the fast-ion distribution function could be obtained by individually tracking the interactions of all of the fast ions, but this is a hopelessly complex task. Three basic simplifications are almost always employed. The first is to note that the time scales associated with modifications to the distribution function are generally considerably longer than the characteristic times associated with orbital motion. For example, little change in the distribution function occurs during a cyclotron period, so the phase of the velocity vector in the plane perpendicular to the field can be safely ignored. Averages over other periodic motions, such as the drift orbit, are also commonly employed. The second simplification is to note that, in typical tokamak plasmas, collisions between fast ions occur infrequently compared to collisions between fast ions and thermal ions, since the fast-ion density is usually an order of magnitude smaller than the thermal density. Jassby [4] discusses modifications to the theory when $n_f = \mathcal{O}(n_e)$. The third basic simplification is to ignore all collisions except those associated with small-angle binary Coulomb scattering. The objective of experimental studies is to ascertain if this highly simplified theoretical model adequately describes the evolution of the distribution function.

At first sight, these approximations appear too crude to describe the fast-ion behavior. Figure 19 illustrates schematically the spectrum of electric field fluctuations that interact with the fast ions. In a cartoon fashion, the spectrum is sketched as a function of “wavelength”; in reality, to evaluate the actual interactions one must consider the three dimensional nature of the wavevectors, the frequencies and polarizations of the waves, and electromagnetic as well as electrostatic fluctuations. Nevertheless, Fig. 19 illustrates the various types of interactions and gives a rough indication of the relevant scalelengths.

Large Energy Transfer (LET) Collisions: Occasionally, a fast ion collides directly with another particle at a distance comparable to the classical distance of closest approach b_0 . These collisions can cause a nuclear or charge-exchange reaction, or can scatter the velocity vector of the fast ion through a large angle due to the Coulomb interaction (known as a *knock-on* collision) or due to nuclear scattering [192]. The cross section for deflection due to these isolated single scattering events is approximately two orders of magnitude smaller than for deflections caused by multiple scattering, so they are usually neglected, although they can be important in the high-energy tail of the distribution function.

Coulomb Scattering: At distances larger than b_0 , a collision between a fast ion and another particle only changes the velocity vector of the fast ion by a small amount. For distances greater than the Debye length λ_D , the field associated with an individual particle is shielded by the plasma, so binary collisions become unimportant. The cumulative effect of many small-angle scattering events suffered in binary collisions is the dominant collisional mechanism in most tokamak plasmas.

Drift and MHD waves: In the derivation of a collision operator from first principles, terms associated with the shielding and dielectric properties of the plasma appear.

If all the plasma waves are stable, a fairly simple operator that has the form of the Fokker-Planck equation is obtained [193]. An actual tokamak plasma contains not only damped normal modes, but a host of unstable modes as well, all of which are capable of altering the fast-ion distribution function. The interaction of fast ions with drift waves and other fluctuations is neglected in the standard treatments of the fast-ion distribution functions.

RF waves: In addition to the spectrum of waves associated with instabilities, waves launched by external antennas can interact with the fast ions. Acceleration by rf heating is usually retained in the standard treatments [194].

DC electric fields: Since the loop voltage parallel to the magnetic field is generally very modest in a tokamak (~ 1 V), acceleration by DC electric fields usually have a small effect on the evolution of the fast-ion distribution function in large tokamaks. In practice, theoretical treatments usually neglect radial electric fields and retain parallel electric fields.

With these approximations, the evolution of the fast-ion distribution function f is governed by the Fokker-Planck equation and can be written in the form

$$\frac{\partial f}{\partial t} = \mathcal{S} + \mathcal{C} + \mathcal{Q}, \quad (7)$$

where \mathcal{S} represents sources (such as from neutral beam injection) and sinks (such as charge exchange losses or unconfined orbit losses). Sources were discussed in Sec. 2 and sinks are considered in Sec. 3.3. \mathcal{C} represents the effect of Coulomb scattering on the distribution function and is discussed in the next section. \mathcal{Q} represents modifications associated with electric fields such as those introduced by rf heating. Acceleration by electric fields is discussed in Sec. 3.2.

3.1. Coulomb scattering

In classical Coulomb scattering theory, collisions between a fast ion and the background plasma are approximated by binary Coulomb collisions at distances between the distance-of-closest approach b_0 and the Debye length λ_D . The ratio of λ_D to b_0 is known as Λ ; a convenient compilation of formulas for Λ_e and Λ_i (in general λ_D and b_0 are different for ions and electrons) appears in the *NRL Plasma Formulary* [195]. Theoretically, the Coulomb scattering formulas are accurate through order $1/\ln \Lambda \simeq 5\%$.

Fast ions are generally characterized by a velocity v_f that is intermediate between the electron thermal velocity v_e and the ion thermal velocity v_i , $v_e \gg v_f \gg v_i$. Since the Coulomb cross section is determined by the relative velocity of the scatterers, this implies that the Coulomb scattering rate with electrons is determined by v_e , while the scattering rate with bulk ions is nearly independent of v_i . The relative importance of electron and ion friction depends upon both v_e and v_f . The fast-ion energy at which the electron friction just balances the bulk-ion friction is known as the *critical energy* E_{crit} and is given by

$$E_{crit} = 14.8 A_f T_e \left\langle \frac{Z_i^2}{A_i} \right\rangle^{2/3}, \quad (8)$$

where A_f is the atomic number of the fast ion, T_e is the electron temperature, and

$$\left\langle \frac{Z_i^2}{A_i} \right\rangle = \frac{\sum_i n_i (Z_i^2/A_i) \ln \Lambda_i}{n_e \ln \Lambda_e} \quad (9)$$

is the average charge-to-mass ratio of the bulk ions. For energies larger than E_{crit} , the electron drag predominates. In this regime, since ions are much more massive than electrons, the fast ions scatter little in direction but, like a bowling ball in a sea of marbles, a fast ion gradually decelerates without scattering in pitch angle. For energies below E_{crit} , collisions with thermal ions predominate. In this regime, pitch-angle scattering (Sec. 3.1.2) and energy diffusion (Sec. 3.1.3) are appreciable.

A standard theoretical review of Coulomb scattering is given by Sivukhin [196]. A complete, convenient summary of formulas appears in the *NRL Plasma Formulary* [195]. We mention two of the most useful formulas here. The slowing-down time on electrons first defined by Spitzer [197] is

$$\tau_{se} = 6.3 \times 10^8 \frac{A_f T_e^{3/2}}{Z_f^2 n_e \ln \Lambda_e}, \quad (10)$$

where Z_f is the fast-ion charge number, T_e is the electron temperature in eV, n_e is the electron density in cm^{-3} , and $\ln \Lambda_e \simeq 16$ is the Coulomb logarithm. Stix [198] introduced the time for a typical fast ion of energy E_f to thermalize,

$$\tau_{th} = \frac{\tau_{se}}{3} \ln \left[1 + \left(\frac{E_f}{E_{crit}} \right)^{3/2} \right], \quad (11)$$

where τ_{se} and E_{crit} are given by Eqs. 10 and 8, respectively. The thermalization time τ_{th} includes the effects of both electron and bulk-ion drag.

When incorporated in the Fokker-Planck equation (Eq. 7), the Coulomb operator \mathcal{C} (neglecting magnetic trapping) is [199]

$$\begin{aligned} \mathcal{C} &= \frac{1}{\tau_{se} v^2} \frac{\partial}{\partial v} [(v^3 + v_c^3) f] \quad (\text{deceleration}) \\ &+ \frac{1}{2\tau_{se} v^2} \frac{\partial}{\partial v} v^2 \left[\frac{v_e^2 m_e}{m_f} + \frac{v_c^3 v_i^2 m_i}{v^3 m_f} \right] \frac{\partial f}{\partial v} \quad (\text{energy diffusion}) \\ &+ \frac{1}{2\tau_{se}} \frac{m_i}{m_f} \frac{Z_{eff}}{[Z]} \frac{v_c^3}{v^3} \frac{\partial}{\partial \zeta} \left[(1 - \zeta^2) \frac{\partial f}{\partial \zeta} \right]. \quad (\text{pitch - angle scattering}) \end{aligned} \quad (12)$$

Here v is the fast-ion speed, $\zeta = v_{||}/v$ is the normalized velocity parallel to the magnetic field, $v_c = \sqrt{2E_{crit}/m_f}$ is the *critical velocity* at which the electron friction equals bulk-ion friction, v_e and v_i are the thermal speeds of the bulk electron and ion populations (assumed Maxwellian), m_e , m_i , and m_f are the masses of electrons, bulk ions, and fast ions, respectively, the effective charge $Z_{eff} = \sum_j (n_j Z_j^2) \ln \Lambda_i / (n_e \ln \Lambda_e)$ (the summation is over all background ion species, with i denoting the dominant species) and the average charge $[Z] = \frac{1}{n_e} \sum_j n_j Z_j^2 (m_i/m_j)$. In the following subsections, rates of deceleration, pitch-angle scattering, and energy diffusion predicted by the Coulomb scattering theory are compared with experimental values.

3.1.1. Deceleration

The deceleration of fast ions agrees well with classical theory over a wide range of fast-ion energies and plasma temperatures and densities. Figure 20 summarizes published comparisons of the time evolution of a fast-ion signal with classical theory, including passive charge-exchange measurements of beam ions in small machines [200–202],

measurements of the decay of the 2.5 MeV neutron emission following deuterium beam injection [203–208], and measurements of the burnup of 0.8 MeV ^3He ions [209] and 1.0 MeV tritons [210,122,123,211,212]. The data are from relatively stable discharges; cases where changes in the fast-ion signal correlated with the appearance of MHD activity are excluded from Fig. 20. (In the interpretation of the data, fast-ion diffusion is neglected.) Figure 20a shows relative errors estimated from the scatter of the data; few authors attempt to quantify systematic errors (Fig. 20b). The most accurate measurements come from short pulses of deuterium beams into DIII-D [206,207] and TFTR [208]; in this technique a nearly monoenergetic initial velocity distribution decelerates in a background plasma that is virtually unperturbed by the beam pulse, so interpretation of the data is straightforward. The three short-pulse experiments have explored the parameter range $E_b = 36\text{--}96$ keV, $\bar{n}_e = (1\text{--}12) \times 10^{19} \text{ m}^{-3}$, and $T_e = 0.6\text{--}3.9$ keV. The data agree with theory to within $\sim 25\%$ on DIII-D [207] and to within $\sim 15\%$ on TFTR [208]. The deceleration agrees with theory when electron friction predominates and when bulk-ion friction is dominant (for $E_b/E_{crit} = 0.5\text{--}2.4$) [207]. Although the short pulse experiments only test the behavior of a dilute fast-ion population, the measurements after a full pulse of intense beams [203–205] indicate that Coulomb drag determines the slowing-down time for larger values of n_f/n_e as well. The fusion product measurements [209,210,122,123,211,212] show that MeV ions also decelerate classically.⁶

In addition to the quantitative comparisons shown in Fig. 20, rough agreement with time-resolved fast-ion measurements has been reported for beam ions in TFR [39,214] and ATC [215], for 0.8 MeV ^3He ions in PDX [20] and JET [60], for 0.1–0.4 MeV ^3He minority ions in PLT [66], for 1.0 MeV tritons in TFTR [216], and for hydrogen [217] and ^3He [218] minority ions in JET.

Many experimentally determined quantities are sensitive to both the fast-ion confinement and to the rate of fast-ion thermalization. Examples include the absolute magnitude of the neutron emission, the absolute magnitude of the triton and ^3He burnup, the steady-state charge-exchange energy spectrum, and the efficiency of neutral beam current drive. Comparison of these quantities with simulations that assume classical thermalization and negligible diffusion are considered in detail in Secs. 3.3 and 4.3 but we note here that the good agreement between the measurements and the simulations also supports the idea that fast ions decelerate classically.

3.1.2. Pitch-angle scattering

In addition to changing the magnitude of the velocity vector through deceleration, Coulomb scattering can modify its direction, a process known as pitch-angle scattering. There has not yet been a rigorous measurement of the pitch-angle scattering of fast ions in tokamaks. Several semi-quantitative checks have been performed, however. Most of these involve measurement of the charge-exchange spectrum during neutral-beam injection as a function of the orientation of the analyzer. Figure 21 shows a representative example of the technique. The steady-state neutral-particle spectrum is customarily plotted on a semi-log plot as a function of energy for various analyzer orientations. The data are compared with simulations of the expected spectrum calculated from the beam

⁶For very long slowing-down times ($\tau_{se} \gtrsim 2$ s) in JET, an anomaly in the time evolution of the triton burnup is observed [213]. The time evolution of the signal suggests that the anomaly is caused by anomalous confinement rather than anomalous slowing-down, so this measurement is not included in Fig. 20.

deposition profile, the Coulomb scattering rates, and a calculated neutral-density profile n_0 . Charge-exchange and prompt losses are normally included in the simulation.

Rough agreement of the steady-state charge-exchange spectrum during neutral beam injection with simulations was observed on CLEO [199,200], ORMAK [219], ATC [215,201], DITE [220], T-11 [221–224], TFR [39,35,214], ISX-B [225,204], PDX [226], JET [227], JT-60 [228,229], and TFTR [230,231]. Studies with multiple chords at different pitch angles on ATC [215], PDX [226], ISX-B [204], and TFTR [231] are consistent with classical pitch-angle scattering. The slowing-down spectrum of helium beams in JET measured by charge-exchange recombination spectroscopy are also roughly consistent with the expected spectrum [232].

Although many authors conclude that their spectral measurements validate classical theory [199–201,223–225,204,226,228], none of the studies quantify the accuracy of this claim. Uncertainties in the theory associated with uncertainties in T_e , T_i , n_e , Z_{eff} , q , and n_0 are large, but are generally not reported. Interpretation of the results is further complicated by the simultaneous dependence upon the deceleration, pitch-angle scattering, energy diffusion, and loss rates, as well as any possible dependence upon anomalous transport. In our estimation, large deviations ($\sim 50\%$) from the classical pitch-angle scattering rate are compatible with the spectral data.

The time evolution of the tangential charge-exchange signal during perpendicular injection into ATC was in agreement with the expected rate of pitch-angle scattering [215], but the uncertainty in Z_{eff} (inferred from the plasma conductivity) was large.

On PLT, charge-exchange measurements of beam ions that scattered onto barely trapped banana orbits gave qualitative support for pitch-angle scattering theory, but uncertainties in the edge neutral density precluded quantitative agreement [233]. The deuterium charge-exchange data from T-11 during $H^0 \rightarrow D^+$ neutral-beam injection suggested the importance of large-energy transfer collisions (possibly off of molybdenum impurities) [222,223] but alternative explanations for the data (e.g., imperfect mass resolution, deuterium in the beam line) were not discussed, so the results must be viewed as inconclusive. Comparison of the charge-exchange spectra from hydrogen and helium minority tail ions in PLT shows greater anisotropy for hydrogen than for helium, which is consistent with the expected dependence of the pitch-angle scattering rate upon charge and mass [126]. In JET, the anisotropy in the minority tail distribution only appears above a threshold in rf power, suggesting that the pitch-angle scattering rate becomes negligible compared to the slowing-down rate above E_{crit} [132].

In summary, the classical pitch-angle scattering rate is a reasonable working hypothesis, but more definitive tests of the theory are needed. ⁷

3.1.3. Energy diffusion

In addition to the mean deceleration discussed in Sec. 3.1.1, Coulomb collisions introduce a spread in energy about the average value. For fast ions, measurements of this *energy diffusion* are in good agreement with theoretical predictions, although the accuracy of the comparisons has not been quantified fully.

⁷One possibility is to perform time-resolved, multichordal, active charge-exchange measurements (similar to those performed on ATC [215]) on a tokamak that is equipped with accurate T_e , n_e , and Z_{eff} diagnostics.

During deuterium beam injection into a hot plasma, the effect of velocity diffusion on the energy spectrum of fast ions is very evident. In TFTR [230], collisions with electrons and bulk ions scatter some beam ions up to energies nearly twice as large as the injection energy (Fig. 22). Physically, this high energy tail is due to very fast particles from the tail of the Maxwellian background population that collide with the fast ions “from behind”, thereby kicking the fast ions up in energy. The slope of the distribution function above the injection energy is consistent with the expected slope found from scattering theory and the measurements of T_e and T_i ; [230]; the accuracy of the comparison is determined primarily by the uncertainties in T_e and T_i , which we estimate as $\sim 20\%$. With the exception of one early measurement [200], all published charge-exchange spectra from beam-heated plasmas are consistent with theory above the injection energy [201,220,223,224,226–228].

Another way to assess energy diffusion is to observe the spread in energy of a short beam pulse as it decelerates. Time resolved charge-exchange measurements from ATC [201] and TFR [202] using this approach are consistent with theoretical expectations.

Measurements of the ^3He burnup following beam injection in TFTR also are consistent with classical energy diffusion [234].

3.2. Acceleration

Collisions tend to reduce the fast-ion population to a thermal distribution. External sources of free energy can combat this tendency and accelerate the fast-ion population to higher energies. In this subsection, we consider the effect of low-frequency electric fields (Sec. 3.2.1), of ICRF waves (Sec. 3.2.2), and of lower hybrid waves (Sec. 3.2.3) on the fast-ion distribution function. A phenomenological discussion of ICRF and of lower hybrid heating was already given in Sec. 2.3; this subsection considers the physical mechanisms responsible for the acceleration.

3.2.1. Low frequency electric fields

A static electric field $\vec{\mathcal{E}}$ parallel to the magnetic field will accelerate particles traveling in the direction of $\vec{\mathcal{E}}$ and decelerate particles travelling in the opposite direction. Theoretically, an applied parallel electric field \mathcal{E}_{\parallel} gives rise to a term in the Fokker-Planck equation [200],

$$\frac{\partial f}{\partial t} = \dots - \frac{Z_f e \mathcal{E}^*}{m_f} \left[\zeta \frac{\partial f}{\partial v} + \frac{(1 - \zeta^2)}{v} \frac{\partial f}{\partial \zeta} \right], \quad (13)$$

where $\mathcal{E}^* = \mathcal{E}_{\parallel}(1 - Z_f/Z_{eff})$ and the other terms are defined in Eq. 12. According to Eq. 13, the applied field is modified by the drift of the electron distribution to an effective field \mathcal{E}^* that both accelerates and distorts the distribution function f .

In an ohmically heated tokamak, the plasma current is driven by the loop voltage. The effect of reversing the sign of the loop voltage on the distribution function of beam ions was studied in CLEO [199,200] and ATC [235,201]. For co-injection of 14.2 keV hydrogen beams in ATC, the peak signal from a tangential charge-exchange analyzer occurred at an energy 0.9 keV larger than for counter injection, consistent with theoretical expectations [201].

In large tokamaks, the ohmic electric field is generally too modest to effect the fast-ion distribution function significantly. During disruptions, however, much larger electric

fields are possible. Rapid ion heating during disruptions was measured on two small tokamaks [236,237], although the acceleration of the ions may have been caused by turbulent heating rather than the induced electric field.

The largest accelerations of fast ions by low-frequency fields are observed when the plasma is compressed by rapidly increasing the vertical (equilibrium) field. The compression occurs on a timescale that is long compared to typical particle orbits but short compared to the Coulomb scattering time of the fast ions. This implies that the constants of the motion μ and p_ϕ should be conserved in the compression. Since $\mu = E_\perp/B$ and the magnetic field is approximately $B = B_0 R_0/R$, the perpendicular energy E_\perp is expected to increase by the compression ratio R_0/R . Conservation of toroidal angular momentum implies⁸ an even greater increase in parallel energy, $E_\parallel \propto (R_0/R)^2$. Accelerations consistent with these predictions have been observed on ATC [235] and TFTR [238,239]. Figure 23 shows representative charge-exchange and neutron data from the TFTR experiment [239]. The parallel deuterium beam ions are observed to accelerate from ~ 80 keV prior to the compression to ~ 150 keV immediately after the compression and the increase in neutron emission is within 15% of the calculated value (Fig. 23). The data from perpendicular charge exchange and from $d(^3\text{He},p)\alpha$ fusion reactions are also consistent with theoretical expectations within experimental error [238,239].

3.2.2. ICRF

In ICRF heating in large tokamaks, the waves tend to be strongly focussed in the plasma center. As the fast ions move along their orbits, they pass through regions where the wave resonates with the cyclotron motion of the fast ions. Each time the ions cross the cyclotron resonance they experience a “kick” in energy. If the phase of these kicks was preserved between successive passes through the resonance layer, the fast ions would oscillate in the phase space island created by the wave. In practice, however, the small level of collisions⁹ between successive transits of the resonance layer is sufficient to decorrelate the orbital motion from the rf field, so the fast ions experience random kicks and gain net energy from the wave. Random small kicks in energy are usually described by quasilinear theory.

A general quasilinear operator that describes the evolution of the particle distribution function under the influence of an uncorrelated spectrum of electromagnetic waves in a uniform magnetic field was derived by Kennel and Engelmann [240]. Stix [194] recognized that this theory could be applied to a single incoherent rf wave in an inhomogeneous field. He averaged the quasilinear operator \mathcal{Q} and solved Eq. 7 for the minority distribution function f during minority heating under the assumption that the acceleration \mathcal{Q} associated with the rf heating is balanced by the friction \mathcal{C} associated with Coulomb collisions. In his derivation, Stix made several simplifying assumptions [194,241].

- During successive passes through the resonance layer the phases are decorrelated. This assumption is well justified theoretically [242].
- An average over the flux surface adequately represents the distribution function. Actually, ions on banana orbits spend more time near the turning points than on

⁸The toroidal angular momentum $p_\phi = mRv_\phi + qRA_\phi$ and the toroidal flux RA_ϕ are conserved during adiabatic compression, so Rv_ϕ is a constant. This implies that $E_\parallel \propto v_\phi^2 \propto R^{-2}$.

⁹or other randomizing process such as intrinsic orbit stochasticity.

the outer leg of the orbit, so the bounce-average of Q is more accurate than the flux-surface average.

- The radial width of the fast-ion orbits are small compared to their mean radial position. This assumption is invalid for strong heating in low-current plasmas, where ions with large poloidal gyroradius are produced.
- The Doppler shift of the wave frequency is negligible ($k_{\parallel}v_{\parallel} \ll \omega$). Retention of finite k_{\parallel} broadens the resonance layer and can result in broader power deposition.
- Only the dominant electric field component is retained.
- The density of the minority ions n_{min} is assumed unchanged by the rf heating. In fact, as the ICRF accelerates particles to high energies, it converts them into trapped particles whose banana tips approach the resonance layer, which increases n_{min} and increases the rf damping.
- The resonance layer is assumed to be on axis. More generally, the power absorbed by the minority ions depends upon R_{res}/R_0 .

With these approximations, Stix derived the fast-ion distribution function below the critical energy E_{crit} , where pitch-angle scattering by background ions keeps the distribution function nearly isotropic, and above the critical energy, where the distribution function becomes highly anisotropic in the perpendicular direction. At high energies, the energy distribution approximates a Boltzmann distribution with a perpendicular tail temperature of T_{Stix}^{\perp}

$$T_{Stix}^{\perp} = T_e + \frac{P_{Stix}\tau_{se}}{2n_{min}}, \quad (14)$$

where P_{Stix} is the rf power density coupled to the minority ions (averaged over a flux surface), τ_{se} is the slowing-down time on electrons (Eq. 10), and n_{min} is the minority density. According to Eq. 14, the tail temperature is determined by the balance between the power absorbed per particle (P_{Stix}/n_{min}) and the rate of energy loss through electron drag ($2/\tau_{se}$).

Comparisons of theory with experiment are complicated by the fact that the fast-ion distribution function is affected by the coupling and propagation of the rf waves, by the magnitude and nature of the wave absorption by the minority species, by the Coulomb collision operator \mathcal{C} , and by any fast-ion transport. In addition, the minority density n_{min} is generally not well known. In light of these complicated dependencies and the many approximations in the theory, the Stix theory agrees surprisingly well with experimental observations. In T-4, the perpendicular charge-exchange spectra were consistent with the Stix model during H-minority heating [104]. During ^3He minority heating in PLT, the dependencies of the $d(^3\text{He},p)\alpha$ reaction rate upon the electron density n_e and temperature T_e , the plasma current I_p , and the rf power P_{rf} were all close to predictions based upon the Stix model (modified to include a simple first orbit loss model) [66]. The $d(^3\text{He},p)\alpha$ reaction rate during deuterium minority heating in a ^3He majority plasma was also consistent [66]. In JIPP T-II, the hydrogen-minority tail temperature measured with passive charge exchange was close to the temperature predicted by a model based upon the Stix formalism [108].

Passive charge-exchange data at various pitch angles were measured for both hydrogen and ^3He minority heating in PLT and compared with simulations based upon a

bounce-averaged quasilinear operator (the Stix model employs a flux-surface averaged operator) [145,241,126]; first-orbit losses (which could be substantial in PLT) were also included in the simulation. Although the fast-wave power deposition was expected to peak strongly on axis, the hydrogen spectra could only be simulated successfully with a hollow deposition profile. Though the discrepancy was smaller, the helium spectra also suggested a broader heating profile than suggested by calculations of wave propagation. Becoulet *et al.*[243] suggest that these discrepancies may reflect a failure of the bounce-averaged quasilinear operator, but their simulations neglect the neutral density profile, which has an important effect upon the charge-exchange spectra. Alternatively, fast-ion transport may account for the discrepancy [241].

The most rigorous tests of the theory of minority heating have been performed on JET [150,131,114,132,134,133,124,136,244]. Because of its large size, large plasma current, and small magnetic field ripple, fast-ion losses are less important in JET than in smaller machines. In addition, modulation of the rf power helps to distinguish the power-deposition profile from the fast-ion response to the waves. Measurements of the response of the electron temperature to modulation of the rf power indicate that the power deposition is centrally peaked and that most of the power flows through the minority species [150,134]. The response of hydrogen minority ions to power modulation was studied using four perpendicular passive charge exchange analyzers that view different radial locations in the plasma [114]. The experiments were performed at low power where the period of the sawtooth instability is independent of the rf modulation period and where the minority distribution function is expected to remain isotropic. The dominant uncertainties in the interpretation of the data are the neutral density profile (which is inferred from the deuterium charge-exchange spectra) and the minority density profile. The data are compatible with the Stix theory if the minority density profile is assumed to peak on axis [114]. Theoretically, the response of the distribution function to modulation of the rf power depends primarily on the quasilinear diffusion operator \mathcal{Q} and upon the rate of energy diffusion associated with Coulomb collisions. The measured response of the hydrogen spectra agree well with theoretical predictions based upon the Stix formalism (Fig. 24) [114].

With the inclusion of finite orbit effects, the perpendicular stored energy associated with the fast-ion tail agrees well with the Stix theory for both hydrogen and ^3He minority heating over the full range of currents in JET [124]. Figure 25 shows data from hydrogen minority plasmas that did not have sawteeth; the agreement between experiment and theory is excellent (better than the estimated systematic error of 20%). In plasmas with large minority concentrations, the experimental values are 1.09 ± 0.10 of the theoretical value [245]; the charge-exchange spectra agree (to within a factor of two) with Stix theory and show the expected dependence upon minority concentration [245]. The distribution function becomes anisotropic at the expected power level as well [132]. Gamma-ray measurements of the $d(^3\text{He},p)\alpha$ reaction rate during ^3He minority heating lend further support to the theory. The measured rate agrees to within $\sim 50\%$ with the Stix theory over variations of nearly two orders of magnitude in reaction rate [131,133,136,246], with the dominant uncertainties stemming from the uncertainties in the deuterium and ^3He densities.

In summary, during minority ICRF heating, cyclotron absorption and Coulomb drag upon electrons are the dominant processes that determine the velocity distribution of energetic tail ions.

Theoretically, second harmonic ICRF heating is also expected to be described by quasilinear diffusion in velocity space. In this case, Q is proportional to the Bessel function $J_1^2(k_\perp v_\perp/\Omega)$. If the fast-ion gyroradius v_\perp/Ω is small compared to the perpendicular wavelength $2\pi/k_\perp$, the quasilinear operator is of the same form as for fundamental heating, but contains an additional multiplicative factor $(k_\perp v_\perp/2\Omega)^2$. Because of this term, the diffusion is stronger for more energetic ions with larger values of $E_\perp \propto v_\perp^2$, so the distribution function deviates from a Boltzmann distribution. Injection of energetic ions with large values of E_\perp can also enhance second harmonic interaction with the waves.

Experimentally, the measured perpendicular charge-exchange spectrum has the expected shape. In PLT, measurements during second harmonic heating of hydrogen showed the characteristic curvature expected for second-harmonic heating and agreed with an isotropic quasilinear theory for reasonable values of absorbed rf power density and perpendicular wave vector [142] (Fig. 26). At higher rf power levels, the spectrum became anisotropic as predicted by theory [142]. In another experiment in PLT, the deuterium spectrum was measured during combined second-harmonic heating of deuterium and fundamental heating of a hydrogen minority [145]. When the rf power was increased both the mean energy and the curvature of the spectrum increased, as more energetic ions become available to interact with the wave [145]. The deuterium spectra measured on JFT-2 were also consistent with the expected shape [139]. An example of the spectrum during second harmonic heating in JT-60 was shown in Fig. 13.

Perhaps the most straightforward test of second-harmonic heating theory was performed by injecting near-perpendicular hydrogen beams into JT-60 while applying ICRF [247,144,148]. Active charge exchange measurements indicate strong heating above the injection energy (Fig. 27). Above the injection energy, the shape of the spectrum is in good agreement with the distribution calculated by an isotropic Fokker-Planck theory (Fig. 27). The slope of the distribution above the injection energy also shows the expected dependencies upon beam power and rf power, and the dependency upon n_e is not inconsistent with theory [247]. The measured change in stored energy is $125 \pm 15\%$ of the expected value [148].

Another test of the theory of rf heating is to study the competition between second harmonic heating of deuterium and fundamental minority heating of hydrogen. An approximate formula for the expected partitioning of power between the deuterium and the hydrogen P_D/P_H is

$$\frac{P_D}{P_H} = \beta_D \frac{n_D}{n_H}, \quad (15)$$

where β_D is the beta of the majority deuterium species and n_H/n_D is the hydrogen concentration. On JFT-2, the power absorbed by the deuterium was larger than expected [139]. As the minority concentration was reduced on PLT, the power to the deuterium increased, but the deuterium absorption increased less gradually than expected [241]. Perhaps losses of minority protons account for these discrepancies [241]. During deuterium beam injection in JET, the enhancement of the neutron emission associated with second-harmonic heating agreed with Eq. 15 (to within 50%) [151] but the neutron energy spectra showed no evidence of a deuterium population with energies higher than the injection energy [65]. In a similar experiment in TFTR, the deuterium charge-exchange spectrum did not change as much as expected during second harmonic heating [152]. In all of these comparisons, uncertainty in the hydrogen density constitutes a major source of error.

Acceleration by waves in the ion cyclotron range of frequencies is observed under other conditions as well, but the data are more difficult to compare with theoretical predictions. In JIPP T-IIU, the charge-exchange spectrum during third and fourth harmonic ion Bernstein wave heating agrees qualitatively with quasilinear theory [166]. Other heating experiments at higher harmonics are summarized in Sec. 2.3.1. Acceleration by ion-cyclotron waves that are driven unstable by the fast-ion population is discussed in Sec. 5.3.

3.2.3. Lower hybrid

It is well established empirically that, under certain circumstances, lower-hybrid waves accelerate fast ions (Sec. 2.3.2), but the physical mechanisms responsible for the acceleration are less well established.

Stochastic ion heating [248,249] is conceptually similar to the Stix theory of minority ICRF heating. Since lower hybrid waves have long parallel wavelengths and short perpendicular wavelengths, the electric field is approximately perpendicular to the magnetic field. The wave frequency ω is very large compared to the ion cyclotron frequency Ω . As a fast ion gyrates around the field line, it receives a kick in energy each time it passes the location where $\omega = \vec{k} \cdot \vec{v}$ (\vec{k} is the wave vector and \vec{v} is the fast ion velocity). For heating to occur (rather than trapping in the wave field), successive kicks must be decorrelated. In stochastic heating, phase mixing between kicks occurs because the islands in phase space that are associated with harmonics of the cyclotron frequency overlap; this island overlap of closely spaced cyclotron harmonics is theoretically predicted to occur at modest electric field amplitudes [248]. The resultant motion is equivalent to motion in incoherent wave fields in a uniform magnetic field [249], and therefore is described by the quasilinear diffusion coefficient derived by Kennel and Engelmann [240]. When this diffusion coefficient is incorporated into the Fokker-Planck equation, the competition between wave acceleration and Coulomb scattering predicts formation of an energetic ion tail. Of course, tail formation only occurs if the resonance condition is satisfied. Resonance occurs for ions with sufficiently large perpendicular velocity v_{\perp} so that $v_{\perp} \gtrsim \omega/k_{\perp}$, where ω/k_{\perp} is the perpendicular phase velocity of the wave. In simple theory, the perpendicular wavenumber is determined by the cold plasma dispersion relation and is a function of the plasma density and of the k_{\parallel} spectrum imposed by the launching antenna.

The most thorough test of this model was performed in JT-60 [187,188,147,189]. In the experiment, low power perpendicular neutral beams were injected to provide a well defined value of v_{\perp} . The lower hybrid waves were launched into low density plasmas, where changes in k_{\perp} due to parametric decay and scattering off fluctuations are minimized. The observed passive charge-exchange spectrum agrees (to within $\sim 50\%$) with the expected distribution function [188]. When the wave frequency and beam energy are varied, tail formation varies with plasma density as expected (Fig. 28) [147,189], thus verifying the expected resonance condition and the validity of the cold plasma dispersion relation for these conditions. The magnitude of the ion heating does not always agree with theory, however [189], so the actual magnitude of the quasilinear diffusion coefficient has not yet been experimentally established.

Another potential mechanism of ion acceleration is ion cyclotron damping. Theoretically, cyclotron damping occurs when the resonance condition $\omega - k_{\parallel}v_{\parallel} = l\Omega$ is satisfied, where l is an integer. This may be the explanation for the acceleration of a tangentially injected beam by lower hybrid waves in ATC [186]. The beam was observed to gain

energy in the perpendicular direction, bulk ion heating was negligible, and acceleration was seen even at relatively low rf power levels, as expected for cyclotron damping [186]. The perpendicular wavenumber k_{\perp} predicted by the cold plasma dispersion relation was too small for direct interaction between the lower hybrid and the beam ions.

Without beam injection, many experiments have noted a direct correspondence between parametric decay of the fundamental lower hybrid wave and tail formation [250,251,169,177,182,178,183]. In these experiments, the tail develops at a lower density than predicted for direct ion heating by lower hybrid waves (that obey the cold plasma dispersion relation). The most detailed study was performed in the small tokamak FT-2 [183]. In this device, the fundamental wave decayed into a daughter lower hybrid wave with $\omega \simeq 0.7\omega_0$ in a narrow region in the plasma [183]. This decay region occurred at a particular density, and moved radially when \bar{n}_e was varied. Fast-ion formation correlated with the appearance of the daughter wave [183]. The observations are consistent with stochastic ion heating by the daughter lower hybrid wave. In other devices, parametric decay was observed at the plasma edge. In this case, the lower hybrid waves may decay into ion cyclotron quasimodes that are heavily damped by ion cyclotron damping [182].

Lower hybrid waves can also scatter off of density fluctuations. The scattering can effectively increase k_{\perp} , with the result that stochastic ion heating occurs at lower values of density than predicted in cold plasma theory. Either this mechanism or parametric decay into a daughter lower hybrid wave probably account for the central tails observed in Alcator A [169], JFT-2 [173], and PLT [69].

In summary, the mechanism of fast-ion acceleration in lower hybrid heating experiments is not well established. Both stochastic ion heating and ion cyclotron damping are probably important under different conditions.

3.3. Loss terms

If acceleration terms are negligible, the Fokker-Planck equation for fusion products or injected beam ions is often approximated by [200]

$$\frac{\partial f}{\partial t} = \mathcal{C} - f/\tau_l + S_0(\zeta, t)\delta(v - v_0), \quad (16)$$

where \mathcal{C} is the collision operator (Eq. 12), v_0 is the birth or injection energy,¹⁰ and S_0 is the creation rate. In Eq. 16, the losses are modelled by an exponential loss time τ_l . In general, τ_l is a function of velocity and pitch angle, but it is often approximated as a constant. If one averages over pitch angle, the steady-state solution to Eq. 16 for velocities between¹¹ $2v_i < v < v_0$ is [4]

$$f = \frac{S_0\tau_{se}}{[1 + (v_{crit}/v_0)^3]^{\tau_{se}/3\tau_l}} (v^3 + v_{crit}^3)^{[(\tau_{se}/3\tau_l)-1]}, \quad (17)$$

where τ_{se} is the slowing down time on electrons (Eq. 10) and v_{crit} is the critical velocity (Eq. 8). If there are no losses, the angle-averaged steady-state, slowing-down distribution is $f \propto (v^3 + v_{crit}^3)^{-1}$. This distribution monotonically decreases with increasing velocity. On the other hand, for strong losses ($\tau_l \ll \tau_{se}$), fast ions do not stay in the plasma long

¹⁰For hydrogenic neutral beam injection, delta functions for the full, half, and third energies are required.

¹¹Energy diffusion is important outside this range.

enough to reach low velocities and the maximum value of f occurs at the birth energy v_0 .

There has not been a rigorous test of Eq. 17. In practice, Eq. 17 is used to infer the loss time τ_l from the measured distribution function, since a quantitative model for the losses rarely exists. The qualitative trends predicted by Eq. 17 have been observed in many experiments, however. In the small ATC device, beam-ion losses due to charge exchange were very strong and the measured neutral-particle distribution peaked near the injection energy [201]. In PDX, a special class of orbits traversed the high neutral density region outside the toroidally localized limiter and the effect of large charge-exchange losses on the neutral-particle spectrum were readily apparent [226]. In TFR, the perpendicular charge-exchange spectrum peaked near the injection energy because of large ripple losses of the injected beam ions. (Ripple losses are discussed in Sec. 4.2.) In PDX, a collective instability known as the fishbone instability (Sec. 5.1) caused large losses of beam ions. By varying the injected beam power, the magnitude of the loss term varied and the shape of the measured charge-exchange spectra (Fig. 29) changed in qualitative agreement with theoretical expectations [252].

4. Confinement

After a fast ion is created (Sec. 2), it changes its velocity and position. In Sec. 3, processes that modify the velocity \vec{v} of the fast ion were examined. In this section, we turn to processes that modify the spatial position \vec{r} .

Fast ions gyrate around the magnetic field while streaming parallel to the field lines (helical orbits). The gyromotion about the magnetic field line is characterized by the gyroradius (in centimeters) ρ_{cm} ,

$$\rho_{\text{cm}} = 14.45 \sqrt{A_f E_{\perp \text{MeV}} / (Z_f B_{\text{Tesla}})}, \quad (18)$$

where A_f and Z_f are the atomic mass and charge numbers of the fast ion, $E_{\perp \text{MeV}}$ is the perpendicular energy in MeV, and B_{Tesla} is the field in Tesla. The gyromotion is apparent in the orbit projections shown in Fig. 1. The effect of the gyromotion on the orbit is usually ignored but this approximation is not always justified. When ρ is a significant fraction of the plasma minor radius a ($\rho/a \gtrsim 0.1$), corrections to a description based solely on the guiding center of the orbit must be retained. For example, in triton burnup studies in PLT ($a = 40$ cm), the triton gyroradius was 11 cm at 2.2 T and calculations indicate that finite gyroradius effects reduced the expected burnup by a factor of two [20].

The first adiabatic invariant μ is associated with the toroidal gyromotion. Unless the field changes at a rate comparable to the frequency of gyromotion Ω or on a scale-length comparable to the gyroradius ρ , $\mu = E_{\perp}/B$ is constant. The dominant spatial dependence of the magnetic field in a tokamak is the radial dependence ($B \simeq B_0 R_0/R$), so μ conservation implies that

$$\mu = E_{\perp}/B \simeq \frac{E_{\perp}}{B_0} \frac{R}{R_0} = \text{constant} \quad (19)$$

along the fast-ion orbit. Since most plasma instabilities have lower frequencies than Ω and do not appreciably modify B on a gyroradius scalelength, fast-ion trajectories usually satisfy Eq. 19.

Because the magnetic field of the tokamak is nonuniform, the guiding centers of the fast-ion orbits drift perpendicular to the field. The *drift orbit* of a particle is determined by these perpendicular drifts and by the free-streaming motion parallel to the field line. Gyromotion and toroidal motion are neglected in the drift-orbit description. The second adiabatic invariant

$$J = \oint v_{\parallel} dl = \text{constant} \quad (20)$$

is associated with the drift motion. [In Eq. 20, the integral is over a complete (closed) drift orbit $\oint dl$.] If the field does not change appreciably on the temporal or spatial scale of the drift orbit, J is conserved. These conditions are often violated by plasma instabilities and J is not always a conserved quantity for actual fast-ion trajectories. Fast-ion drift orbits are discussed in Sec. 4.1.

The drift-orbit description assumes that the magnetic field is axisymmetric. In a real tokamak, the toroidal field is produced by a finite set of field coils and varies in strength as a function of toroidal angle ϕ . This *toroidal field ripple* can affect the confinement of fast ions and is discussed in Sec. 4.2.

In addition to the fields produced by the external coils and by the plasma current, tokamak plasmas exhibit electrostatic and electromagnetic fluctuations caused by instabilities, collisions, and rf waves. Random changes in velocity associated with these fluctuations can cause a fast ion to gradually move away from its initial drift orbit. Fast-ion diffusion induced by fluctuations is considered in Sec. 4.3.

Long wavelength MHD instabilities also modify the tokamak magnetic field configuration by introducing helical distortions to the field. In addition to rippling the flux surfaces, these distortions can affect the confinement of fast ions in a manner similar to the toroidal field ripple. For large amplitude MHD activity, orbit stochasticity may be induced. The effect of MHD instabilities on the confinement of fast ions is considered in Sec. 4.5.

Intense fast-ion populations can drive plasma instabilities (Sec. 5). The resonance between the driven instability and the orbital motion can induce rapid transport of fast ions, as discussed in Sec. 4.4.

4.1. Drift orbit

The drift orbit of a fast ion is determined by the competition between the poloidal component of the parallel motion and the ∇B and curvature drifts caused by the inhomogeneity of the field. In general, three constants of the motion suffice to specify a particular drift orbit.¹² Often the energy E , the magnetic moment μ , and the toroidal canonical angular momentum p_ϕ are selected as the three constants, but other choices may be more convenient [the energy, the pitch angle $\cos^{-1}(v_{\parallel}/v)$, and the major radius R constitute another common choice]. A rough measure of the relative importance of the drifts relative to the parallel motion is given by the size of the poloidal gyroradius ρ_θ relative to the plasma minor radius a . For thermal particles, $\rho_\theta \ll a$, the parallel motion predominates over the gradient drifts, and the particle orbits remain close to the flux surfaces. On the other hand, for fast ions, $\rho_\theta \gtrsim a$, the gradient drifts and parallel motion are comparable, and the orbits do not follow the flux surfaces (Fig. 1).

Very energetic ions are not confined by the poloidal field but strike a first wall component prior to completion of their first drift orbit; these losses are termed *prompt losses* or *first-orbit losses*. In general, whether a particle is lost or not depends upon the magnitude and profile of the plasma current, upon the shape of the flux surfaces, and upon the initial velocity and position. As a rule of thumb, a critical energy E_{loss} can be defined [241],

$$E_{loss} \equiv \frac{2(I_{MA} Z_f)^2}{A_f} \frac{R_0}{a(1 + a/R_0)}, \quad (21)$$

where E_{loss} is in MeV, I_{MA} is the plasma current in MA, Z_f and A_f are the fast-ion charge and mass numbers, and R_0 and a are the major and minor radii of the plasma. A trapped ion at the center of a circular tokamak is barely lost when its energy $E \simeq E_{loss}$. Most of the ions from an isotropic population of energy E are confined if $E < E_{loss}$. On the other hand, if the energy significantly exceeds E_{loss} , most fast ions in an isotropic distribution are lost on their first drift orbit. Equation 21 can be reexpressed in terms

¹²In general, six constants (velocity and position) are needed to specify an orbit but the gyrophase, toroidal angle, and toroidal velocity are ignorable in the drift approximation.

of the plasma current I_{loss} (in MA) required to confine fast ions of energy E_{MeV}

$$I_{loss} = \frac{1}{Z_f} \sqrt{\frac{A_f}{2} E_{MeV} \frac{a}{R_0} (1 + a/R_0)}. \quad (22)$$

A complete specification of the drift orbit requires a knowledge of all three constants of the motion. The topology of fast-ion orbits is complex [253–255]. Figure 30 shows a map of the first-orbit loss boundaries in velocity space for fast ions near the magnetic axis in a circular cross-section tokamak. Fast ions travelling in the direction of the plasma current ($v_{\parallel} > 0$) are called *co-going* and those streaming in the opposite direction ($v_{\parallel} < 0$) are termed *counter-going*. (Note that the direction of the toroidal field has no effect upon the drift orbit.) Several general features are evident:

- For small enough energies, all fast ions are confined. (Ions of equal energy lie on a circle in velocity space.) If the energy is too large, the fast ions are all promptly lost independent of the value of v_{\parallel}/v_{\perp} .
- Circulating particles with parallel velocities $|v_{\parallel}| \gg v_{\perp}$ are better confined than trapped particles with little parallel velocity ($|v_{\parallel}| \ll v_{\perp}$).
- The loss boundary is not symmetric in velocity space. Co-going fast ions are better confined than counter-going ions. The lowest energy unconfined orbit (the cusp of the loss boundary) is for a counter-going particle with large v_{\perp}/v .

The loss boundary shown in Fig. 30 is for a particular particle birth position in the plasma (close to the magnetic axis). At other positions, different boundaries apply, but they usually retain a similar shape. There are exceptions, however, and, in some peculiar instances, the boundary may even be multiple valued [256].

Many experiments have tested the drift-orbit theory. One way to study prompt losses is to measure the burnup of fusion products (Sec. 1.2) as a function of plasma current. The fusion-product source is close to isotropic and is centered around the magnetic axis (Sec. 2.1), so that the technique effectively integrates over velocity space. As the current increases, the poloidal field increases, and the confinement of the fusion products improves. Figure 31 shows data from all reported current scans in the regime where prompt losses are important. The expected variation associated with changes in the fraction of confined orbits is also shown. In addition to the direct effect of the current upon confinement, the plasma current may also affect the magnitude of the burnup indirectly through changes in electron temperature (and possibly deuterium concentration). With the exception of the TFTR data, discharges with strong MHD activity are excluded from Fig. 31. (As discussed in Sec. 4.5, MHD instabilities can degrade the confinement of fast ions.) Theoretically, the prompt losses are expected to decrease dramatically between $I_p \simeq 0.4I_{loss}$ and $I_p \simeq I_{loss}$. The data are in rough agreement with this theoretical expectation for both 1 MeV tritons and 0.8 MeV ^3He ions (Fig. 31).

The burnup technique provides a quantitative, averaged measure of the fast-ion confinement. Other experiments have explored the properties of particular orbits in phase space, as shown schematically in Fig. 30. The sketches illustrate the class of orbit explored in the various experiments. One of the first studies of fast-ion drift orbits was performed by Bol *et al.* on ATC [215]. In this experiment, a neutral beam was injected

into the tokamak at an angle of 7° to the normal. When the direction of the plasma current was reversed, the majority of beam ions were predicted to jump across the loss boundary and become unconfined. The observed passive charge-exchange signal was two orders of magnitude smaller for counter-injection than for co-injection (Fig. 32), verifying that the loss boundaries are asymmetric in velocity space.

Kaita *et al.* have observed two different classes of banana orbits with horizontally scanning passive charge-exchange analyzers during neutral beam injection. The first, measured on PLT [233], is the customary banana orbit (the orbit near $v_{\parallel} = 0$ in Fig. 30). The second orbit, which was observed on PDX [226], is peculiar to high-energy particles. In orbit theory, the parallel motion and gradient drifts can exactly cancel on the inside of the magnetic axis, producing a *pinch* or *stagnation* orbit. Physically, the exact cancellation between free-streaming and gradient drifts is unstable and small changes in plasma parameters result in markedly different orbits. (Mathematically, the pinch orbit is an X point in phase space at the trapped-passing boundary [254].) A barely confined orbit close to a pinch orbit was observed by Kaita *et al.* [226]. A similar orbit was studied by Heidbrink and Strachan [43,257] in their measurements of lost 3 MeV protons from PLT (Fig. 30). As expected, the orbit near the pinch point was extremely sensitive to the plasma current while another class of orbits with little parallel velocity was barely affected by changes in I_p [43]; the variation in flux was qualitatively consistent with the predicted variation [257].

Similar orbits have also been studied by Zweben *et al.* with scintillators mounted on the wall of TFTR [258–261]. As indicated in Fig. 30, the acceptance angle of these detectors spans a range of pitch angles in velocity space; the largest signals are produced by fusion products on orbits similar to the sketched one. The signal after integration over pitch angle is plotted versus plasma current in Fig. 33. As the current increases, the arc in velocity space in Fig. 30 decreases in length and the signal is expected to decrease. In other words, as the current increases, the particles seen by the detector originate farther from the magnetic axis where fewer fusion products are born, so the signal falls. As expected, the signal strength decreases with increasing current (Fig. 33).

Meyerhofer *et al.* used active charge exchange to study the orbit shifts of counter-going beam ions (Fig. 30) injected onto a narrow annulus in PDX [262]. The observed displacement of the drift axis from the magnetic axis was consistent with calculated values based upon modelling of the current profile [262].

On ISX-B, Carnevali *et al.* [204] studied the effect of the plasma current upon the passive charge exchange signal from barely trapped, co-going beam ions (Fig. 30). When the current was decreased, the loss boundary approached the orbits of the detected particles, and the signal decreased by a factor of four [204].

On D-III, drift orbit losses were studied by measuring the temperature of a single-blade limiter with an infrared camera during neutral-beam injection [263]. The power loss inferred from the measurements was 14-15% of the injected power, while Monte Carlo calculations based upon classical beam deposition and orbit theory predicted 10-11% [263]. Power loss measurements with a calorimeter probe during perpendicular injection into PDX were also close to the expected prompt losses of beam ions [264].

In summary, the qualitative features of drift orbit theory are experimentally confirmed. Calculations of the fraction of particles that are lost agree with experiment within the errors, but uncertainties of 5-10% in the fraction of the *total* population that is lost are typical.

In addition to these relatively direct studies of the properties of fast-ion drift orbits, many other experiments have explored aspects of drift-orbit theory in conjunction with other effects. These studies include direct measurements of minority tail ions lost during ICRF [120,119,72], charge-exchange measurements of minority banana orbits [106], drift-orbit corrections to the Stix theory [124], measurements of the poloidal distribution of escaping 15 MeV protons created in $d(^3\text{He},p)\alpha$ reactions during ^3He minority ICRF [128], and measurements of the charge-exchange spectrum during neutral-beam injection (Sec. 3.1.2).

4.2. Toroidal field ripple

In the drift orbit approximation, the magnetic field is treated as uniform toroidally. In an actual tokamak, the toroidal field is corrugated because of the finite number of toroidal field coils. This toroidal field *ripple* is generally greatest on the outside of the tokamak (at large major radius R where the coils are farthest apart) and is usually less important on the inside of the tokamak. Field perturbations in the outer edge of 1% are typical and are often orders of magnitude smaller near the magnetic axis.

Theoretically, the toroidal field ripple has a negligible effect upon the orbits of most circulating particles. The effect upon trapped or barely-passing particles can be dramatic, however. Recall that the magnetic moment $\mu = E_{\perp}/B$ is usually conserved. At the turning point of a trapped ion, the parallel velocity vanishes and $\mu = E/B$. Since the energy of the particle E is another constant of the motion, small changes in the magnitude of B associated with field ripple cause perturbations in the position of the turning point. Two main classes of effects are distinguished: ripple trapping and ripple-induced stochastic diffusion.

In ripple trapping, the toroidal field ripple creates a secondary magnetic well. The criterion for the existence of secondary ripple wells in a circular large-aspect ratio tokamak is [265,266]

$$\alpha^* \equiv \frac{\epsilon |\sin \theta|}{N_{\text{coils}} q \delta} < 1, \quad (23)$$

where ϵ is the local inverse aspect ratio, θ is the poloidal angle, N_{coils} is the number of toroidal field coils, q is the field-line pitch, and $\delta \equiv (B_{\text{max}} - B_{\text{min}})/(B_{\text{max}} + B_{\text{min}})$ is the ripple amplitude. In tokamaks with only a few, closely fitting, coils the criterion $\alpha^* < 1$ can be satisfied in much of the plasma but in most operating tokamaks it is only satisfied at the outer edge of the plasma. An ion trapped in the secondary well executes an orbit known as a *superbanana* and begins to drift vertically because the ∇B drift is no longer compensated by the rotational transform. The subsequent motion depends upon the collisionality of the fast ions. If the fast ions are collisionless, they continue drifting vertically until they are lost to the wall. This is known as *convective* ripple trapping. This is the usual case for fast ions. Thermal ions are sometimes sufficiently collisional that they only drift a small distance vertically before a collision knocks them out of the ripple well. Transport associated with this process is known as *diffusive* ripple trapping. In this collisional regime, the confinement of ions that barely skim over the tops of the ripple wells is also affected.

The second process does not require trapping, but arises from the small variations in the radial position of the turning points introduced by the field ripple. This change

in the flux surface corresponds to a radial step size Δr of [267]

$$\Delta r \simeq \left(\frac{N\pi}{|\sin \theta_b|} \right)^{\frac{1}{2}} \left(\frac{q}{\epsilon} \right)^{\frac{3}{2}} \rho_f \delta \cos(N\phi_b), \quad (24)$$

where ρ_f is the fast-ion gyroradius and ϕ and θ are evaluated at the turning point. Because the step size is proportional to the gyroradius, fast ions are more sensitive to ripple diffusion than thermal ions. The variations in the turning point only produce transport, however, if the radial “kicks” received at each turning point are decorrelated. One mechanism that can decorrelate the phase between kicks is Coulomb collisions; this mechanism is important if the collision rate $\nu_{collision}$ is comparable to the bounce frequency ω_{bounce} . Fast ions diffuse at either the ripple-plateau rate $D \sim (\Delta r)^2 \omega_{bounce} / 2\pi$ (if $\nu_{collision} \gtrsim \omega_{bounce}$) or at the banana-diffusion rate $D \sim (\Delta r)^2 \nu_{collision}$ (if $\nu_{collision} \lesssim \omega_{bounce}$).

Another mechanism that can decorrelate the radial kicks (Eq. 24) is the toroidal precession motion of the drift orbits. The criterion for decorrelation due to this mechanism is approximately¹³ [269]

$$\delta > \left(\frac{\epsilon}{N\pi q} \right)^{\frac{3}{2}} \frac{1}{(2\rho_f q')}, \quad (25)$$

where q' is the radial derivative of q . When this *stochastic toroidal field diffusion* is operative, it results in large diffusion rates of order $D \sim (\Delta r)^2 \omega_{bounce} / 2\pi$. Stochastic diffusion is important because the criterion Eq. 25 is usually fulfilled in a much larger region of the plasma than the trapping criterion (Eq. 23) for fast ions with large values of ρ_f .

Evidence of transport associated with ripple trapping was first seen in charge-exchange measurements. Figure 34 shows the vertical profile of the “ion temperature” measured by perpendicular neutral-particle analyzers in T-4 [270], a machine with $> 1\%$ toroidal field ripple throughout the plasma. The passive charge-exchange profile is strongly asymmetric due to the vertical drift of ripple-trapped ions in the tail of the distribution function and the observed distortion is consistent with theoretical predictions for convective ripple transport (Fig. 34). Vertical asymmetries in the passive charge-exchange profile were also reported on T-3 [271,272], T-4 [272,273], T-10 [274–276,270], Alcator A [277], and TEXT [278]. Petrov *et al.* showed that the asymmetry was present in the large-ripple tokamaks T-3 and T-4, but was absent in the low-ripple tokamak T-6 [272] and a similar result was found for Alcator A (large ripple) and Alcator C (smaller ripple) [277]. The first asymmetric profiles were for ions in the tail of a thermal distribution. In later work, asymmetries were also observed for perpendicular beam injection [278]. In TFR, the slowing-down spectrum of perpendicular beam ions was strongly depleted, in rough agreement with calculated losses associated with ripple trapping [39]. In Alcator C, the heating efficiency during lower hybrid [279] and H-minority ICRF [116] suggested large ripple losses of trapped fast ions. In JT-60U, ripple losses are probably responsible for the weak current dependence of the triton burnup [212].

Direct measurements of fast ions lost in ripple wells were made on TFR [39,280], JT-60 [281,282,212,283], and TORE SUPRA [117] during perpendicular neutral beam injection and during hydrogen minority ICRF heating in TORE SUPRA [117]. On TFR, Faraday cups arranged in a poloidal array midway between a pair of toroidal field coils measured the escaping beam ions [280]. (The ripple in TFR varied from $\mathcal{O}(0.1\%)$ on

¹³The theoretical threshold is modified by finite orbit width effects [268].

axis to $\sim 3.7\%$ at the outer edge of the plasma.) The Faraday cup current scaled approximately linearly with beam power and was largest for the detector situated ~ 7 cm from the center of the coil, as expected for ripple losses [280]. The measured current was about twice as large as theoretically expected, however. Experimental uncertainties (such as secondary electron emission from the Faraday cups) may account for the discrepancy, or the results may indicate a loss process in addition to ripple trapping. In contrast, measurements in JT-60U (with a fast infrared TV camera and with a poloidal and toroidal array of 40 thermocouples installed on the first wall) are in good quantitative agreement with the theoretical predictions [281,282]. (The ripple in JT-60U is $\lesssim 0.8\%$ for the case shown in Fig. 35.) The losses are concentrated both poloidally and toroidally, as theoretically predicted. The toroidal distribution at the angle of maximum poloidal flux is shown in Fig. 35, together with the theoretical prediction from a Monte Carlo code [282]. The magnitude of the losses (to within 18%), the poloidal and toroidal distribution, and the dependencies upon the ripple δ and safety factor q are all consistent with calculations of ripple-trapped loss [281]. The results from TFR and JT-60U indicate that ripple trapping can cause large losses of perpendicular fast ions when Eq. 23 is satisfied.

In ST [284], PLT [285], ISX-B [286,287], and JET [157], the magnitude of the ripple was varied by connecting or disconnecting one or more coils. In ST a single additional coil created an enormous (30% on axis) ripple “hill” at one location, while on PLT a toroidally localized ripple “well” of either 0.4% or 2.7% was created. Theoretically, a single perturbation has less effect than periodic field ripple. In ST, the passive charge-exchange signal decreased but the neutron signal increased in the presence of the ripple hill, so the results of the experiment were indeterminate [284]. In PLT, the localized dip of 2.7% in the field strength on axis had no discernible effect on the confinement of tangentially injected beam ions [285] or circulating 1 MeV tritons [20]. The ISX-B and JET experiments varied the periodic field ripple by halving the number of energized field coils. In ISX-B, the number of field coils was reduced from 18 to 9 (at constant $\bar{B} = 0.84$ T) during tangential neutral beam injection. The reduction caused the ripple at the plasma edge to increase from $\delta = 0.8\%$ to $\delta \simeq 8\%$; in the 9-coil configuration the ripple trapping condition (Eq. 23) was satisfied in most of the plasma volume. Experimentally, the change in ripple scarcely affected the circulating fast ions (Fig. 36a), but caused a dramatic reduction in the passive charge exchange signal from beam ions near the trapped/passing boundary (Fig. 36b) and in the signal from deeply trapped beam ions [287]. These results confirm the theoretical expectation that the orbits of passing particles average the perturbations associated with toroidal field ripple while trapped ions do not. In JET, the number of field coils was reduced from 32 to 16 during beam injection and during ICRF heating [157]. The reduction increased the ripple at the outer limiter from 1% to 12.5%, creating a substantial ripple-trapping region in the outer plasma. The triton burnup dropped by 30-60%, which is somewhat larger than the 25% reduction expected from ripple-well and stochastic ripple losses. During H-minority heating, the resonance layer was scanned outward into the large ripple region. When the resonance layer was at $R_{res} \simeq 3.0$ m, the fusion-gamma signal produced by energetic protons was insensitive to the number of field coils but for $R_{res} = 3.4$ m, the signal was ~ 3 times smaller with 16 coils than with 32 coils [157]. An even larger reduction at $R_{res} = 3.4$ m was observed in the vertical charge-exchange flux of 1.4 MeV protons [157,288]. These observations confirm the detrimental effect of toroidal-field ripple on the confinement of trapped fast ions.

A detailed study of stochastic ripple diffusion was performed on TFTR [289–292]. In this experiment, scintillators with pitch-angle resolution that are located near the edge of the plasma measured escaping 1 MeV tritons and 3 MeV protons produced in $d(d,p)t$ fusion reactions. Figure 37 shows the signal measured by a movable probe mounted just below the midplane ($\theta \simeq -20^\circ$) as a function of plasma current. As discussed in Sec. 4.1, prompt losses to the probe are expected to decrease as the plasma current increases, a result observed with a similar detector mounted near the bottom of TFTR (Fig. 33). For the midplane probe, however, the signal peaks at 1.4 MA, in contradiction to the drift-orbit prediction (Fig. 37). Calculations including stochastic ripple diffusion reproduce the observed maximum, although the observed signal strength is larger than predicted (Fig. 37). The discrepancy between the signal strength and the prediction may be due to the $\sim 50\%$ uncertainty in the calculation (caused by uncertainties in the current and d-d emission profiles) or due to incomplete modelling of the detector and wall geometries. The pitch-angle distribution also indicates that stochastic ripple diffusion is an important loss process. Figure 38 shows the pitch-angle distribution of the signal at $I_p = 0.6$ MA, where drift-orbit losses dominate, and at $I_p = 1.8$ MA, where ripple losses prevail. The dramatic shift to higher pitch angles is evident. The data from a radial scan of the probe position and from the poloidal distribution of the losses as a function of current further confirm that the losses are caused by ripple diffusion [289,291]. The data from the scans suggest that the threshold for stochasticity is 1-3 times the threshold given by Goldston, White and Boozer [267] (Eq. 25). In another set of experiments, obstacles were moved into the scrape-off region to intercept the fast ions measured by the scintillator. From the radial dependence of the signal it was concluded that the measured radial step size (0.3 ± 0.1 cm) agrees with the theoretical prediction of Eq. 24 [289,292].

4.3. Fluctuation-induced transport

Fast ions are subjected to field fluctuations associated with Coulomb collisions, microturbulence, and rf waves (Fig. 19). The effect of these fluctuations on the velocity distribution of the fast ions was discussed in Sec. 3. In this section, we consider the impact of the velocity fluctuations on the confinement of the fast ions. The discussion is restricted to steady-state, short wavelength fluctuations. Transport associated with transient MHD instabilities is the subject of Secs. 4.5 and 4.4.

Consider a fast ion in a fluctuating electric field. (If the fast-ion population is sufficiently dilute, the response of the fast ions does not alter the fluctuating fields, so a test-particle treatment is adequate.) In a uniform magnetic field, an electric field perturbation $\tilde{\mathbf{E}}$ can create an $\tilde{\mathbf{E}} \times \mathbf{B}$ drift, and this perturbation in perpendicular velocity perturbs the motion of the particle. If the velocity “kicks” are random, cross-field diffusion occurs, with an effective step length of approximately ρ_f and a collision frequency ν , so the diffusion coefficient D is approximately

$$D \sim \rho_f^2 \nu. \quad (26)$$

Kicks in perpendicular velocity δv_\perp are more effective in altering the fast-ion orbit than kicks in parallel velocity δv_\parallel . For example, the friction associated with Coulomb drag on electrons usually improves fast-ion confinement by reducing the banana width (which depends upon v) and drawing the ion closer to the flux surface. On the other hand, pitch-angle scattering events do lead to non-negligible changes in v_\perp . Transport produced

by Coulomb scattering in a uniform field is termed *classical*. The classical diffusion coefficient for fast ions is given by Eq. 26 with ν replaced by the collision frequency between fast ions and thermal ions, $\nu = \nu_{fi}$. Because these collisions are infrequent, classical diffusion is very small for fast ions. For example, for ~ 100 keV beam ions in TFTR, the classical diffusion coefficient is $D \sim 10^{-3} \text{ m}^2/\text{s}$, which is negligible in comparison to typical thermal transport coefficients ($\sim 1 \text{ m}^2/\text{s}$).

Neoclassical theory refers to the enhancement in classical transport associated with toroidal effects. Depending upon the relative frequencies of Coulomb collisions ν_{fi} and the bounce motion of trapped particles ω_{bounce} , neoclassical theory is subdivided into different collisionality regimes; fast ions are sufficiently collisionless that they are almost always in the *banana* regime ($\nu_{fi} \ll \omega_{\text{bounce}}$). In this regime, toroidal effects do not appreciably modify the expected transport for circulating fast ions but do increase the transport of trapped fast ions. The tip of the banana orbit moves by a *poloidal* gyroradius ρ_θ (rather than the *toroidal* gyroradius ρ_f) in a pitch-angle scattering collision, so that the diffusion coefficient is [293,294]

$$D_{\text{neo}} \simeq \frac{1}{2} \rho_\theta^2 \nu_{fi}, \quad (27)$$

where ρ_θ is given by Eq. 18 with the field B evaluated using the poloidal field. The collision frequency ν_{fi} is

$$\nu_{fi} = \frac{2 \times 10^{-21} Z_f^2 Z_{eff} n_e}{\sqrt{A_f} E_{\text{MeV}}^3} \text{ s}^{-1}, \quad (28)$$

where n_e is in m^{-3} and E_{MeV} is the fast-ion energy in MeV. Equations 27 and 28 imply that $D_{\text{neo}} \propto 1/\sqrt{E}$, so that neoclassical transport of fast ions is smaller than neoclassical transport of thermal ions. For example, for beam ions near the center of TFTR, $D_{\text{neo}} \sim 10^{-2} \text{ m}^2/\text{s}$, which is generally negligible. Only a small fraction of initially confined fast ions subsequently pitch-angle scatter onto a loss orbit, even if first-orbit losses are appreciable [295]. Neoclassical transport may be important in rf heating, however, because the rf power density can be highly concentrated on axis (where the poloidal field is small) and even fast-ion transport of order $(10^{-2}) \text{ m}^2/\text{s}$ can appreciably broaden the power deposition [293].

In neoclassical theory, Coulomb collisions introduce drifts as well as diffusion. For example, a toroidal electric field \mathcal{E}_\parallel causes trapped particles to drift inward with a velocity of approximately $V_{\text{ware}} \simeq \mathcal{E}_\parallel / B_\theta$, where B_θ is the poloidal field. In a large tokamak, this drift is $\mathcal{O}(10 \text{ cm/s})$, which is usually negligible.

Fluctuations in velocity caused by rf waves can also cause convection and diffusion. The radial step size δr of a trapped ion that gains a kick in energy δE from the rf wave is [293]

$$\delta r = -\frac{k_\phi(\delta E)}{m_f \omega \Omega_\theta}, \quad (29)$$

where k_ϕ and ω are the toroidal wave number and frequency of the wave, and Ω_θ is the poloidal gyrofrequency of the fast ion. For high-energy minority tail ions, these kicks give rise to a radial drift V_{rf} of order [293]

$$V_{\text{rf}} \sim \overline{k_\phi} \rho_f \frac{\rho_\theta}{2\tau_{se}} \quad (30)$$

and a diffusion coefficient D_{rf} of

$$D_{\text{rf}} \sim \overline{k_\phi^2} \rho_f^2 \frac{\rho_\theta^2}{2\tau_{se}} \quad (31)$$

where $\overline{k_\phi}$ is the average of k_ϕ over the wave spectrum at the turning point. The diffusion coefficient D_{rf} is usually even smaller than neoclassical diffusion (Eq. 27). The convective drift V_{rf} may be significant for an asymmetric wave spectrum, however.

Microturbulence may dominate the transport of thermal particles. This transport may be caused by either electrostatic fluctuations that impart radial $\tilde{\mathbf{E}} \times \mathbf{B}$ kicks to the particles, or by electromagnetic fluctuations that allow parallel transport along braided field lines. Naively, one might think that fast ions are particularly vulnerable to these transport mechanisms because of their large gyroradius ρ_f (large radial step size) and relatively large velocity v_f along field lines. However, if the microturbulence has a radial correlation length Δ_r that is comparable to the thermal ion gyroradius ρ_i and the waves propagate at velocities $\omega/k \sim v_i$, the expected fast-ion transport is *much smaller* than the thermal ion transport. Two effects are responsible for this reduction [296,297].

Gyroradius averaging The large gyromotion of the fast ions spatially averages over many waves in a gyroperiod, reducing the expected transport by a factor of order $J_0^2(\rho_f/\Delta_r)$. (Here, J_0 is the zeroth order Bessel function.)

Drift averaging The large drifts of the fast ions “detune” the fast ions from any resonant interaction with the waves (temporally averages over the fluctuation spectrum), reducing the expected transport by a factor of form $\mathcal{S}(x/\Delta_r)$, where \mathcal{S} is the spatial form factor of the fluctuation spectrum, and x is related to the orbit size.

The expected transport level depends upon the details of the microturbulence, which are not well established experimentally. If the fluctuation spectrum is peaked around $k_\perp \rho_i \sim 1$, fast-ion transport is expected to be orders of magnitude smaller than thermal ion transport. Formulas for fluctuation-induced transport are summarized by White and Mynick [269].

In the comparison of beam-ion measurements with theoretical expectations, spatial transport can often be neglected altogether. For example, many workers have compared the absolute magnitude of the 2.5 MeV neutron emission during deuterium beam injection with calculations that assume classical beam deposition and thermalization. The drift orbits of the beam ions are generally taken into account, but spatial transport is assumed negligible. Tritium experiments on JET extended this comparison to include the magnitude of the 14 MeV neutron emission as well as of the 2.5 MeV neutron emission (Fig. 39). The time evolution and absolute magnitude of both signals agree well with the simulations for various combinations of deuterium and tritium beams [1,298–301]. In deuterium injection experiments, the magnitude of the total $d(d,n)^3\text{He}$ rate agreed with calculations on PLT [203], TFR [214], PDX [302], ASDEX [77], ISX-B [204], TFTR [303,205,304,80,305], and JET [65,1,306] (Fig. 40). The accuracy of this comparison has steadily improved, and is now approximately 10-15%. Qualitatively, this good agreement implies that beam ions remain near the center of the plasma during the initial stages of the thermalization process (when the fusion reaction cross section is still appreciable). The only calculation of the effect of spatial transport on the expected reaction rate was

performed by the PLT group, who set an upper bound of $D \lesssim 0.5 \text{ m}^2/\text{s}$ on the beam-ion diffusion coefficient [203].

Measurements of the profile of fusion reactions during beam injection are also consistent with negligible fast-ion transport during the initial stages of thermalization (Sec. 2.2).

Neutral beams injected into hot, low density plasmas can drive an appreciable current. Measurements of the loop voltage during current-drive experiments usually agree with theoretical predictions based upon the assumptions that beam ions experience no spatial transport while decelerating classically. Figure 41 shows the response of the loop voltage to tangential beam injection into a low density JET plasma [307]. The measured evolution of the surface voltage only agrees with calculations if beam-driven currents and bootstrap currents associated with the pressure gradient are included [307–309]. Similar studies on DITE [310,311], DIII-D [312,313], and TFTR [314,315,121] also found agreement between the measured surface voltage or driven plasma current and calculations that assume negligible beam-ion transport. In addition to the assumptions of classical beam deposition and thermalization and negligible fast-ion transport, these calculations also assume classical diffusion of the poloidal flux. The sensitivity of these results to fast-ion transport has not been quantified, but the observations lend qualitative support to the notion that beam ions are confined for a slowing-down time.

The confinement of fusion products can be assessed using the so-called “burnup” technique (Sec. 1.2). Measurements of 15 MeV protons produced by thermalizing 0.8 MeV ^3He ions and of 14 MeV neutrons produced by thermalizing 1.0 MeV tritons are compared with calculations of the expected rates. The calculations [234] employ the (measured or calculated) d-d emission profile, which is the birth profile for the ^3He ions and tritons, assume classical Coulomb drag, and generally take into account drift-orbit effects. Spatial diffusion of the fusion products is assumed negligible. Measurements of the triton burnup on PLT [20,316] and of the ^3He burnup on PDX [20] are consistent with the calculated burnup to within a factor of three in discharges without large MHD activity. In FT, the triton burnup [317–321] agrees with calculations to within 60% [321], with some tendency for the agreement to degrade at low values of the safety factor q (Sec. 4.5). The ^3He burnup in TFTR was found to be a factor of 2-3 larger than calculated values, which is a little beyond experimental uncertainties [209]. The triton burnup on TFTR [322,323] is $50 \pm 25\%$ of the calculated value in discharges with long slowing-down times ($\tau_{se} \sim 1 \text{ s}$). On DIII-D, the triton burnup agrees with the calculations to within 45% except in discharges with large MHD activity [211]. On JT-60U, the burnup is 20-30% less than calculated, which is comparable to the uncertainty in the measurement [212]. Triton burnup studies on JET [122,210,324,325,213,71,123,326] were performed at large plasma current ($I_p \gtrsim 3 \text{ MA}$), where drift-orbit effects are of reduced importance. The measured burnup is typically 80% of the calculated value (Fig. 42), which is within the experimental errors of $\sim 20\%$. In discharges with long slowing-down times ($\tau_{se} \gtrsim 2 \text{ s}$), the measured value falls to $\sim 50\%$ of the calculated value, however [71,213,326,298].

The spatial profile of the ^3He burnup was measured on TFTR [209] and the triton burnup profile was measured on JET [326,298] and TFTR [327]. In all cases, the profile is highly peaked on axis.

When the measured burnup is smaller than the calculated burnup, the discrepancy can be related to a spatially averaged fusion product confinement time [20,328,329] or diffusion coefficient [328,329]. Of course, the actual mechanism responsible for the

reduction in burnup need not be diffusive. The measured $d(^3\text{He,p})\alpha$ profile implies an effective diffusion coefficient smaller than $1.0 \text{ m}^2/\text{s}$ for $0.8 \text{ MeV } ^3\text{He}$ ions in TFTR [209] and the magnitude of the triton burnup in DIII-D implies that $D \lesssim 0.2 \text{ m}^2/\text{s}$. The TFTR triton burnup data imply an effective diffusion coefficient of $\sim 0.1 \text{ m}^2/\text{s}$ [323]. The absolute magnitude of the triton burnup in the JET discharges with $\tau_{se} \gtrsim 2 \text{ s}$ imply a similar D ($0.1\text{-}0.3 \text{ m}^2/\text{s}$) [71,213,329] but the $d(\text{t,n})\alpha$ profile implies a much smaller diffusion coefficient [329], suggesting that the actual losses occur rapidly rather than diffusively [330].

In a qualitative study of fusion-product confinement, the burst of 14 MeV neutrons created by injecting a deuterium pellet following beam injection into TFTR confirmed that 1.0 MeV tritons are confined for $> 0.75 \text{ s}$ [331].

The burnup technique effectively integrates over velocity space. A complementary approach to the study of fusion-product confinement is to measure particles on loss orbits near the vacuum vessel wall. Figure 30 illustrates one of the orbits measured by Zweben *et al.* using scintillators on the bottom of TFTR. The detectors are sensitive to spatial transport that moves 1 MeV tritons and 3 MeV protons across the trapped-passing boundary in velocity space (i.e, from counter-circulating orbits to an unconfined banana orbit). Comparison of the current dependence, the time evolution, the gyroradius distribution, and the pitch-angle distribution of the signal with model calculations all indicate that the diffusion of these counter-circulating fusion products is very small during neutral-beam heating. [261]. Figure 43 shows the measured pitch-angle distribution and the expected distribution for various values of the diffusion coefficient D in a plasma with $R_0 \simeq 2.6 \text{ m}$. If the diffusion was large, most detected ions would appear near the trapped-passing boundary. Instead, the relatively broad pitch-angle distribution expected from prompt losses is observed (Fig. 43), implying that $D < 0.03 \text{ m}^2/\text{s}$. In plasmas with smaller major radius ($R_0 = 2.45 \text{ m}$), however, the pitch-angle distribution deviates markedly from the expected distribution for $D = 0$ (Fig. 44) [290]. The anomalous pitch-angle distribution is produced by the loss of fusion products with energies about half the birth energy; the ions begin to escape $0.2 \pm 0.1 \text{ s}$ after the start of beam injection. Anomalies are also observed during combined ICRF and neutral beam heating [72,290]. In this case, a detector located 45° below the midplane detects delayed losses of ions with reduced gyroradii (relative to prompt losses), suggesting the loss of confined tritons under these conditions [290].

Fast ions accelerated during rf heating are better confined than thermal ions. From the observation of $400 \text{ keV } ^3\text{He}$ tail ions in PLT and an estimate of the acceleration rate, Chrien and Strachan [66] concluded that the tail-ion diffusion coefficient was $\lesssim 0.5 \text{ m}^2/\text{s}$. The excellent agreement between the measured fast-ion stored energy and the stored energy predicted by Stix theory (Fig. 25) implies that the diffusion of tail ions in JET is less than $0.2 \text{ m}^2/\text{s}$ [124]; the observations of very large tail temperatures ($T_\perp \simeq 1.5 \text{ MeV}$) and energies ($> 7.5 \text{ MeV}$) [136,71] lend qualitative support to this conclusion. The good energy confinement of JT-60 plasmas with combined neutral-beam and rf heating [144,188] and with second harmonic heating [148,143] also suggests good fast-ion confinement.

Some measurements during minority heating do suggest modest transport, however. On PLT, passive charge-exchange measurements of the hydrogen tail implied a broader rf deposition profile than theoretically expected [145,241], perhaps due to fast-ion transport. Similar measurements of the ^3He tail on PLT [126] do not necessarily imply a

broadened profile, however. JET charge-exchange measurements of the hydrogen tail are also compatible with the expected power deposition without invoking spatial diffusion [114], but the variation of the gamma-ray signal during a toroidal field scan [132] and the rise in electron temperature following a sawtooth [134] did imply broadened power deposition. Figure 45 shows the temporal evolution of gamma rays produced by energetic minority protons during rf heating in JET [65]. Calculations that incorporate rf-induced spatial diffusion can reproduce the signal, while neglect of transport results in a discrepancy (Fig. 45). Measurements of the time evolution of the plasma rotation also suggest an outward flow of fast ions from the plasma center during minority heating in JET [332]. Stored energy measurements during minority heating in TEXTOR suggest that the energy confinement time for fast ions is roughly twice as large as the thermal energy confinement time [125].

Several direct studies of fast-ion diffusion have been attempted in TFTR. In one study, an annular ring of beam ions was deposited in the edge of the plasma [231,297]. Transport of the beam ions into the plasma center was monitored with horizontally scanning passive charge-exchange detectors. The steep radial profile of the charge-exchange signal (Fig. 46) indicates that the inward radial transport of the co-circulating beam ions is small ($D < 0.05 \text{ m}^2/\text{s}$) in these low density, low beta plasmas with weak MHD activity. In another study, a short pulse of deuterium neutral beams was injected into low-density, ohmically heated TFTR plasmas to create a population of nearly monoenergetic beam ions in the plasma center [323,208]. The subsequent evolution of this population was monitored with neutron and passive charge-exchange diagnostics (Fig. 47). The data from the central neutron and charge-exchange diagnostics imply $D \ll 0.1 \text{ m}^2/\text{s}$, while the signals from channels at $r/a \simeq 0.5$ imply somewhat larger transport of $D \sim 0.1 \text{ m}^2/\text{s}$ (Fig. 47). In a third study, the resonance layer was scanned across the sightline of a vertically viewing charge-exchange analyzer during hydrogen minority ICRF heating [121]. In the absence of spatial diffusion, the turning points of high-energy protons are expected to lie in the resonance layer. The observed flux of 100 keV protons peaked strongly when the resonance layer approached the detector sightline, and the radial dependence of the signal implies a diffusion coefficient smaller than $0.05 \text{ m}^2/\text{s}$ for these trapped ions [121].

During high-power neutral-beam injection, some charge-exchange measurements suggest enhanced spatial transport of beam ions. A common technique is to increase the beam power in steps while observing the charge-exchange flux. If changes in temperature and density profiles may be neglected, the neutral-particle flux is expected to increase linearly with the beam power. In practice, the active charge-exchange signal was observed to saturate with increasing beam power on TFR [202] and ISX-B [204] and the passive charge-exchange signal saturated in Doublet III [333,334]. These data were obtained in intensely heated plasmas and it is possible that MHD activity are responsible for the degradation in flux.

Figure 48 summarizes all published measurements of the effective diffusion coefficient of fast ions. The measurements include averages over velocity space (as for the burnup studies) as well as studies of co-circulating, trapped, and counter-circulating fast ions. As indicated in the figure, fast ions are generally confined within the plasma for a slowing-down time. The data show no systematic dependence upon the ratio of fast-ion gyroradius to thermal-ion gyroradius in the range $4 < \rho_f/\rho_i < 24$; this is consistent with the interpretation that all of the fast ions were sufficiently energetic to average over the thermal fluctuation spectrum spatially and temporally. Most of the measurements are

of dilute “test-particle” populations (that are unlikely to modify the spectrum of the microturbulence) but, in a few cases, the fast-ion beta was a significant fraction of the total plasma beta (although not sufficiently large to drive collective MHD instabilities). Figure 48 indicates that, in the absence of severe MHD activity, most fast ions thermalize in the plasma.

4.4. Resonant losses

As discussed in the previous section (Sec. 4.3), fast ions rarely resonate with instabilities driven by the thermal plasma (since the phase velocity of a typical mode coincides with an aspect of the motion of thermal particles and $v_i \ll v_f \ll v_e$). Occasionally, however, the fast-ion population can become sufficiently intense to drive collective instabilities. Under these conditions, plasma modes do resonate with the fast-ion orbits and rapid transport of fast ions is observed. The conditions under which fast-ion driven instability occur are discussed in Sec. 5; in this section, we consider the effect of resonant instabilities on the confinement of fast ions, irrespective of the stability properties of the mode.

Although fast ions can drive instabilities with frequencies ω greater than the cyclotron frequency Ω (Sec. 5.3), resonant transport has been measured only for modes with $\omega \ll \Omega$. Under these conditions, the first adiabatic invariant μ is expected to be conserved and a drift-orbit approximation captures the essential physics [335]. Trapped particles may resonate with modes that propagate toroidally at the precession frequency ($\omega = \omega_{pre}$), and passing particles may resonate with modes that propagate at the circulation frequency ω_{circ} ; the resonance condition for circulation instabilities is $\omega = \omega_{circ}(nq - m + N)/q$, where n and m are the toroidal and poloidal mode numbers of the wave, q is the safety factor and N is an integer. In both cases, outward radial motion that is linearly proportional to the mode amplitude is predicted [335]. For the circulation frequency resonance, the average outward radial motion associated with a single toroidal mode is approximately [335]

$$\langle \dot{\psi} \rangle \simeq - \sum_m \cos(\delta_{nm}) \frac{N \omega_{circ} \alpha_{nm}}{\epsilon(1 - nq/m)} J_N \left(\frac{mqv_d}{\omega_{circ} r_0} \right), \quad (32)$$

where ψ is the toroidal flux coordinate, α_{nm} and δ_{nm} are the amplitude (normalized to the toroidal field) and phase of the various harmonics of the perturbation field, ϵ is the inverse aspect ratio, J_N is the Bessel function for resonant harmonic N , r_0 is the mode rational surface, and v_d is the vertical drift velocity (gradient plus curvature) of the resonant ions. A similar expression holds for radial transport caused by a mode that resonates with the precessional drift of trapped ions (Eq. 24 of Ref. [335]). If the fast ion remains in resonance throughout the plasma (the various harmonics in Eq. 32 have appreciable amplitudes α_{nm} and the proper phase relations δ_{nm}), transport from the plasma center to the edge is possible [335]. Ejected particles are expected to have a particular phase relation with respect to the mode [335]. The expected energy loss is relatively modest ($\Delta E/E \lesssim 10\%$) [335].

Resonant interaction with the bounce motion of trapped particles is also possible.

An alternative loss channel for resonant circulating particles on barely passing orbits is to transfer parallel energy to the mode, thereby crossing the passed/trapping boundary in velocity space and subsequently escaping the plasma on a large banana orbit [255,336]. These losses are also predicted to scale linearly with the mode amplitude [336].

The most detailed measurements of resonant fast-ion transport were made in the PDX tokamak during investigation of the fishbone instability. The fishbone instability is described in detail in Sec. 5.1 but, briefly, in PDX it was a large wavelength MHD mode with toroidal mode number $n = 1$ that propagated at a frequency near the precession frequency of trapped beam ions. The instability occurred in bursts. Figure 49 illustrates the effect of one of these bursts on the passive charge-exchange flux and on the $d(d,n)^3\text{He}$

neutron emission rate. The charge-exchange flux increases at the burst because beam ions are expelled from the center of the plasma to the plasma edge, where the neutral density is higher. Concurrently, the neutron emission, which is dominated by beam-plasma reactions, decreases as beam ions are lost from the plasma.

The losses of trapped beam ions caused by the fishbone instability are in excellent qualitative agreement with theoretical predictions. Vertically viewing passive charge exchange detectors found that the losses were two orders of magnitude larger on the outside (large R) than on the inside of the torus [337,338]. Even the relatively small flux on the inside of the tokamak could be explained by a small amount of pitch-angle scattering in conjunction with resonant transport [338]. The signal for the outer detector was strongly modulated at the frequency of the instability [337,252] (c.f., Fig. 49), as expected for resonant losses. The phase relation between two toroidally separated analyzers that viewed the edge of the plasma showed the same $n = 1$ symmetry as the instability [337]. Moreover, the charge-exchange signal was modulated most strongly near the injection energy (Fig. 50), suggesting that the resonance was sharpest for this class of beam ions. In the mode-particle resonance theory [335], the beam ions were predicted to escape in a beacon, with the fast-ion losses preceding the hot spot of the kink mode by 90° for fishbone instabilities. Experimentally, the phase difference between the outer charge-exchange signal and the instability was a function of energy, but the class of particles that exhibited the strongest resonant behavior ($-10 \text{ keV} < E - E_{inj} < 0$ in Fig. 50) led the hot spot (inferred from the maximum of the soft x-ray signal) by $65^\circ \pm 50^\circ$, consistent with theory. The effect of the instability on the charge-exchange spectrum [339,252], the pitch-angle distribution of the losses [252], the energy dependence of the temporal duration of each burst [337], and the reduction in signal at the injection energy [252] also suggest resonant losses. Direct losses of beam ions were measured with a silicon detector mounted inside the vacuum vessel near the top (in the direction of the ∇B drift) [340-343]. The flux to this detector was also strongly modulated at the fishbone frequency (Fig. 50) and was proportional to the fractional drop in the neutron emission [342]. The absolute magnitude and phase relation of the flux was also consistent with theory [342].

Quantitative measurements of the severity of the losses were inferred from the slope of the neutron emission [302]. The slope of the neutron emission within a single burst depended linearly upon the amplitude of the mode (Fig. 51). It was also found that the minimum value of the slope scaled approximately linearly with the maximum amplitude of the instability (Fig. 51). These results constitute further confirmation that the losses are resonant. Within a factor of 2-5, the magnitude of the losses was consistent with theoretical expectations, although the data suggest [302] that the resonance is not as sharp as assumed by White *et al.* [335]. The other quantitative measurement of the losses during fishbones was obtained in PBX using a diamagnetic loop with excellent temporal response [344]. It was found that both the time evolution [344] and the magnitude of the reduction in stored perpendicular energy scaled linearly with the changes in the neutron signal, implying that resonant fast-ion losses could account for all of the energy lost at a fishbone burst (Fig. 52).

The fishbone instability also affected the confinement of fast ions in Doublet III [333,334], PBX [344,345], TFTR [346], DIII-D [347], JET [71,348-350,1], and PBX-M [351,352], although resonant transport did not necessarily occur in all of these devices. During weak fishbones in TFTR, passive charge-exchange measurements indicated that

the losses were greatest for perpendicular fast ions near the injection energy, even though tangential injection was employed [346]. In PBX-M discharges with fishbones, subtle details in the plasma equilibrium had a strong effect on the passive perpendicular charge exchange signal (which measures particles that move on a particular class of orbits in phase space) but a weaker effect upon the neutron signal (which effectively integrates over phase space) [351,352], possibly due to changes in the efficacy of coupling to edge harmonics.

Circulating fast ions can resonate with higher frequency modes. Transport of beam ions associated with instabilities with $\omega/2\pi = 50 - 200$ kHz has been observed during perpendicular injection into PDX [302] and during tangential injection into PBX [345,344], TFTR [353-355], and DIII-D [356,211]. Although some of these instabilities may be different plasma modes (Sec. 5.2), they have similar frequencies and mode structures and so are expected to resonate with the circulating beam ions and to affect their confinement similarly. Figure 53 shows an example from TFTR. Drops in the neutron emission correlate with bursts observed by a Mirnov coil. A scintillator located inside the vacuum vessel $\sim 20^\circ$ below the midplane detects beam ions at each burst [355,357,358].

The first detailed study of resonant transport of passing particles was performed on PBX [344]. Six features of the data suggest resonant transport of full-energy circulating beam ions.

- The bursts of neutrals measured by a passive charge-exchange detector were largest for the most tangential orientation of the analyzer.
- During a burst, the charge-exchange flux near the injection energy dropped suddenly at the peak of the instability, and the reduction in flux following the burst was greatest for particles with energies close to the injection energy.
- The slope of the neutral spectrum was modified near the injection energy when strong instabilities were present.
- For bursts with frequencies near the circulation frequency, the fractional drop in the neutron emission scaled approximately linearly with the peak mode amplitude. Losses during combined low and high frequency bursts also scaled linearly with mode amplitude.
- The perpendicular stored energy of the plasma did not drop during the instability, as it did during fishbone bursts.
- The frequencies of the instabilities were comparable to the beam circulation frequency.

In addition to the PBX study, the dependence of the neutron emission upon the mode amplitude was studied in PDX and in DIII-D. The correlation of the slope of the neutron emission with the mode amplitude is shown in Fig. 54 for a single burst in DIII-D [359]. The losses scale linearly with mode amplitude, as expected for resonant transport. Examination of many bursts shows that the fractional drop in neutron emission also scales linearly with the average mode amplitude [359]. Similar dependencies were observed on PDX [302] and PBX [344]. Measurements of the poloidal distribution of the losses using an array of three foil bolometers showed that the beam-ion losses in

DIII-D are concentrated on the midplane [359], in qualitative agreement with theoretical predictions.

Other fast-ion measurements have been performed in regimes where TAE modes (Sec. 5.2) may have been unstable, but the absence of measurements of the instabilities in these plasmas limits the utility of the observations. In Doublet III, the fraction of power to the limiter increased at the beta limit, possibly indicating fast-ion losses [360]. In T-11, the charge-exchange spectrum was not severely distorted during beam injection with super-Alfvénic beam ions [224].

The losses of beam ions inferred from the fractional reduction in neutron emission $\Delta S/S$ at MHD bursts are summarized in Table 3. Only the results from “pure” modes are listed; data from combined fishbone and TAE activity are excluded. The severity of the instability is estimated from the field perturbation measured by a Mirnov coil positioned near the wall; the field strength in the plasma depends upon the distance from the plasma and the poloidal structure of the instability. For fishbones the observations are similar on most devices. Reductions in neutron emission of a few percent occur for $\tilde{B}_\theta/B_\theta \simeq 3 \times 10^{-3}$, while $> 20\%$ losses occur for $\tilde{B}_\theta/B_\theta = O(10^{-2})$. For a given field amplitude, the losses are somewhat smaller in DIII-D. More scatter is observed in the results for the circulation instabilities, perhaps due to the greater sensitivity to differences in the radial positions of the coils for these higher m number instabilities. No systematic dependence upon the ratio of ρ_f/a is observed, probably because the losses are caused by globally extended modes that perturb most of the plasma.

It is experimentally observed that transport is enhanced by the presence of multiple instabilities. In PDX, combined fishbone and ~ 100 kHz activity resulted in losses that were approximately the sum of the losses for each of the instabilities considered individually [302]. In PBX, the largest losses occurred during combined internal kink and high-frequency activity, although the high-frequency activity appeared to account for the losses [344]. In DIII-D, a synergistic effect seems to occur, with the losses during combined fishbone and TAE activity exceeding the losses expected from the sum of the losses of each instability considered individually [359].

In practice, resonant instabilities can have a disastrous effect on fast-ion confinement. For example, in a particular case in PDX, it was estimated that 25% of the beam power was lost due to the fishbone instability [361], circulation-frequency instabilities were estimated to eject 20% of the beam power in PBX [362], and up to 70% of the beam power is lost during combined fishbone and TAE activity in DIII-D [359].

4.5. Transport by nonresonant MHD instabilities

There have been many observations of enhanced spatial transport of fast ions caused by MHD activity.¹⁴ Although several possible theoretical explanations have been proposed, detailed comparisons of experiment with theory have not yet appeared. Possible transport mechanisms include the following.

- The helical distortion of the flux surface associated with the MHD activity causes the fast ion to move radially an equal amount, causing a fast ion to cross a loss boundary. Unless the classical confinement (Sec. 4.1) of the fast ions is very poor, these additional losses to the walls are too small to account for the observations.

¹⁴By definition, the power spectrum of a “nonresonant” MHD instability does not peak at one of the characteristic frequencies of the fast-ion motion.

- The MHD activity creates ergodic magnetic field lines. Fast ions with large parallel velocities move radially through parallel transport along stochastic field lines.
- The helical perturbation of the field introduces new resonances between the complex orbital motion of the fast ions and the spatial structure of the field. If both the field perturbation and the fast-ion drifts are large, island overlap can occur in phase space. Stochastic ion motion ensues. Calculations [336] indicate that the stochasticity threshold for a single-helicity mode is roughly $\tilde{B}/B \sim 10^{-3}$, but the threshold is considerably reduced if multiple perturbations are considered.

Appreciable fast-ion transport is observed at large sawtooth crashes. Figure 55 shows tomographic reconstructions of the neutron emissivity during deuterium beam injection into JET just before and after a sawtooth crash [363]. The emissivity profile is strongly peaked prior to the crash but hollow afterwards (Fig. 55) because the instability causes beam ions to move from the center of the plasma to larger minor radii [363,364]. Indeed, inverted sawteeth are regularly observed in the outer channels of the neutron profile monitor [71]. The data are usually compatible with a simple redistribution within the plasma [364]; on the other hand, some particularly violent “monster” sawteeth (Sec. 5.1) and beta limit sawteeth eject fast ions from the plasma [71,348].

The redistribution of fast ions at a sawtooth crash can extend to larger radii than for thermal electrons. In JET, the “inversion radius” (the radius at which the signal begins to increase at a sawtooth crash rather than decrease) is sometimes at a larger radius than for the electron diagnostics [71]. On PDX, inverted sawtooth oscillations were seen in the active charge-exchange flux out to the edge of the plasma (Fig. 56), with a delay of less than 0.1 ms between the sawtooth crash and the rise in edge signal [365,252].

During deuterium beam injection into circular low-beta plasmas with $q \gtrsim 3$, sawtooth crashes caused small ($< 5\%$) drops in the total neutron emission in PLT [203] and TFTR [36] on the timescale of the beam slowing-down time τ_{se} . No redistribution of fast ions at the sawtooth crash was required to explain these results [203]. On the other hand, in plasmas with strong coupling between poloidal harmonics (high beta or strong shaping), sudden, large reductions in neutron emission are often observed. Sudden drops implying redistribution or expulsion of beam ions at the sawtooth crash have been reported for PLT [302], PDX [302], TFTR [322], JET [71,348], and DIII-D [359]. As shown in Table 3, the magnitude of these reductions is comparable to the reductions associated with the fishbone instability, but the losses do not scale linearly with the amplitude of the field perturbation [302].

The time evolution of the 15 MeV proton signal produced by ${}^3\text{He}$ tail ions in $d({}^3\text{He},p)\alpha$ reactions is also affected by the sawtooth instability. On PLT, a detector that was sensitive to central ${}^3\text{He}$ tail ions measured normal (downward) reductions in signal at sawtooth crashes [66]. In later work on PLT, a different detector observed either normal or inverted sawteeth depending upon the relative locations of the resonance layer and the sawtooth inversion radius [36]. On JET, a detector that measured off-axis protons observed inverted sawteeth at sawtooth crashes [59,71]. Although it was not necessary to invoke spatial transport of the ${}^3\text{He}$ ions to explain the PLT observations [66,36], the JET observations imply radial redistribution of ${}^3\text{He}$ tail ions at sawtooth crashes [71]. The rate of rise of the electron temperature following sawtooth crashes in JET also suggested radial fast-ion transport [218]. On TORE SUPRA, bursts of ripple-trapped hydrogen tail ions are observed at sawtooth crashes [117,366] but, on TFTR, a

reduction in the tail losses is seen [367].

Fusion products also are affected by sawtooth crashes. In PLT, the triton burnup was measured during a toroidal field scan [20]. At high toroidal field, the drops in neutron emission associated with the sawtooth crashes were only 3% and the triton burnup was consistent with classical expectations [20]. At low toroidal field, the drops in neutron emission associated with the sawtooth crashes were 15% and the sawtooth inversion radius extended to within a triton gyroradius of the limiter. The triton burnup was at least an order of magnitude smaller than expected classically [20]. A reduction in the triton burnup at low safety factor q was also observed in FT [319,320]. This reduction might have been caused by radial transport at sawtooth crashes, although classical effects associated with changes in the current profile can account for much of the reduction [368,321]. On JET, the radial profile of the triton burnup broadens at sawtooth crashes, implying redistribution of the energetic tritons [298]. On DIII-D, sawtooth crashes produce sudden $\sim 15\%$ reductions in the total neutron emission and $\sim 20\%$ reductions in the ^3He burnup, implying that 10-15% of the ^3He ions are redistributed to the plasma edge or lost at the events [211]. Bursts of lost fusion products are detected in TFTR with edge scintillators during sawtooth crashes [322,290].

The fishbone instability also has an adverse effect upon the confinement of fusion products. In PDX, reductions in ^3He burnup were correlated with the amplitude of fishbone activity [369] (Fig. 57). The observations were in good agreement with Monte Carlo simulations of the effect of the instability upon the ^3He ions (Fig. 57). Unlike the resonant beam-ion losses, the computed ^3He losses were insensitive to both the duration of the fishbone and to the mode precession frequency [369]. Losses of both copropagating and counterpropagating ^3He ions were predicted and the computed radial distortion of the ^3He drift orbits was generally several times larger than the radial distortion of the flux surfaces alone [369]. Large reductions in ^3He and triton burnup associated with the fishbone instability have also been observed in DIII-D [211]. Losses are also observed with edge scintillators in TFTR [290].

TAE modes (Sec. 5.2) also degrade the confinement of fusion products. In DIII-D, the triton and ^3He burnup is reduced by a factor of two or more in all discharges with large amplitude MHD bursts in the plasma interior [211].

Fusion products are also affected by $m = 2$ MHD activity. In PDX, the ^3He burnup fell an order of magnitude as B was reduced in a toroidal field scan [20] (Fig. 58). Concurrently, the amplitude of $m = 2$ activity increased an order of magnitude (Fig. 58), suggesting that the MHD activity was responsible for the degraded fusion product confinement. In TFTR, an edge scintillator has directly detected losses of 1 MeV tritons and 3 MeV protons during $m = 2$ activity [322,260,259,290]. The flux to the detector approximately doubles over the quiescent level [260] and the flux is modulated at the same frequency as the MHD oscillations (Fig. 59). Modulation at the $m = 2$ frequency has also been observed in the 15 MeV proton signal produced by ^3He minority tail ions in PLT [66].

In PBX, the events that precede collapse of the plasma beta caused large losses of beam ions [370]. Passive charge-exchange measurements suggested fast-ion transport during $m = 3$, $n = 1$ activity in PBX-M [371] and during giant sawtooth activity in Doublet III [372]. In PDX, a minor disruption during the initial rampup of the plasma current caused a rapid jump in active charge-exchange signal for all angles of observation, suggesting rapid parallel transport along field lines at the event [262].

In contrast, edge instabilities such as ELMs generally have little effect on the total beam-plasma neutron emission or on the fusion-product burnup [257], probably because the density of fast ions is usually concentrated in the plasma interior. Although the effect on the total population is minor, measurements of the ion cyclotron emission in JET [373,374] and of escaping fusion products in TFTR [290] suggest that ELMs do cause a loss of edge fast ions.

5. Collective Effects

The processes discussed in the previous sections are independent of the number of fast ions in the plasma. Essentially, the fast ions were treated as a collection of independent test particles that neither perturb the plasma nor one another. For a dilute fast-ion population, this approximation is valid but, for higher densities, the fast ions can modify the background plasma by driving instabilities. These instabilities are the subject of this section.

As a rough guideline, fast-ion driven instabilities are unlikely to occur unless the fast-ion pressure p_f is of the same order of magnitude as the thermal pressures p_e and p_i ; [or possibly $p_f \sim \mathcal{O}(0.1p_e)$]. Since the typical fast-ion energy E_f is large in comparison to T_e and T_i , even intense fast-ion populations are usually dilute ($n_f \ll n_e$). Thus, in most circumstances, the basic dielectric properties of the medium are determined by the thermal plasma. The most important instabilities are weakly damped normal modes of the plasma that are destabilized by the free energy in the fast-ion population.

To tap the free energy available in the fast-ion population, a mode must resonate with the fast ions.¹⁵ Instabilities in different frequency regimes interact with different aspects of the orbital motion. In the lowest frequency band (in the rest frame of the plasma), the internal kink modes interact with the precessional motion of trapped fast ions (Sec. 5.1). Alfvén waves and ballooning modes can interact with the circulating motion of passing particles and with the bounce motion of trapped ions (Sec. 5.2). Another characteristic frequency of the fast-ion population is the drift frequency associated with the spatial gradient, ω_{*f} . Theoretically, drift waves can interact with an intense fast-ion population but there has not yet been any experimental work on this topic, and fast-ion driven drift waves are not discussed here. Instabilities that interact with the gyromotion occupy the ion cyclotron range of frequencies (Sec. 5.3). Lower hybrid instabilities driven by fast ions have also been observed (Sec. 5.3).

5.1. Internal kink modes

A typical sawtooth in a low beta plasma begins with a growing $n = 1$, $m = 1$ “precursor” instability and terminates with a rapid $m = 0$ internal disruption [375]. At the internal disruption, the temperature and density within the $q = 1$ surface flatten. Following the sawtooth “crash”, the plasma reheats and the temperature and density profiles gradually reapeak until the precursor instability triggers another crash. The repetitive nature of the instability creates a characteristic sawtooth waveform in the central temperature. When auxiliary power is added to the plasma, both the amplitude of the temperature excursions and the period between crashes usually increase. With increasing beta, the plasma shifts outward, thereby increasing the coupling between poloidal harmonics. The amplitude of $n = 1$ magnetic oscillations (detected by Mirnov coils) during the precursor phase often increases, and more power is observed in the higher poloidal harmonics ($m = 2, 3 \dots$). (In some plasmas, however, precursor oscillations are absent [376]).

Fast ions dramatically alter the stability of the $m = 1$ mode. Depending on the

¹⁵Instabilities may be destabilized by the pressure in the fast-ion distribution but, if thermal ions of equal pressure would also destabilize the mode, we do not classify the mode as a fast-ion driven instability.

velocity distribution and density of the fast ions, fast ions can stabilize the $m = 1$ precursor to the sawtooth crash or can destabilize $m = 1$ modes. Stabilization of the $m = 1$ internal kink was first discovered in JET and the very large sawtooth crash observed at the end of the stabilization phase was dubbed a *monster sawtooth crash* (and the whole cycle referred to as a monster sawtooth) [150,376]. Repetitive instabilities driven by fast ions were first observed in PDX and were named *fishbones* [361,377]. In addition, fast ions may indirectly affect $m = 1$ stability by driving currents or modifying the pressure profile, but these effects are outside the scope of this review. Unfortunately, these indirect effects complicate interpretation of the results, since direct and indirect effects usually coexist.

The theory of the interaction of fast ions with the $n = 1$, $m = 1$ internal kink mode is complex and is still under development (despite extensive work on the topic). The basic ideas are easily grasped, however. The banana orbits of trapped fast ions precess around the torus with a frequency ω_{pre} . For a very low frequency $n = 1$ mode, the third adiabatic invariant Φ of the trapped fast ions is conserved if $\omega \ll \omega_{pre}$. (Φ is the flux through the area defined by the toroidal precession of the banana orbits.) In order to preserve Φ , the orbits of fast ions that are trapped within the $q = 1$ surface must contract in response to an $m = 1$ kink mode (which takes work), so these ions have a stabilizing effect upon the instability [5]. In contrast, for $\omega \simeq \omega_{pre}$, the trapped particles can resonate with another branch of the dispersion relation, and this mode can grow at the expense of the free energy in the fast-ion pressure gradient [378]. This instability is known as the precessional-drift fishbone instability. Alternatively, the fast ions may resonate with the diamagnetic drift of the thermal plasma ω_{*i} . This unstable fishbone mode with $\omega \simeq \omega_{*i}$ is associated with the low frequency branch of the dispersion relation and taps the free energy in the thermal pressure gradient [379].

Qualitatively, the theoretical relationship between these effects is as follows (Fig. 60). The currents and pressure gradients of the thermal plasma constitute the most important source of free energy in the system. The fluid response of the plasma is characterized by the ideal MHD growth rate γ_I . Fast ions only modify the stability picture near marginal ideal stability ($\gamma_I \sim 0$); if the fluid plasma is strongly stable or unstable, realistic concentrations of fast ions cannot alter the mode stability. In the absence of fast ions, the low frequency branch is most important. This mode causes ordinary sawtooth precursor oscillations when $\gamma_I \sim 0$, with resistive effects probably playing an important role. As the fast-ion concentration increases inside the $q = 1$ radius, the stabilizing effect of Φ conservation becomes important. Competing against this stabilizing effect is the destabilizing effect of fast-ion resonances with bulk-plasma motion, which can improve access to the free energy in the ideal fluid. For large fast-ion concentrations, the precessional-drift fishbone is destabilized.

These basic effects only occur in their pure form in rather idealized limits. The actual effect of a fast-ion population upon the theoretical stability depends upon the relative magnitude of (at least) six frequencies and growth rates [380]. These frequencies and growth rates are listed below (as well as the experimental quantities that must be measured in order to calculate them).

1. Alfvén frequency $\omega_A \propto v_A/R$ where $v_A = B/\sqrt{\mu_0 n_i m_i}$ is the Alfvén velocity. (The density profile and the average charge-to-mass ratio of the ions.)
2. Precession frequency ω_{pre} . For deeply trapped ions, ω_{pre} is approximately

$cE_f/2q_f B_\theta R$, where E_f is the average energy but, for accurate work, ω_{pre} must be evaluated numerically. (The fast-ion distribution function and the poloidal field.)

3. **Ion diamagnetic frequency** ω_{*i} evaluated at the radius r_1 of the $q = 1$ surface, $\omega_{*i} = c(dp_i/dr)/r_1 n_i q_i B$. (The thermal ion temperature and density profiles and r_1 .)
4. **Electron diamagnetic frequency** $\hat{\omega}_{*e}, \hat{\omega}_{*e} = c(dp_e/dr)/r_1 n_e e B + 0.71c(dT_e/dr)/e B r_1$. (The electron temperature and density profiles.)
5. **Ideal MHD growth rate** γ_I . This is roughly $\gamma_I \sim \epsilon_1^2(\beta_p^2 - \beta_{pc}^2)$, where ϵ_1 is the inverse aspect ratio evaluated at the $q = 1$ surface, β_p is the poloidal beta of the plasma, and $\beta_{pc} \simeq 0.1-0.3$ in JET [5]. For accurate work, γ_I must be evaluated numerically. (The pressure and q profiles and the plasma shape.)
6. **Resistive growth rate** $\gamma_R = S^{-1/3}\omega_A$, where S is the magnetic Reynolds number.

In addition to the effects associated with each of these parameters, possible resonances with bulk-ion transit and bounce motion must be considered, and the effects of plasma shaping, coupling to poloidal harmonics, sheared plasma flows, and equilibrium electric fields on $m = 1$ stability have not yet been treated.

Clearly, detailed quantitative comparison between theory and experiment is a daunting task, requiring extensive numerical calculations and accurate measurements of the q profile, the fast-ion population, and the thermal temperature and density profiles. Only a few, quantitative comparisons (discussed below) have been attempted, and these either have very large error bars or neglect important effects. Although a quantitative confirmation of the theory is lacking, the general qualitative trends do seem consistent with the theoretical picture sketched in Fig. 60.

Sawtooth stabilization by fast ions was discovered during ICRF minority heating in JET [150,376] and was subsequently observed on TFTR [367,381]. Stabilizing effects associated with a trapped fast-ion population have also been seen during hydrogen minority heating in TORE SUPRA [366], during ICRF [125] and beam heating [382] in TEXTOR, and during second harmonic hydrogen heating in JT-60 [147]. Figure 61 shows an example from JET [5]. During the rf pulse, an energetic anisotropic fast-ion population is created (Sec. 2.3.1). The sawtooth instability, which normally modulates the central electron temperature, is stabilized and the electron temperature saturates until the rf is turned off (Fig. 61). The delay between the termination of the rf pulse and the “monster sawtooth” crash is 60-80 ms for this case (Fig. 61), which is comparable to the slowing-down time of the energetic tail ions.

The experimental observations are in qualitative agreement with kink-mode theory [5].

- Stabilization occurs in a regime where the precessional frequency is high. Theoretically, it is predicted that ω_{pre} must exceed ω_{*i} for stabilization. Since ω_{pre} is proportional to the fast-ion energy E_f but $\omega_{*i} \propto T_i$, it is expected that large energies but low temperatures T_i should be stabilizing. Experimentally, stabilization is more readily obtained with rf heating, where the tail energies are 0.1-10 MeV (Sec. 2.3.1), than with beam injection, where $E_f \lesssim 0.1$ MeV. Most beam heating experiments are in a regime where $\omega_{pre} \sim \omega_{*i}$. The reported sawtooth stabilization

in TEXTOR during beam heating [382] occurred in a device with relatively low values of ω_{*i} .¹⁶

- During rf heating, conditions that are conducive to energetic tail formation are conducive to sawtooth stabilization. Stability tends to be enhanced by low minority concentration, low electron density, and high rf power. Figure 62 shows data obtained during a ^3He concentration scan in a ^4He majority plasma in JET [5]. Gamma rays produced in reactions between ^3He and carbon impurities monitored the intensity of the fast-ion population. At low concentrations, the energetic population was larger and the sawteeth were stabilized (Fig. 62). A correlation of sawtooth stabilization with the intensity of gamma-ray emission is generally observed in JET [5]. In TEXTOR, the sawtooth period is longest under conditions that favor energetic tail formation [125]. In TFTR, a rf power threshold is observed below which sawtooth stabilization does not occur [381]. The threshold is higher for ^3He minority heating than for hydrogen minority heating [381], presumably because energetic tails are more readily achieved with hydrogen than with helium (owing to the reduced Coulomb drag). (The duration of the stabilized phase in JET is generally longer with ^3He minority heating than with hydrogen heating, however.)
- After the end of the rf pulse, stabilization persists for about a fast-ion slowing time (Fig. 61). This observation eliminates direct effects associated with the rf waves (e.g., a ponderomotive force) as an explanation for the stabilization phenomenon.
- In both JET [383] and TFTR [381], stabilization is achieved when the resonance layer is positioned inside the sawtooth inversion layer. This is in accord with theory, which predicts that only energetic ions within the $q = 1$ radius have a stabilizing effect. In TFTR, stabilization is not achieved at low values of plasma current, presumably because the small value of inversion radius precludes an intense peaked population of fast ions within the $q = 1$ surface [381]. This also suggests a possible explanation for the absence of stabilization in the PLT ICRF experiments [381]. In PLT, the sawtooth period was short in comparison to the fast-ion slowing-down time and the theoretical power deposition profile was relatively broad. Because of the frequent periodic flattening of the electron temperature [and probably the fast-ion distribution function (Sec. 4.5)], the fast ions may never have developed the peaked, energetic distribution required for stabilization.
- In JET, stability is easier to obtain when the inversion radius is small. For central heating in JET, the deposition of rf power is always expected to occur within the $q = 1$ surface. Under these conditions, an increase in the $q = 1$ radius r_1 reduces the stabilizing effect of the fast ions. Several experimental observations are compatible with this expectation, including the dependence of the sawtooth-free period on the inversion radius, the greater difficulty in obtaining stabilization at high plasma current, and the beneficial effect of a rapid current ramp prior to the rf pulse [5].

¹⁶It should be noted, however, that sawtooth stabilization sometimes occurs in hot plasmas during tangential beam injection. For example, in TFTR supershots [305], sawteeth are usually absent. Whether stabilization is caused by modified current and pressure profiles or by a direct fast-ion effect is not known.

In addition to exhibiting the expected parametric dependencies, the data are in rough agreement with the expected stability boundaries. Figure 63 shows the calculated ideal MHD growth rate and the fast-ion poloidal beta for a subset of JET [383] and TFTR [381] plasmas that were stable to the sawtooth instability during ICRF. Although the theoretical stability boundary has not been calculated for the actual experimental conditions, the observations are consistent with the expected trends. More extensive and accurate comparisons are needed to confirm these qualitative results.

An observation that seems inconsistent with the theoretical model is the occasional coexistence of fishbones with sawtooth stabilization in JET [349].

An alternative explanation for sawtooth stabilization during ICRF is that the current associated with precessing tail ions indirectly suppresses the sawtooth instability through modifications of the q profile [384]. However, this hypothesis seems inconsistent with the low central values of q measured near the end of the stable phase [376,381]. On the other hand, scans of the antenna phasing and of the position of the resonance layer in JET do indicate that currents driven by fast ions can effect sawtooth stability [246,309].

In contrast to rf-generated fast-ion populations, beam ions usually have a destabilizing effect upon the internal kink. The fishbone instability was discovered in PDX [361,377] and was subsequently observed on most tokamaks. Waveforms for a PDX plasma with very strong fishbone activity are shown in Fig. 64. The instability occurs in repetitive bursts and has a much faster repetition rate than the sawtooth cycle. This is evident in Fig. 64, where nine fishbone bursts occur prior to a sawtooth crash that causes a $\sim 15\%$ reduction in the soft x-ray signal. The $n = 1$ oscillations associated with each burst are evident in both the soft x-ray emission and in the magnetic fluctuations detected at the plasma edge (Fig. 69), but the average value of the soft x-ray signal does not drop markedly during a fishbone because there is no sawtooth crash. The soft x-ray emission has an $m = 1$ structure, while the magnetics signals are usually dominated by $m = 2$ or $m = 3$ modes. The frequency of the oscillations is higher than the bulk plasma rotation frequency, indicating that the mode propagates in the plasma frame. A typical burst lasts about 1 ms. Large fishbone bursts have a devastating effect upon fast-ion confinement (Sec. 4.4) and can cause large reductions in neutron emission during deuterium injection (Fig. 64).

In a classic fishbone burst, the growth rate and decay rate of the instability are comparable (Fig. 64). Wide variations in the relative duration of the growth and decay phases are observed even in the same device, however [342]. Under some conditions, most of the $m = 1$ bursts end in a sawtooth crash. For example, virtually all of the intense $m = 1$ bursts during tangential injection in PBX [362] exhibited this hybrid sawtooth-fishbone behavior. An example of one of these *sawbone* bursts during deuterium injection into PDX is shown in Fig. 66. The growth of the $n = 1$ instability on the soft x-ray and Mirnov coil signals is virtually indistinguishable from a classic fishbone burst. At the sawtooth crash, the soft x-ray and neutron emission drop suddenly (Fig. 66). Presumably, the $m = 1$ mode is stabilized after the crash by both the reduction in ideal MHD growth rate γ_I and the large reduction in fast-ion pressure. During tangential injection the period between these bursts can be much shorter than the usual period between sawteeth [385,386,362].

The internal frequency of the $m = 1$ oscillations often decreases during a fishbone burst. On PDX, the frequency usually fell by a factor of two, from about 20 kHz to about 10 kHz [377,337,342,302]. On JET, the frequency variation can be as large as

a factor of three [349], as shown in Fig. 65. During tangential injection, the internal frequency of a sawbone is often not much greater than the plasma rotation speed and the reduction in frequency at a burst is only about 10% [362].

Fishbones have been observed during perpendicular injection in PDX [361,339,377,341,342], PBX [345,362,44], PBX-M [351,352], and JT-60 [387], during injection at intermediate angles in Doublet III [388,389], DIII-D [347], and JET [349,1,350,390], during tangential injection into TFTR [346], and during ICRF heating in JET [349]. In addition, sawbones were seen during tangential injection into JFT-2 [385], ISX-B [386,391], PLT [302], PBX [362,344], and, possibly, T-11 [222]. The observations are summarized in Table 4.

Detailed, quantitative agreement of the theoretically predicted frequency with observations has not yet been demonstrated. Theoretically, the precessional-drift branch and the ω_{*i} branch of the fishbone merge for $\omega_{*i} \sim \omega_{pre}$, a condition that often holds in the experiments. In PDX, the fishbone frequency scaled with the precessional frequency of the fast ions [377,342], but the observed mode frequency actually agreed with the precessional drift speed of fast ions near the outer edge of the plasma, rather than the drift speed of beam ions within the $q = 1$ surface [342] (Fig. 67). This observation motivated Kaita *et al.* to postulate that coupling of the different poloidal harmonics permits fast ions throughout the plasma to resonate with the internal kink [346]. With this assumption, the computed average precession frequency was close to the measured frequency in PDX [346], TFTR [346], and PBX-M [351]. In JT-60, the observed frequency was close to ω_{pre} [387]. In DIII-D [347] and JET [349], on the other hand, the mode frequency sometimes agreed with ω_{*i} and sometimes with ω_{pre} , with significant scatter observed. The reduction in frequency during a burst has not been fully explained either. It was first suggested that the mode frequency decreases during a burst because energetic beam ions are lost first, causing the average precession frequency to drop with time; however, this hypothesis is very difficult to reconcile with the time evolution of the neutron emission through a fishbone [302]. Although the time evolution of dp_i/dr has not been measured during a fishbone, it also seems quite unlikely that ω_{*i} drops a factor of two during a burst. Perhaps the frequency reduction is associated with a shift from a predominately precessional-drift fishbone to a predominately ω_{*i} fishbone in the hybrid regime where $\omega_{*i} \sim \omega_{pre}$.

The stability properties of fishbone modes are not convincingly established either, although the general trends are compatible with theoretical expectations. Instability was more likely at large values of β_p in PDX [342] and DIII-D [347], presumably due to an increase in the ideal MHD drive γ_I . In PBX, bean shaping had a stabilizing effect [345], probably because of a reduction in γ_I . For a given beam power, instability was more likely at low density in PBX [362] and DIII-D [347], probably because the beam pressure was larger (due to of the longer slowing-down time). In PDX, fishbones were always observed for $\beta_N \gtrsim 1.2$, but considerable variability in stability properties are observed on other devices. For example, in DIII-D, stable plasmas with sawteeth exist with $\beta_p > 2$ [347]. In JET, instability is sometimes observed at very low values of β_p [349] (Fig. 68), in apparent contradiction of analytical estimates of γ_I . Although fishbones usually occur in high β_N and β_p plasmas with large fast-ion populations, these observations highlight the wide range of behavior possible (Table 4).

The most detailed study of fishbone stability completed to date employed measurements of the q profile in PBX-M [352]. Unfortunately, the ion temperature was not measured in this experiment and ω_{*i} effects were not considered. Within the framework

of the simplified theory of the precessional-drift fishbone [378], the unstable discharges were predicted to be unstable [352]. Simple estimates of stability in PDX and TFTR also agreed with experiment [346].

The nonlinear saturation of fishbones seems to be governed by fast-ion loss. As additional beam power is added to the plasma, the $n = 1$ activity typically evolves as shown in Fig. 69, which shows the signal from a Mirnov coil for four DIII-D discharges during neutral beam injection. Similar progressions of MHD activity were observed in JFT-2 [385,341], ISX-B [386,341], PDX [341] and PBX. The first effect of neutral beam injection is to increase the period and amplitude of sawtooth activity. The increase in period is probably caused by the heating associated with beam injection (increased T_e), rather than the fast-ion population directly. The $m = 1$ precursor to the sawtooth is detected by pickup loops at the plasma edge, but the amplitude of the oscillations is relatively modest (Fig. 69). As the density of the fast-ion population and the plasma beta increase further, semi-continuous $m = 1$ activity is sometimes observed (Fig. 69), particularly just prior to a sawtooth crash. There probably is not a single universal explanation for these *run-on fishbones* but, in many cases, this phenomenon seems to occur near the marginal stability point for the fishbone instability.¹⁷ If the power is increased still further, isolated fishbone bursts develop (Fig. 69). Close to the marginal stability point, fishbone bursts are more likely just prior to a sawtooth crash than immediately following a crash and the growth rate is larger later in the cycle [342,347], probably because the ideal growth rate γ_I is larger later in the sawtooth cycle. If the beam power is very large, the amplitude and period of the fishbones usually increase (Fig. 69) and the losses associated with the fishbone bursts can become very large, as in Fig. 64.

Several semi-empirical models have been proposed to explain the evolution of the fishbone cycle [378,392,346,393]; the simplest formulation is in Ref. [394]. In these models, the amplitude of the instability is driven unstable by the beam population but the mode amplitude causes the loss of beam ions, resulting in a nonlinear predator-prey cycle [379]. Near marginal stability, the number of beam ions is barely sufficient to sustain instability, the mode amplitude is small, and the transport of fast ions is modest, so the near-equilibrium situation of run-on fishbones occurs. As the rate of beam fuelling increases, the fast-ion pressure overshoots the point of marginal stability and the mode grows to larger amplitude. When the mode amplitude is sufficiently large, fast ions are expelled (Sec. 4.4) and the fast-ion pressure falls below the marginal stability point. Following the burst, the fast-ion pressure increases due to beam fuelling and the cycle repeats. Further increases in the rate of beam fuelling result in more explosive growth of the instability and more catastrophic fast-ion losses, so the amplitude and period of the bursts increases with increasing power. In these models, the beam beta is effectively clamped near the point of marginal stability. With reasonable choices of the free parameters in the models, the theories can match the time evolution of the magnetics and neutron signals for selected cycles in PDX [378,392,346,394], TFTR [346], and JET [393]. (A systematic comparison with a large set of data has not yet been performed.) Extensions of the basic model can also account for the irregular cycles that are sometimes observed [393].

¹⁷In the published literature, run-on fishbones are sometimes called “continuous $m = 1$ activity.” We prefer the more descriptive name, “run-on fishbone,” because the amplitude and frequency of the magnetic fluctuations oscillate in time [342], just as they do in fishbones.

5.2. Alfvén waves and ballooning modes

Theoretically, several plasma modes exist that can resonate with the parallel motion of circulating fast ions or with the bounce motion of trapped ions. In early work, the modes that are now known as *kinetic Alfvén waves* were suggested as modes that a circulating fast-ion population might destabilize [395,396]. Within the framework of ideal MHD, these modes reside in the continuum of the Alfvén spectrum, and so are subject to relatively strong damping.¹⁸ Modes also exist with a frequency below the minimum of the Alfvén continuum [397]; these modes, which can exist in a cylinder, are known as *global Alfvén eigenmodes* (GAE) and have opposite helicity from the equilibrium field. In circular cylindrical geometry the poloidal wavevector is characterized by a particular poloidal mode number m . Subsequent study in toroidal geometry revealed the existence of modes that reside in “gaps” in the Alfvén continuum [398]; these *toroidicity-induced Alfvén eigenmodes* (TAE) couple neighboring poloidal harmonics m and $m + 1$. An example of the gap structure for a measured equilibrium in DIII-D is shown in Fig. 70; TAE modes lie in the first gap. Higher poloidal harmonics can also be coupled by toroidicity or by shaping effects. Modes that couple m and $m + 2$ are known as *ellipticity-induced Alfvén eigenmodes* (EAE) and modes that couple m and $m + 3$ are called NAE (triangularity-induced) modes [399] (Fig. 70). Finite pressure and the geodesic curvature of field lines create an additional gap underneath the continuum [400] and *beta-induced Alfvén eigenmodes* (BAE) can reside in this gap [401].

The frequencies of these Alfvén modes depends upon the parallel wavevector k_{\parallel} of the mode and upon the Alfvén velocity v_A , $\omega = k_{\parallel}v_A$. For the GAE, $k_{\parallel} = (n + \frac{m}{q})/R$ (m and n have opposite signs). It is customary to define the *Alfvén frequency*, $\omega_A = v_A/qR$. The center of the TAE, EAE, and NAE gaps occur near

$$\omega_{TAE} = \frac{1}{2}(v_A/qR), \quad (33)$$

$$\omega_{EAE} = (v_A/qR), \quad (34)$$

and

$$\omega_{NAE} = \frac{3}{2}(v_A/qR), \quad (35)$$

respectively. The BAE mode frequency is roughly half the TAE mode frequency. Both v_A and q are functions of position so that the frequencies of these modes depend upon the radial structure of the eigenfunction. Calculations with realistic equilibria show that the mode frequency is usually somewhat lower than the nominal values given in Eqs. 33-35 [401].

The theoretical stability of these modes is complicated. As a concrete example, let us consider TAE modes. Circulating fast ions can resonate with the mode, generating a drive term of the form¹⁹ [403]

$$\frac{\gamma_{drive}}{\omega_{TAE}} = \frac{9}{4}\beta_f \left(\frac{\omega_{*f}}{\omega_{TAE}} - \frac{1}{2} \right) F, \quad (36)$$

¹⁸The damping mechanism is not specified in the MHD model but the physical idea is that, in the continuum, driven modes rapidly exchange energy with nearby damped modes.

¹⁹The actual form of the drive term depends upon the details of the fast-ion distribution function. The expression here stems from an approximate calculation based upon a Boltzmann fast-ion distribution. Cheng [402] and Betti and Friedberg [399] have treated an isotropic slowing-down distribution.

where γ_{drive} is the contribution of the fast ions to the growth rate. The drive increases for an intense population with a large fast-ion beta β_f . The free energy is provided by the gradient in the fast-ion pressure (ω_{*f}) and this gradient must be large enough to overcome Landau damping on the fast-ion distribution function ($\omega_{*f} \gtrsim \omega_{TAE}$). Finally, the drive depends upon the fraction of the fast-ion population F that resonates with the wave. The primary resonance occurs for fast ions with $v_{||} = v_A$, but some drive can also occur on a sideband for $v_{||} = v_A/3$ [399,404]. Further modifications to Eq. 36 and broadening of the resonance condition are associated with the radial extent of the mode and the finite poloidal gyroradius of the fast ions [405]. The drive term (Eq. 36) is opposed by various damping terms associated with electron Landau damping [403], electron collisions and the effect of a parallel electric field [406], ion Landau damping at both the fundamental and the sideband [399], and continuum damping [407,408]. Some of the formulas for these effects are only approximate for TAE modes. As a general rule of thumb, gaps that are wide (in space) minimize continuum damping, while high gaps (in frequency) minimize coupling to kinetic Alfvén waves. Other Alfvén modes in this frequency range presumably are opposed by similar damping mechanisms, but the stability theory of these modes is even less developed.

Theoretically, a second class of potentially dangerous modes are the ballooning modes [409]. Like the internal kink, ballooning modes can be driven unstable by the bulk plasma but, when the ideal MHD growth rate is marginally stable, kinetic effects may become important. As with the fishbone, two distinct branches appear: an MHD gap mode with frequency $\sim \omega_{*i}$ and an energetic-particle continuum mode with the characteristic frequency of the fast-ion motion [410]. Theoretically, resonant interaction with both circulating and trapped particles is possible [409].

Experimentally, modes in this frequency range are observed when the fast-ion beta is large. The observations are summarized in Table 5 and Fig. 71. The modes usually occur in bursts; they often (but not always) occur in conjunction with $n = 1$ internal kinks (Sec. 5.1). An example of an isolated burst during tangential beam injection into PBX is shown in Fig. 72. Phenomenologically similar bursts were observed during perpendicular injection into PDX [377,341,302], during tangential injection into TFTR [353,354,411], during near-tangential injection into DIII-D [356,412,413], and during tangential injection into PBX-M [414]. In all of these cases, the bursts were associated with radial transport of the beam ions (Sec. 4.4).

In TFTR [353,354,411] and DIII-D [356,412,413] these bursts have been identified as TAE modes. Figure 73 compares the measured frequency of the high frequency burst with Eq. 33 during a scan of the toroidal field in TFTR [353]. Similar scaling has been observed during a toroidal field scan in DIII-D [401,412,413]. The observed mode structure in DIII-D [356] and TFTR [353,411,358] is compatible with theoretical expectations for TAE modes, within large experimental uncertainties.

The observed stability properties of TAE modes are in semi-quantitative agreement with theory. The mode amplitude tends to be largest when $v_{||} \simeq v_A$ [413], although instability is observed for lower values of $v_{||}/v_A$ (Fig. 71). Large values of β_f are destabilizing [413]. Calculations indicate that electron damping by temporal [406] and spatial [407] coupling to kinetic Alfvén waves are the dominant damping terms in the DIII-D [413] and TFTR [415] experiments; the observed threshold in γ_{drive} is within a factor of three of theoretical expectations [413]. By ramping the plasma current in order to modify the gap structure, experiments on both DIII-D [413] and TFTR [358] have verified

qualitatively that continuum damping plays an important role in the stability of low n modes.

TAE modes are also driven by energetic perpendicular tail ions during hydrogen minority ICRF heating in TFTR [416]. Theoretically, TAE modes can be driven by trapped ions through resonance with harmonics of the bounce motion, as well as by resonance with circulating fast ions [404].

A mode that is probably the EAE mode has been observed in DIII-D [401] and possibly in TFTR [354].

As the plasma approaches the beta limit, the frequency of beam-driven modes in DIII-D tends to decrease (Fig. 74). The instability with $\omega \simeq \frac{1}{2}\omega_{TAE}$ is probably a BAE mode [417] but it might be a kinetic ballooning mode [409]. Other modes that are driven by tangential beam ions are observed in TFTR [418], but are not yet identified.

Perpendicular beam ions destabilized modes similar to TAE modes in PDX [377,341,302]. It has been suggested that these modes are ballooning modes [409], or they could be TAE modes that are driven unstable by harmonics of the bounce motion [404].

Experimentally, beam-driven TAE modes saturate nonlinearly through bursts that expel beam ions [394], just as fishbones do. As a result, the fast-ion beta clamps near the marginal stability point when the beam power exceeds the stability threshold [354,412,359] (Fig. 75). To within $\sim 50\%$ uncertainty, the duration of the bursts and the period between bursts scale with beam power as theoretically predicted [394]. In contrast, bursts were not observed when TAE modes were driven unstable by ICRF heating [416]. The fishbone saturation model [394] is not expected to apply to rf heating, however, because fast ions are not generated steadily at a fixed birth energy.

5.3. Ion cyclotron and lower hybrid instabilities

Fast ion populations emit radiation in the ion cyclotron range of frequencies and, occasionally, in the lower hybrid band. Experimentally, ion cyclotron emission (ICE) has been observed in TFR [39,214], PDX [340,342,419], and JT-60 [420,147] during perpendicular beam injection, in JET [421–423,350,373,374,299] and TFTR [424–426] during ohmic heating and beam injection, and in DIII-D [359] during near-tangential beam injection. Lower hybrid emission driven by beam ions was also observed in PDX [342], as illustrated in Fig. 76.

The only controlled ICE experiment was conducted by injecting repetitive short pulses of hydrogen neutral beams into JFT-2M [427]. Figure 77 summarizes the results of the experiment. When the pulses were short, the beam-ion distribution function at the center of the plasma did not decrease monotonically with velocity (Figs. 77b,c) and strong ion cyclotron emission at the central hydrogen fundamental was observed (Fig. 77a). When the pulse length was increased, the distribution function became smoother (Figs. 77b,c) and the ICE disappeared (Fig. 77). Based on the parallel wavelength, and the observed dependences upon pulse duration, plasma density, and hydrogen concentration, the mode was identified as an Alfvén eigenmode that is a combination of a compressional Alfvén wave, an ion Bernstein wave, and a modified ion cyclotron wave [427]. Similar bursts of ICE are often observed on other devices in the initial stages of beam injection [342].

The passive ICE observations can be separated into two categories: ICE produced by beam ions and ICE produced by fusion products. The strongest emission correlates

with instabilities that expel beam ions. The spectrum in this case often consists of a set of relatively narrow peaks at harmonics of the cyclotron frequency, as observed (for example) during fishbone activity in PDX (Fig. 78). The peaks are separated by the cyclotron frequency at the outer edge of the plasma [39,340,342]. Following each MHD event that expels beam ions a burst of ICE occurs [340,342,359,350]. Figure 79 shows an example during combined fishbone and TAE activity in DIII-D [359]. ICE with similar features can also be generated by prompt loss orbits. This is the likely cause of the emission observed on TFR [39,214], of the ICE measured during counter-perpendicular injection on PDX [342], and of the second harmonic emission seen on JT-60 [420,147], and may account for the emission observed during hydrogen injection into JET [422].

In PDX [337] and JT-60 [420], fast ions were accelerated to energies nearly twice the injection energy by the ICE.

The second type of ICE is generated by fusion products. In JET, the second-harmonic ICE power scales linearly with the total neutron emission over a variation of six orders of magnitude for both d-d and d-t plasmas (Fig. 80) [373,374]. The ICE intensity is delayed with respect to the neutron emission as the fusion product population builds up [373,374]. The emission is from the outer (large R) edge [374]. Modelling of the time evolution of the alpha density suggests that the signal is produced by fusion products whose orbits pass through the edge region [374]. The generation of ICE is anti-correlated with large ELM activity [350,373,374], presumably because the ELMs degrade the confinement of edge fusion products [374]. Narrow emission peaks are observed ($\Delta\omega/\omega \simeq 0.1$) but the spectra tend to be broader than during beam injection [422]. In contrast to the ICE generated by beam ions (Fig. 79), ICE from fusion products in JET sometimes peaks ~ 12 ms after the sawtooth, when the heat pulse arrives at the plasma edge (Fig. 81) [423]. The edge fusion product density is not expected to change significantly on this timescale; perhaps the accessibility of the waves to the antenna is affected by the density of the edge plasma [426], and these variations cause the sawtooth oscillations.

Both types of emission are observed on TFTR [425]. A broad feature that scales with the d-d emission is observed above the fifth harmonic [425,426], as well as narrow peaks at lower frequencies that appear to be produced by beam ions in the plasma edge [425].

No theoretical explanation for the phenomena has gained wide acceptance yet. Several authors [419,422,428] have suggested that ICE is a wave driven unstable by an anisotropic or inverted fast-ion distribution in the plasma edge. Others [426] suggest that spontaneous cyclotron and spin-flip emission account for the observations.

6. Conclusions

In this section, we summarize the observations, identify issues that need further clarification, and speculate about the behavior of alpha particles in future devices.

In Sec. 2, we found that measurements of the initial spatial and velocity distribution of fast ions are in good agreement with theoretical expectations for most fast-ion populations. For thermonuclear emission, the fusion-product birth profile peaks very strongly on axis and the initial energies are close to the nominal birth energy. For fusion products created in beam-plasma and beam-beam reactions, the birth profile peaks on axis, although usually not quite as strongly as for thermonuclear emission. The initial energy is centered about the nominal birth energy, but the distribution often contains substantial energy broadening (> 1 MeV) and can be anisotropic. For beam ions, calculations of beam deposition agree (to within $\sim 20\%$) with the measured profiles. The bulk of the data seem to favor the cross sections that include multistep ionization processes, but more work in this area is desirable. For hydrogenic neutral beams, the initial energy distribution consists of three essentially monoenergetic populations at E_b , $E_b/2$, and $E_b/3$. During ICRF minority heating, the measurements indicate that fast ions gain perpendicular energy near the resonance layer (where $\Omega_f = \omega_{rf}$). The distribution is quite anisotropic and is characterized by a Boltzmann distribution with $T_\perp \gg T_\parallel$. The energies can be very large, with “temperatures” T_\perp in excess of 1 MeV and maximum measured energies of $\mathcal{O}(10$ MeV).

Observations of the fast-ion tail created by lower hybrid waves are less conclusive. Modest tail temperatures of $\mathcal{O}(10$ keV) are observed and the distribution is fairly isotropic. The spatial profile seems to depend upon the electron density profile, with peaked profiles correlating with central tail formation and broad profiles correlating with peripheral tails (Table 2).

Coulomb drag by thermal ions and electrons governs the deceleration of fast ions (Fig. 20). Additional processes, if they are important at all, only cause modifications of $\mathcal{O}(10\%)$ in the deceleration rate. The energy diffusion of fast ions also is in good agreement with Coulomb scattering theory (Sec. 3.1.3). The rate of pitch-angle scattering (Sec. 3.1.2) has only been determined to an accuracy of $\sim 50\%$, but is probably described by classical theory too. A more accurate measurement of the pitch-angle scattering rate is desirable because losses caused by toroidal field ripple depend sensitively on this rate.

Despite its simplicity, with appropriate modifications for orbit effects, the Stix theory of minority ICRF heating gives good agreement with the experimental observations (Sec. 3.2.2). The discrepancy between the measured fast-ion stored energy and the calculated energy is $\sim 20\%$ (Fig. 25). The acceleration of beam ions during lower hybrid is consistent with stochastic ion heating, but quantitative agreement between the absorbed power and theory has not been demonstrated yet (Sec. 3.2.3). The mechanism responsible for acceleration of ions in the tail of the thermal distribution is even more uncertain. Stochastic ion heating by scattered or daughter lower hybrid waves probably play a role, but harmonic damping on edge ion quasimodes may also be important. Further progress in this area requires simultaneous measurements of the wave spectrum in the plasma and of the fast-ion distribution.

The confinement of fast ions is governed by a number of processes (Sec. 4). Prompt losses are determined primarily by the plasma current and the energy of the fast ion, and are described by drift orbit theory (Sec. 4.1). Transport associated with toroidal field rip-

ple is also observed (Sec. 4.2). Ripple trapping can cause large losses of trapped fast ions in devices with large ripple ($\delta \gtrsim 1\%$); the observed losses agree to within 20% with calculations (Fig. 35). In machines with smaller values of ripple, stochastic ripple diffusion gains in relative importance. The first measurements of the losses caused by stochastic ripple diffusion agree with theory to within a factor of two; more work in this area is needed. Transport associated with Coulomb scattering, microturbulence, and rf waves is relatively unimportant for fast ions (Sec. 4.3), probably because the large orbits of fast ions temporally and spatially averages over the fluctuation spectrum. Losses caused by steady-state turbulence are generally negligible in a slowing-down time (Fig. 48). More detailed studies that combine accurate fast-ion measurements with measurements of the fluctuation spectrum are desirable. In contrast to steady-state turbulence, violent MHD events can cause catastrophic losses. Through resonance between the phase velocity of the mode and the fast-ion orbital motion, both the fishbone instability and TAE modes transport beam ions to the outer edge of the plasma (Sec. 4.4). Non-resonant MHD events such as high-beta sawteeth can also cause large transport (Sec. 4.5). Studies that combine fast-ion measurements with detailed documentation of the MHD activity are needed to identify the mechanisms responsible for fast-ion transport under these conditions.

Intense fast-ion populations can alter the stability of the plasma (Sec. 5). Stabilization of sawteeth by a high energy, perpendicular fast-ion population appears consistent with theory (Sec. 5.1), although quantitative confirmation of the stability boundary has not been demonstrated. On the other hand, lower energy beam-ion populations can drive the internal kink unstable. Both fishbone and sawbone bursts are observed. Some measurements are consistent with theory, but possible exceptions are also observed (Sec. 5.1). Detailed quantitative comparisons that employ the complete theory and measured profiles of q , T_i , and the fast-ion distribution are needed. Fast ions also drive instabilities that resonate with the parallel orbital motion (Sec. 5.2). TAE modes have been identified and other instabilities may also occur. The stability properties of TAE modes are in rough agreement with theory (to within a factor of three). More accurate comparisons require better measurements of the fast-ion distribution and of the eigenfunction, or new ways to measure the damping rate. Fast-ion populations also drive instabilities in the ion cyclotron range of frequencies (Sec. 5.3). Some instabilities are driven by fusion products, while others owe their origin to edge beam ions. To clarify these phenomena, injection of a known fast-ion population into the plasma edge is highly desirable.

Some aspects of alpha behavior in a reactor can be predicted with confidence, but some of the most important properties are murky. Alphas will be centrally born. If beam-plasma reactions are employed, the initial alpha energies will be shifted substantially from 3.5 MeV and the distribution function could be anisotropic. The deceleration rate of the alphas will be determined primarily by drag on thermal electrons. Since efficient second harmonic ICRF heating of deuterium beam ions has been observed, second harmonic heating of the energetic alphas is probably possible if desired. Interaction with lower hybrid waves is also likely, but the spatial location and mechanism of the interaction is uncertain. Prompt losses will be governed by drift-orbit theory. The reactor should be designed with a sufficiently low value of ripple that the poloidally and toroidally concentrated losses associated with ripple losses do not damage the first wall. Under these conditions, the power losses associated with stochastic ripple diffusion will

be unimportant in the total energy balance, but potential hot spots could be an issue. If MHD activity is controlled, most alphas will thermalize before they are lost from the plasma. In a low-density regime, some broadening of the deposition profile seems likely, however, because typical values of the fusion-product diffusion coefficient are $0.1 \text{ m}^2/\text{s}$ in existing experiments. MHD activity is of greater concern. Strong sawteeth will transport alphas well past the $q = 1$ surface, resulting in substantial broadening of the power deposition profile. Alpha particles that reach the edge of the plasma will produce ion cyclotron emission, which may be useful as a diagnostic.

The key unresolved issues are associated with collective instabilities. The present degree of agreement between theory and experiment makes reliable predictions of the internal kink or TAE stability problematic. Because the energy of alphas is large compared to T_i ($\omega_{pre} \gg \omega_{*i}$), alphas may help stabilize sawteeth. On the other hand, destabilization of fishbones might occur. The expected alpha-particle beta may exceed the minimum beam beta that can destabilize TAE modes, so these instabilities are also potentially dangerous. Although stability boundaries cannot be confidently predicted, the consequences of instability are easier to discern. Nonlinear stability will likely be achieved through a cycle of alpha particle losses during MHD bursts, as it is in present beam-heated experiments. The bursts will clamp the alpha beta near the marginal stability point. The alpha particle losses will likely be concentrated near the midplane, with potentially devastating consequences for the first wall.

In conclusion, in two decades of research into the properties of fast ions much has been learned, but the most exciting experiments lie ahead.

ACKNOWLEDGEMENTS

We thank the many scientists worldwide who sent us papers and figures and answered questions on their work. Dr. S. Bosch graciously contributed his fusion products bibliography, and Cris Barnes sent an updated version. The bibliography compiled by Hively and Sigmar [429] was also helpful. The many detailed comments on the manuscript by Jim Strachan and Stewart Zweben are greatly appreciated. This work was partially supported by U.S. Department of Energy grant DE-FG03-92ER54145.

LIST OF SYMBOLS AND ACRONYMS

A_f	fast-ion atomic mass
a	minor radius
b_0	distance of closest approach
B	toroidal field
B_θ	poloidal field
\tilde{B}_θ	poloidal field perturbation
BAE	beta-induced Alfvén eigenmode
c	speed of light
C	Coulomb scattering term
D	Diffusion coefficient
e	electron charge
E_b	beam injector voltage
E_{crit}	critical energy
E_f	fast-ion energy
E_\perp	perpendicular energy
EAE	ellipticity-induced Alfvén eigenmode
ELM	edge localized mode
\vec{E}	electric field
\tilde{E}	electric field perturbation
f	distribution function
FWHM	full-width half-maximum
I_p	plasma current
ICE	ion cyclotron emission
ICRF	ion cyclotron range of frequencies
J	second adiabatic invariant
$k_{ }$	parallel wave number
k_\perp	perpendicular wave number
K	kinetic energy
l	cyclotron harmonic
m	poloidal mode number
m_e	electron mass
m_f	fast-ion mass
m_i	thermal-ion mass
n	toroidal mode number
n_b	beam density
n_d	deuterium density
n_e	electron density
\bar{n}_e	line-average electron density
n_f	fast-ion density
n_i	thermal-ion density
n_{min}	minority ion density
n_0	neutral density
n_p	target density
N_{coil}	number of toroidal field coils
N_f	number of fast ions

p_e	electron pressure
p_f	fast-ion pressure
p_i	thermal-ion pressure
p_ϕ	toroidal angular momentum
P_{rf}	rf power
P_b	beam power
q	safety factor
q'	radial derivative of q
q_f	fast-ion charge ($Z_f e$)
q_i	thermal-ion charge
Q	fusion energy released
\mathcal{Q}	quasilinear diffusion term
r	minor radius
r_1	$q = 1$ radius
R	major radius
R_0	major radius of magnetic axis
R_{res}	ICRF resonance layer
R_{tan}	tangency radius of beam or sightline
rf	radio frequency
s	fusion emissivity
S	volume-integrated fusion emission
\mathcal{S}	source or sink term
T_e	electron temperature
T_i	ion temperature
T_{\parallel}	parallel temperature
T_{\perp}	perpendicular temperature
TAE	toroidicity-induced Alfvén eigenmode
v_A	Alfvén velocity
v_c	critical velocity
v_e	electron thermal speed
v_f	fast-ion velocity
v_i	ion thermal speed
v_0	birth velocity
v_{\parallel}	parallel velocity
v_{\perp}	perpendicular velocity
Z_{eff}	effective ion charge
Z_f	dimensionless fast-ion charge
β_f	toroidal fast-ion beta
β_N	normalized beta $\beta_t / (I_p / aB)$
β_p	poloidal beta
β_t	toroidal beta
γ_I	ideal MHD growth rate
δ	toroidal field ripple
Δ_r	decorrelation length
Δr	radial step size
ϵ	inverse aspect ratio
θ	poloidal angle
λ_D	Debye length

$\ln \Lambda$	Coulomb logarithm
$\ln \Lambda_e$	electron Coulomb logarithm
$\ln \Lambda_i$	ion Coulomb logarithm
μ	first adiabatic invariant
ν	collision frequency
ρ_e	electron gyroradius
ρ_f	fast-ion gyroradius
ρ_i	thermal-ion gyroradius
ρ_θ	poloidal gyroradius
σ	fusion cross section
$\langle \sigma v \rangle$	fusion reactivity
τ_l	loss time
τ_{se}	slowing-down time on electrons
τ_{th}	thermalization time
ϕ	toroidal angle
Φ	third adiabatic invariant
χ	pitch angle
ω	wave frequency
ω_A	Alfven frequency
ω_{bounce}	bounce frequency
ω_{circ}	circulation frequency
ω_{LH}	lower hybrid frequency
ω_{pi}	ion plasma frequency
ω_{pre}	precession frequency
ω_{*f}	fast-ion diamagnetic frequency
ω_{*i}	ion diamagnetic frequency
Ω	cyclotron frequency

References

- [1] JET Team, Nucl. Fusion **32** (1992) 187.
- [2] ENGELMANN, F., Plasma Phys. Controlled Fusion **31** (1989) 1823.
- [3] FURTH, H. P., GOLDSTON, R. J., ZWEBEN, S. J., and SIGMAR, D. J., Nucl. Fusion **30** (1990) 1799.
- [4] JASSBY, D. L., Nucl. Fusion **17** (1977) 309.
- [5] PORCELLI, F., Plasma Phys. Controlled Fusion **33** (1991) 1601.
- [6] KOLESNICHENKO, Y. I., Nucl. Fusion **20** (1980) 727.
- [7] WHITE, R. B., *Theory of Tokamak Plasmas*, North Holland, Amsterdam, 1989.
- [8] HUTCHINSON, I. H., *Principles of plasma diagnostics*, Cambridge University Press, Cambridge, 1987.
- [9] OLINSKIJ, D. V. and MAGYAR, G., Nucl. Fusion **28** (1988) 611.
- [10] STOTT, P., Reports on Progress in Physics **55** (1992) 1715, [also JET-P(92)16].
- [11] WESSON, J., *Tokamaks*, Clarendon Press, Oxford, 1987.
- [12] HUDDLESTONE, R. H. and LEONARD, S. L., *Plasma diagnostic techniques*, chapter 12, Academic Press, New York, 1965.
- [13] DAVIS, S. L., MUELLER, D., and KEANE, C. J., Rev. Sci. Instrum. **54** (1983) 315.
- [14] BOSCH, H.-S. and HALE, G. M., Nucl. Fusion **32** (1992) 611, and references therein. Note that Eq. 16 is valid only up to 100 keV (not 200 keV as incorrectly stated).
- [15] OLSSON, M., VAN BELLE, P., CONROY, S., ELEVANT, T., and SADLER, G., Plasma Phys. Controlled Fusion **35** (1993) 179.
- [16] HEIDBRINK, W. W., Nucl. Instrum. Methods Phys. Research **A248** (1986) 491.
- [17] HEIDBRINK, W. W., MILORA, S. L., SCHMIDT, G. L., SCHNEIDER, W., and RAMSEY, A., Nucl. Fusion **27** (1987) 3.
- [18] CECIL, F. E. and WILKINSON III, F. J., Phys. Rev. Lett. **53** (1984) 767.
- [19] CECIL, F. E., COLE, D. M., PHILBIN, R., JARMIE, N., and BROWN, R. E., Physical Review C **32** (1985) 690.
- [20] HEIDBRINK, W. W., CHRIEN, R. E., and STRACHAN, J. D., Nucl. Fusion **23** (1983) 917.
- [21] KNOLL, G. F., *Radiation detection and measurement*, Wiley, New York, second edition, 1989.

- [22] Proceedings of the Topical Conferences on High-Temperature Plasma Diagnostics, published biannually in special editions of the Rev. Sci. Instrum. in 1986, 1988, 1990, and 1992.
- [23] *Diagnostics for fusion reactor conditions*, Varenna, 1982.
- [24] *Basic and advanced diagnostic techniques for fusion plasmas*, Varenna, 1986, EUR10797EN.
- [25] *Diagnostics for contemporary fusion experiments*, Varenna, 1991, Società Italiana di Fisica, ISPPG, ISBN 88-7794-043-3.
- [26] ARTSIMOVICH, L. A., ANASHIN, A. M., GORBUNOV, E. P., et al., Soviet Physics JETP **34** (1972) 306.
- [27] ZAVERYAEV, B. S. and Luk'yanov, S. Y., Soviet Physics JETP **46** (1977) 937.
- [28] GRISHAM, L. R. and STRACHAN, J. D., Nucl. Tech./Fusion **4** (1983) 46.
- [29] PAPPAS, D. S., FURNSTAHL, R. J., KOCHANSKI, G. P., and WYSOCKI, F. J., Nucl. Fusion **23** (1983) 1285.
- [30] ABE, M., NAGAMI, M., HIRAYAMA, T., et al., Nucl. Fusion **27** (1987) 963.
- [31] HÜBNER, K., BÄTZNER, R., BOMBA, B., et al., in *Proc. of the 15th European Conference on Controlled Fusion and Plasma Heating, Dubrovnik, 1988*, volume III, pp. 1191–1194, Petit-Lancy, 1988, EPS.
- [32] HÜBNER, K., LUTZ, S., KUCINSKI, J., et al., in *Proc. of the 16th European Conference on Controlled Fusion and Plasma Physics, Venice, 1989*, volume IV, pp. 1457–1460, Petit-Lancy, 1989, EPS.
- [33] GONDHALEKAR, A., GRANETZ, R., GWINN, D., et al., in *Plasma Physics and Controlled Nuclear Fusion Research 1978*, volume 1, Vienna, 1979, IAEA.
- [34] GWINN, D. and GRANETZ, R., Observation of neutron and x-ray sawteeth in Alcator, Technical Report RR-78-8, MIT Plasma Fusion Center, 1978.
- [35] Equipe TFR, in *Plasma Physics and Controlled Nuclear Fusion Research 1980*, volume 2, p. 547, Vienna, 1981, IAEA.
- [36] LOVBERG, J. A., HEIDBRINK, W. W., STRACHAN, J. D., and ZAVERYAEV, V. S., Phys. Fluids B **1** (1989) 874.
- [37] BATISTONI, P., RAPISARDA, M., and ANDERSON, D., Nucl. Fusion **30** (1990) 625.
- [38] STRACHAN, J. D., HENDEL, H. W., LOVBERG, J., and NIESCHMIDT, E. B., in *Basic and advanced fusion plasma diagnostic techniques*, volume III, p. 687, Varenna, 1986.
- [39] Equipe TFR, Nucl. Fusion **18** (1978) 1271.
- [40] JARVIS, O. N., ADAMS, J. M., BALET, B., et al., Nucl. Fusion **30** (1990) 307.

- [41] LOUGHLIN, M. J., ADAMS, J. M., CONROY, S., et al., in *Proc. of the 18th European Conference on Controlled Fusion and Plasma Physics, Berlin, 1991*, volume IV, pp. 281–284, Petit-Lancy, 1991, EPS.
- [42] STRACHAN, J. D., BHATTACHARJEE, A., JASSBY, D. L., and TOWNER, H. H., *Physics Letters* **66 A** (1978) 295.
- [43] HEIDBRINK, W. W. and STRACHAN, J. D., *Rev. Sci. Instrum.* **56** (1985) 501.
- [44] HEIDBRINK, W. W., LOVBERG, J., STRACHAN, J. D., and BELL, R. E., *Nucl. Fusion* **27** (1987) 129.
- [45] LOVBERG, J. and STRACHAN, J. D., *Nucl. Fusion* **30** (1990) 2533.
- [46] ADAMS, J. M., CHEETHAM, A., CONROY, S., et al., in *Proc. of the 16th European Conference on Controlled Fusion and Plasma Physics, Venice, 1989*, volume I, pp. 63–66, Petit-Lancy, 1989, EPS.
- [47] ESPOSITO, B., MARCUS, F. B., ADAMS, J. M., et al., in *Proc. of the 18th European Conference on Controlled Fusion and Plasma Physics, Berlin, 1991*, volume IV, pp. 277–280, Petit-Lancy, 1991, EPS.
- [48] MARCUS, F. B., ADAMS, J. M., BARTLETT, D. V., et al., *Plasma Phys. Controlled Fusion* **34** (1992) 1371.
- [49] ESPOSITO, B., MARCUS, F. B., ADAMS, J. M., et al., Ohmic ion temperature and thermal diffusivity profiles from the jet neutron emission profile monitor, Technical Report JET-P(92)102, JET, 1992.
- [50] SASAO, M., ADAMS, J. M., CONROY, S., et al., Determination of the ion thermal diffusivity from neutron emission profiles in decay, Technical Report JET-P(92)75, JET, 1992.
- [51] VAN BELLE, P. and SADLER, G., in *Basic and advanced fusion plasma diagnostic techniques*, volume III, p. 767, Varenna, 1986, EUR 10697 EN.
- [52] BRUSATI, M., DAVIS, S. L., HOSEA, J. C., STRACHAN, J. D., and SUCKEWER, S., *Nucl. Fusion* **18** (1978) 1205.
- [53] STRACHAN, J. D., COLESTOCK, P., EUBANK, H., et al., *Nature* **279** (1979) 626.
- [54] FISHER, W. A., CHEN, S. H., GWINN, D., and PARKER, R. R., *Phys. Rev. A* **28** (1983) 3121.
- [55] JARVIS, O. N., GORINI, G., HONE, M., et al., *Rev. Sci. Instrum.* **57** (1986) 1717.
- [56] NISHITANI, T. and STRACHAN, J. D., Neutron spectroscopy on TFTR, Technical Report PPPL-2512, PPPL, Princeton, NJ, 1988.
- [57] HÜBNER, K., BÄTZNER, R., HINSCH, H., et al., in *Proc. of the 16th European Conference on Controlled Fusion and Plasma Physics, Venice, 1989*, volume IV, pp. 1453–1456, Petit-Lancy, 1989, EPS.

- [58] ELEVANT, T., V. BELLE, P., GROSSHÖG, G., et al., *Rev. Sci. Instrum.* **63** (1992) 4586.
- [59] MARTIN, G., JARVIS, O. N., KÄLLNE, J., et al., *Physica Scripta T* **16** (1987) 171, The reported downshift in the spectrum was later retracted.
- [60] KÄLLNE, J., GORINI, G., JARVIS, O. N., et al., *Physica Scripta T* **16** (1987) 160.
- [61] BOSCH, H., *Diagnostik geladener Fusionsreaktionsprodukte in ASDEX*, PhD thesis, Technische Universität München, 1986.
- [62] BOSCH, H., *Rev. Sci. Instrum.* **61** (1990) 1699.
- [63] ZAVERYAEV, V. S., MAIASYUKOV, V. D., POPOVICHEV, S. V., et al., *Sov. J. Plasma Phys.* **16** (1990) 754.
- [64] MORGAN, G. L. and ENGLAND, A. C., *Nucl. Instrum. Methods* **129** (1975) 1.
- [65] ADAMS, J. M., BALET, B., BOYD, D. A., et al., *Nucl. Fusion* **31** (1991) 891.
- [66] CHRIEN, R. E. and STRACHAN, J. D., *Phys. Fluids* **26** (1983) 1953.
- [67] HEIDBRINK, W. W., *Nucl. Fusion* **24** (1984) 636.
- [68] CHRIEN, R. E., KAITA, R., and STRACHAN, J. D., *Nucl. Fusion* **23** (1983) 1399.
- [69] HEIDBRINK, W. W., STRACHAN, J. D., BELL, R. E., et al., *Plasma Phys. Controlled Fusion* **28** (1986) 871.
- [70] HEIDBRINK, W. W., *Rev. Sci. Instrum.* **56** (1985) 1098.
- [71] SADLER, G. J., CONROY, S. W., JARVIS, O. N., et al., *Fusion Tech.* **18** (1990) 556.
- [72] ZWEBEN, S. J., HAMMETT, G., BOIVIN, R., PHILLIPS, C., and WILSON, R., *Nucl. Fusion* **32** (1992) 1823.
- [73] THEUS, R. B., MCGARRY, W. I., and BEACH, L. A., *Nuclear Physics A* **80** (1966) 273.
- [74] POSPIECH, G., GENZ, H., MARLINGHAUS, E. H., RICHTER, A., and SCHRIEDER, G., *Nuclear Physics A* **239** (1975) 125.
- [75] KRAUSS, A., BECKER, H. W., TRAUTVETTER, H. P., ROLFS, C., and BRAND, K., *Nuclear Physics A* **465** (1987) 150.
- [76] BROWN, R. E. and JARMIE, N., *Physical Review C* **41** (1990) 1391.
- [77] HÜBNER, K., BÄTZNER, R., HINSCH, H., et al., in *Proc. of the 12th European Conference on Controlled Fusion and Plasma Physics, Budapest, 1985*, volume 1, pp. 231–234, Petit-Lancy, 1985, EPS.

- [78] CORE, W. G. F., VAN BELLE, P., and SADLER, G., in *Proc. of the 14th European Conference on Controlled Fusion and Plasma Physics, Madrid, 1989*, volume I, pp. 49–52, Petit-Lancy, 1989, EPS.
- [79] HENDEL, H. W., JASSBY, D. L., BITTER, M. L., and TAYLOR, G., in *Proc. of the 14th European Conference on Controlled Fusion and Plasma Physics, Madrid, 1987*, volume I, pp. 53–56, Petit-Lancy, 1987, EPS.
- [80] JASSBY, D. L., BARNES, C. W., BELL, M. G., et al., *Phys. Fluids B* **3** (1991) 2308.
- [81] JANEV, R. K. and KATSONIS, K., *Nucl. Fusion* **27** (1987) 1493.
- [82] SHAH, M. B., ELLIOTT, D. S., and GILBODY, H. B., *J. Phys. B.: AT. Mol. Phys.* **20** (1987) 2481.
- [83] BARNETT, C. F., Technical Report ORNL-6086, Vol-1, Controlled Fusion Atomic Data Center, ORNL, 1990.
- [84] RUDD, M. E., KIM, Y. K., MADISON, D. H., and GALLAGHER, J. W., *Rev. Mod. Phys.* **57** (1985) 965.
- [85] OLSON, R. E. and HASELTON, H. H., *Phys. Rev. A* **16** (1977) 531.
- [86] RIVIERE, A. C., *Nucl. Fusion* **11** (1971) 363.
- [87] PERRAUDIN, J. C., Technical Report REP. EUR-CEA 872, 1977.
- [88] BOLEY, C. D., JANEV, R. K., and POST, D. E., *Phys. Rev. Lett.* **52** (1984) 534.
- [89] JANEV, R. K., BOLEY, C. D., and POST, D. E., *Nucl. Fusion* **29** (1989) 2125.
- [90] HAWRYLUK, R. J., in *Physics of Plasmas close to thermonuclear conditions*, volume 1, p. 19, Brussels, 1980, CEC.
- [91] GOLDSTON, R. J., MCCUNE, D. C., TOWNER, H. H., et al., *J. Comput. Phys.* **43** (1981) 61.
- [92] TFR, E., *Plasma Phys. Controlled Fusion* **29** (1986) 37.
- [93] NAKAMURA, H., HIRAYAMA, T., KOIDE, Y., et al., *Phys. Rev. Lett.* **67** (1991) 2658.
- [94] PARK, H. K., BARNES, C. W., BUDNY, R., et al., *Nucl. Fusion* **32** (1992) 1042.
- [95] SERAYDARIAN, R. P., BURRELL, K. H., and GROEBNER, R. J., *Rev. Sci. Instrum.* **59** (1988) 1530.
- [96] MANDL, W., Development of active balmer-alpha spectroscopy at JET, Technical Report JET-IR(92)05, JET, 1992.
- [97] MANDL, W., WOLF, R. C., VON HELLERMANN, M. G., and SUMMERS, H. P., Beam emission spectroscopy as a comprehensive diagnostic tool, Technical Report JET-P(92)93, JET, 1992.

- [98] VON HELLERMANN, M. G. and SUMMERS, H. P., *Rev. Sci. Instrum.* **63** (1992) 5132.
- [99] JOHNSON, L. C., *Rev. Sci. Instrum.* **63** (1992) 4517.
- [100] STRACHAN, J. D. and CHAN, A., *Nucl. Fusion* **27** (1987) 1025.
- [101] GOLANT, V. E. and FEDOROV, V. I., *RF plasma heating in toroidal fusion devices*, Plenum, New York, 1989.
- [102] IVANOV, N. V., KOVAN, I. A., and SOKOLOV, Y. A., *Sov. Phys.-JETP* **24** (1976) 316.
- [103] BUZANKIN, V. V., VERSHKOV, V. A., IVANOV, N. V., et al., in *Plasma physics and controlled nuclear fusion research 1976*, volume 3, p. 61, Vienna, 1977, IAEA.
- [104] IVANOV, N. V., KOVAN, I. A., SOKOLOV, Y. A., and CHUDNOVSKII, A. N., *Sov. J. Plasma Phys.* **4** (1978) 1211.
- [105] HOSEA, J., BERNABEI, S., COLESTOCK, P., et al., *Phys. Rev. Lett.* **43** (1979) 1802.
- [106] KAITA, R., GOLDSTON, R. J., BEIERSDORFER, P., et al., *Nucl. Fusion* **23** (1983) 1089.
- [107] ROQUEMORE, A. L., GAMMEL, G., HAMMETT, G. W., KAITA, R., and MEDLEY, S., *Rev. Sci. Instrum.* **56** (1985) 1120.
- [108] ICHIMURA, M., FUJITA, J., HIROKURA, S., et al., *Nucl. Fusion* **24** (1984) 709.
- [109] MATSUMOTO, H., KIMURA, H., ODAJIMA, K., et al., *Nucl. Fusion* **24** (1984) 283.
- [110] Equipe TFR, *Plasma Phys. Controlled Fusion* **26** (1984) 165.
- [111] TFR Group and SAND, F., *Nucl. Fusion* **25** (1985) 1719.
- [112] STEINMETZ, K., FUSSMANN, G., GRUBER, O., et al., *Plasma Phys. Controlled Fusion* **28** (1986) 235.
- [113] STEINMETZ, K., NIEDERMEYER, H., NOTERDAEME, J., et al., *Nucl. Fusion* **29** (1989) 277.
- [114] GIANNELLA, R., ZANZA, V., BARBATO, E., et al., *Nucl. Fusion* **28** (1988) 193.
- [115] KHUDOLEEV, A. V., AFANASYEV, V. I., CORTI, S., et al., Technical Report JET-P(92)31, JET, 1992.
- [116] SHEPARD, T. D., FIORE, C. L., MCDERMOTT, F. S., PARKER, R. R., and PORKOLAB, M., *Phys. Fluids* **B3** (1991) 1657.
- [117] BASIUK, V., ROUBIN, J., BÉCOULET, A., et al., in *Proceedings of the 1992 International Conference on Plasma Physics, Innsbruck*, volume 1, Petit-Lancey, 1992, EPS.

- [118] SADLER, G., VAN BELLE, P., HONE, M., et al., in *Proc. of the 13th European Conference on Controlled Fusion and Plasma Heating, Schliersee, 1986*, volume I, pp. 105–108, Petit-Lancy, 1986, EPS.
- [119] MANOS, D. M., STANGEBY, P. C., BUDNY, R. V., et al., *J. Nucl. Mater.* **129** (1984) 319.
- [120] HWANG, D., BITTER, M., BUDNY, R., et al., in *Plasma Physics and Controlled Nuclear Fusion Research 1982*, volume 2, p. 3, Vienna, 1983, IAEA.
- [121] HAWRYLUK, R. J., ARUNASALAM, V., BARNES, C. W., et al., *Plasma Phys. Controlled Fusion* **33** (1991) 1509.
- [122] THOMAS, P. R. and The JET Team, in *Plasma Physics and Controlled Nuclear Fusion Research 1988*, volume I, pp. 247–255, Vienna, 1988, IAEA.
- [123] JET Team, in *Plasma Physics and Controlled Nuclear Fusion Research 1990*, Vienna, 1991, IAEA.
- [124] COTTRELL, G. A. and START, D. F. H., *Nucl. Fusion* **31** (1991) 61.
- [125] WEYNANTS, R. R., BEUKEN, J., DEKEYZER, L., et al., in *Plasma Physics and Controlled Nuclear Fusion Research 1988*, volume 1, p. 571, Vienna, 1989, IAEA.
- [126] HAMMETT, G. W., KAITA, R., and WILSON, J. R., *Nucl. Fusion* **28** (1988) 2027.
- [127] PETROV, M. P., AFANASYEV, V. I., CORTI, S., et al., in *Proc. of the 19th European Conference on Controlled Fusion and Plasma Physics (Innsbruck, 1992)*, 1992.
- [128] CHRIEN, R. E., COLESTOCK, P. L., EUBANK, H. P., et al., *Phys. Rev. Lett.* **46** (1981) 535.
- [129] MURPHY, T. J. and STRACHAN, J. D., *Nucl. Fusion* **25** (1985) 383.
- [130] SADLER, G., JARVIS, O. N., VAN BELLE, P., HAWKES, N., and SYME, B., in *Proc. of the 14th European Conference on Controlled Fusion and Plasma Physics, Madrid, 1987*, volume III, pp. 1232–1235, Petit-Lancy, 1987, EPS.
- [131] START, D. F. H., BHATNAGAR, V. P., BOYD, D. A., et al., in *Proc. 12th Intern. Conf. on Plasma Physics and Controlled Nuclear Fusion Research, Nice 1988*, volume I, pp. 593–603, Vienna, 1988, IAEA.
- [132] START, D. F. H., BHATNAGAR, V. P., BOYD, D. A., et al., Confinement of MeV ions in JET created by Ion Cyclotron Resonance Heating, Technical Report JET-P(89)84, JET, Culham, GB, 1989.
- [133] BOYD, D. A., CAMPBELL, D. J., CORDEY, J. G., et al., *Nucl. Fusion* **29** (1989) 593.

- [134] ERIKSSON, L.-G., HELLSTEN, T., BOYD, D. A., et al., *Nucl. Fusion* **29** (1989) 87.
- [135] The JET Team, in *Plasma Physics and controlled Nuclear Fusion Research 1990*, Vienna, 1991, IAEA.
- [136] JACQUINOT, J., SADLER, G., and the JET-Team, *Fusion Tech.* **21** (1992) 2254.
- [137] CARRUTHERS, E. V., ZHU, J., STANGEBY, P. C., et al., *Journal of Nuclear Materials* **176 & 177** (1990) 1027.
- [138] KIMURA, H., MATSUMOTO, H., ODAJIMA, K., et al., in *Plasma Physics and Controlled Nuclear Fusion Research 1982*, volume 2, p. 113, Vienna, 1983, IAEA.
- [139] MIURA, Y., MATSUMOTO, H., KIMURA, H., et al., *Nucl. Fusion* **24** (1984) 211.
- [140] ADAM, J., CHANCE, M., EUBANK, H., et al., in *Plasma Physics and Controlled Nuclear Fusion Research 1974*, volume 1, p. 65, Vienna, 1975, IAEA.
- [141] ANDO, R., SATO, K., WATARI, T., et al., *Nucl. Fusion* **28** (1988) 577.
- [142] HWANG, D. Q., HOSEA, J., THOMPSON, H., et al., *Phys. Rev. Lett.* **51** (1983) 1865.
- [143] FUJII, T., KIMURA, H., SAIGUSA, M., et al., *Nucl. Fusion* **31** (1991) 137.
- [144] FUJII, T., KIMURA, H., SAIGUSA, M., et al., in *Plasma Physics and Controlled Nuclear Fusion Research ?*, volume ?, pp. 605–610, Vienna, ?, IAEA.
- [145] HAMMETT, G. W., COLESTOCK, P. L., GAMMEL, G., et al., in *Radiofrequency Plasma Heating (Sixth topical conference, Callaway Gardens, GA, 1985)*, pp. 67–70, New York, 1985, AIP.
- [146] KÖPPENDÖRFER, W., ANDELFINGER, C., BALLICO, M., et al., in *Plasma Physics and Controlled Nuclear Fusion Research 1992*, p. in press, Vienna, 1993, IAEA.
- [147] IMAI, T., KIMURA, H., KUSAMA, Y., et al., in *Plasma Physics and Controlled Nuclear Fusion Research 1990*, volume 1, p. 645, Vienna, 1991, IAEA.
- [148] KUMURA, H., FUJII, T., TOBITA, K., et al., *Nucl. Fusion* **31** (1991) 83.
- [149] RYTER, F., BROCKEN, H., IZVOZCHIKOV, A., et al., in *Proceedings of the 13th European Conference on controlled fusion and plasma heating (Schliersee, 1986)*, volume 1, p. 101, Petit-Lancey, 1986, EPS.
- [150] JET team, in *Plasma Physics and Controlled Nuclear Fusion Research 1986*, volume 1, p. 449, Vienna, 1987, IAEA.
- [151] COTTRELL, G. A., BHATNAGAR, V. P., CORDEY, J. G., et al., in *Application of radiofrequency power to plasmas (Proc. 7th topical conference Kissimmee, FL, 1987)*, p. 290, New York, 1987, American Institute of Physics.

- [152] HAMMETT, G. W., DORLAND, W., KAITA, R., et al., in *Radio-frequency power in plasmas (Eighth topical conference, Irvine, CA, 1989)*, pp. 258–261, New York, 1989, AIP.
- [153] NOTERDAEME, J. et al., in *Proc. of the 13th European conference on controlled fusion and plasma heating, Schliersee, 1986*, volume 2, p. 137, Petit-Lancey, 1986, EPS.
- [154] SEKI, T., KUMAZAWA, R., TAKASE, Y., et al., *Nucl. Fusion* **31** (1991) 1369.
- [155] UEHARA, K., KIMURA, H., and JT-60 Team, in *Radio-frequency power in plasmas (Proc. 8th Top. conf. Irvine, CA, 1989)*, p. 106, New York, 1989, AIP.
- [156] BIDDLE, A. P. and SPROTT, J. C., *Plasma Phys.* **23** (1981) 679.
- [157] SADLER, G., BARABASCHI, P., BERTOLINI, E., et al., *Plasma Phys. Controlled Fusion* **34** (1992) 1971.
- [158] TAKASE, Y., WATARI, T., KUMAZAWA, R., et al., *Nucl. Fusion* **30** (1990) 1585.
- [159] EVANS, J. D., MORALES, G. J., and TAYLOR, R. J., *Phys. Rev. Lett.* **69** (1992) 1528.
- [160] ONO, M., BEIERSDORFER, P., BELL, R., et al., in *Plasma Physics and Controlled Nuclear Fusion Research 1986*, volume 1, p. 477, Vienna, 1986, IAEA.
- [161] PORKOLAB, M., BONOLI, P., CHEN, K., et al., in *Plasma Physics and Controlled Nuclear Fusion Research 1986*, volume 1, p. 509, Vienna, 1987, IAEA.
- [162] ONO, M., BEIERSDORFER, P., BELL, R., et al., *Phys. Rev. Lett.* **60** (1988) 294.
- [163] PINSKER, R. I., MAYBERRY, M. J., PORKOLAB, M., and PRATER, R., in *Radio-frequency power in plasmas (Eighth topical conference, Irvine, CA, 1989)*, p. 314, New York, 1989, AIP.
- [164] OGAWA, Y., KAWAHATA, K., ANDO, R., et al., *Nucl. Fusion* **27** (1987) 1379.
- [165] ONO, M., WATARI, T., ANDO, R., et al., *Phys. Rev. Lett.* **54** (1985) 2339.
- [166] SEKI, T., KUMAZAWA, R., WATARI, T., et al., *Nucl. Fusion* **32** (1992) 2189.
- [167] PINSKER, R. I., PETTY, C. C., PORKOLAB, M., and HEIDBRINK, W. W., *Nucl. Fusion* **33** (1993) in press.
- [168] SCHUSS, J. J., FAIRFAX, S., KUSSE, B., et al., *Phys. Rev. Lett.* **43** (1979) 274.
- [169] SCHUSS, J. J., PORKOLAB, M., TAKASE, Y., et al., *Nucl. Fusion* **21** (1981) 427.
- [170] BRIAND, P., DUPAS, L., GOLOVATO, S. N., et al., in *Plasma physics and controlled nuclear fusion research 1978*, volume 1, p. 65, Vienna, 1979, IAEA.

- [171] VAN HOUTTE, D., AGARICI, G., BLANC, P., et al., in *Heating in Toroidal Plasmas (Proc. 4th Int. Symp. Rome, 1984)*, volume 1, p. 554, Varenna, 1984, International School of Plasma Physics.
- [172] FUJII, T., FUJISAWA, N., FUNAHASHI, A., et al., in *Plasma Physics and controlled nuclear fusion research 1978*, volume 1, p. 85, Vienna, 1985, IAEA.
- [173] SUZUKI, N., IMAI, T., FUJISAWA, N., et al., in *Plasma physics and controlled nuclear fusion research 1980*, volume 2, p. 525, Vienna, 1981, IAEA.
- [174] UEHARA, K. and NAGASHIMA, T., in *Heating in Toroidal Plasmas (Proc. 4th Int. Symp. Rome, 1984)*, volume 1, p. 485, Varenna, 1984, International School of Plasma Physics.
- [175] GORMEZANO, C., BLANC, P., EL SHEAR, M., et al., in *Heating in Toroidal Plasmas (Proc. 4th Int. Symp. Rome, 1984)*, volume 1, p. 439, Varenna, 1984, International School of Plasma Physics.
- [176] OHKUBO, K., TAKAMURA, S., and JIPP T-II Group, in *Heating in Toroidal Plasmas (Proc. 4th Int. Symp. Rome, 1984)*, volume 1, p. 543, Varenna, 1984, International School of Plasma Physics.
- [177] ECKHARTT, D., MUNICH, M., IZVOZTCHIKOV, A., et al., in *Heating in Toroidal Plasmas (Proc. 4th Int. Symp. Rome, 1984)*, volume 1, p. 501, Varenna, 1984, International School of Plasma Physics.
- [178] LEUTERER, F., SOLDNER, F., ECKHARTT, D., et al., *Plasma Phys. Controlled Fusion* **27** (1985) 1399.
- [179] BOSCH, H.-S., SCHUMACHER, U., and ASDEX-team, in *Proc. of the 13th European Conference on Controlled Fusion and Plasma Heating, Schliersee, 1986*, volume II, pp. 124–127, Petit-Lancy, 1986, EPS.
- [180] FAHRBACH, H., HERRMANN, W., SOLDNER, F., et al., in *17th EPS Conference on Controlled Fusion and Plasma Heating (Amsterdam, 1990)*, volume 14B, Part III, pp. 1171–1174, European Physical Society, 1990.
- [181] FAHRBACH, H. et al., in *Proc. 18th conference on controlled fusion and plasma heating, Berlin, 1991*, p. 1171, Petit-Lancey, 1991, EPS.
- [182] TAKASE, Y., PORKOLAB, M., SCHUSS, J. J., et al., *Phys. Fluids* **28** (1985) 983.
- [183] BUDNIKOV, V. N., *Nucl. Fusion* **31** (1991) 611.
- [184] ALLADIO, F., BARBATO, E., BARDOTTI, G., et al., *Nucl. Fusion* **24** (1984) 725.
- [185] CHRIEN, R. E., *Measurements of Fusion Reactions from a Tokamak Plasma*, PhD thesis, Princeton University, 1981.
- [186] KRITZ, A. H., MAHAJAN, S. M., BERGER, R. L., et al., *Nucl. Fusion* **18** (1978) 835.

- [187] USHIGUSA, K., IMAI, T., IKEDA, Y., et al., Nucl. Fusion **29** (1989) 265.
- [188] IMAI, T., USHIGUSA, K., IKEDA, Y., et al., Nucl. Fusion **30** (1990) 161.
- [189] NEMOTO, M., USHIGUSA, K., IMAI, T., et al., Phys. Rev. Lett. **67** (1991) 70.
- [190] OHKUBO, K., HAMADA, Y., OGAWA, Y., et al., Phys. Rev. Lett. **56** (1986) 2040.
- [191] PINSKER, R. I., COLESTOCK, P. L., and BERNABEI, S., in *Applications of radio-frequency power to plasmas (7th topical conference, Kissimmee, FL, 1987)*, p. 175, New York, 1987, AIP.
- [192] HELANDER, P., LISAK, M., and RYUTOV, D. D., Plasma Phys. Controlled Fusion **35** (1993) 363, and references therein.
- [193] KRALL, N. A. and TRIVELPIECE, A. W., *Principles of plasma physics*, pp. 599–605, McGraw-Hill, New York, 1973.
- [194] STIX, T. H., Nucl. Fusion **15** (1985) 737.
- [195] BOOK, D. L., *NRL Plasma Formulary*, Naval Research Laboratory, Washington, D.C., 1990.
- [196] SIVUKHIN, D. V., *Reviews of Plasma Physics*, volume 4, pp. 93–241, Consultants Bureau, New York, 1966.
- [197] SPITZER JR., L., *Physics of fully ionized gases*, Interscience, New York, 1962.
- [198] STIX, T. H., Plasma Phys. **14** (1972) 367, Stix's expression for E_{crit} uses the same value of $\ln \Lambda$ for both ions and electrons. For hot tokamaks, the distance of closest approach differs for ions and electrons because ions reach the classical distance of closest approach while electrons reach the quantum-mechanical one. For DIII-D, $(\ln \Lambda_i / \ln \Lambda_e)^{2/3} \simeq 1.2$.
- [199] CORDEY, J. G., HUGILL, J., PAUL, J. W. M., et al., Nucl. Fusion **14** (1974) 441.
- [200] CORDEY, J. G., GORBUNOV, E. P., HUGILL, J., et al., Nucl. Fusion **15** (1975) 441.
- [201] GOLDSTON, R. J., Nucl. Fusion **15** (1975) 651.
- [202] TFR, E., in *Plasma Physics and Controlled Nuclear Fusion Research 1986*, volume I, pp. 179–185, Vienna, 1987, IAEA.
- [203] STRACHAN, J. D., COLESTOCK, P. L., DAVIS, S. L., et al., Nucl. Fusion **21** (1981) 67.
- [204] CARNEVALI, A., SCOTT, S. D., NEILSON, H., et al., Nucl. Fusion **28** (1988) 951.
- [205] HENDEL, H. W., ENGLAND, A. C., JASSBY, D. L., MIRIN, A. A., and NIESCHMIDT, E. B., Journal of Fusion Energy **5** (1986) 231.

- [206] HEIDBRINK, W. W., KIM, J., and GROEBNER, R. J., *Nucl. Fusion* **28** (1988) 1897.
- [207] HEIDBRINK, W. W., *Phys. Fluids B* **2** (1990) 4.
- [208] HEIDBRINK, W. W., BARNES, C. W., HAMMETT, G. W., et al., *Phys. Fluids B* **3** (1991) 3167.
- [209] STRACHAN, J. D., *Nucl. Fusion* **29** (1988) 163.
- [210] CONROY, S., JARVIS, O. N., SADLER, G., and HUXTABLE, G. B., *Nucl. Fusion* **28** (1988) 2127.
- [211] DUONG, H. H. and HEIDBRINK, W. W., *Nucl. Fusion* **33** (1993) 211.
- [212] NISHITANI, T., TOBITA, K., TANI, K., et al., in *Plasma Physics and Controlled Nuclear Fusion Research 1992*, p. in press, Vienna, 1993, IAEA.
- [213] CONROY, S., JARVIS, O. N., PILLON, M., and SADLER, G., in *Proc. of the 17th EPS Conference on Controlled Fusion and Plasma Heating, Amsterdam, 1990*, volume 14B, part I, pp. 98–101, Petit-Lancy, 1990, EPS.
- [214] TFR Group, *Nucl. Fusion* **23** (1983) 425.
- [215] BOL, K., CECCHI, J. L., DAUGHNEY, C. C., et al., in *Plasma Physics and Controlled Nuclear Fusion Research 1974*, volume 1, pp. 77–82, Vienna, 1975, IAEA.
- [216] JASSBY, D. L., HENDEL, H. W., BARNES, C. W., et al., in *Proc. of the 14th European Conference on Controlled Fusion and Plasma Physics, Madrid, 1987*, volume III, pp. 1264–1267, Petit-Lancy, 1987, EPS.
- [217] GAMBIER, D. J., EVRARD, M. P., ADAM, J., et al., *Nucl. Fusion* **30** (1990) 23.
- [218] ERIKSSON, L. and HELLSTEN, T., *Nucl. Fusion* **29** (1989) 875.
- [219] BERRY, L. A., BUSH, C. E., DUNLAP, J. L., et al., in *Plasma Physics and Controlled Nuclear Fusion Research 1974*, volume 1, Vienna, 1975, IAEA.
- [220] PAUL, J. W. M., AXON, K. B., BURT, J., et al., in *Plasma Physics and Controlled Nuclear Fusion Research 1976*, volume 2, p. 269, Vienna, 1977, IAEA.
- [221] VLASENKOV, V. S., KULYGIN, V. M., LEONOV, V. M., et al., in *Plasma Physics and Controlled Nuclear Fusion Research 1976*, volume 1, p. 85, Vienna, 1977, IAEA.
- [222] LEONOV, V. M., MERZHKIN, V. G., MUKHOVATOV, V. S., SANNIKOV, V. V., and TILININ, G. N., in *Plasma physics and controlled nuclear fusion research 1980*, volume 1, p. 393, Vienna, 1981, IAEA.
- [223] LEONOV, V. M., *Sov. J. Plasma Phys.* **15** (1989) 267.
- [224] LEONOV, V. M., MUKHOVATOV, V. S., POLEVOI, A. R., and TILININ, G. N., *Sov. J. Plasma Phys.* **15** (1989) 1521.

- [225] SWAIN, D. W., MURAKAMI, M., BATES, S. C., et al., Nucl. Fusion **21** (1981) 1409.
- [226] KAITA, R., GOLDSTON, R. J., BEIERSDORFER, P., et al., Nucl. Fusion **25** (1985) 939.
- [227] CORTI, S., BRACCO, G., CORE, W., GIANNELLI, A., and ZANZA, V., in *14th European Conference on Controlled Fusion and Plasma Heating (Madrid)*, volume 11D, part III, p. 1030, Petit-Lancey, 1987, EPS.
- [228] KUSAMA, Y., NEMOTO, M., TOBITA, K., et al., in *15th European Conference on Controlled Fusion and Plasma Heating (Dubrovnik, 1988)*, volume 12B, part 1, p. 167, EPS, 1988.
- [229] TOBITA, K., KUSAMA, Y., NAKAMURA, H., et al., Nucl. Fusion **31** (1991) 956.
- [230] FIORE, C. L., MEDLEY, S. S., HAMMETT, G. W., et al., Nucl. Fusion **28** (1988) 1315.
- [231] RADEZTSKY, R. H., SCOTT, S. D., KAITA, R., et al., in *Controlled Fusion and Plasma Heating (Proc. 15th European Conference Dubrovnik, 1988)*, volume 12B, Part I, pp. 79–82, European Physical Society, 1988.
- [232] VON HELLERMANN, M. G., CORE, W. G. F., FRIELING, J., et al., Plasma Phys. Controlled Fusion **35** (1992) 799.
- [233] KAITA, R., GOLDSTON, R. J., and BUSSAC, J., Nucl. Fusion **21** (1981) 953.
- [234] BATISTONI, P. and BARNES, C. W., Plasma Phys. Controlled Fusion **33** (1991) 1735.
- [235] BOL, K., CECCHI, J. L., DAUGHNEY, C. C., et al., Phys. Rev. Lett. **32** (1974) 661.
- [236] BYDDER, E. L., LILEY, B. S., and MORTON, A. H., Plasma Phys. **21** (1979) 669.
- [237] ALABYAD, A. M., IVANOV, N. V., and KHUDOLEEV, A. V., Sov. J. Plasma Phys. **10** (1984) 117.
- [238] WONG, K. L., BITTER, M., HAMMETT, G. W., et al., Phys. Rev. Lett. **55** (1985) 2587.
- [239] KAITA, R., HEIDBRINK, W. W., HAMMETT, G. W., et al., Nucl. Fusion **26** (1986) 863.
- [240] KENNEL, C. F. and ENGELMANN, F., Phys. Fluids **9** (1966) 2377.
- [241] HAMMETT, G. W., *Fast ion studies of ion cyclotron heating in the PLT tokamak*, PhD thesis, Princeton University, 1986.
- [242] HELANDER, P. and LISAK, M., Phys. Fluids B **4** (1992) 1927.

- [243] BÉCOULET, A., GAMBIER, D. J., and SAMAIN, A., *Phys. Fluids B* **3** (1991) 137.
- [244] RIGHI, E., COTTRELL, G. A., ERIKSSON, L., START, D. F. H., and TIBONE, F., Modelling of fast ion orbit effects on electron heating profiles in minority ICRF scenarios, Technical Report JET-P(92)31, JET, 1992.
- [245] BHATNAGAR, V. P., JACQUINOT, J., START, D. F. H., and TUBBING, B. J. D., High-concentration minority ion-cyclotron resonance heating in the JET tokamak, Technical Report JET-P(92)49, JET, 1992.
- [246] JACQUINOT, J., BURES, M., and the JET Team, *Phys. Fluids B* **4** (1992) 2111.
- [247] YAMAGIWA, M., TAKIZUKA, T., KIMURA, H., and AZUMI, M., *Plasma Phys. Controlled Fusion* **30** (1988) 943.
- [248] KARNEY, C. F. F., *Phys. Fluids* **21** (1978) 1584.
- [249] KARNEY, C. F. F., *Phys. Fluids* **22** (1979) 2188.
- [250] PORKOLAB, M., BERNABELI, S., HOOKE, W. M., MOTLEY, R. W., and NAGASHIMA, T., *Phys. Rev. Lett.* **38** (1977) 230.
- [251] IMAI, T., NAGASHIMA, T., YAMAMOTO, T., et al., *Phys. Rev. Lett.* **43** (1979) 586.
- [252] GOLDSTON, R. J., KAITA, R., BEIERSDORFER, P., et al., *Nucl. Fusion* **27** (1987) 921.
- [253] ROME, J. A., MCALEES, D. G., CALLEN, J. D., and FOWLER, R. H., *Nucl. Fusion* **16** (1976) 55.
- [254] ROME, J. A. and PENG, Y. M., *Nucl. Fusion* **19** (1979) 1193.
- [255] HSU, C. T. and SIGMAR, D. J., *Phys. Fluids B* **4** (1992) 1492.
- [256] HIVELEY, L. M. and MILEY, G. H., *Nucl. Fusion* **17** (1977) 1031.
- [257] HEIDBRINK, W. W., *Tokamak Diagnostics using Fusion Products*, PhD thesis, Princeton University, 1984.
- [258] ZWEBEN, S. J., *Nucl. Fusion* **29** (1989) 825.
- [259] ZWEBEN, S. J., BOIVIN, R. L., DUVALL, R. E., et al., *Phys. Fluids B* **2** (1990) 1411.
- [260] ZWEBEN, S. J., BOIVIN, R. L., DIESSO, M., et al., *Nucl. Fusion* **30** (1990) 1551.
- [261] ZWEBEN, S. J., BOIVIN, R. L., CHANG, C., HAMMETT, G. W., and MYNICK, H. E., *Nucl. Fusion* **31** (1991) 2219.
- [262] MEYERHOFER, D. D., GOLDSTON, R. J., KAITA, R., et al., *Nucl. Fusion* **25** (1985) 321.

- [263] PETRIE, T. W., ARMENTROUT, C. J., BURRELL, K. H., et al., *J. Nucl. Mater.* **128 & 129** (1984) 487.
- [264] MANOS, D. M., BUDNY, R., SATAKE, T., and COHEN, S. A., *J. Nucl. Mater.* **111-112** (1982) 130.
- [265] GOLDSTON, R. J. and TOWNER, H. H., *J. Plasma Phys.* **26** (1981) 283.
- [266] BOIVIN, R. L., *Measurements of charged fusion product diffusion in TFTR*, PhD thesis, Princeton University, 1991.
- [267] GOLDSTON, R. J., WHITE, R. B., and BOOZER, A. H., *Phys. Rev. Lett.* **47** (1981) 647.
- [268] ERIKSSON, L. and HELANDER, P., Finite orbit-width effects on stochastic ripple diffusion, Technical Report JET-P(92)98, JET, 1992.
- [269] WHITE, R. B. and MYNICK, H. E., *Phys. Fluids B* **1** (1989) 980.
- [270] BEREZOVSKIJ, E. L., IZVOZCHIKOV, A. B., PETROV, M. P., et al., *Nucl. Fusion* **23** (1983) 1575.
- [271] ARTSIMOVICH, L. A., AFROSIMOV, V. V., GLADKOVSKIJ, I. P., et al., in *Plasma Physics and Controlled Nuclear Fusion Research 1965*, volume 2, p. 595, Vienna, 1966, IAEA.
- [272] PETROV, M. P., in *Plasma Physics and Controlled Nuclear Fusion Research 1974*, volume 1, p. 43, Vienna, 1975, IAEA.
- [273] AFROSIMOV, V. V., BEREZOVSKIJ, E. L., IZVOZCHIKOV, A. B., and PETROV, M. P., *Sov. J. Plasma Phys.* **6** (1980) 133.
- [274] BERLIZOV, A. B., BOBROVSKIJ, G. A., BAGDASAROV, A. A., et al., in *Plasma Physics and Controlled Nuclear Fusion Research 1976*, volume 1, p. 3, Vienna, 1977, IAEA.
- [275] BAGDASAROV, A. A., BERLIZOV, A. B., VASIN, N. L., et al., in *Plasma Physics and Controlled Nuclear Fusion Research 1978*, volume 1, p. 35, Vienna, 1979, IAEA.
- [276] ZAVERYAEV, V. S., IZVOZCHIKOV, A. B., LYSENKO, S. E., and PETROV, M. P., *Sov. J. Plasma Phys.* **4** (1978) 1205.
- [277] GREENWALD, M. J., SCHUSS, J. J., and COPE, D., *Nucl. Fusion* **20** (1980) 783.
- [278] OUROUA, A., *Ion thermal diffusion in the Texas Experimental Tokamak*, PhD thesis, University of Texas, 1989.
- [279] SCHUSS, J. J., ANTONSEN JR., T. M., and PORKOLAB, M., *Nucl. Fusion* **23** (1983) 201.
- [280] TUSZEWSKI, M. and ROUBIN, J. P., *Nucl. Fusion* **28** (1988) 499.

- [281] TOBITA, K., TANK, K., NEYATANI, Y., et al., *Phys. Rev. Lett.* **69** (1992) 3060.
- [282] NINOMIYA, H. and JT-60 Team, *Phys. Fluids B* **4** (1992) 2070.
- [283] JT-60 team, in *Plasma Physics and Controlled Nuclear Fusion Research 1992*, p. in press, Vienna, 1993, IAEA.
- [284] STODIEK, W., BOL, K., EUBANK, H., VON GOELER, S., and GROVE, D. J., in *Plasma Physics and Controlled Nuclear Fusion Research 1970*, volume 1, pp. 465–478, Vienna, 1971, IAEA.
- [285] STODIEK, W., GOLDSTON, R., SAUTHOFF, N., et al., in *Plasma Physics and Controlled Nuclear Fusion Research 1980*, volume 1, p. 9, Vienna, 1981, IAEA.
- [286] SCOTT, S. D., *An experimental investigation of magnetic field ripple effects on tokamak plasmas*, PhD thesis, Massachusetts Institute of Technology, 1982.
- [287] SCOTT, S. D., LYON, J. F., MUNRO, J. K., et al., *Nucl. Fusion* **25** (1985) 359.
- [288] The JET TEAM, in *Plasma Physics and Controlled Nuclear Fusion Research 1992*, p. in press, Vienna, 1993, IAEA.
- [289] BOIVIN, R. L., ZWEBEN, S. J., CHANG, C. S., et al., in *Proc. of the 18th European Conference on Controlled Fusion and Plasma Physics, Berlin, 1991*, volume 15C, part I, pp. 49–52, Petit-Lancy, 1991, EPS.
- [290] ZWEBEN, S. J., BOIVIN, R., DARROW, D. S., et al., in *Plasma Physics and Controlled Nuclear Fusion Research 1992*, p. in press, Vienna, 1993, IAEA.
- [291] BOIVIN, R. L., ZWEBEN, S. J., and WHITE, R. B., *Nucl. Fusion* **33** (1993) in press.
- [292] BOIVIN, R. L. and ZWEBEN, S. J., *Phys. Fluids B* **5** (1993) in press.
- [293] CHEN, L., VACLAVIK, J., and HAMMETT, G. W., *Nucl. Fusion* **28** (1988) 389.
- [294] CATTO, P. J. and TESSAROTTO, M., *Phys. Fluids* **31** (1988) 2292.
- [295] HIVELY, L. M. and MILEY, G. H., *Nucl. Fusion* **20** (1980) 969.
- [296] MYNICK, H. E. and KROMMES, J. A., *Phys. Rev. Lett.* **43** (1979) 1506.
- [297] EFTHIMION, P. C., BITTER, M., FREDRICKSON, E. D., et al., in *Plasma Physics and Controlled Nuclear Fusion Research 1988*, volume I, pp. 307–321, Vienna, 1989, IAEA.
- [298] JARVIS, O. N., *Rev. Sci. Instrum.* **63** (1992) 4511.
- [299] The JET TEAM, in *Plasma Physics and Controlled Nuclear Fusion Research 1992*, p. in press, Vienna, 1993, IAEA.
- [300] The JET Team, *Plasma Phys. Controlled Fusion* **34** (1992) 1749.

- [301] THOMPSON, E., STORK, D., DE ESCH, H. P. L., and the JET team, The use of neutral beam heating to produce high performance fusion plasmas, including the injection of tritium beams into JET, Technical Report JET-P(92)68, JET, 1992.
- [302] STRACHAN, J. D., GREK, B., HEIDBRINK, W., et al., Nucl. Fusion **25** (1985) 863.
- [303] BARNES, C. W., BELL, M. G., HENDEL, H. W., et al., Rev. Sci. Instrum. **61** (1990) 3151.
- [304] ZARNSTORFF, M. C., ARUNASALAM, V., BARNES, C. W., et al., in *Plasma Physics and Controlled Nuclear Fusion Research 1988*, volume 1, p. 183, Vienna, 1989, IAEA.
- [305] STRACHAN, J. D., BELL, M. G., BITTER, M., et al., Neutron emission from TFTR supershots, Technical Report PPPL-2858, Princeton Plasma Physics Laboratory, 1992.
- [306] WOLLE, B. and ERIKSSON, L., Time-dependent neutron rate interpretation for neutral beam heated tokamaks, Technical Report JET-P(92)30, JET, 1992.
- [307] CHALLIS, C. D., CORDEY, J. G., HAMNÉN, H., et al., Nucl. Fusion **29** (1989) 563.
- [308] CHALLIS, C., CORDEY, J. G., HAMNÉN, H., et al., in *Proceedings of the 14th European Conference on controlled fusion and plasma physics (Madrid, 1987)*, volume 11D, part III, p. 290, Petit-Lancy, 1987, EPS.
- [309] JET Team, in *Plasma Physics and Controlled Nuclear Fusion Research 1992*, p. in press, Vienna, 1993, IAEA.
- [310] CLARK, W. H. M., CORDEY, J. G., COX, M., et al., Phys. Rev. Lett. **45** (1980) 1101.
- [311] AXON, K. B., CLARK, W. H. M., CORDEY, J. G., et al., in *Plasma Physics and controlled Nuclear Fusion Research 1980*, volume 1, p. 413, Vienna, 1981, IAEA.
- [312] SIMONEN, T. C., MATSUOKA, M., BHADRA, D. K., et al., Phys. Rev. Lett. **61** (1988) 1720.
- [313] POLITZER, P. A. and PORTER, G. D., Nucl. Fusion **30** (1990) 1605.
- [314] HAWRYLUK, R. J., ARUNASALAM, V., BELL, M. G., et al., in *Plasma Physics and Controlled Nuclear Fusion Research 1986*, volume 1, p. 51, Vienna, 1987, IAEA.
- [315] ZARNSTORFF, M. C., BELL, M. G., BITTER, M., et al., Phys. Rev. Lett. **60** (1988) 1306.
- [316] COLESTOCK, P., STRACHAN, J. D., ULRICKSON, M., and CHRIEN, R. E., Phys. Rev. Lett. **43** (1979) 768.

- [317] BITTONI, E., FUBINI, A., HAEGI, M., et al., in *Proc. of the 12th European Conference on Controlled Fusion and Plasma Physics, Budapest, 1985*, volume 11D, part III, pp. 211–214, Petit-Lancy, 1985, EPS.
- [318] BATISTONI, P., MARTONE, M., PILLON, M., PODDA, S., and RAPISARDA, M., in *Proc. of the 14th European Conference on Controlled Fusion and Plasma Physics, Madrid, 1987*, volume 11D, part III, p. 1228, Petit-Lancy, 1987, EPS.
- [319] BATISTONI, P., MARTONE, M., PILLON, M., PODDA, S., and RAPISARDA, M., *Nucl. Fusion* **27** (1987) 1040.
- [320] PILLON, M. and VANNUCCI, A., *Nucl. Instrum. Methods Phys. Research* **A255** (1987) 188.
- [321] BATISTONI, P., BITTONI, E., and HAEGI, M., *Nucl. Fusion* **29** (1989) 673.
- [322] STRACHAN, J. D., ZWEBEN, S., BARNES, C. W., et al., in *Proc. 12th Intern. Conf. on Plasma Physics and Controlled Nuclear Fusion Research, Nice 1988*, volume I, pp. 257–263, Vienna, 1988, IAEA.
- [323] SCOTT, S. D., BARNES, C. W., GRISHAM, L. R., et al., in *Proc. 13th Intern. Conf. on Plasma Physics and Controlled Nuclear Fusion Research, Washington 1990*, volume I, pp. 235–259, Vienna, 1991, IAEA.
- [324] KÄLLNE, J., BATISTONI, P., GORINI, G., et al., *Nucl. Fusion* **28** (1988) 1291.
- [325] BATISTONI, P., ARGYLE, J., CONROY, S., et al., in *Proc. of the 15th European Conference on Controlled Fusion and Plasma Heating, Dubrovnik, 1988*, volume 12B, part I, pp. 135–138, Petit-Lancy, 1988, EPS.
- [326] JARVIS, O. N., ADAMS, J. M., CONROY, S. W., et al., in *Proc. of the 18th European Conference on Controlled Fusion and Plasma Physics, Berlin, 1991*, volume 15C, part I, pp. 21–24, Petit-Lancy, 1991, EPS.
- [327] MCCAULEY, JR., J. S., *Measurement and interpretation of dt neutron emission from TFTR*, PhD thesis, Princeton University, 1993.
- [328] ANDERSON, D., BATISTONI, P., and LISAK, M., *Nucl. Fusion* **31** (1991) 2147, There is a mistake in Eq. 13 that is corrected in Ref. [329].
- [329] ANDERSON, D., BATISTONI, P., and LISAK, M., *Physica Scripta* **45** (1992) 138.
- [330] YAMAGIWA, M., *Plasma Phys. Controlled Fusion* **34** (1992) 1503.
- [331] MURPHY, T. J., *Tokamak Diagnostics using Nuclear Techniques*, PhD thesis, Princeton University, 1988.
- [332] ERIKSSON, L., GIANNELLA, R., HELLSTEN, T., KALLNE, E., and SUNDSTROM, G., *Plasma Phys. Controlled Fusion* **34** (1992) 863.
- [333] LOHR, J. and ARMENTROUT, C. J., in *Basic Physical Processes of Toroidal Fusion Plasmas, Varenna, 1985*, volume I, pp. 225–233, Citta di Castello, 1985, Monotypia Franchi.

- [334] ARMENTROUT, C. J. and STRAIT, E. J., A method for estimating prompt fast ion loss from plasmas during neutral beam injection, Technical Report GA-A17891, GA Technologies, 1986.
- [335] WHITE, R. B., GOLDSTON, R. J., MCGUIRE, K., et al., Phys. Fluids **26** (1983) 2958.
- [336] SIGMAR, D. J., HSU, C. T., WHITE, R., and CHENG, C. Z., Phys. Fluids B **4** (1992) 1506.
- [337] BEIERSDORFER, P., KAITA, R., and GOLDSTON, R. J., Nucl. Fusion **24** (1984) 487.
- [338] HEIDBRINK, W. W. and BEIERSDORFER, P., Nucl. Fusion **27** 608.
- [339] MCGUIRE, K., BELL, M., BITTER, M., et al., Study of high beta pressure driven modes in PDX, Technical Report PPPL-1946, PPPL, 1982.
- [340] BUCHENAUER, D., HWANG, D. Q., MCGUIRE, K., and GOLDSTON, R. J., in *Heating in Toroidal Plasmas (Proc. 4th Int. Symp. Rome, 1984)*, volume 1, p. 111, ISPP and ENEA, 1984.
- [341] MCGUIRE, K. M., in *Proc. of the Int. Conf. on Plasma Physics (Lausanne, 1984)*, volume 1, p. 123, Brussels, 1984, CEC.
- [342] BUCHENAUER, D. A. J., *Fast ion effects on magnetic instabilities in the PDX tokamak*, PhD thesis, Princeton University, 1985.
- [343] BUCHENAUER, D., HEIDBRINK, W. W., ROQUEMORE, L., and MCGUIRE, K., Rev. Sci. Instrum. **58** (1987) 2264.
- [344] HEIDBRINK, W. W., KAITA, R., TAKAHASHI, H., et al., Phys. Fluids **30** (1987) 1839.
- [345] KAITA, R., BOL, K., COUTURE, P., et al., Plasma Phys. Controlled Fusion **28** (1986) 1319.
- [346] KAITA, R., WHITE, R. B., MORRIS, A. M., et al., Phys. Fluids **B2** (1990) 1584.
- [347] HEIDBRINK, W. W. and SAGER, G., Nucl. Fusion **30** (1990) 1015, The large losses reported in this paper are for *combined* fishbone and TAE bursts.
- [348] SMEULDERS, P., ADAMS, J., BALET, M., et al., in *Proceedings of the 17th EPS Conference Amsterdam*, volume 14B, part I, p. 323, 1990.
- [349] NAVE, M. F. F., CAMPBELL, D. J., JOFFRIN, E., et al., Nucl. Fusion **31** (1991) 697.
- [350] NAVE, M. F. F., BORBA, D., CRIPWELL, P., et al., in *Proc. of the 19th European Conference on Controlled Fusion and Plasma Physics (Innsbruck, 1992)*, volume 16C, part I, p. 136, 1992.
- [351] ROBERTS, D. W., *Stability studies of PBX-M plasmas with neutral probe beam q-profile diagnostics*, PhD thesis, Princeton University, 1991.

- [352] ROBERTS, D. W., KAITA, R., LEVINTON, F., et al., The effect of internal magnetic structure on the fishbone instability, Technical Report PPPL-2815, PPPL, 1992.
- [353] WONG, K. L., FONCK, R. J., PAUL, S. F., et al., Phys. Rev. Lett. **66** (1991) 1874.
- [354] WONG, K. L., DURST, R., FONCK, R. J., et al., Phys. Fluids B **4** (1992) 2122.
- [355] DARROW, D. S., FREDRICKSON, E. D., MYNICK, H. E., et al., in *Proc. of the 19th European Conference on plasma physics and controlled fusion, Innsbruck, 1992*, volume 16C, part I, p. 431, EPS, 1992.
- [356] HEIDBRINK, W. W., STRAIT, E. J., DOYLE, E., SAGER, G., and SNIDER, R. T., Nucl. Fusion **31** (1991) 1635.
- [357] DARROW, D. S., BOIVIN, R. L., and ZWEBEN, S. J., Rev. Sci. Instrum. **63** (1992) 4562.
- [358] ZARNSTORFF, M. C., BATEMAN, G., BATHA, S., et al., in *Plasma Physics and controlled nuclear fusion research 1992*, p. in press, Vienna, 1993, IAEA.
- [359] DUONG, H. H., HEIDBRINK, W. W., STRAIT, E. J., et al., Nucl. Fusion **33** (1993) in press.
- [360] PETRIE, T. W., ARMENTROUT, C. J., BURRELL, K. H., et al., J. Nucl. Mater. **121** (1984) 322.
- [361] JOHNSON, D., BELL, M., BITTER, M., et al., in *Plasma physics and controlled nuclear fusion research 1982*, volume 1, p. 9, Vienna, 1983, IAEA.
- [362] HEIDBRINK, W. W., BOL, K., BUCHENAUER, D., et al., Phys. Rev. Lett. **57** (1986) 835.
- [363] MARCUS, F. B., ADAMS, J. M., CHEETHAM, A. D., et al., Plasma Phys. Controlled Fusion **33** (1991) 277.
- [364] WISING, F., ANDERSON, D., and LISAK, M., Plasma Phys. Controlled Fusion **34** (1992) 853.
- [365] EUBANK, H. et al., in *Heating in toroidal plasmas (Proc. of the 3rd Varenna-Grenoble Int. Symposium)*, volume 1, p. 15, Brussels, 1982, Commission of the European communities.
- [366] MOREAU, D., SAOUTIC, B., AGARICI, G., et al., in *Plasma Physics and Controlled Nuclear Fusion Research 1992*, p. in press, Vienna, 1993, IAEA.
- [367] HOSEA, J. C., PHILLIPS, C. K., STEVENS, J. E., et al., ICRF sawtooth stabilization-application on TFTR and CIT, Technical Report PPPL-2738, Princeton Plasma Physics Laboratory, 1991.
- [368] ANDERSON, D. and BATISTONI, P., Nucl. Fusion **28** (1988) 2151.

- [369] HEIDBRINK, W. W., HAY, R., and STRACHAN, J. D., *Phys. Rev. Lett.* **53** (1984) 1905.
- [370] KAYE, S. M., JAHNS, G. L., MORRIS, A. W., et al., *Nucl. Fusion* **28** (1988) 1963.
- [371] KAYE, S. M., LEVINTON, F. M., HATCHER, R., et al., *Phys. Fluids* **B4** (1992) 651.
- [372] PFEIFFER, W., MARCUS, F. B., ARMENTROUT, C. J., et al., *Nucl. Fusion* **25** (1985) 655.
- [373] COTTRELL, G. A., BHATNAGAR, V. P., DA COSTA, O., et al., in *Proc. of the 19th European conference on controlled fusion and plasma physics, Innsbruck, 1992*, volume 16C, 1992.
- [374] COTTRELL, G. A., BHATNAGAR, V. P., DA COSTA, O., et al., Identification of ion cyclotron emission from fusion alpha particles during JET deuterium-tritium experiments, Technical Report JET-P(92)54, JET, 1992.
- [375] VON GOELER, S., STODIEK, W., and SAUTHOFF, N., *Phys. Rev. Lett.* **33** (1974) 1201.
- [376] CAMPBELL, D. J., START, D. F. H., WESSON, J. A., et al., *Phys. Rev. Lett.* **60** (1988) 2148, The strange neutron signal in Fig. 5 was later retracted.
- [377] MCGUIRE, K., GOLDSTON, R., BELL, M., et al., *Phys. Rev. Lett.* **50** (1983) 891.
- [378] CHEN, L., WHITE, R. B., and ROSENBLUTH, M. N., *Phys. Rev. Lett.* **52** (1984) 1122.
- [379] COPPI, B. and PORCELLI, F., *Phys. Rev. Lett.* **57** (1986) 2272.
- [380] WHITE, R. B., ROMANELLI, F., and BUSSAC, M. N., *Phys. Fluids B* **2** (1990) 745.
- [381] PHILLIPS, C. K., HOSEA, J., MARMAR, E., et al., *Phys. Fluids B* **4** (1992) 2142.
- [382] ONGENA, J. et al., in *Proc. 17th Eur. Conf. on Controlled fusion and plasma heating Amsterdam, 1990*, volume 14B, part III, p. 383, Petit-Lancey, 1990, EPS.
- [383] CAMPBELL, D. J. and the JET Team, in *Plasma Physics and Controlled Nuclear Fusion Research 1990*, volume 1, p. 437, Vienna, 1991, IAEA.
- [384] CORE, W. G. F. and COTTRELL, G. A., *Nucl. Fusion* **32** (1992) 1637.
- [385] YAMAMOTO, S., MAENO, M., SUZUKI, N., et al., *Nucl. Fusion* **21** (1981) 993.
- [386] MURAKAMI, M., SWAIN, D. W., BATES, S. C., et al., in *Plasma physics and controlled nuclear fusion research 1980*, volume 1, p. 377, Vienna, 1981, IAEA.

- [387] NINOMIYA, H., YOSHINO, R., AKIBA, M., et al., in *Plasma physics and controlled nuclear fusion research 1988*, volume 1, p. 111, Vienna, 1989, IAEA.
- [388] STRAIT, E. J., BERNARD, L. C., LEE, J. K., et al., in *Controlled Fusion and Plasma Physics (Proc. 11th Eur. Conf. Aachen 1983)*, volume 7D, part I, p. 62, Petit-Lancey, 1983, EPS.
- [389] OVERSKEI, D. O., ARMENTROUT, C. J., BAUR, J. F., et al., in *Heating in Toroidal Plasmas (Proc. 4th Int. Symp. Rome 1984)*, volume 1, p. 21, Rome, 1984, ENEA.
- [390] The JET Team, in *Plasma Physics and Controlled Nuclear Fusion Research 1992*, p. in press, Vienna, 1993, IAEA.
- [391] DUNLAP, J. L., CARRERAS, B. A., PARÉ, V. K., et al., *Phys. Rev. Lett.* **48** (1982) 535.
- [392] COPPI, B., MIGLIUOLO, S., and PORCELLI, F., *Phys. Fluids* **31** (1988) 1630.
- [393] BORBA, D., NAVE, M. F. F., and PORCELLI, F., The non linear behaviour of fishbones, Technical Report JET-P(92)82, JET, 1992.
- [394] HEIDBRINK, W. W., DUONG, H. H., MANSON, J., et al., *Phys. Fluids B* **5** (1993) in press.
- [395] MIKHAILOVSKIJ, A. B., *Sov. Phys.-JETP* **41** (1975) 890.
- [396] ROSENBLUTH, M. N. and RUTHERFORD, P. H., *Phys. Rev. Lett.* **34** (1975) 1428.
- [397] GLOEDBLOED, J. P., *Phys. Fluids* **18** (1975) 1258.
- [398] CHENG, C. Z. and CHANCE, M. S., *Phys. Fluids* **29** (1986) 3695.
- [399] BETTI, R. and FREIDBERG, J. P., *Phys. Fluids B* **4** (1992) 1465.
- [400] CHU, M. S., GREENE, J. M., LAO, L. L., TURNBULL, A. D., and CHANCE, M. S., *Phys. Fluids B* **4** (1992) 3713.
- [401] TURNBULL, A. D., CHU, M. S., STRAIT, E. J., et al., *Phys. Fluids B* **5** (1993) in press.
- [402] CHENG, C. Z., *Phys. Fluids B* **3** (1991) 2463.
- [403] FU, G. Y. and VAN DAM, J. W., *Phys. Fluids B* **1** (1989) 1949.
- [404] BIGLARI, H., ZONCA, F., and CHEN, L., *Phys. Fluids B* **4** (1992) 2385.
- [405] BERK, H. L., BREIZMAN, B. N., and YE, H., *Phys. Lett. A* **162** (1992) 475.
- [406] METT, R. R. and MAHAJAN, S. M., *Phys. Fluids B* **4** (1992) 2885.
- [407] ROSENBLUTH, M. N., BERK, H. L., VAN DAM, J. W., and LINDBERG, D. M., *Phys. Rev. Lett.* **68** (1992) 596.

- [408] ZONCA, F. and CHEN, L., *Phys. Rev. Lett.* **68** (1992) 592.
- [409] BIGLARI, H. and CHEN, L., *Phys. Rev. Lett.* **67** (1991) 3681.
- [410] TSAI, S.-T. and CHEN, L., *Phys. Fluids B* **5** (1993) submitted.
- [411] DURST, R. D., WONG, K. L., CHENG, C. Z., et al., *Phys. Fluids B* **4** (1992) 3707.
- [412] STRAIT, E. J., HEIDBRINK, W. W., CHU, M. S., et al., in *Plasma Physics and Controlled Nuclear Fusion Research 1992*, p. in press, Vienna, 1993, IAEA.
- [413] STRAIT, E. J., HEIDBRINK, W. W., TURNBULL, A. D., CHU, M. S., and DUONG, H. H., The stability of tae modes in diiii-d, Technical Report GA-A21037, General Atomics, 1993, submitted to *Nucl. Fusion*.
- [414] SESNIC, S., KAITA, R., KAYE, S., and OKABAYASHI, M., in *Bull. American Physical Society*, volume 36, p. 2316, New York, 1991, AIP.
- [415] WONG, K., 1992.
- [416] WILSON, J. R., BELL, M. G., BIGLARI, H., et al., in *Plasma physics and controlled nuclear fusion research 1992*, p. in press, Vienna, 1993, IAEA.
- [417] HEIDBRINK, W. W., STRAIT, E. J., CHU, M. S., and TURNBULL, M. S., Observation of beta-induced alfvén eigenmodes in the DIII-D tokamak, Technical Report GA-A21191, General Atomics, 1993, submitted to *Phys. Rev. Lett.*
- [418] FREDRICKSON, E. D. et al., in *Proceedings of the 16th European Conference on Plasma Physics*, volume 2, p. 481, Petit-Lancey, 1989, EPS.
- [419] BHADRA, D. K., CHIU, S. C., BUCHENAUER, D., and HWANG, D., *Nucl. Fusion* **26** (1986) 201.
- [420] SEKI, M., SAIGUSA, M., NEMOTO, M., et al., *Phys. Rev. Lett.* **62** (1989) 1989.
- [421] COTTRELL, G. A., LALLIA, P. P., SADLER, G., and VAN BELLE, P., in *Proc. of the 13th European Conference on Controlled Fusion and Plasma Heating, Schliersee, 1986*, volume 10C, Part II, pp. 37-40, Petit-Lancey, 1986, EPS.
- [422] COTTRELL, G. A. and DENDY, R. O., *Phys. Rev. Lett.* **60** (1988) 33.
- [423] SCHILD, P., COTTRELL, G. A., and DENDY, R. O., *Nucl. Fusion* **29** (1989) 834.
- [424] GREENE, G. J., COLESTOCK, P. L., FREDRICKSON, E. D., et al., in *Proc. 15th EPS (Dubrovnik, 1988)*, volume 12B, part 1, p. 107, Petit-Lancey, 1988, EPS.
- [425] GREENE, G. J. and TFTR group, in *Proc. 17th EPS (Amsterdam, 1990)*, volume 14B, part IV, p. 1540, Petit-Lancey, 1990, EPS.
- [426] ARUNASALAM, V., GREENE, G. J., and YOUNG, K. M., Ion cyclotron and spin flip emissions from fusion products in tokamaks, Technical Report PPPL-2875, Princeton Plasma Physics Laboratory, 1993.

- [427] YAMAMOTO, S., Experiment Group, Operation Group, et al., in *Plasma physics and controlled nuclear fusion research 1984*, volume 1, pp. 665–672, Vienna, 1985, IAEA.
- [428] DENDY, R. O., LASHMORE-DAVIES, C. N., and KAM, K. F., *Phys. Fluids B* **4** (1992) 3996.
- [429] HIVELEY, L. M. and SIGMAR, D. J., *Fusion Tech.* **17** (1990) 316.
- [430] BATISTONI, P., MARTONE, M., PILLON, M., et al., in *Proc. of the 14th European Conference on Controlled Fusion and Plasma Physics, Madrid, 1987*, volume III, pp. 1228–1231, Petit-Lancy, 1987, EPS.
- [431] FELT, J., BARNES, C. W., CHRIEN, R. E., et al., *Rev. Sci. Instrum.* **61** (1990) 3262.
- [432] HELLSTEN, T., *Plasma Phys. Controlled Fusion* **31** (1989) 1391.

Tables

Table I. PRINCIPAL SOURCES OF FAST IONS.

Source	Physical Mechanism	Spatial Distribution	Angular Distribution	Initial Energy
Fusion reactions	Nuclear reactions	Centrally peaked	Nearly isotropic*	Eq. 6
Neutral beam injection	Charge exchange, electron impact ionization	Depends upon energy and line density	Anisotropic (depends upon injection angle)	Injection energies
ICRF minority heating	Cyclotron damping	Peaked near resonance layer	Anisotropic (perpendicular)	-

*Not accurately measured.

Table II. FAST-ION TAIL DURING LOWER HYBRID HEATING.

Tokamak	ω/ω_{pi}	E_{min}/T_{i0}	n_{e0}/\bar{n}_e	Location
FT-2 [183]	0.6-1.0	8	1.8	center→edge
JFT-2 [173]	0.6-1.1	8	1.7	center
Alcator A [169]	1.1-1.4		1.5	center
PLT [69,68]	1.4-1.7	12	1.5	center
Alcator C [182]	1.1-1.8		1.3	edge
ASDEX [177]	0.8-1.1	9	1.2	edge

Table III. EFFECT OF MHD BURSTS UPON BEAM IONS.

Instability	Tokamak	B_θ/B_θ	$\Delta S/S$	Comment
Fishbone	PDX	10^{-2}	0.25	linear scaling
	PBX	10^{-2}	0.22	perpendicular injection
	TFTR	5×10^{-4}	< 0.03	tangential injection
	JET	3×10^{-4}	< 0.05	oblique injection
			3×10^{-3}	0.09
Circulation	DIII-D	2.5×10^{-2}	0.11	linear scaling
	PDX	10^{-4}	0.04	
	PBX	10^{-3}	0.08	
Sawtooth	DIII-D	5×10^{-3}	0.30	linear scaling
	PDX	$\lesssim 10^{-3}$	0.20	threshold behavior

Table IV. FISHBONE AND SAWBONE OBSERVATIONS.

Tokamak	Heating	Frequency	β_p	β_N
PDX [342]	\perp 45 keV D $^\circ$	$\omega_{*i} \lesssim \omega \lesssim \omega_{pre}$	0.6-1.8	1.2-3.4
JT-60 [387]	\perp H $^\circ$ + ICRF	$\sim \omega_{pre}$	~ 0.5	
DIII-D [347]	75 keV D $^\circ$ /H $^\circ$	$\sim \omega_{*i}, \omega_{pre}$	1.5-3.1	2.4-5.5
PBX-M [351]	45 keV D $^\circ$	$\sim \omega_{pre}, \omega_{*i}$	2.3	3.5
JET [349]	80 keV D $^\circ$, ICRF	$\omega_{*i} \lesssim \omega \lesssim \omega_{pre}$	0.1-0.8	0.3-2.4
TFTR [346]	Tang. 95 keV D $^\circ$	$\sim \omega_{pre}, \omega_{*i}$	1.2	1.2
PBX [362]	\parallel 44 keV D $^\circ$	$< \omega_{*i}$	0.6	1.2-2.3
ISX-B [386]	\parallel 32 keV H $^\circ$	10-20 kHz	~ 2	
JFT-2 [385]	Tang. 40 keV H $^\circ$		~ 2.4	3.3-3.5

Table V. CIRCULATION INSTABILITIES.

	PDX	PBX	TFTR	DIII-D
Beam Energy (keV)	45	45	100	75
Beam Species	D $^\circ$	D $^\circ$	D $^\circ$	D $^\circ$
R_{tan}/R	0.16	0.87	~ 0.9	0.66
Frequency (kHz)	50-150	140-220	60-120	70-220
Toroidal mode number	$\sim 2 - 6$?	2-3	1-10
Radial eigenfunction	$q \simeq 1$?	$r/a \simeq 0.5, 0.9$	$q \simeq 1.5$
v_{\parallel}/v_A	$\lesssim 0.2$	0.6	0.7-1.1	0.4-1.1
β_f/β_t	~ 0.3	0.3	0.5	0.3-0.7
β_N	1.2-4.0	1.1-2.3	1.8	1.6-6.4

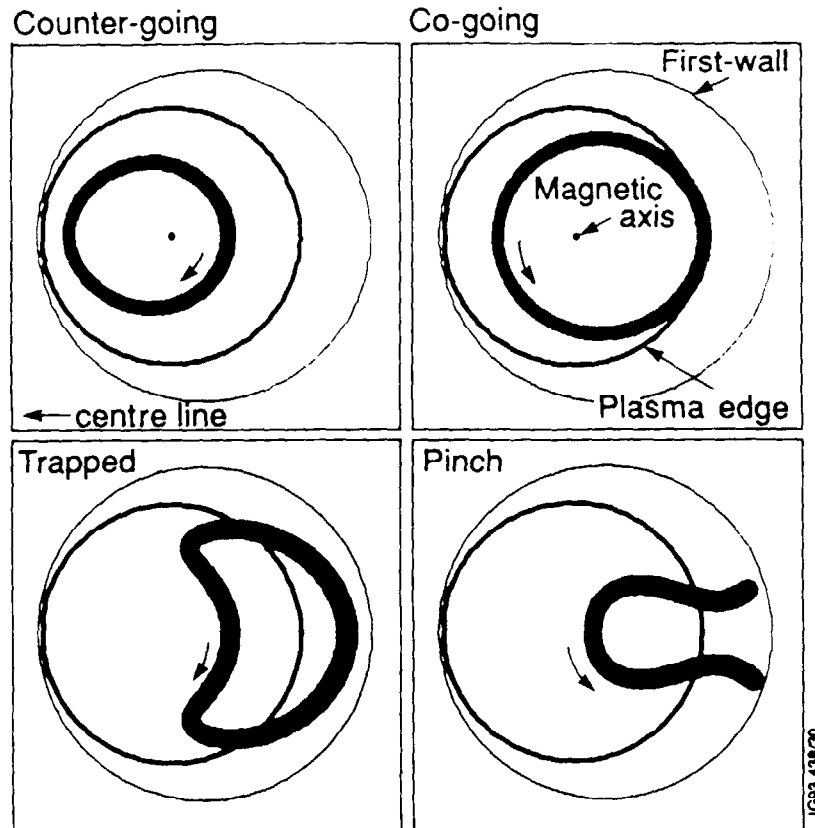


Fig. 1. Poloidal projection of different types of fast-ion orbits, calculated for 3 MeV protons in TFTR [289]. The overlapping loops are caused by the relatively large gyromotion in the toroidal magnetic field. A line drawn through the center of the orbit is the trajectory of the *guiding center*. The trajectory of the guiding center, which is known as the *drift orbit*, depends upon the orientation of the velocity vector relative to the magnetic field. This orientation is often denoted by the *pitch angle* χ , where $\chi = \cos v_{\parallel}/v$. Drift orbits are grouped into two categories: trapped or passing. Passing or *circulating* particles travel in one toroidal direction only; examples of these orbits are illustrated in the upper two panels. Passing orbits are further distinguished by the sign of their toroidal velocity; *co-going* orbits circulate in the direction of the plasma current and *counter-going* orbits circulate anti-parallel to the current. In contrast, the direction of toroidal motion of trapped particles reverses at the *turning points*, where the velocity parallel to the magnetic field vanishes. Trapped particle orbits are also called *banana* orbits. A final class of orbits, the *pinch* orbits, do not encircle the magnetic axis. Fast-ion drift orbits are discussed in more detail in Sec. 4.1.

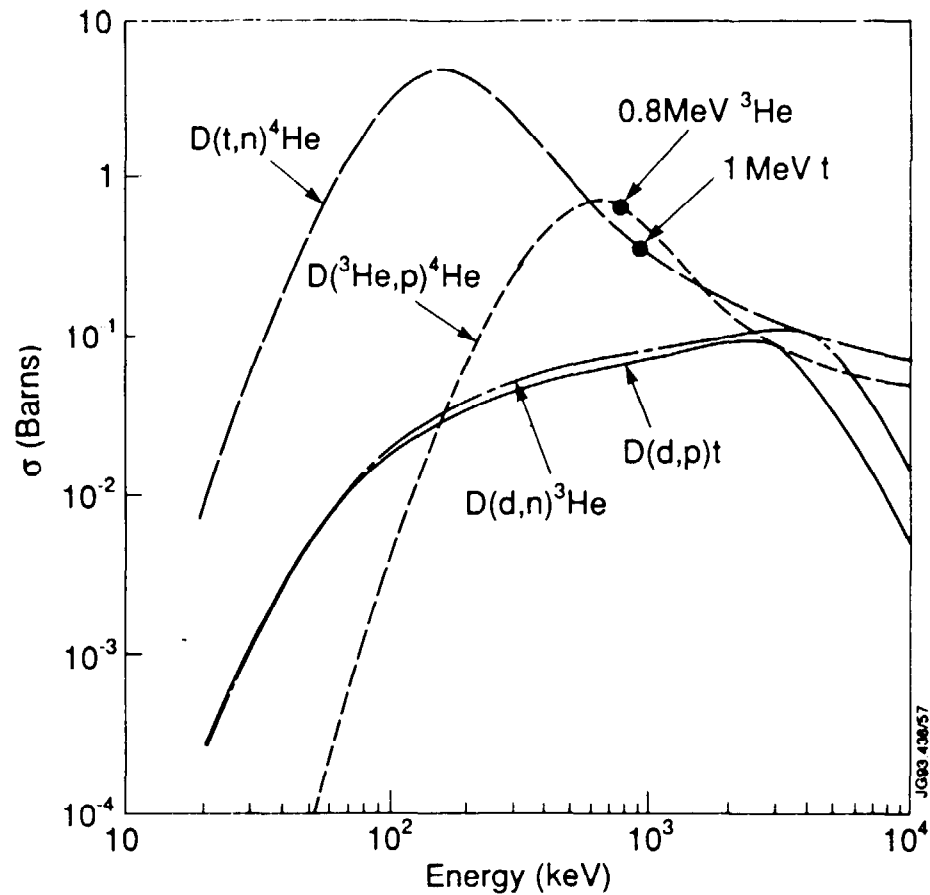


Fig. 2. Fusion reaction cross sections. In triton burnup measurements, 1 MeV tritons produced in $d(d,p)t$ fusion reactions slow down through the peak of the $d(t,n)\alpha$ cross section and produce 14 MeV neutrons. In ^3He burnup measurements, 0.8 MeV ^3He ions produced in $d(d,n)^3\text{He}$ fusion reactions slow down through the peak of the $d(^3\text{He},p)\alpha$ cross section and produce 15 MeV protons.

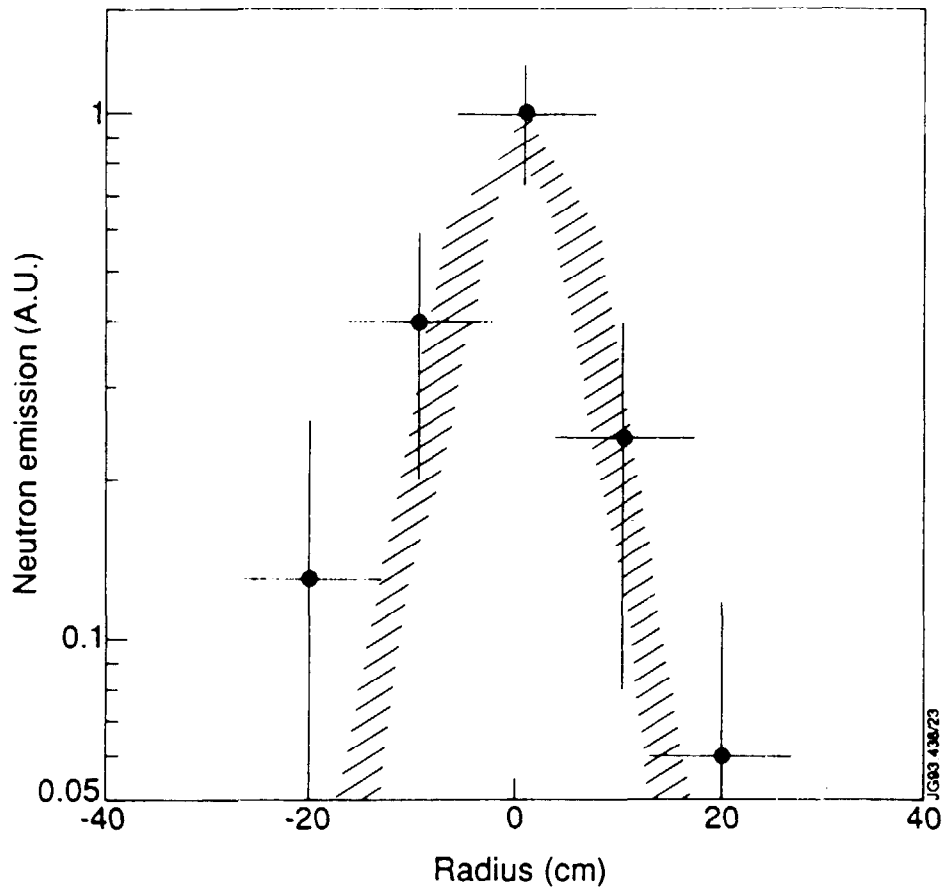


Fig. 3. Neutron emission profile measured during $H^0 \rightarrow D^+$ neutral beam injection into PLT [42]. The profile was obtained by measuring recoil proton tracks in nuclear emulsion foils; the vertical error bars are due to counting statistics and the horizontal error bars are determined by the angular bins employed in counting the tracks. The shaded region is the expected emission profile based on a neoclassical calculation of the ion temperature profile. The profile is very narrow compared to the plasma minor radius of 40 cm.

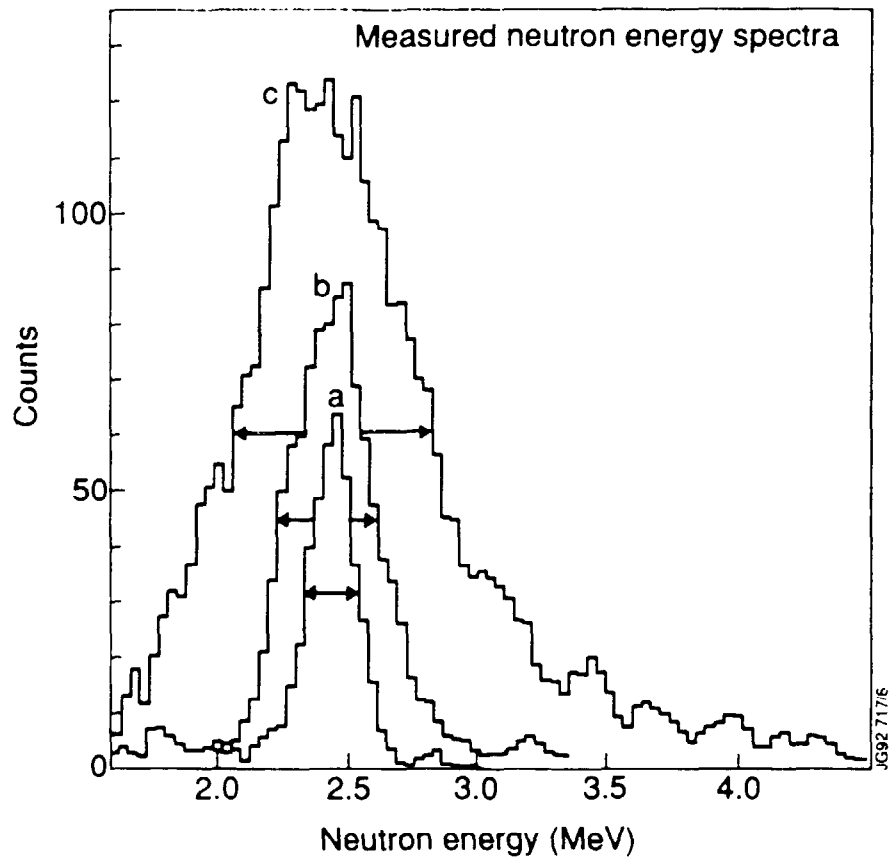


Fig. 4. D-D neutron spectra measured with a vertically viewing time-of-flight spectrometer at JET [15]. (a) Thermonuclear spectrum from a plasma heated by rf. (b) Spectrum dominated by beam-plasma and beam-beam reactions during injection of ~ 80 keV deuterium beams. (c) Broad spectrum from a plasma with deuterium beam ions that are further accelerated by rf heating [including some neutrons from ${}^9\text{B}(d,n){}^{10}\text{B}$ reactions].

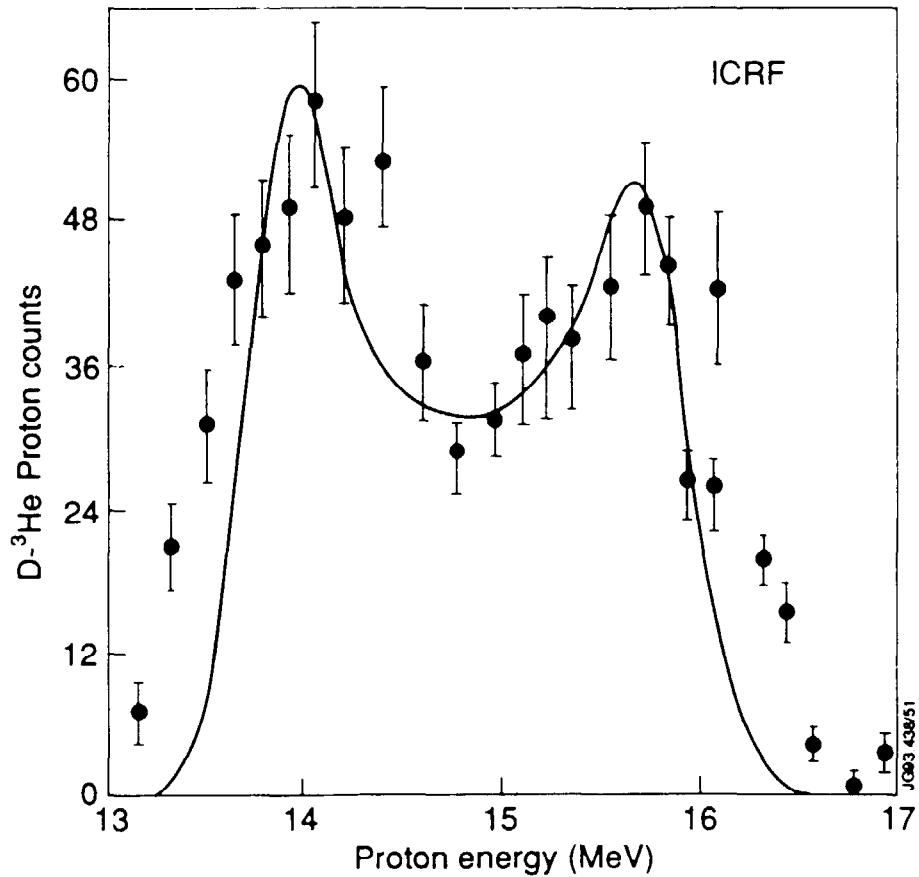


Fig. 5. Spectrum of $d(^3\text{He},p)\alpha$ protons produced by anisotropic ^3He ions in PLT during ^3He minority ICRF heating [67]. The proton spectrometer had a resolution of 0.5 MeV (full line-width) and was collimated to measure perpendicular protons (collimator FWHM=6.5°); the error bars indicate the counting statistics. The curve is the spectrum produced by an anisotropic perpendicular ^3He beam with maximum energy of 400 keV and temperature of 30 keV. The data illustrate that the birth energy of fusion products can deviate significantly from the nominal birth energy (14.64 MeV in this case) and that the birth distribution function can be anisotropic.

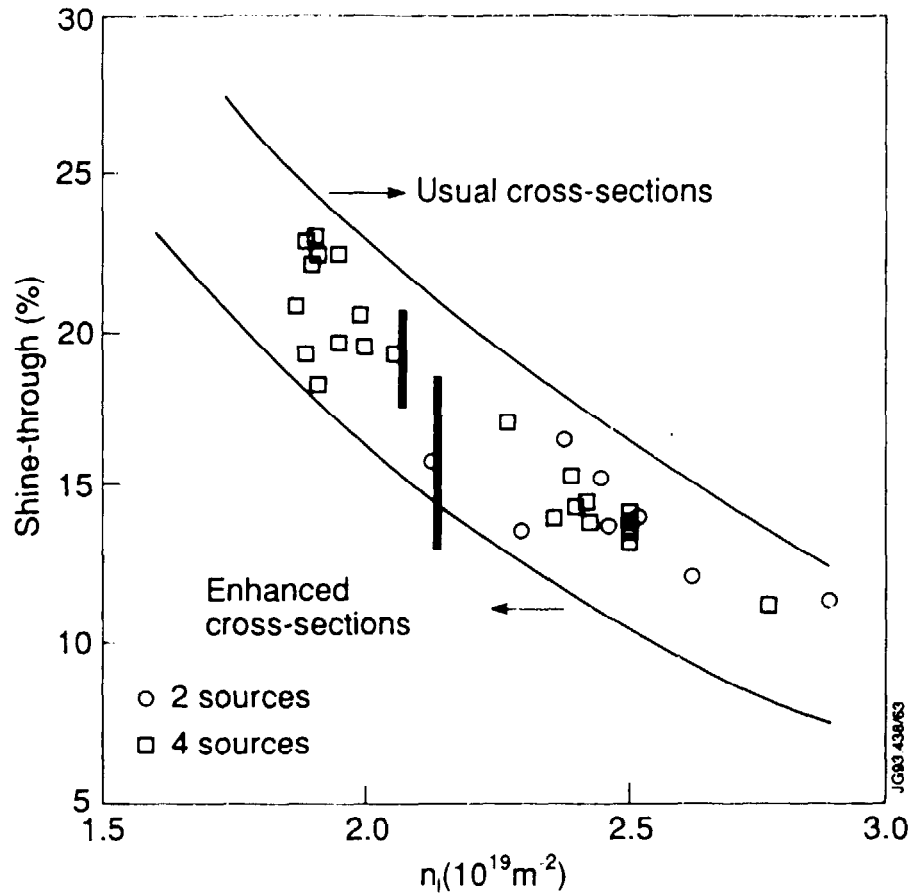


Fig. 6. Measured shine-through of 34 keV hydrogen beams versus line density $n_e l$ for two sources (\circ) and for four sources (\square) in TFR [92]. Plasma heating of the calorimeter accounts for most of the experimental error; uncertainties in the density and temperature profiles affect the theoretical calculations but were not quantified.

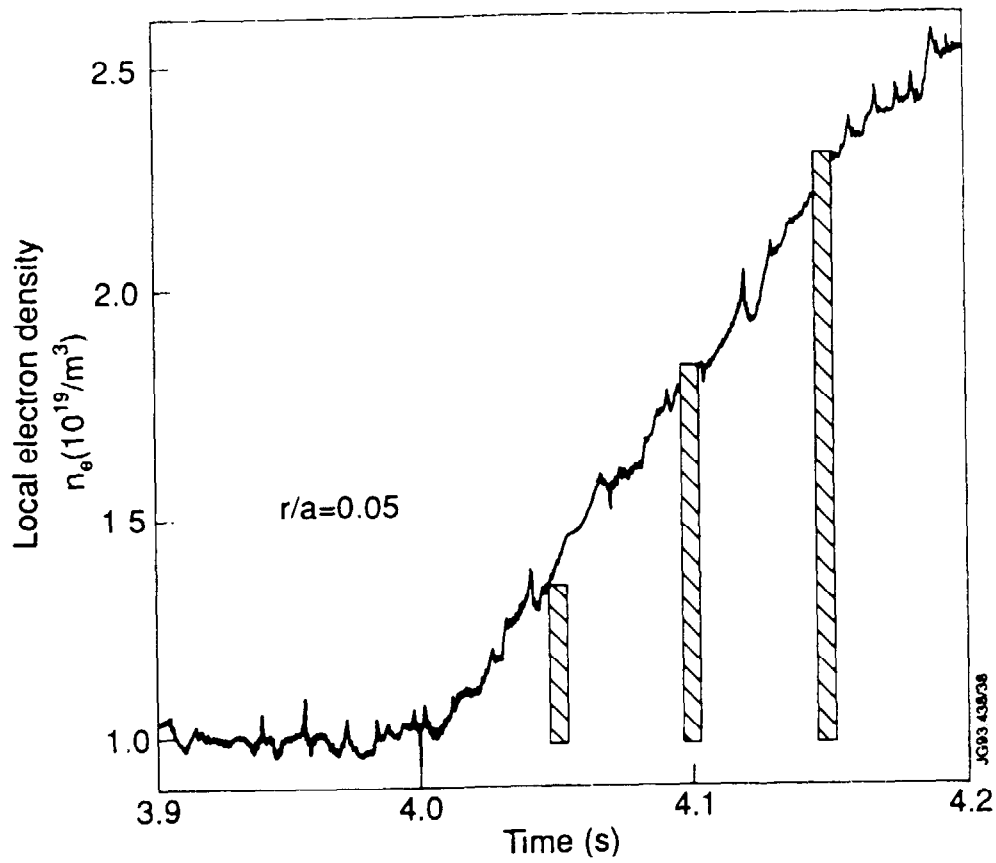


Fig. 7. Time evolution of the central electron density during ~ 100 keV deuterium beam injection into TFTR [94]. The histograms represent the increase in electron density calculated by TRANSP (estimated error $\pm 10\%$). The electron density is obtained by inversion of 10-channel interferometer data and has an estimated absolute error of $\pm 1.5 \times 10^{18} \text{ m}^{-3}$.

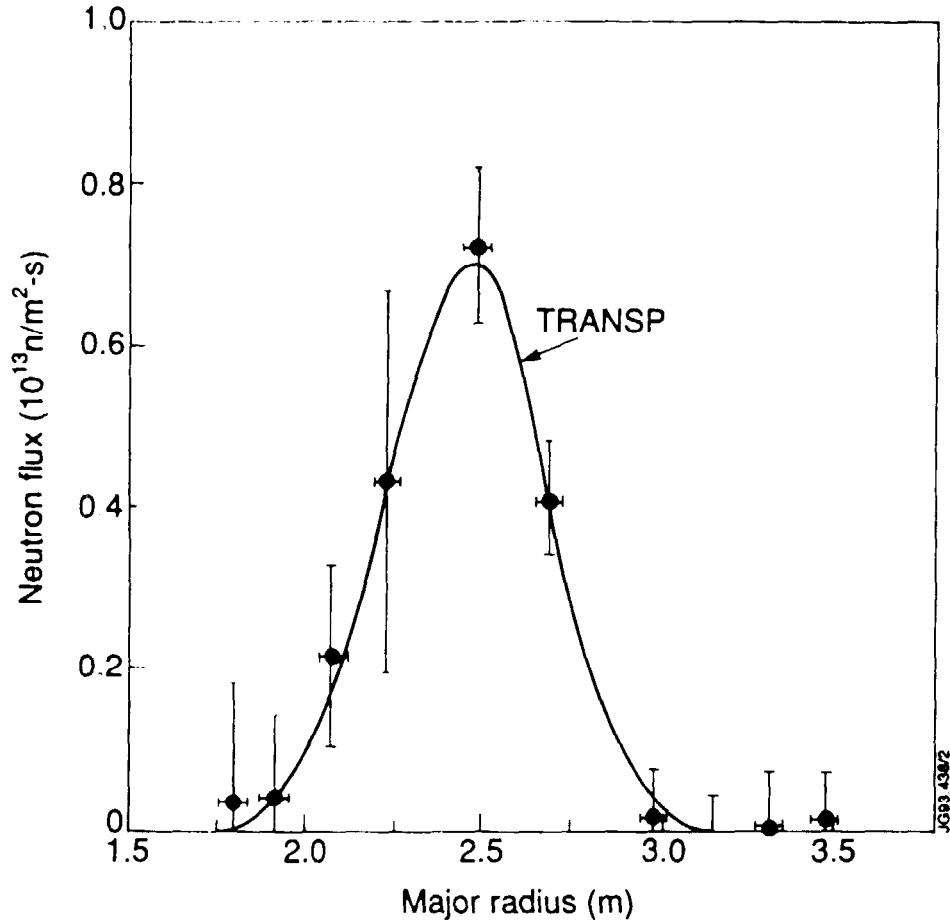


Fig. 8. Profile of the line-integrated 2.5 MeV neutron flux (measured by a multichannel neutron collimator) immediately following a 20 ms, ~ 90 keV deuterium beam pulse in TFTR [208]. The errors in the data are associated with counting statistics and neutron scattering corrections; the theoretical error associated with uncertainties in n_e and T_e was not quantified. The TRANSP calculation neglected multistep ionization processes.

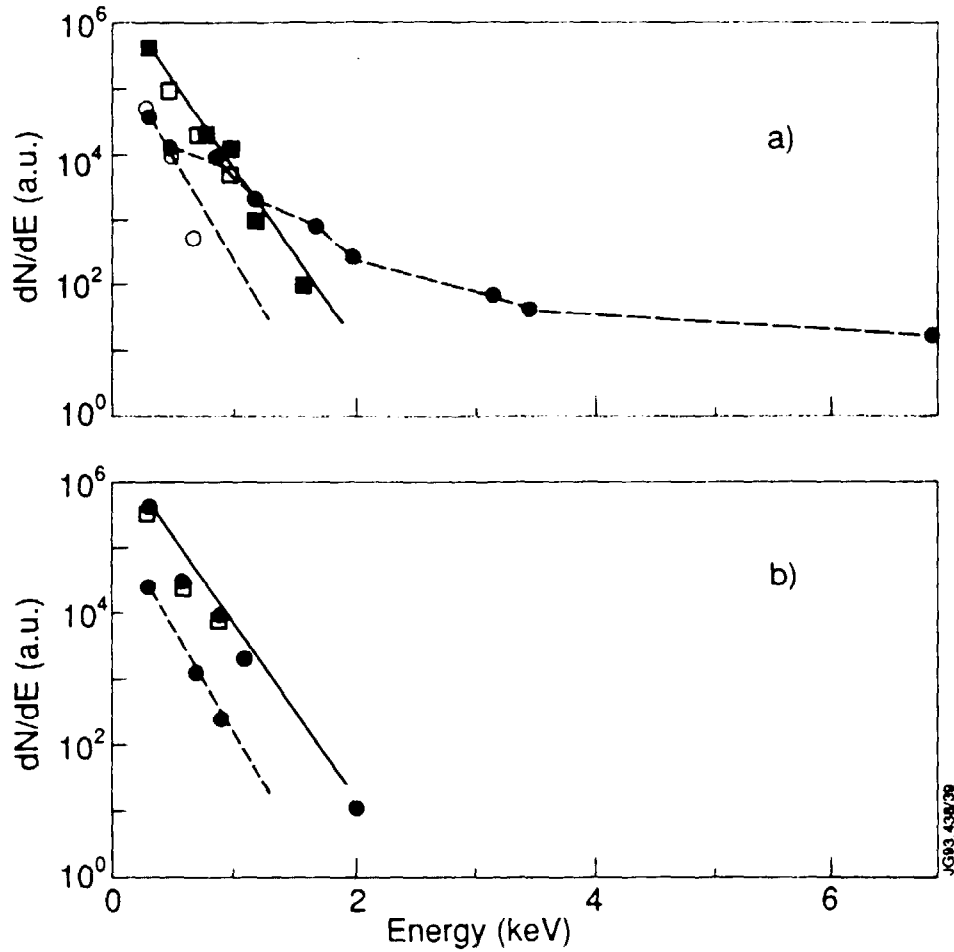


Fig. 9. Energy spectra of the charge-exchange atoms of hydrogen (circles) and deuterium (squares) in T-4 with (solid) and without (open) rf heating [102]. (a) Resonance layer near magnetic axis (1.5 T). (b) Resonance layer outside the plasma (2.1 T).

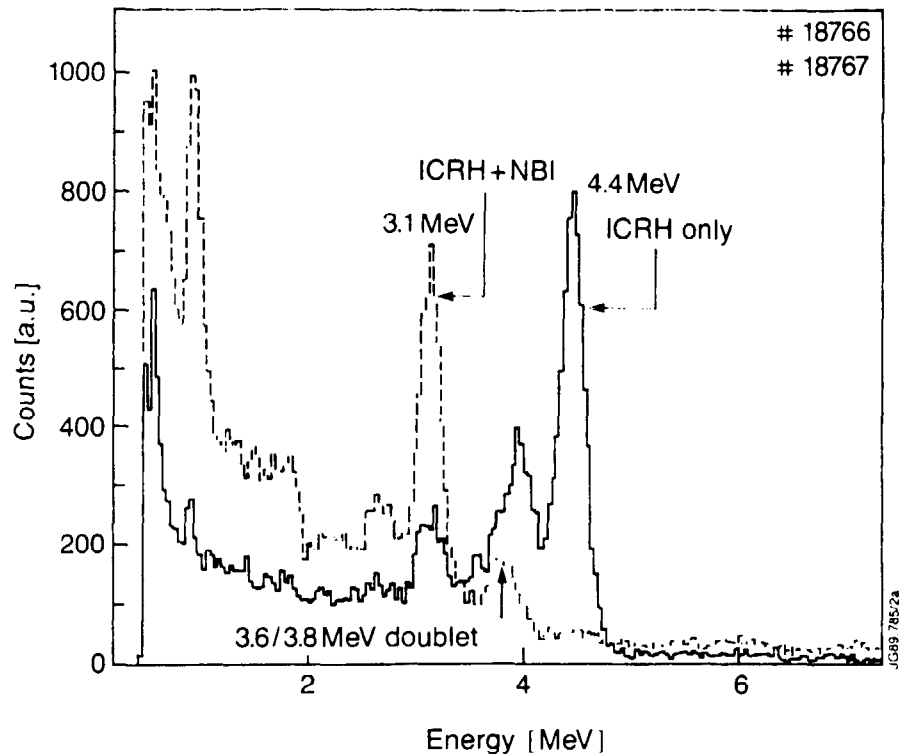


Fig. 10. Gamma-ray spectra measured during fast-wave H-minority heating in JET [65]. The solid spectrum is for ICRF heating alone, while the dashed spectrum is during combined ICRF and deuterium neutral-beam injection heating. The 4.4 MeV line is produced by reactions between ^{12}C impurities and protons with energies greater than ~ 5 MeV. The 3.1 MeV line and the 3.6/3.8 MeV doublet are produced by reactions between ^{12}C impurities and deuterons with energies greater than ~ 0.8 MeV and ~ 1.7 MeV, respectively. The spectrometer has a vertical view of the center of the plasma.

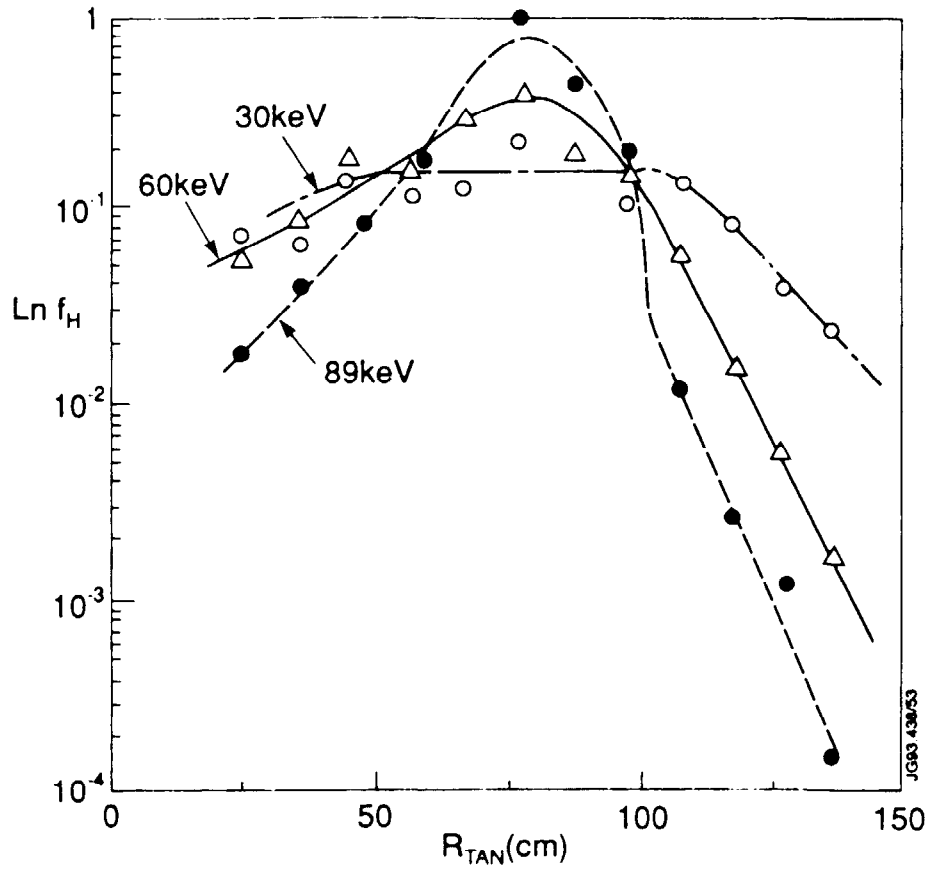


Fig. 11. Proton flux as a function of spectrometer line of sight for three different energies during H-minority ICRF heating in PLT [106]. The abscissa shows the tangency radius R_{tan} of the horizontally viewing analyzer. The peak in the signal is due to protons on banana orbits that have their turning point in the resonance layer. The outer leg of these orbits lies in the high neutral-density region.

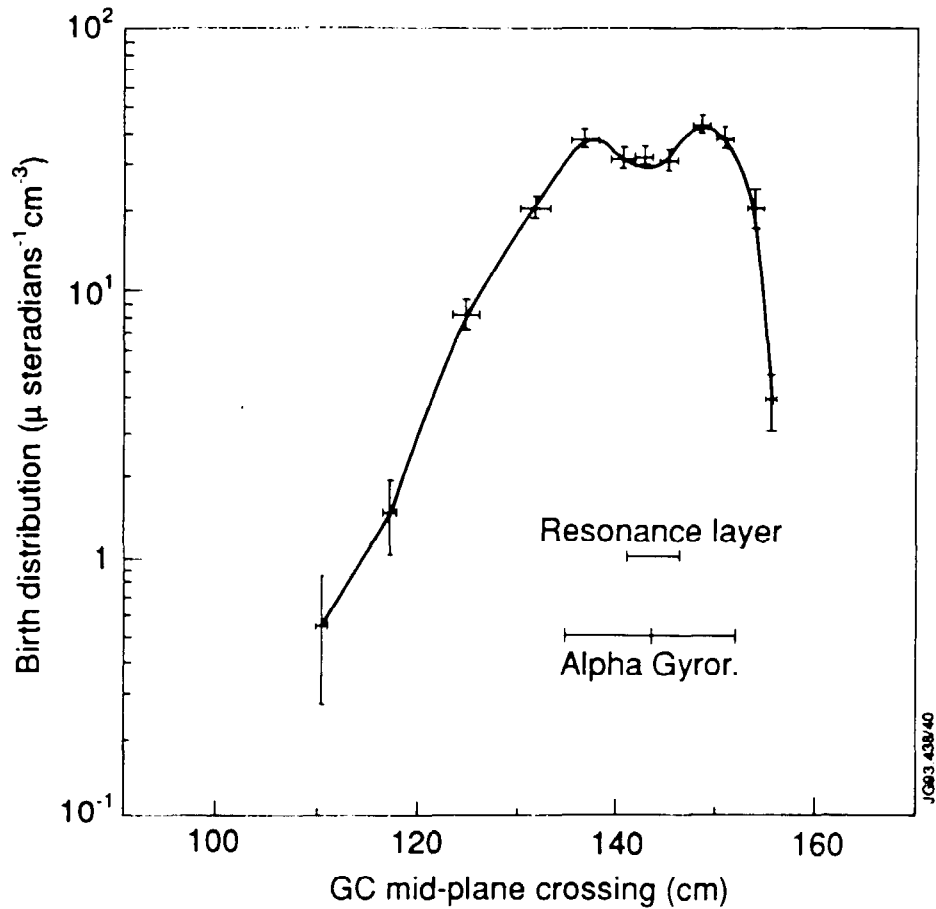


Fig. 12. Birth distribution of $d(^3\text{He},p)\alpha$ reactions as a function of major radius during ^3He minority ICRF heating in PLT [129]. The distribution is inferred from the pitch-angle distribution of escaping alphas measured using a nuclear track detector at the bottom of the machine. The ordinate is related to the number of tracks per angular bin and the abscissa is determined by tracing alpha guiding-center orbits back into the plasma. The data indicate that the $d(^3\text{He},p)\alpha$ reactions occur near the ^3He resonance layer.

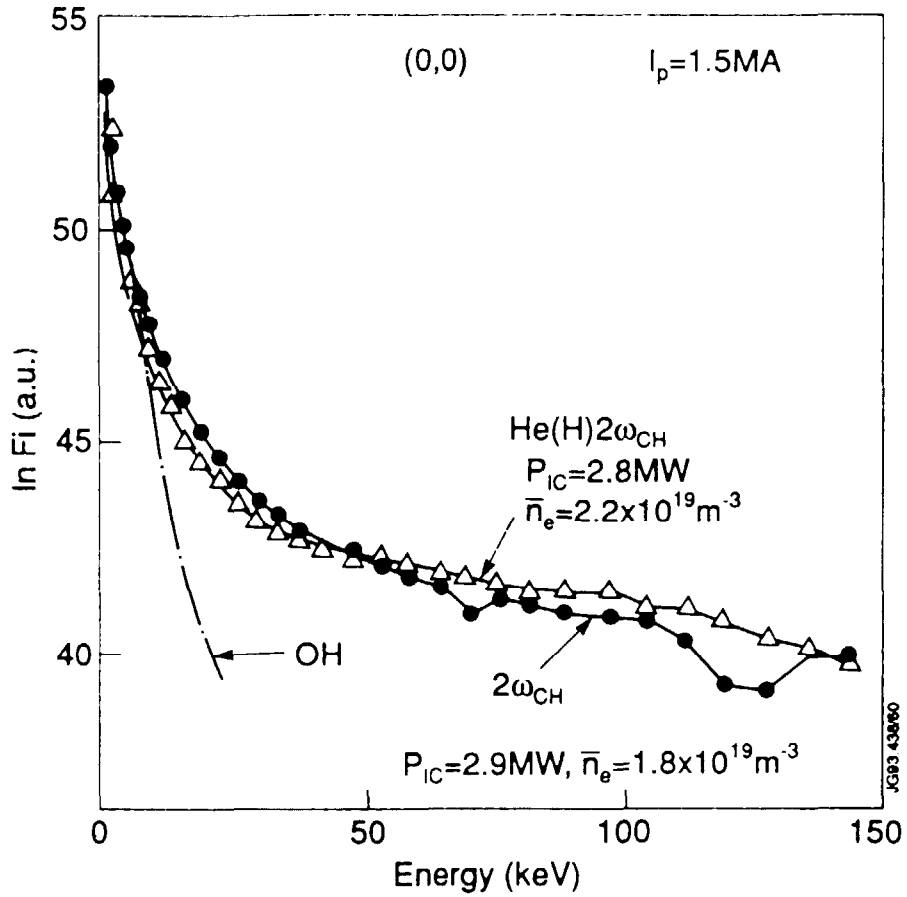


Fig. 13. Perpendicular ion energy spectra from passive charge exchange during second harmonic heating in JT-60 [143]. The curve labeled $\text{He(H)} 2\omega_{\text{CH}}$ is from a helium plasma with a hydrogen concentration of $\sim 10\%$. The curve labelled $2\omega_{\text{CH}}$ is from a hydrogen plasma. The antenna straps were in phase (0,0).

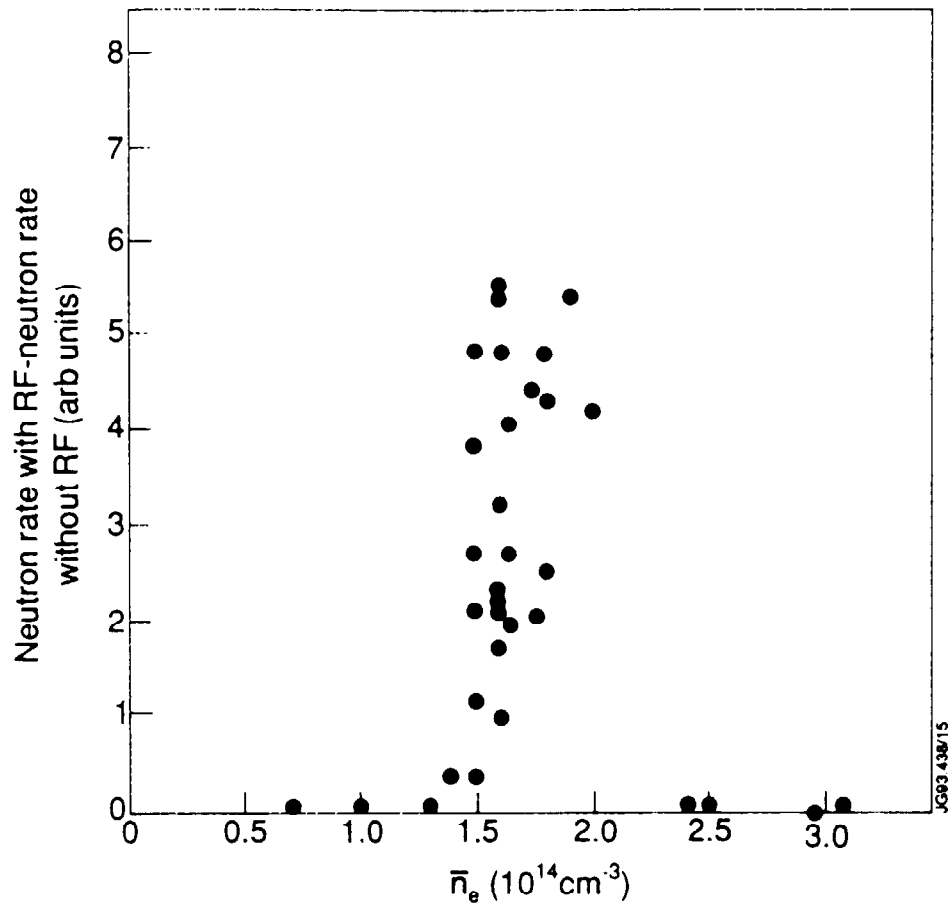


Fig. 14. Increase in the $d(d,n)^3\text{He}$ neutron rate during lower-hybrid heating as a function of density in Alcator A [168]. The enhanced neutron emission near $1.5 \times 10^{14} \text{cm}^{-3}$ is caused by formation of a fast-ion tail in the deuterium population.

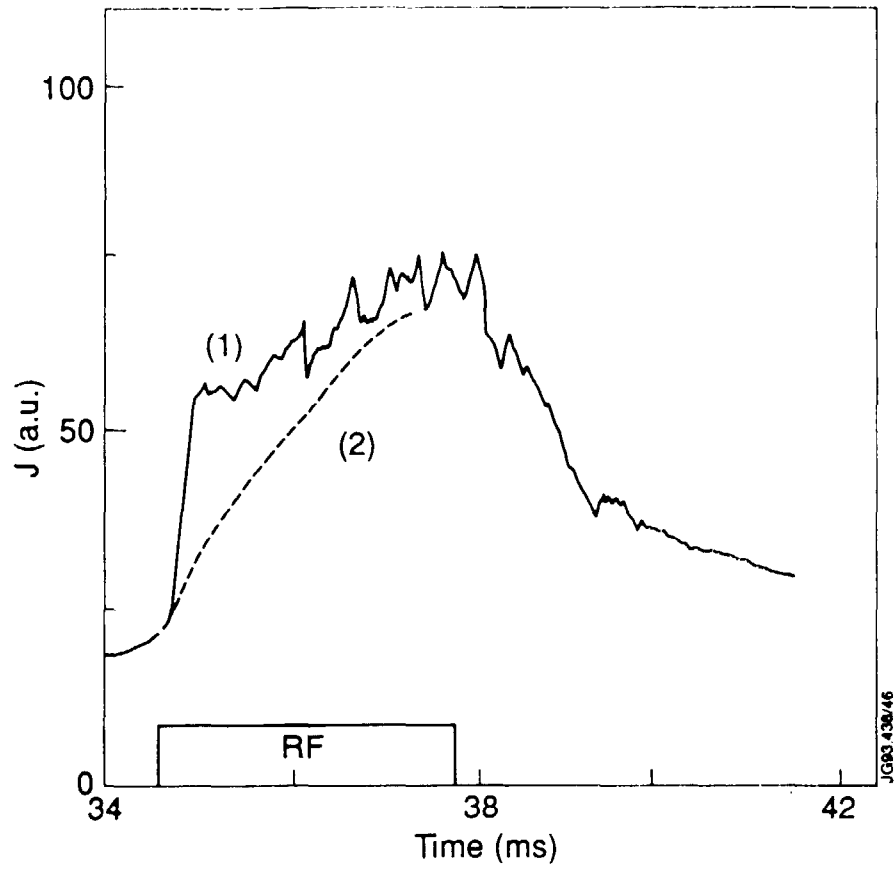


Fig. 15. Time evolution of the perpendicular passive charge exchange flux during lower hybrid heating in FT-2 for (1) $E = 975$ eV and (2) $E = 950$ eV [183]. $T_{i0} \simeq 120$ eV. The data illustrate the sharp energy threshold for direct lower hybrid heating.

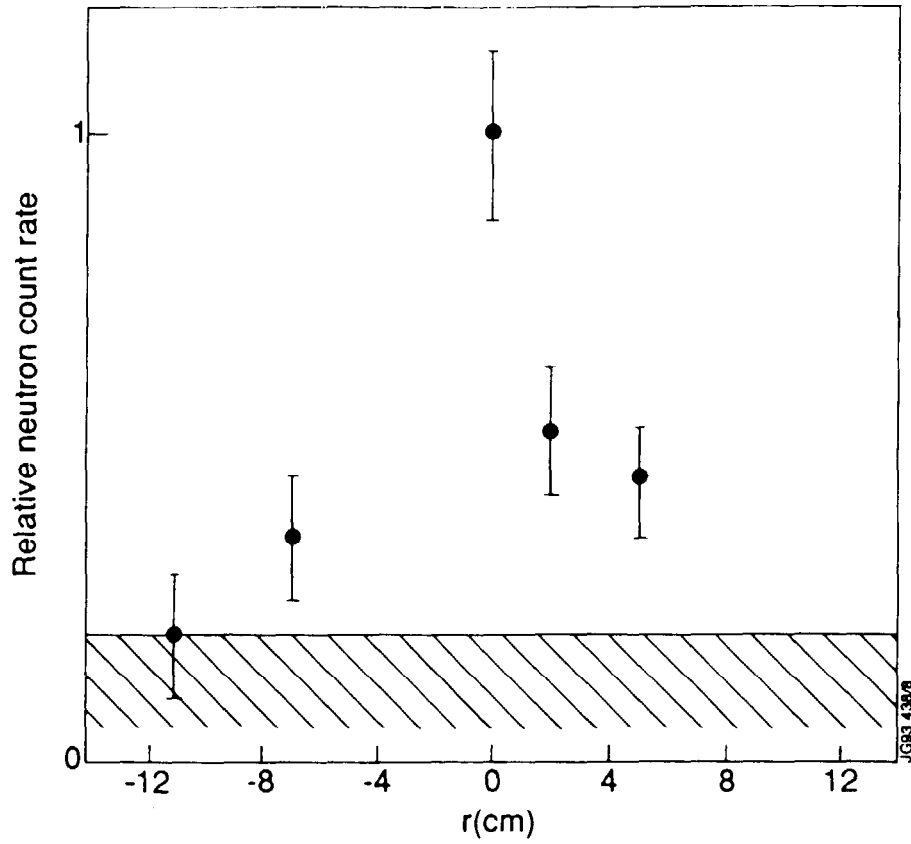


Fig. 16. Profile of the $d(d,n)^3\text{He}$ emission during fast-ion tail formation by lower hybrid waves in Alcator A [169]. The data are averaged over many shots, all of which had at least a ten times greater yield during the lower-hybrid pulse than during the rest of the discharge. The shaded area is the level of neutron leakage into the detector due to imperfect collimation. The profile indicates that the fast ions are concentrated near the center of the 10-cm radius plasma.

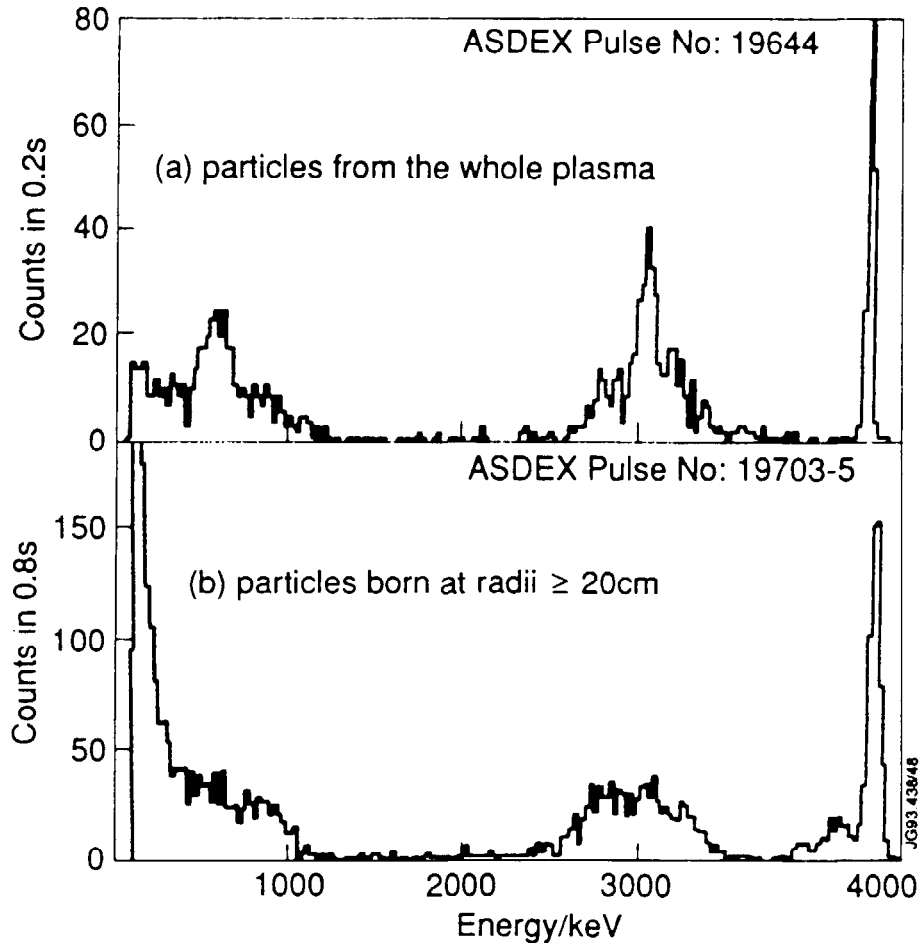


Fig. 17. Fusion product spectra during fast-ion tail formation by lower hybrid waves in ASDEX [179]. The peak near 0.6 MeV is from 1 MeV tritons (that lose energy in a detector window made out of a thin foil), the peak near 3.0 MeV is from 3 MeV protons, and the peak at 4.3 MeV monitors noise in the diagnostic. (a) Collimator rotated to detect tritons and protons produced throughout the plasma. Note the central peak due to thermonuclear reactions and the broad wings due to the fast-ion tail produced by lower hybrid. (b) Collimator rotated to detect tritons and protons produced in the plasma edge. Note that the central peak has disappeared but the broad wings produced by the fast-ion tail are still present. The flux in the wings is similar for the two orientations, indicating that the majority of the fast ions is outside $r \geq 20$ cm.

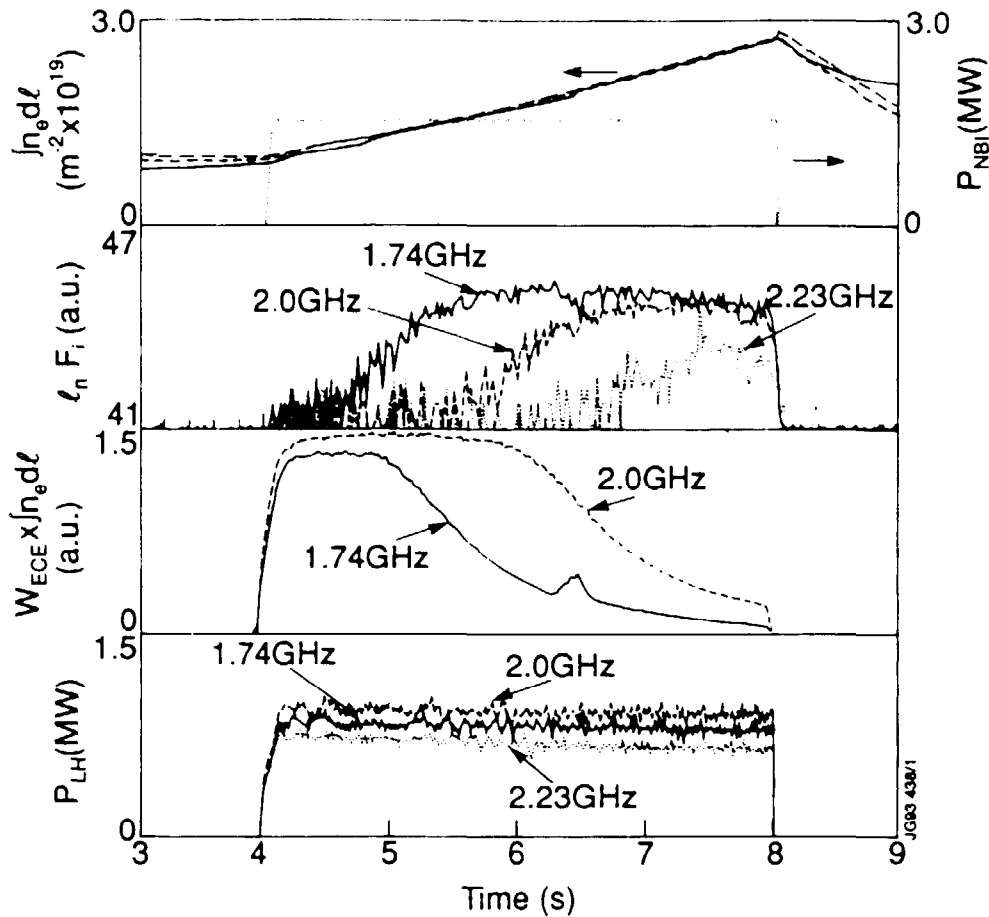


Fig. 18. Acceleration of beam ions during combined neutral beam and lower hybrid heating at three different wave frequencies in JT-60 [189]. The traces are the line density, the power injected by a 65 keV hydrogen beam, the flux of perpendicular 150 keV neutrals (on a logarithmic scale) measured by a perpendicular charge-exchange analyzer whose sightline intersects the neutral beam, the nonthermal electron cyclotron emission at $1.5\omega_{ce}$ times the line-integrated density, and the injected lower hybrid power. As the wave frequency increases, the transition from electron heating to ion heating occurs at higher density.

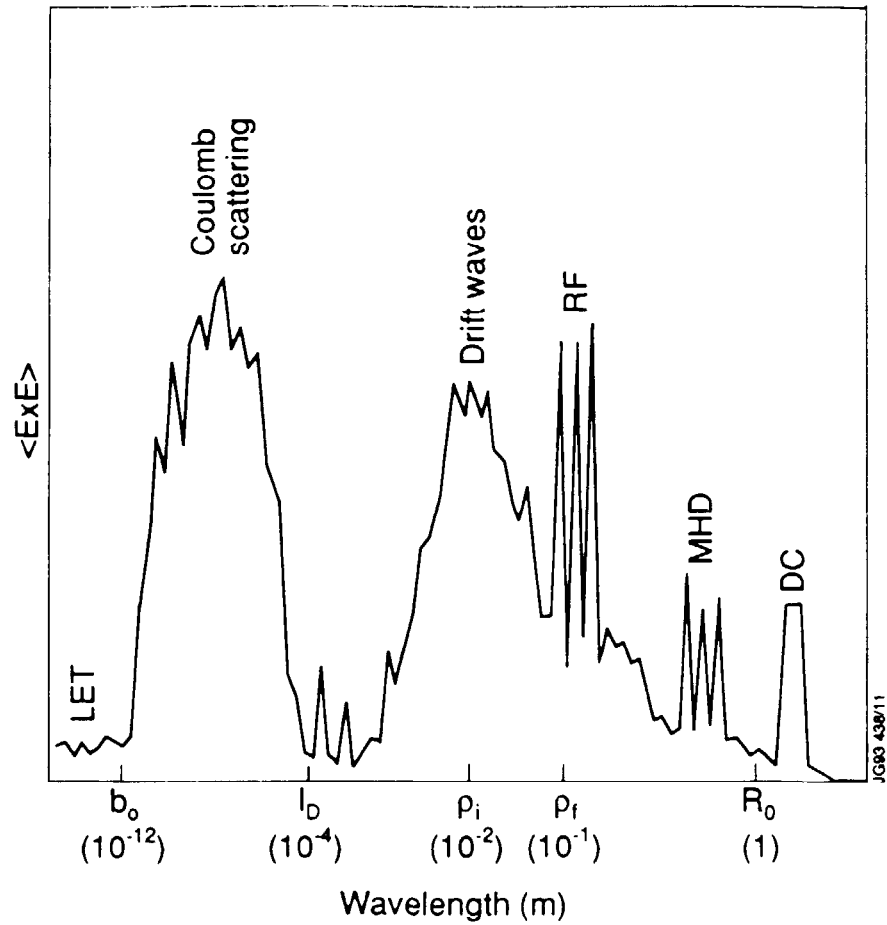


Fig. 19. Schematic illustration of the magnitude of the electric field fluctuations in a tokamak plotted versus wavelength on a log-log scale. The characteristic lengths are the distance of closest approach (b_0), the Debye length (λ_D), the thermal ion gyroradius (ρ_i), the fast-ion gyroradius (ρ_f), and the tokamak major radius (R_0); the typical order of magnitude for these lengths is given in parenthesis.

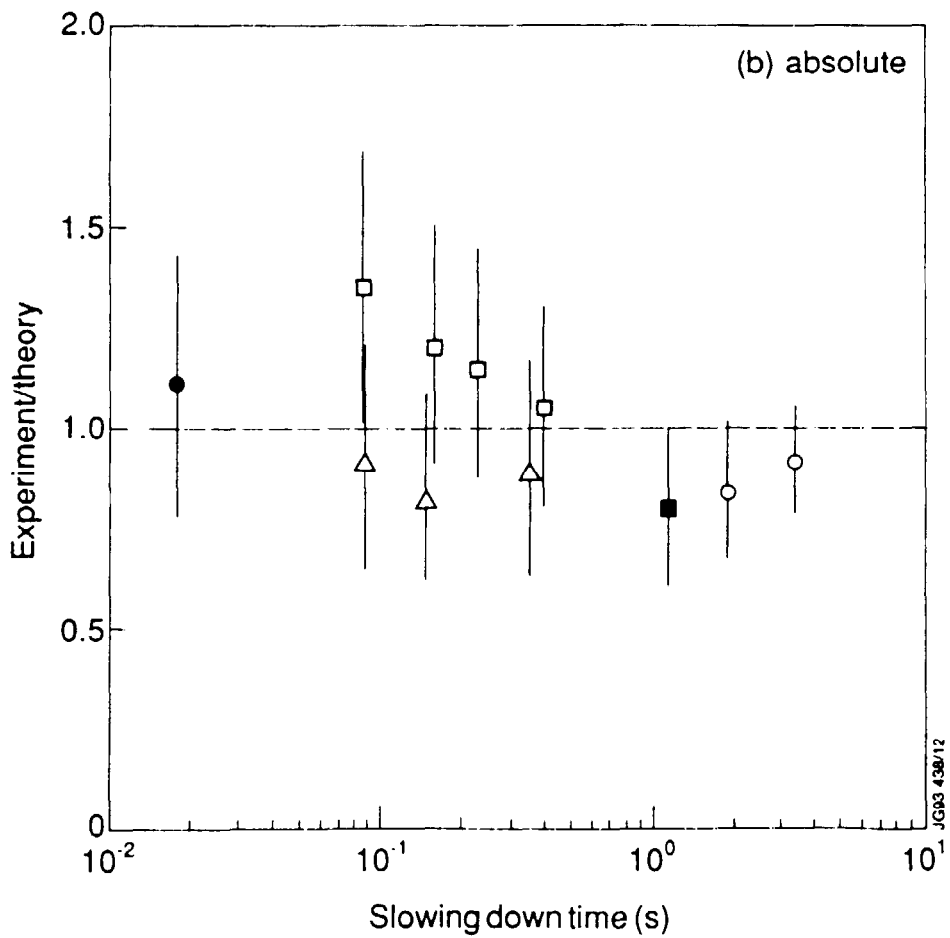
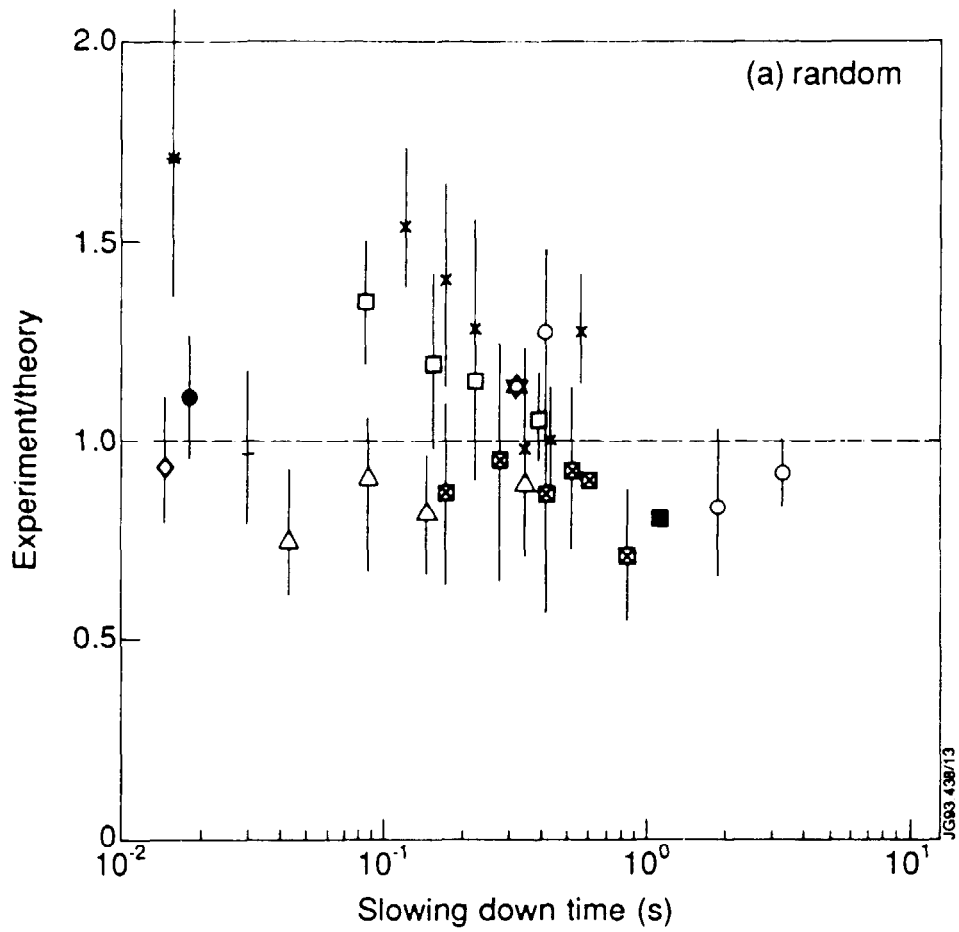


Fig. 20. Ratio of the measured slowing-down time to the expected slowing-down time versus the approximate value of τ_{se} . The error bars represent (a) the random error and (b) the total uncertainty.

- ◇ Hydrogen beam ions (14.2 keV) measured by passive charge exchange at the beginning of beam injection and after a 1 ms pulse in ATC [201].
- * Hydrogen beam ions (16 keV) measured by passive charge exchange at the beginning of beam injection in CLEO [200].
- × Deuterium beam ions (45 keV) inferred from the decay in the 2.5 MeV neutron emission in PLT [203].
- Hydrogen beam ions (33 keV) measured by active charge exchange in TFR after the beam pulse [92].
- ▽ Deuterium beam ions (80 keV) inferred from the decay in the 2.5 MeV neutron emission in TFTR [205].
- Deuterium beam ions (30 keV) inferred from the decay in the 2.5 MeV neutron emission in ISX-B [204].
- octagon** ^3He fusion products (0.8 MeV) inferred from the 15 MeV proton emission in TFTR [209]. The theory is taken from Batistoni and Barnes [234].
- Triton fusion products (1.0 MeV) inferred from the 14 MeV neutron emission in JET [210].
- △ Deuterium beam ions (75 keV) inferred from the decay in the 2.5 MeV neutron emission following a 2 ms beam pulse in DIII-D [206].
- Deuterium beam ions (38-75 keV) inferred from the decay in the 2.5 MeV neutron emission following a 2 ms beam pulse in DIII-D [207].
- Deuterium beam ions (92 keV) inferred from the decay in the 2.5 MeV neutron emission following a 20 ms beam pulse in TFTR [208].
- ☆ Triton fusion products (1.0 MeV) inferred from the 14 MeV neutron emission in DIII-D [211].
- ⊠ Triton fusion products (1.0 MeV) inferred from the 14 MeV neutron emission in JT-60U [212]. No errors were quoted.

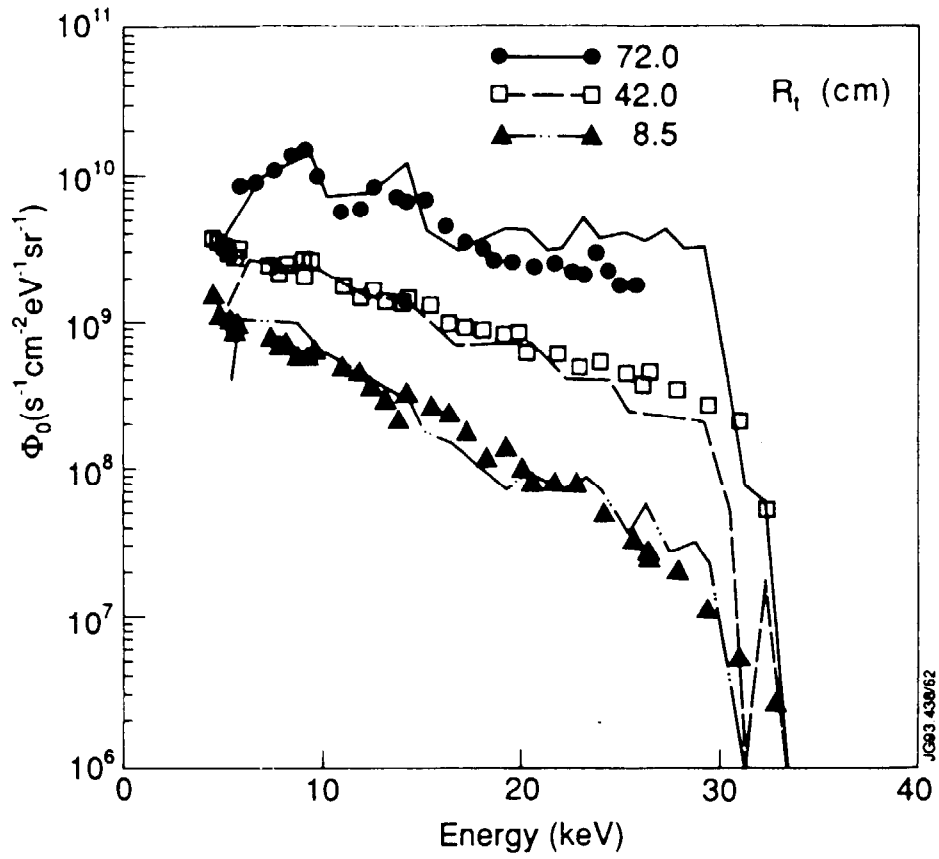


Fig. 21. Comparison of experimental and predicted fast neutral particle spectra during hydrogen beam injection into ISX-B [204]. The analyzers scan in the horizontal midplane; R_t represents the tangency radius. 30 keV co-going neutrals were injected at $R_{tan} = 74.5$ cm ($R_0 = 93$ cm).

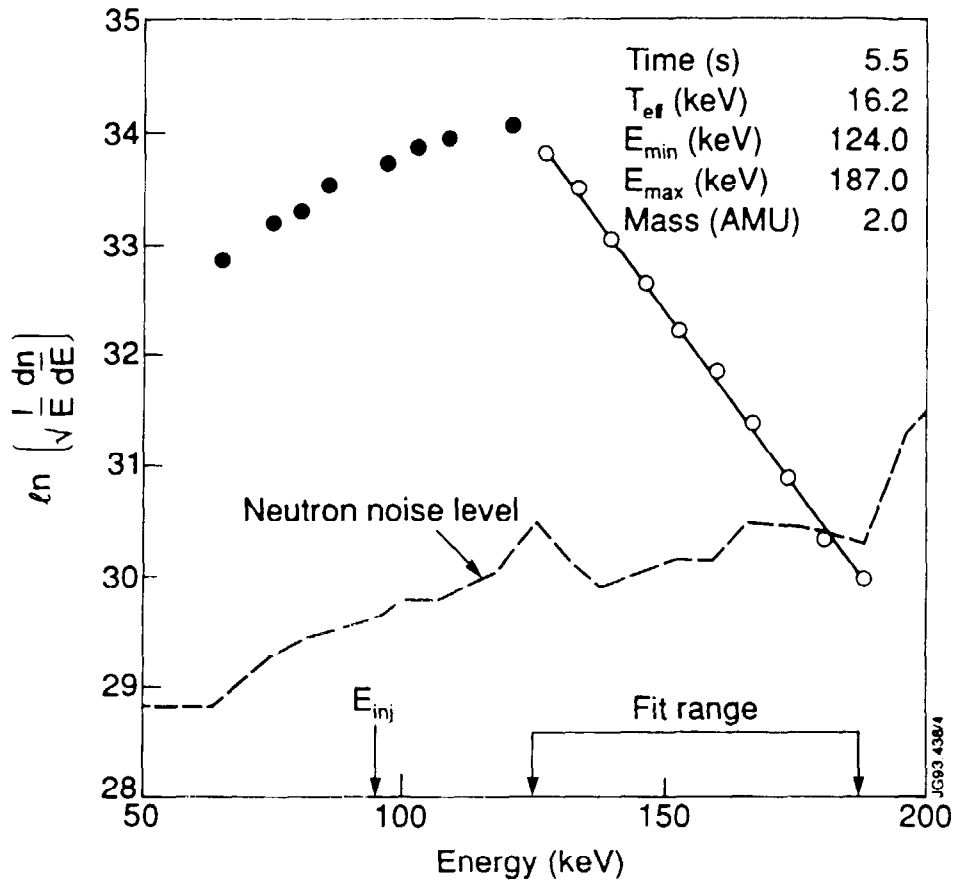


Fig. 22. Deuterium charge exchange spectrum during injection parallel to the current of 90-105 keV neutrals into a hot ($T_i \simeq 23$ keV), low-density ($\bar{n}_e = 0.6 \times 10^{13} \text{ cm}^{-3}$), TFTR plasma [230]. The noise level caused by 2.45 MeV neutrons is indicated. Analyzer sightline $R_{tan} = 2.0$ m; $R_0 = 2.45$ m.

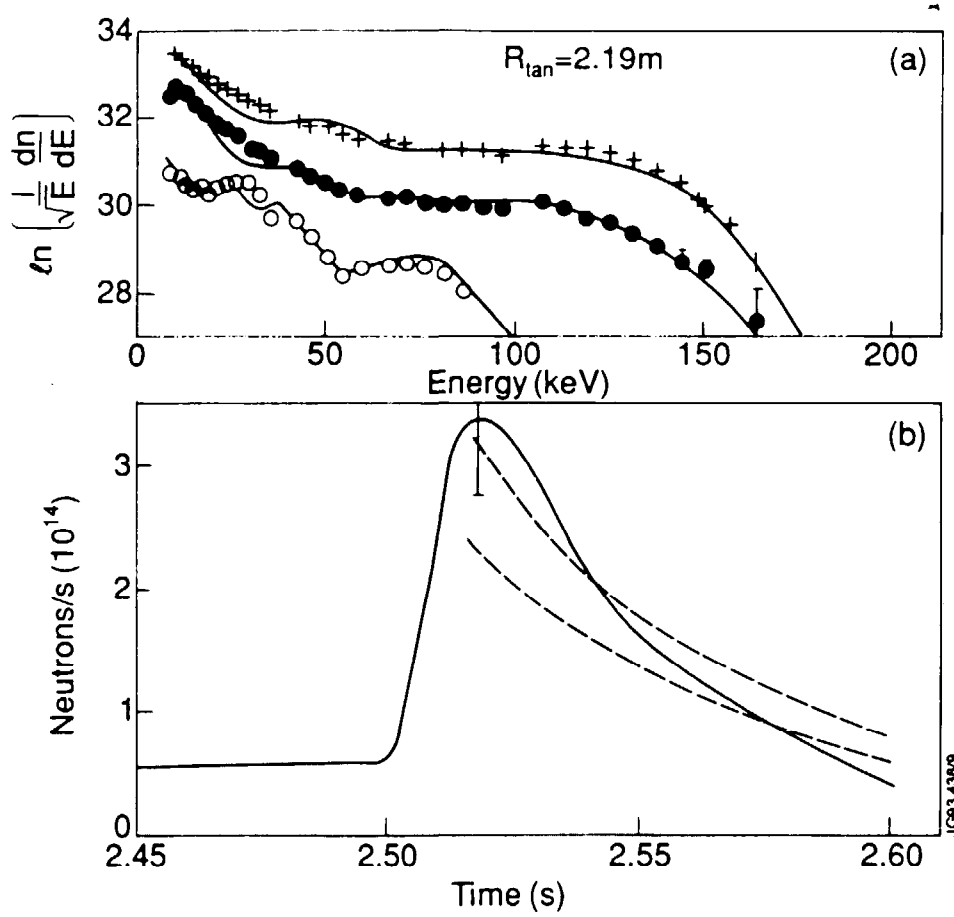


Fig. 23. Tangential deuterium charge exchange spectra (a) and $d(d,n)^3\text{He}$ neutron emission (b) during compression of a TFTR plasma heated by tangential deuterium beams [239]. The beams were turned off at 2.5 s, when the 15 ms compression from $R_0 = 3.0$ m to $R_0 = 2.17$ m commenced. The error bar on the neutron trace is the uncertainty associated with the sensitivity of the detector to the radial position of the plasma; the predictions of a Fokker-Planck calculation are shown using a solid line in (a) and dashed lines in (b).

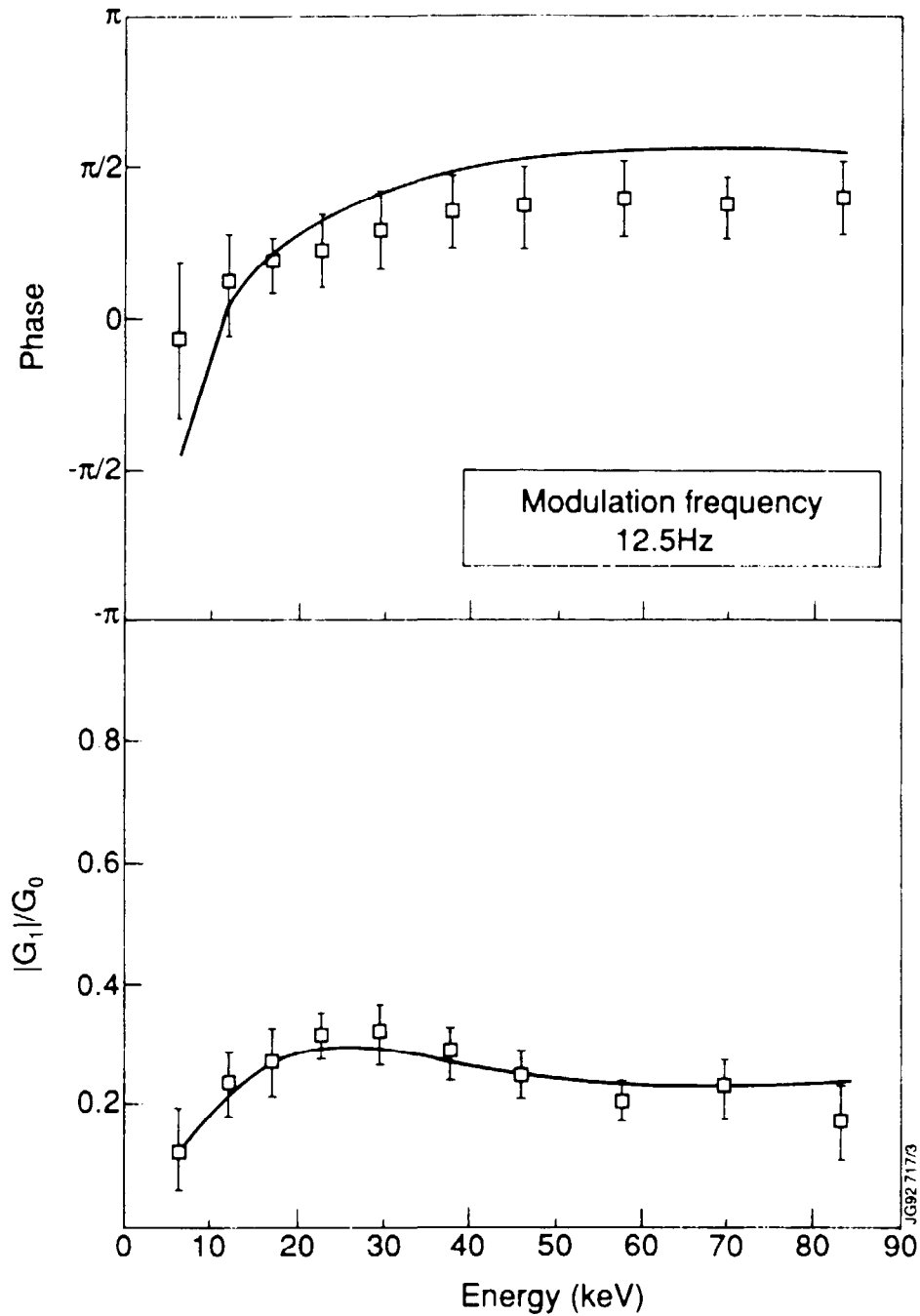


Fig. 24. Phase and amplitude of the first harmonic of the neutral-particle flux versus energy during modulated, low-power, hydrogen minority ICRF heating in JET [114]. The amplitude of the modulated flux is normalized to the steady-state value. The solid lines are the expected response for an isotropic fast-ion tail population that experiences quasilinear diffusion balanced by Coulomb scattering.

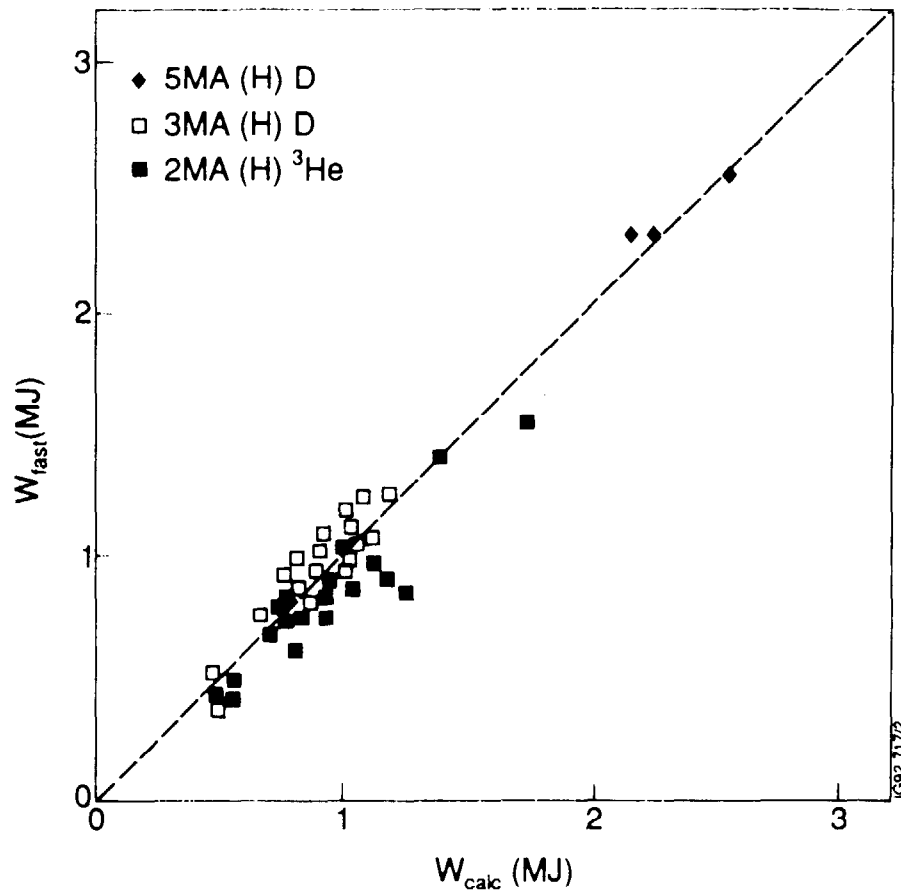


Fig. 25. Measured total perpendicular fast ion energy versus theory during hydrogen minority heating in JET [124]. The fast ion energy is derived from the difference between the stored energies derived from diamagnetic and equilibrium measurements, with an estimated error of $\pm 20\%$. The theory uses a Stix model but includes finite orbit width effects. The only normalization in the theory is the fraction of rf power absorbed by the minority (65%), which was inferred from modulation experiments.

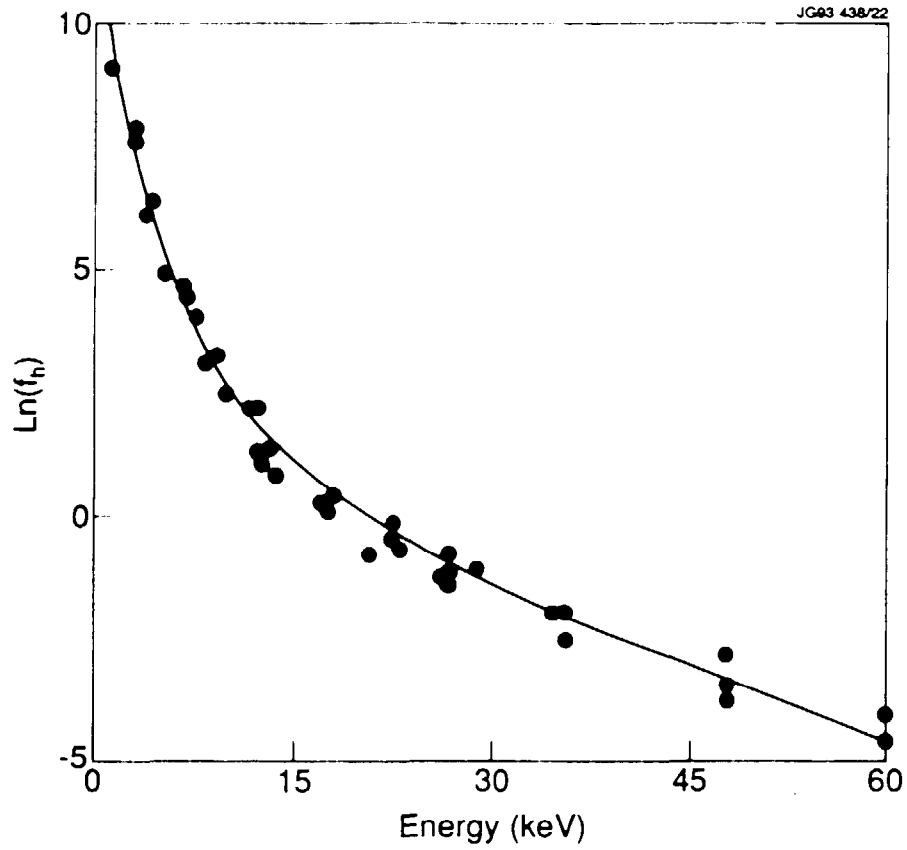


Fig. 26. Passive perpendicular charge-exchange spectrum measured during second-harmonic heating of hydrogen in PLT [142]. The data are fitted by a quasilinear distribution [assumed isotropic in velocity space for this relatively low-power ($P_{rf} \simeq 140$ kW) case], with the rf power density and wave vector adjusted to optimize the fit.

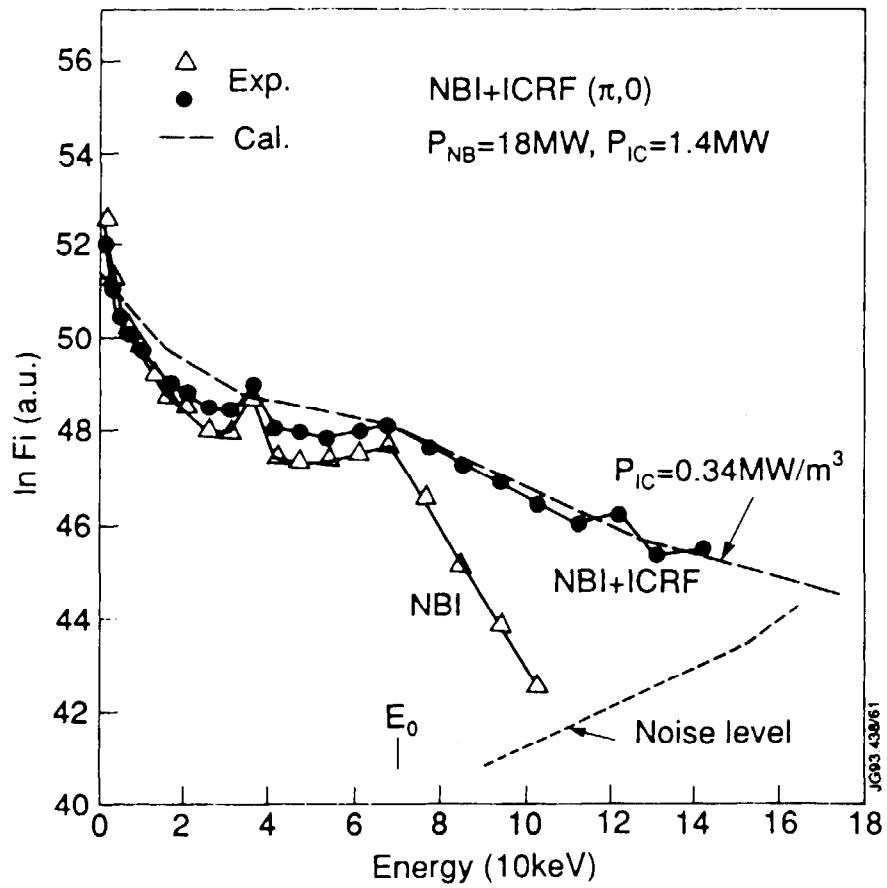


Fig. 27. Active perpendicular charge-exchange spectrum measured during simultaneous hydrogen beam injection (70 keV) and second harmonic heating in JT-60 [148]. The analyzer noise level is indicated. The dashed line is the distribution function predicted by an isotropic quasilinear calculation with the rf power density treated as an adjustable parameter.

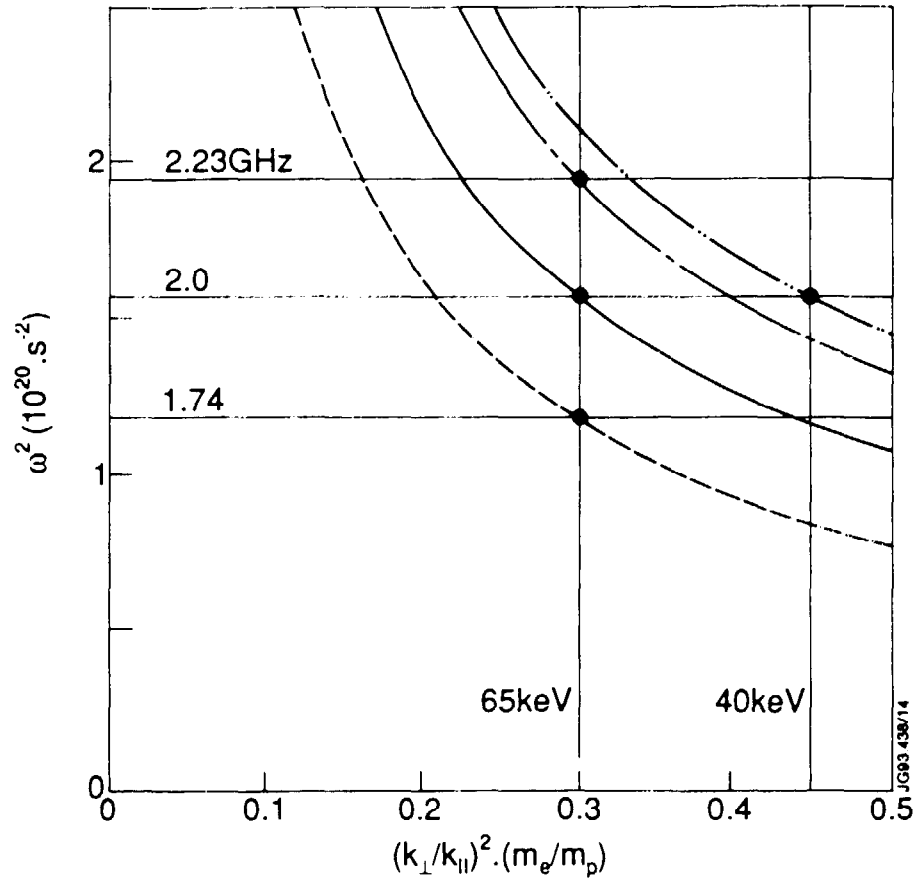


Fig. 28. Cold plasma dispersion relations for lower hybrid waves at the densities where beam acceleration is observed in JT-60 [147]. (Raw data are shown in Fig. 18.) The frequency of the launched waves is indicated by the horizontal lines. The injection energy of the beam ions is represented by the vertical lines and is mapped to the abscissa using the resonance condition $v_{\perp} = \omega/k_{\perp}$ and the parallel wave number launched by the antenna. The lines and dispersion curves intersect (points) at the appropriate values of ω , E_b , and \bar{n}_e , confirming the expected resonance condition. Critical densities: $\bar{n}_{ec} = 1.2$ (broken line), 1.7 (solid line), 2.2 (dash-dotted line), and 2.4 (dotted line) $\times 10^{19} \text{ m}^{-3}$.

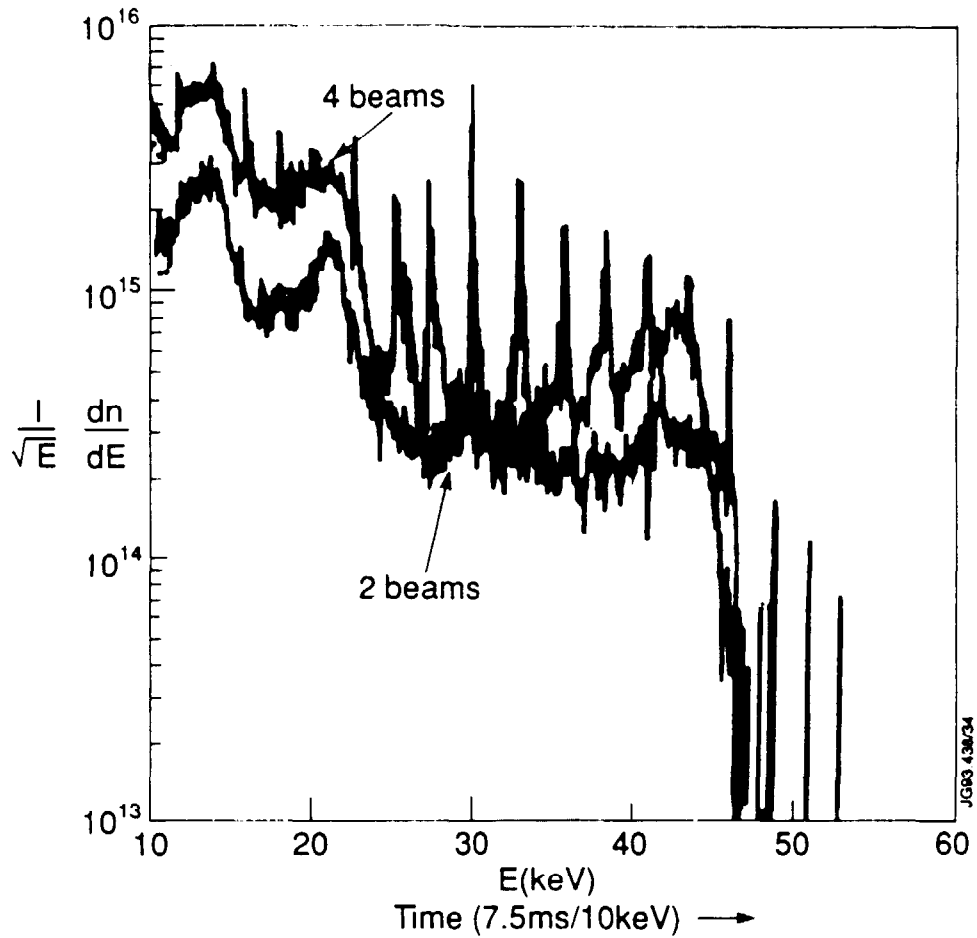


Fig. 29. Passive perpendicular charge exchange spectrum measured during perpendicular deuterium beam injection (45 keV) into PDX [252]. During injection of four beams, the fishbone instability was strongly excited and caused large losses of beam ions but the instability was barely excited when only two beams were used. The spectrum was obtained by sweeping the analyzer energy in time; the spikes on the four-beam spectrum are an artifact associated with expulsion of beam ions at fishbone bursts. The slope of the spectrum near the birth energy changes dramatically in the presence of large losses.

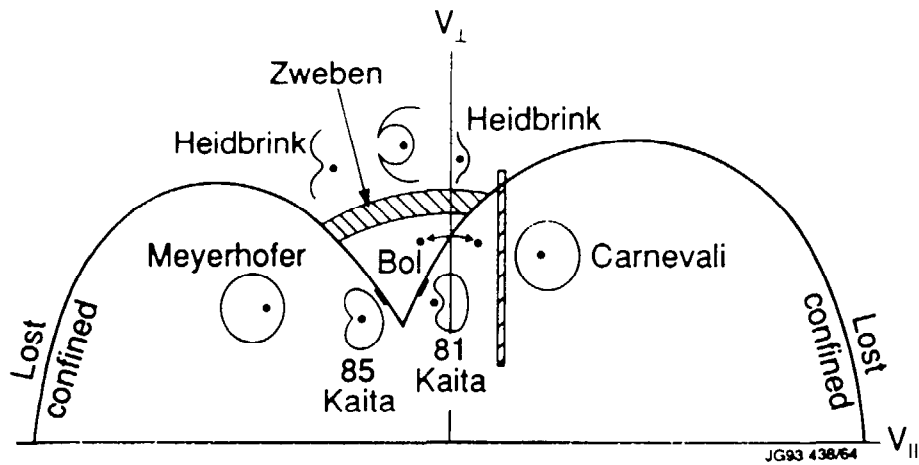


Fig. 30. The portion of velocity space sampled by various experiments. The loss boundary is calculated using the formalism of Hively and Miley [256] for fast ions near the center of PLT. Typical investigated orbits are sketched, with a dot indicating the magnetic axis. (See Fig. 1 for several examples of actual orbits.) Particles that circulate in the the direction of the plasma current (v_{\parallel}) lie to the right of the axis, and counter-circulating orbits lie to the left of the axis. In most cases, the investigated orbits did not originate near the magnetic axis, so the loss boundary is only a qualitative guide.

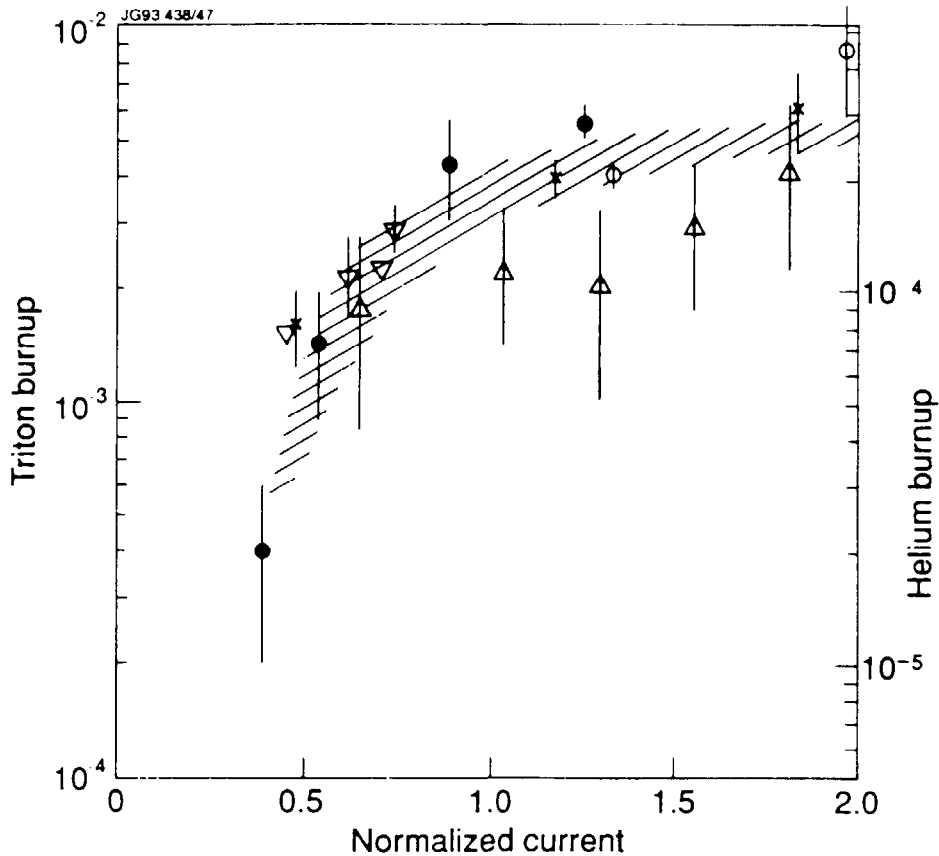


Fig. 31. Fusion product burnup data versus plasma current I_p . The plasma current is normalized to I_{loss} (Eq. 22). The shaded region is the expected variation associated with the improved confinement of the fusion products as the plasma current increases (for broad and narrow source and current profiles); variations associated with changes in T_e or n_d/n_e are not included. The error bars represent random errors only.

- Ratio of $d(^3\text{He},p)\alpha$ reactions (measured by a silicon diode) to $d(d,n)^3\text{He}$ reactions in PDX for high field (2.2 T) discharges (0.14-0.44 MA) [20].
- ▽ Ratio of $d(t,n)\alpha$ reactions (measured by copper activation) to $d(d,n)^3\text{He}$ reactions in FT for high-field (8 T) discharges (0.31-0.50 MA) [430].
- Ratio of $d(^3\text{He},p)\alpha$ reactions (measured by silicon diodes) to $d(d,n)^3\text{He}$ reactions in TFTR (0.5-1.0 MA) [209]. These data are already corrected for the expected $T_e^{3/2}$ dependence of the burnup and the absolute normalization is approximate.
- △ Ratio of $d(t,n)\alpha$ reactions (measured by foil activation) to $d(d,n)^3\text{He}$ reactions in TFTR (0.5-1.4 MA) [322].
- × Ratio of $d(t,n)\alpha$ reactions (measured by a silicon diode) to $d(d,n)^3\text{He}$ reactions in DIII-D for high-field (2 T) discharges (0.4-1.6 MA) [211].

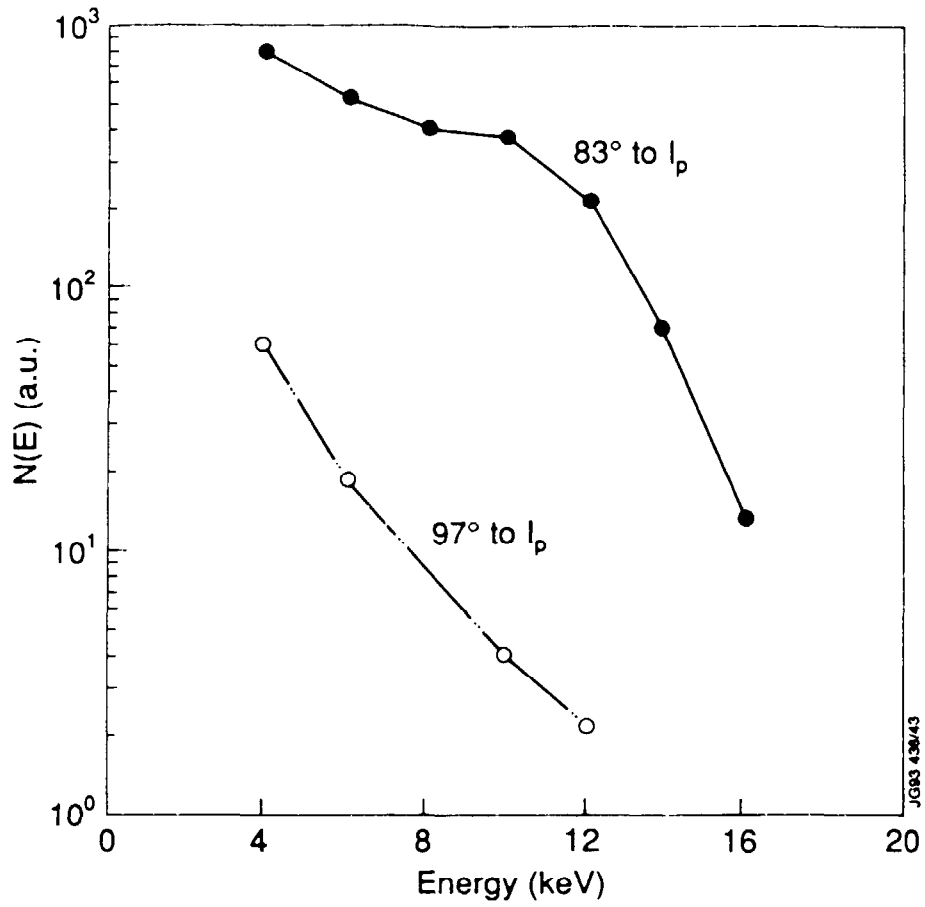


Fig. 32. Passive deuterium charge-exchange flux observed tangentially during near-perpendicular injection into ATC for two different directions of the plasma current [215]. The calculated fraction of confined orbits was 56% for 83° and 27% for 97°.

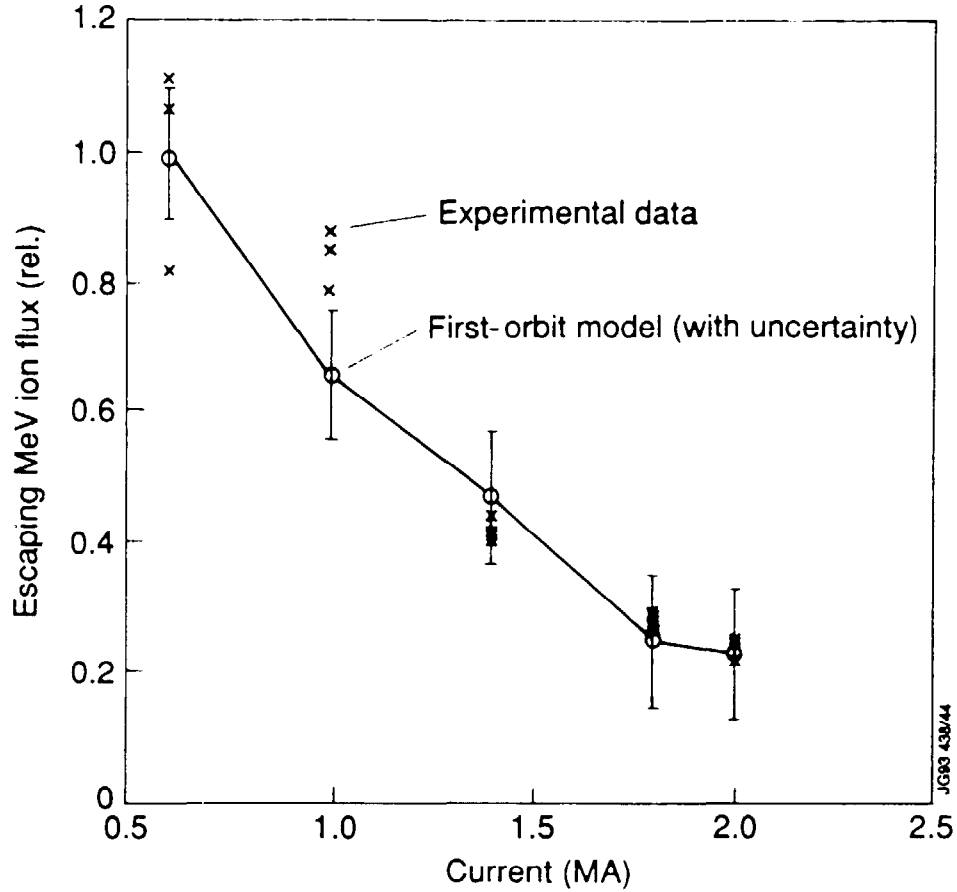


Fig. 33. Steady-state signal from 1 MeV tritons and 3 MeV protons as a function of plasma current in TFTR [261]. The signal (\times) is from a detector at the bottom of TFTR, is integrated over pitch angle and gyroradius, and is normalized to the average neutron rate during the shot. The first-orbit model points (\circ) are obtained by integrating orbit code calculations [431] over the same range in pitch angle. The model curve is normalized to the average of the data at 0.6 MA.

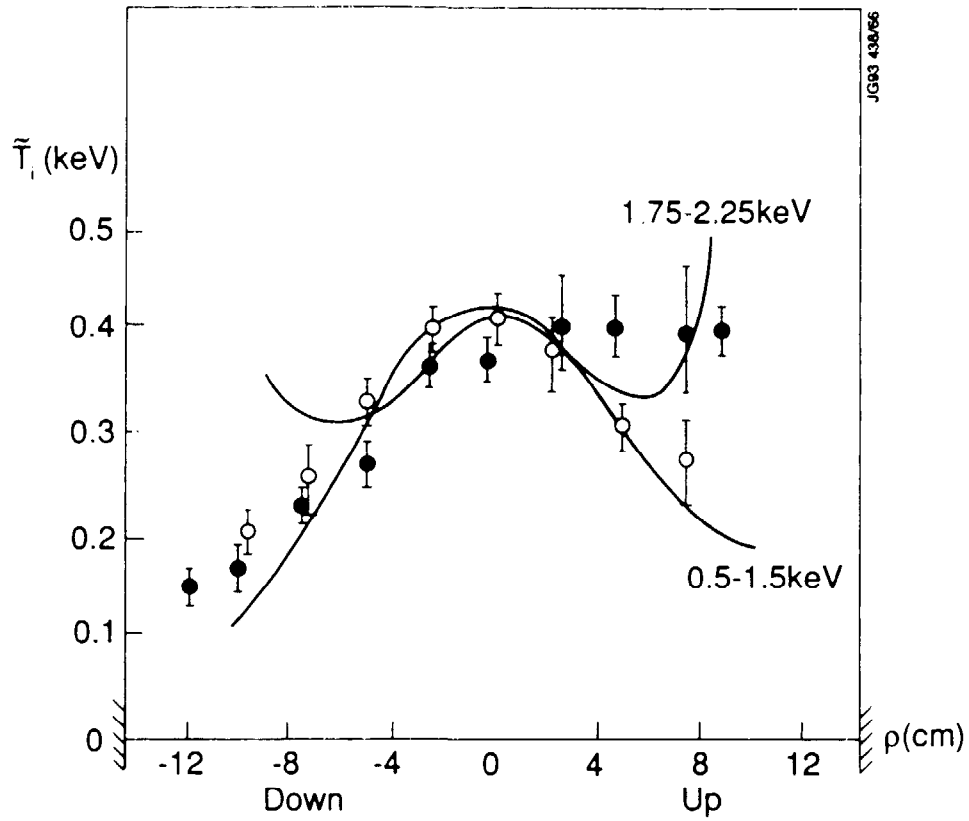


Fig. 34. Vertical distribution of the slope \tilde{T}_i of the perpendicular distribution function measured by active (open circles) and passive (solid circles) charge exchange in T-4 [270]. The ∇B drift is upward. The solid lines are theoretical predictions based upon an approximate solution of the Fokker-Planck equation including convective ripple transport.

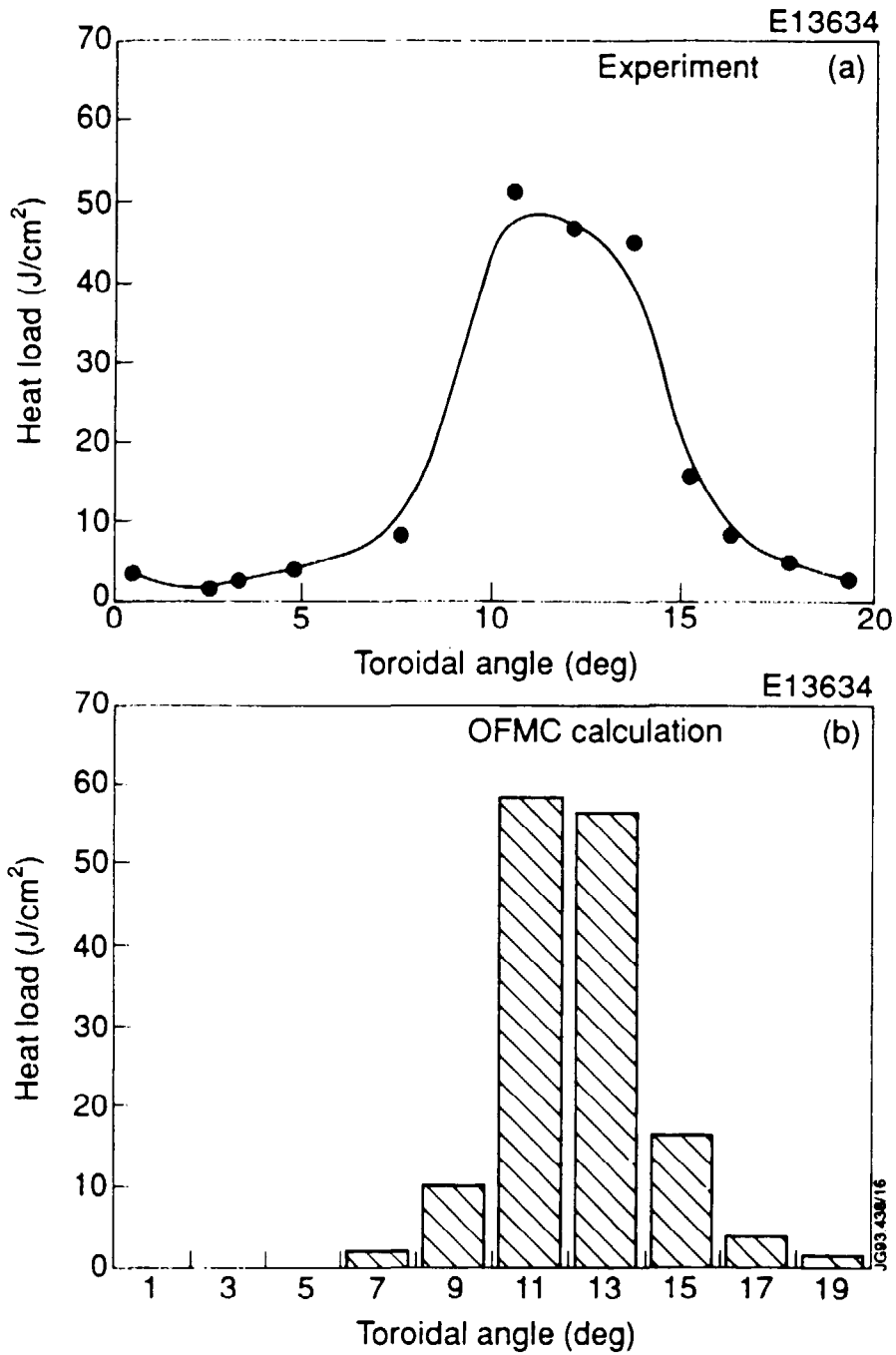


Fig. 35. Toroidal distribution of the measured (a) and predicted (b) heat load to the first wall during perpendicular beam injection into JT-60U [282]. Poloidal angle = -64°. The calculated heat load is from a Monte Carlo orbit following code that includes the effects of ripple trapping (which dominates in this case) and ripple diffusion.

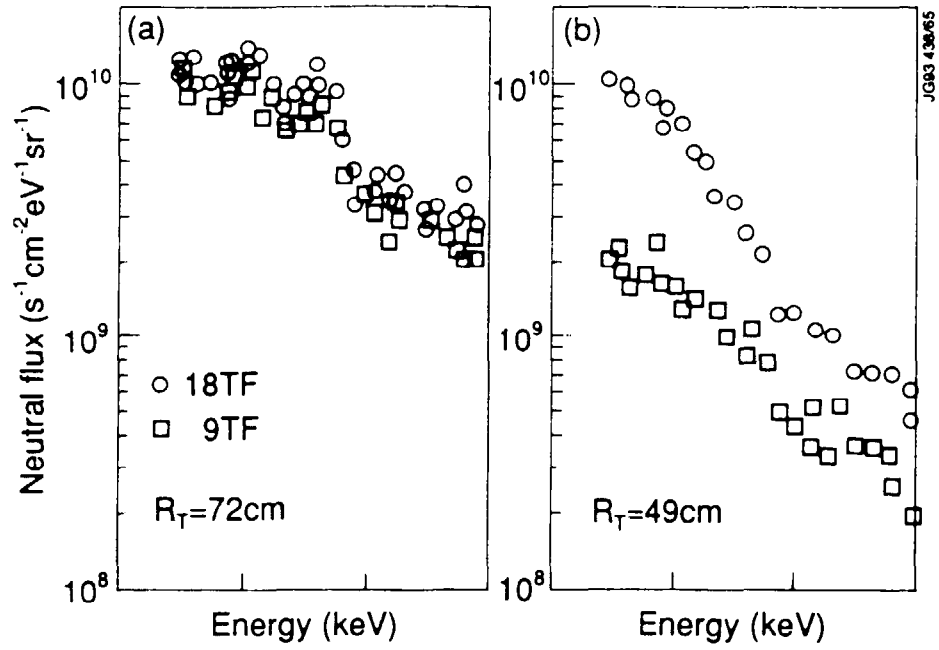


Fig. 36. Passive charge-exchange spectra during tangential neutral beam injection (30-35 keV) into ISX-B with either 18 (\circ) or 9 (\square) toroidal field coils energized [287]. (a) Sightline viewing passing particles ($R_{tan} = 72$ cm; $R_0 = 93$ cm). (b) Sightline viewing particles near the trapped/passing boundary ($R_{tan} = 49$ cm).

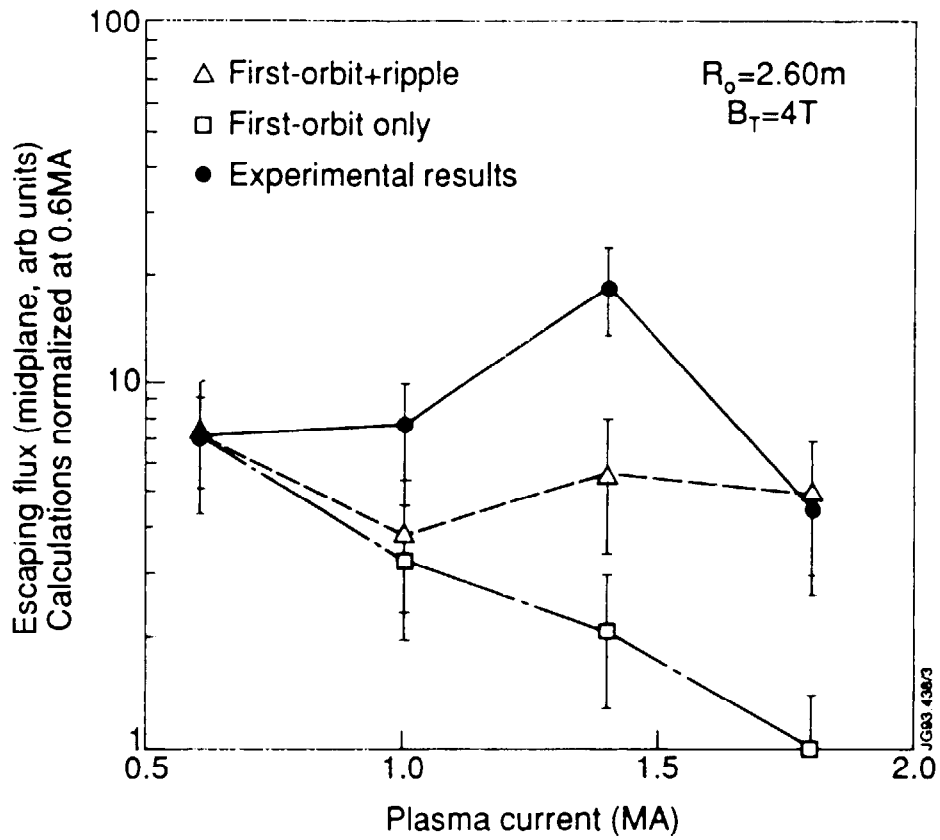


Fig. 37. Flux of d-d fusion reaction products measured by a probe $\sim 20^\circ$ below the midplane as a function of plasma current in TFTR [289]. The signals are integrated over pitch angle. The curve labelled "first-orbit only" indicates the expected variation with current of prompt (drift-orbit) losses and the curve labelled "first-orbit + ripple" is the variation calculated by a Monte Carlo guiding center code assuming a simplified wall geometry.

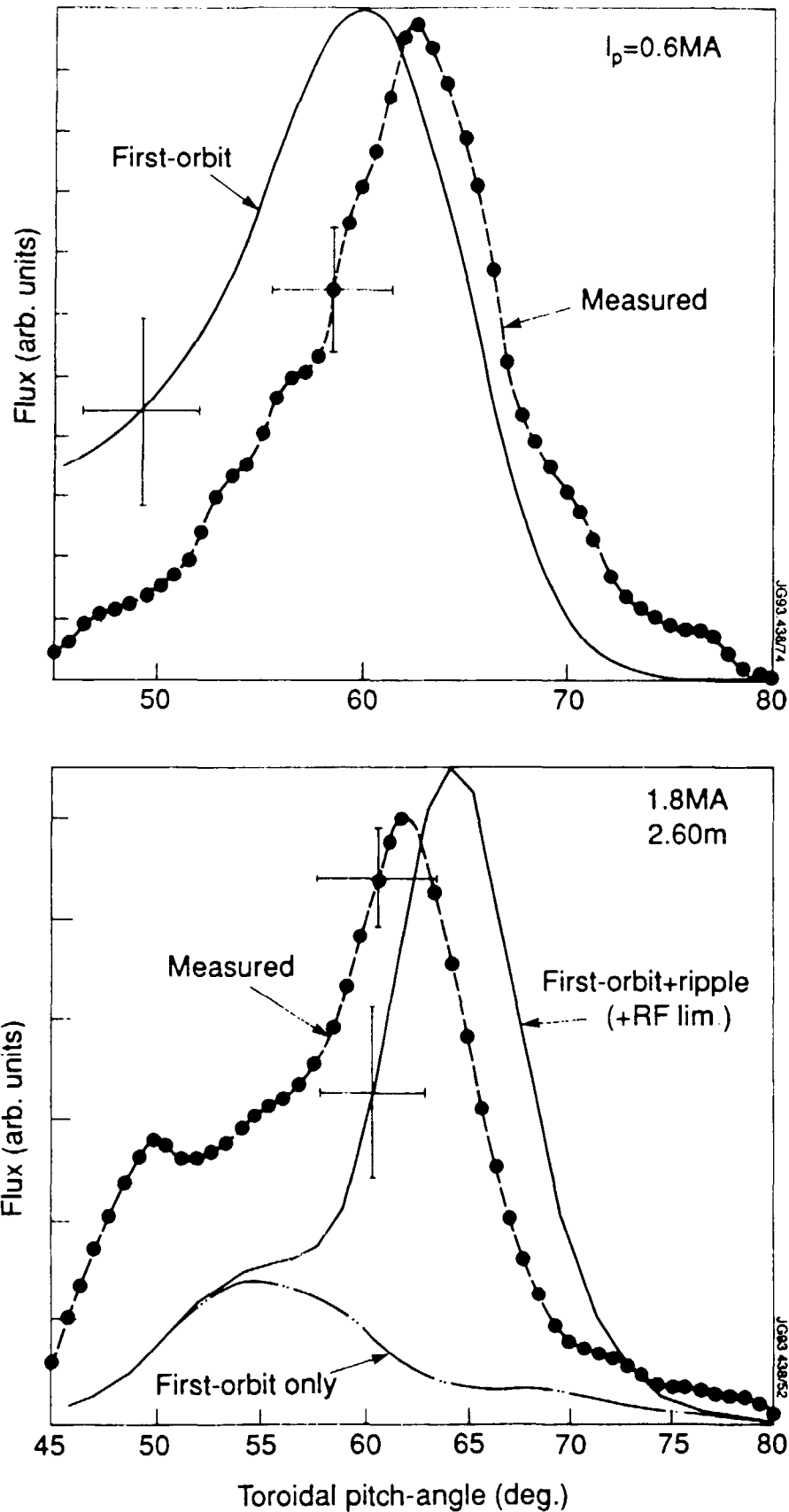


Fig. 38. Flux of d-d fusion reaction products versus toroidal pitch angle ($\cos^{-1}(v_\phi/v)$) for $I_p = 0.6 \text{ MA}$ and $I_p = 1.8 \text{ MA}$ in TFTR [289]. At low current, the measured distribution (data points) is consistent with the distribution predicted by calculations of drift orbits losses, while at high current, calculations that include ripple losses give a better fit to the data. The error bars on the calculated curves are associated with uncertainties in the current and d-d emission profiles, while the error bars on the experiment are associated with uncertainties in the calibration and orientation of the detector.

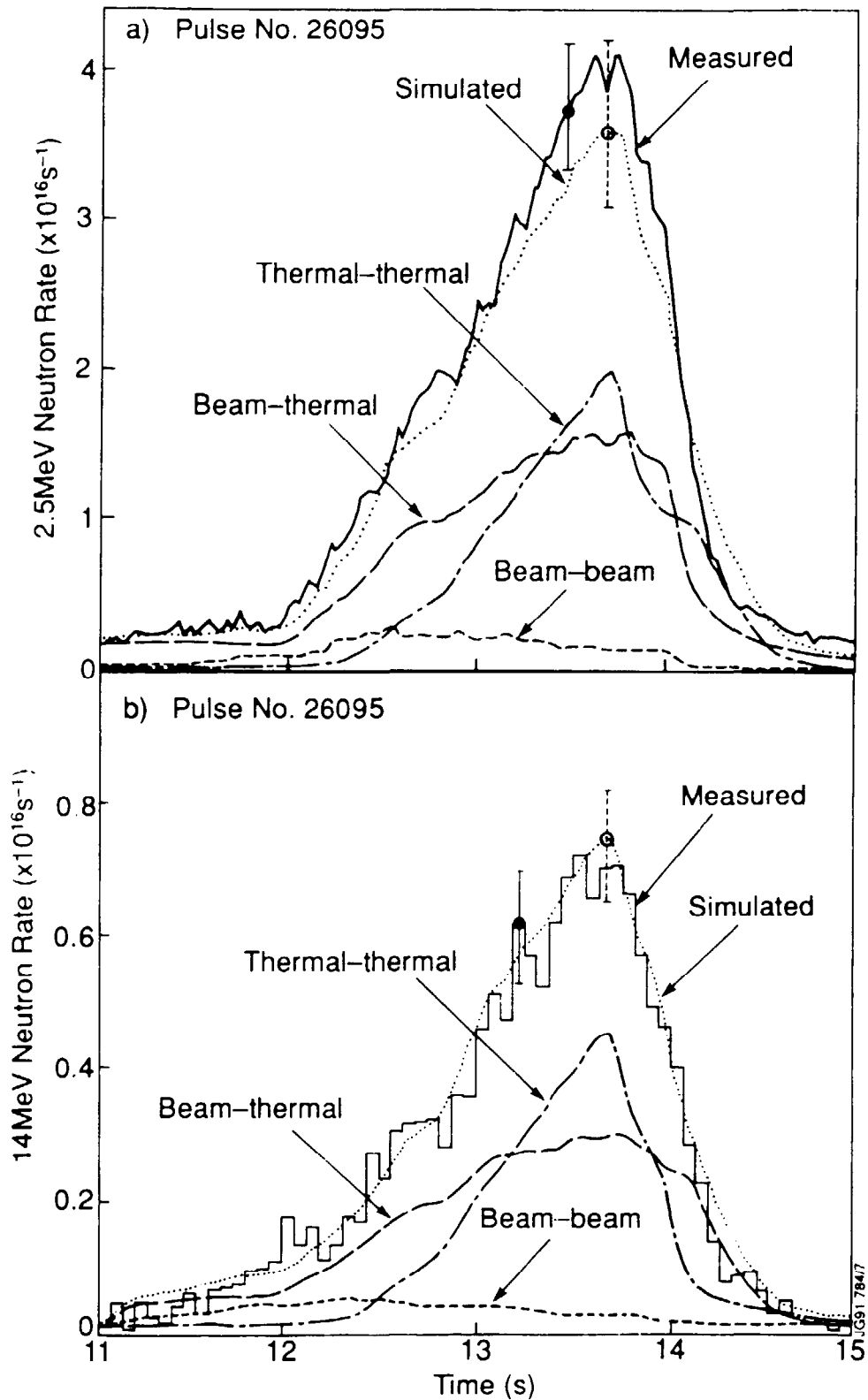


Fig. 39. Time evolution of the $d(d,n)^3\text{He}$ and $d(t,n)\alpha$ neutron rates during D^0 and trace tritium beam injection into JET [1]. Fission chambers were used to measure the total neutron yield (a) and the 14 MeV component (b) was deduced using silicon diodes. The simulations were performed using the TRANSP code and indicate the relative contributions of beam-beam, beam-plasma, and thermonuclear emission.

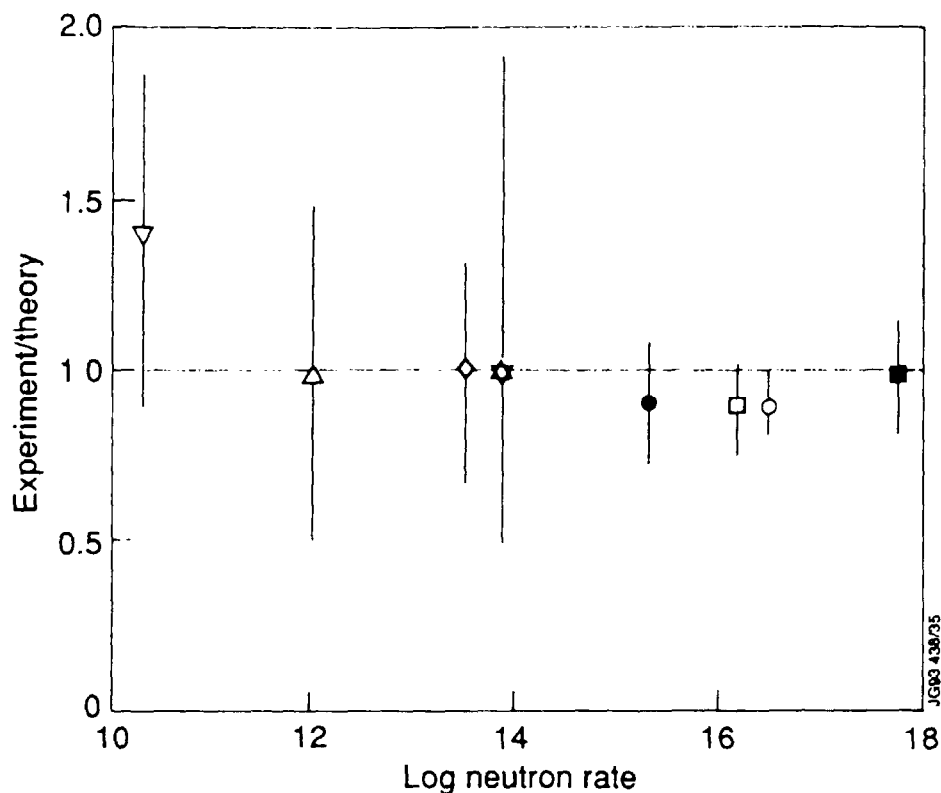


Fig. 40. Average ratio of the measured neutron rate to the expected neutron rate for several tokamaks, as a function of the approximate value of the neutron rate (in neutrons/sec). All cases are for deuterium injection, except for the highest emission point (tritium injection). Uncertainty in the measurements of T_e , n_e , and Z_{eff} are the dominant sources of uncertainty in the theoretical prediction.

ISX-B (∇) [204]. The random error for 21 discharges is shown; the quoted accuracy of the neutron calibration ($\sim 30\%$) is comparable.

TFR (Δ) [214]. The average value for four discharge conditions is shown; the error bar is estimated from the published uncertainties in experiment and theory.

PDX (\diamond) [302]. The random error for 14 discharges is shown; the quoted accuracy of the neutron measurement is $\sim 50\%$.

PLT (\star) [203]. The error bar is the quoted accuracy of the neutron measurement.

TFTR (\bullet) [303]. The random error for 28 discharges is shown and is comparable to the quoted accuracy of the neutron measurement. The data are from 1988 and 1989 and the theory is from TRANSP.

TFTR (\circ) [305]. The random error for 118 discharges is shown; the estimated absolute errors are slightly larger. The data are from 1990 supershots and the theory is from the SNAP code.

JET (\square) [65]. The comparison is for a single discharge; the error bar is the quoted accuracy of the neutron calibration.

JET (\blacksquare) [1]. The comparison is for a single discharge; the error bar is the quoted accuracy of the theory.

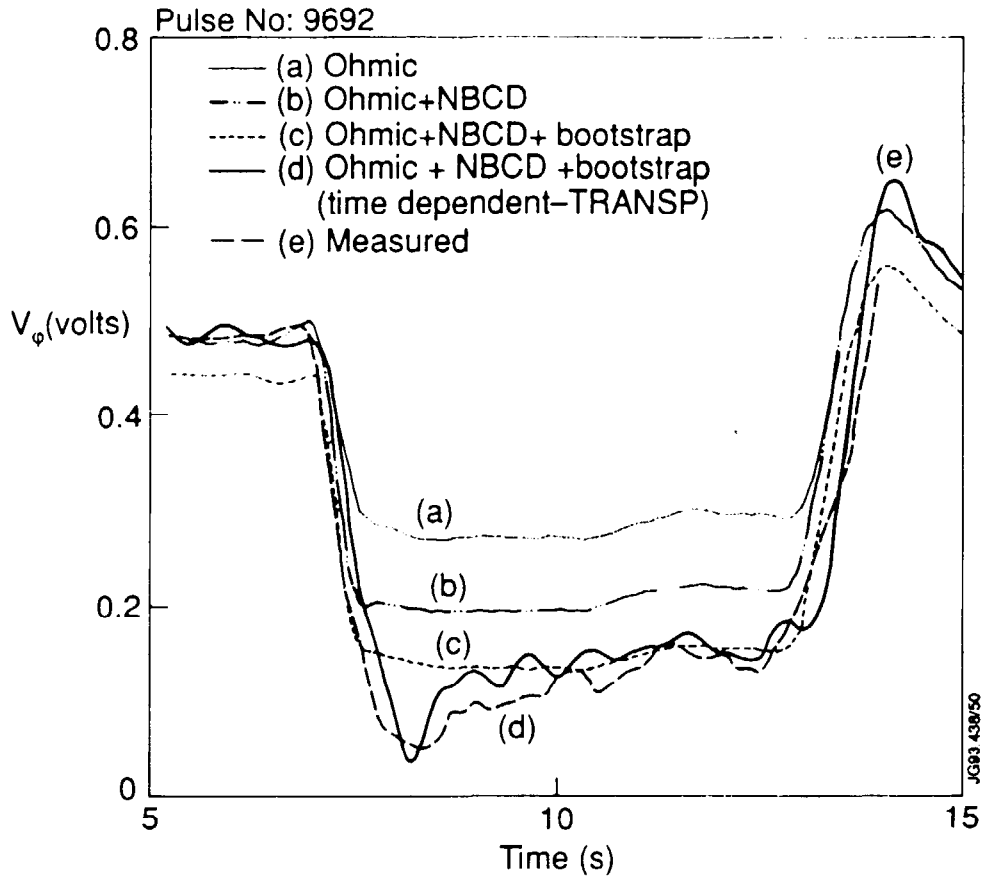


Fig. 41. Time evolution of the surface loop voltage deduced from magnetic measurements (e) and of the calculated evolution during co-injection of 5 MW of deuterium beams into a low density JET plasma from 7-13 s [307]. The observed time evolution agrees with the TRANSP calculation that includes bootstrap, beam-driven, and Ohmic currents (d). Also shown are calculations that assume instantaneous current diffusion for the cases of Ohmic current alone (a), Ohmic and beam-driven currents (b), and Ohmic, beam-driven, and bootstrap currents (c). The uncertainty in the calculated V_l (associated with uncertainties in Z_{eff} and T_e) is approximately 0.07 V.

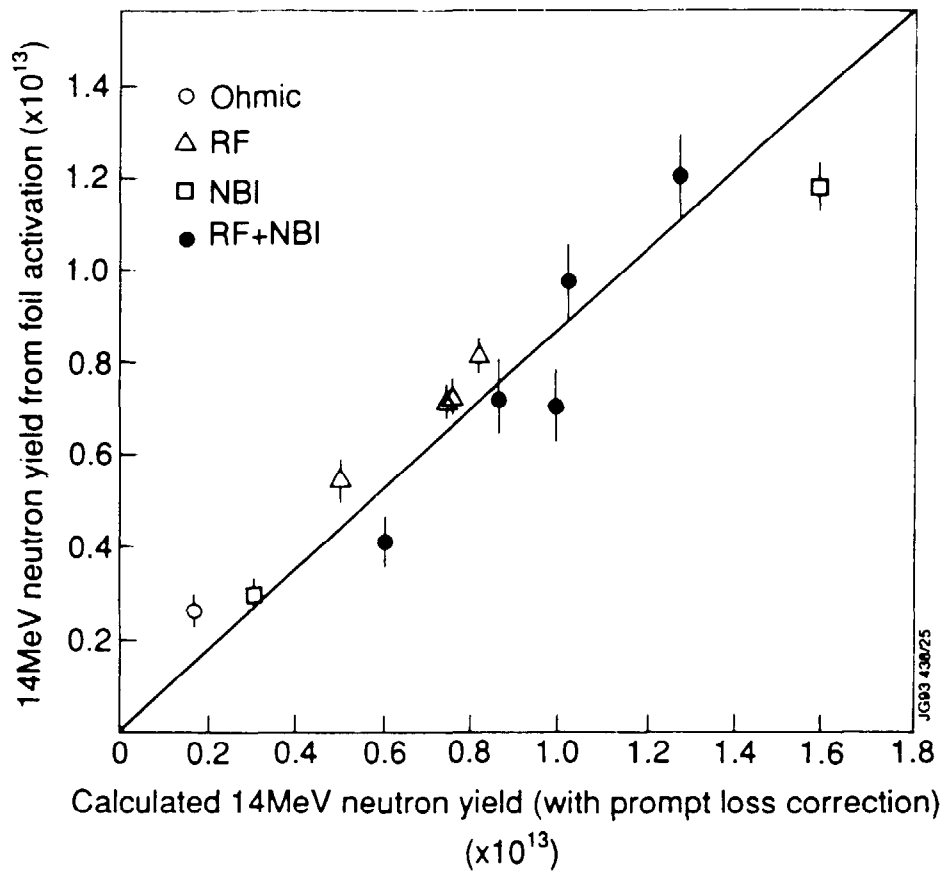


Fig. 42. Measured yield of 14 MeV neutrons from the burnup of 1.0 MeV tritons versus the expected yield in JET discharges with $I_p > 4.5$ MA [210]. The calculations assume classical Coulomb scattering (arbitrarily increased by a factor of 1.2) and no spatial diffusion.

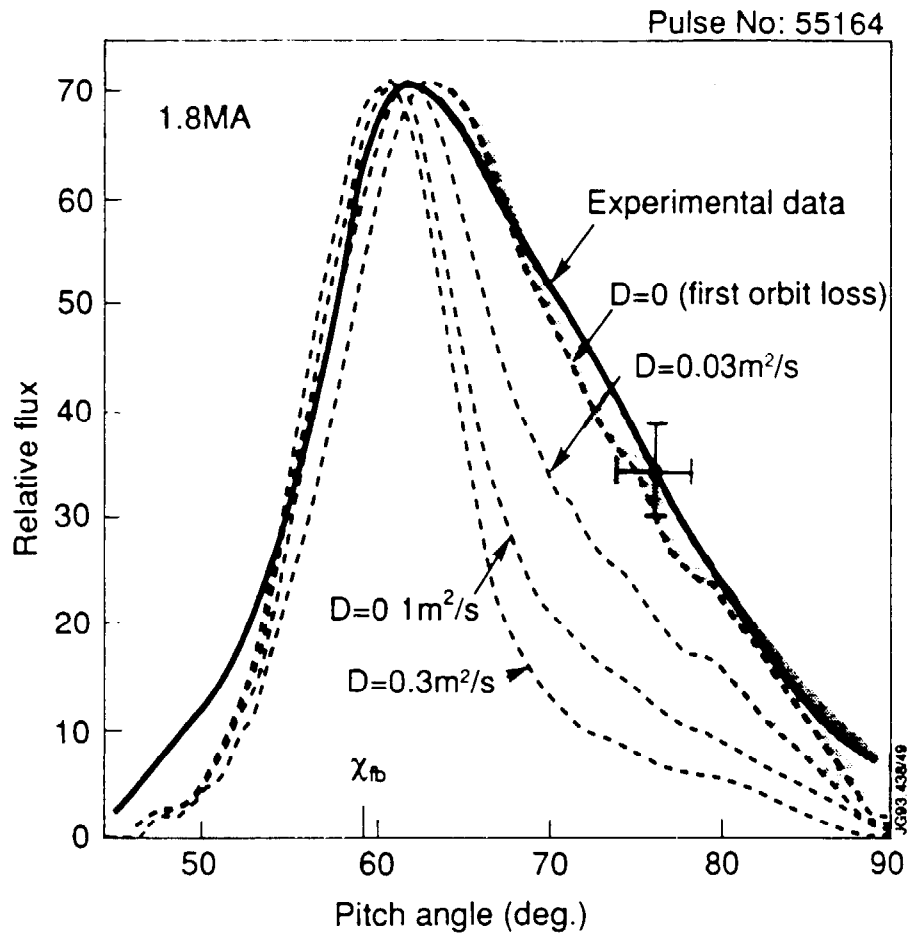


Fig. 43. Flux of 1 MeV tritons and 3 MeV protons to a detector located at the bottom of TFTR as a function of pitch angle in a plasma with $R_0 = 2.6$ m [261]. The flux is normalized to the measured d-d neutron emission. Also shown are the calculated pitch-angle distributions for various assumed values of the diffusion coefficient D . The error bar shows the approximate shot-to-shot variation, and there is an additional systematic uncertainty of $\pm 3\%$ in the measured pitch angle. The shaded area indicates the uncertainty in the $D = 0$ model curve associated with uncertainty in the source profile, and provides an approximate measure of the accuracy of the theory.

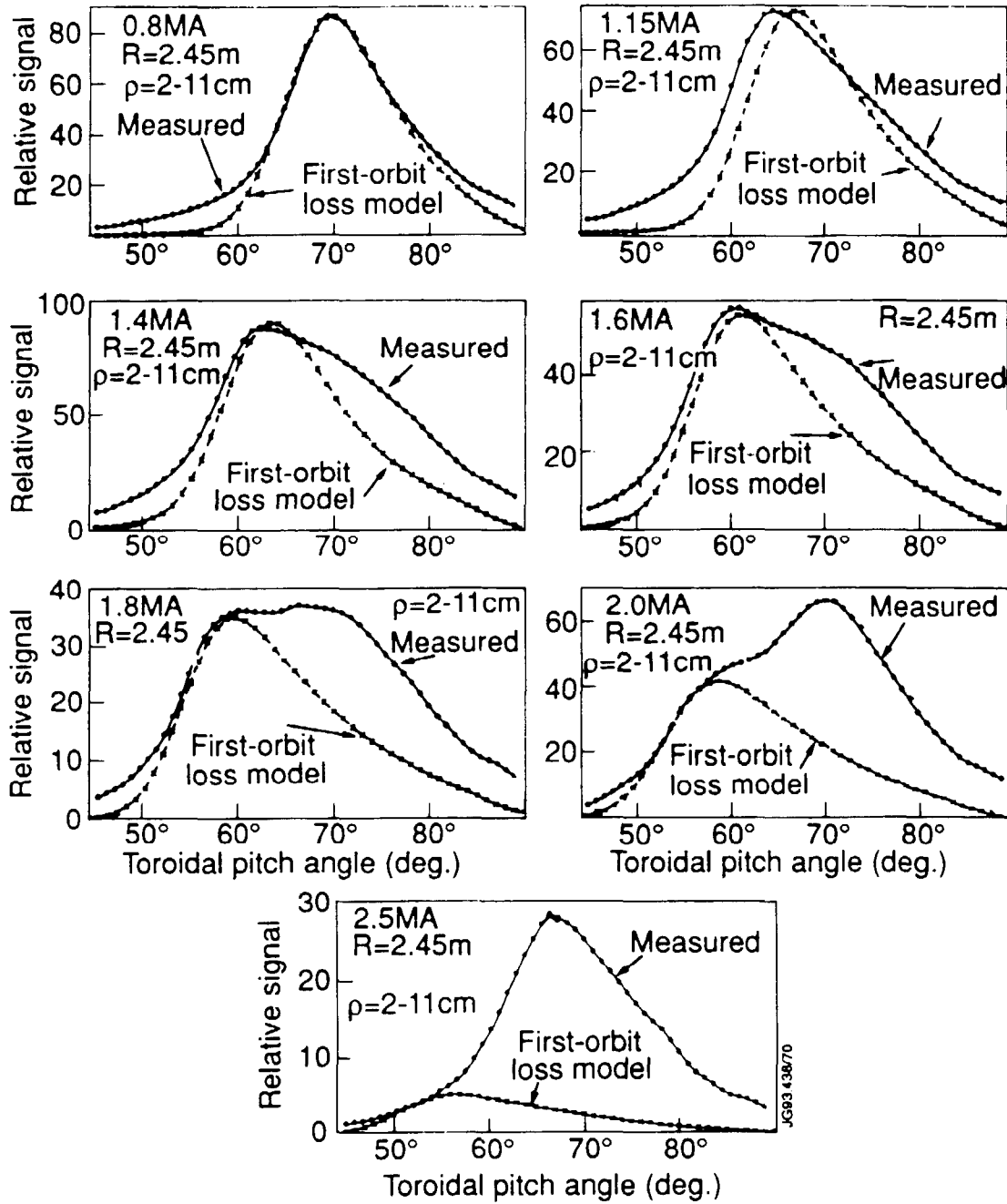


Fig. 44. Flux of 1 MeV tritons and 3 MeV protons to a detector located at the bottom of TFTR as a function of pitch angle in a plasma with $R_0 = 2.45\text{ m}$ [290]. The flux is averaged over the beam pulse and normalized to the neutron emission. An anomalous feature associated with delayed losses of fusion products shifts the distribution from the classical prediction.

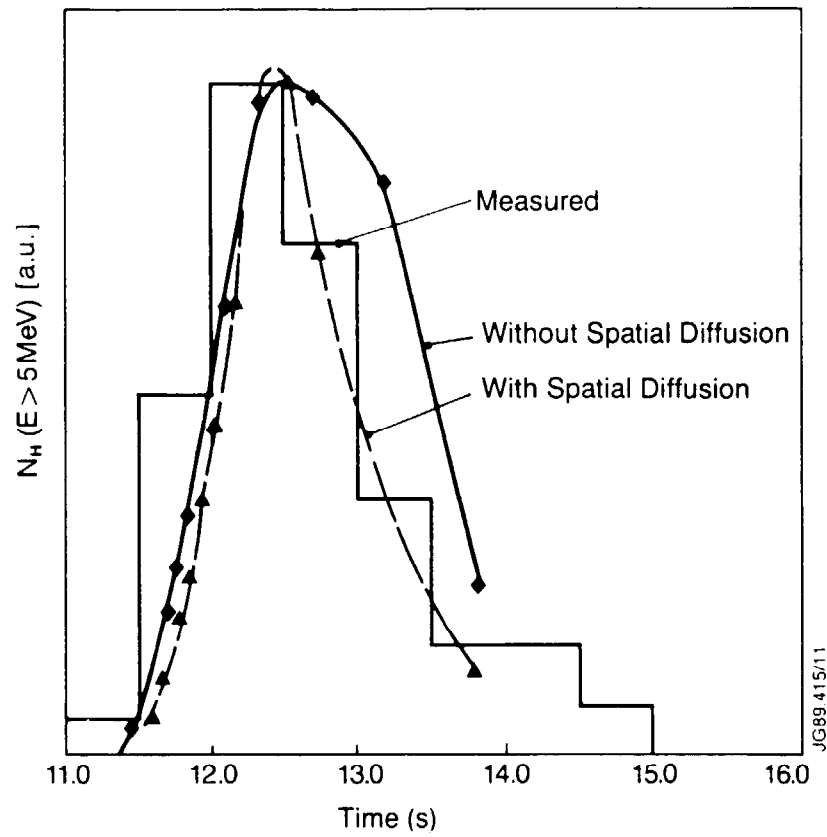


Fig. 45. Intensity of the 4.4 MeV gamma-ray flux as a function of time during combined deuterium neutral-beam injection and hydrogen-minority ICRF heating in JET [65]. The gammas are produced by reactions between protons with energies above ~ 5 MeV and carbon impurity ions. Also shown is the expected time evolution of the number of energetic protons with and without rf-induced spatial diffusion, as calculated by the time dependent rf diffusion code BACCHUS-DIFUS [432].

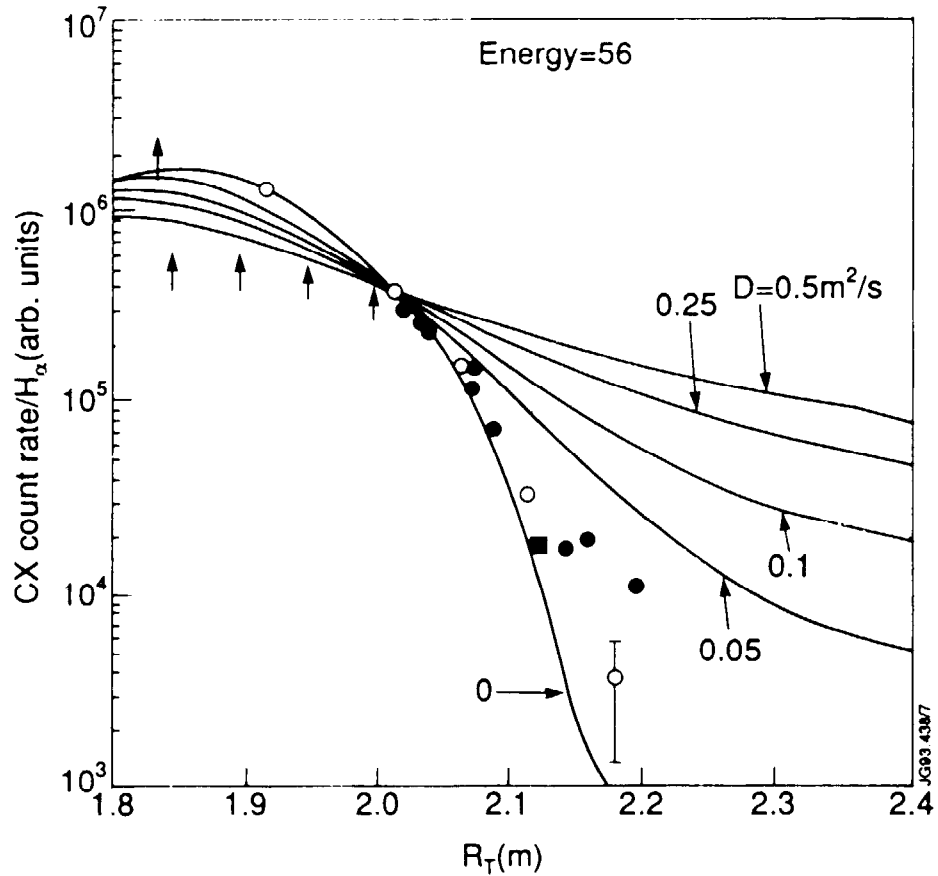


Fig. 46. Passive flux of 56 keV neutrals as a function of the tangency radius of the analyzer sightline during co-injection of an annulus ($R_{tan} = 2.84$ m) of 95 keV neutrals into TFTR ($R_0 = 2.35$ m) [297]. The line of sight of the analyzer was changed on a shot-to-shot basis and the flux has been normalized to the H_α light measured near the inside of the annulus. For both data and simulations, the contribution to the signal from pitch-angle scattered ions from $R > 2.4$ m has been subtracted. The simulations are from a Fokker-Planck calculation that includes an *ad hoc* diffusion term. The data and all simulations are normalized to equality at $R_{tan} = 2.05$ m. The up arrows indicate measurements near detector saturation and are a lower bound on the actual value; the open and closed signals indicate measurements made with two different analyzers.

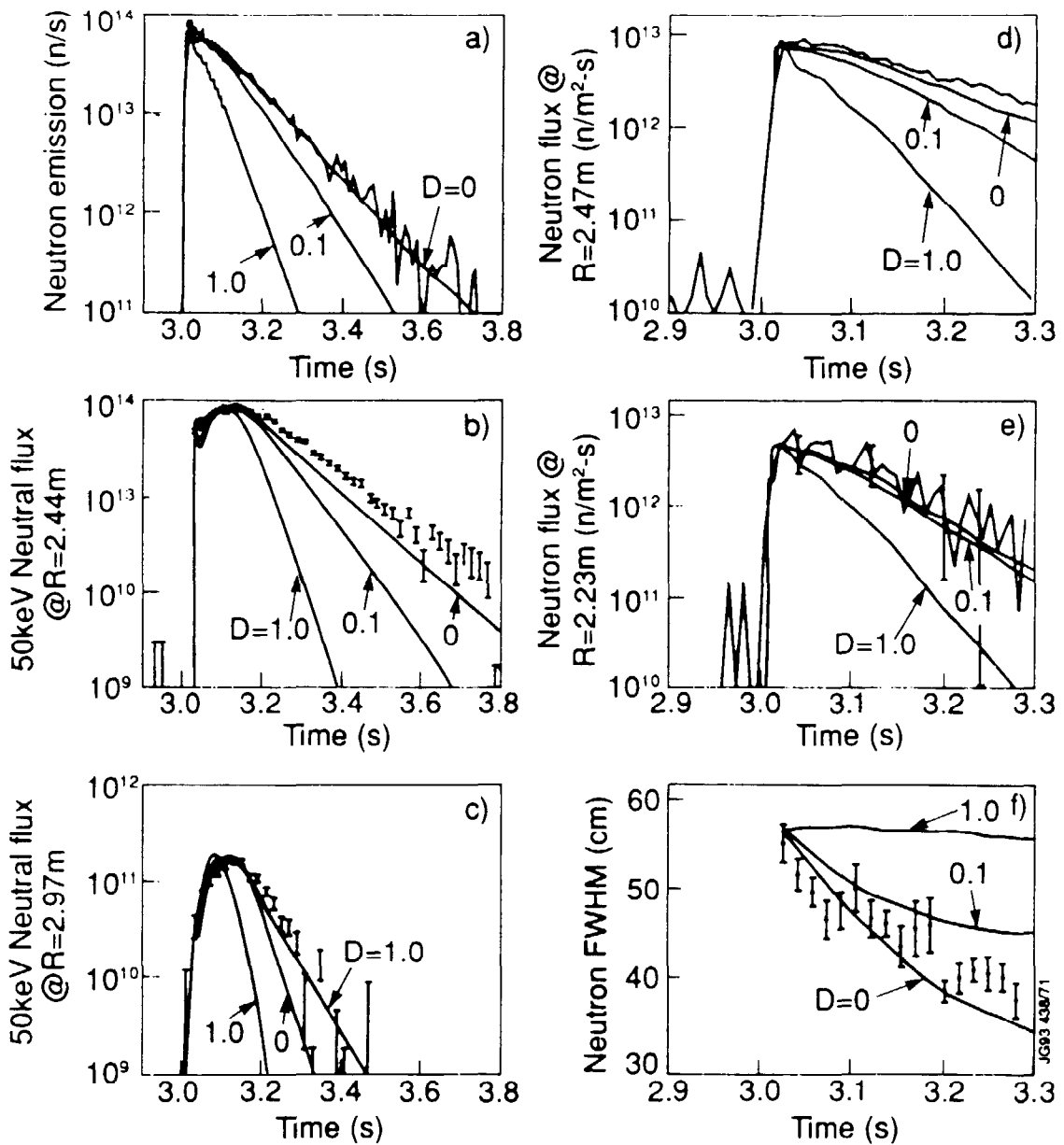


Fig. 47. Time evolution of the neutron and charge-exchange signals following a 20 ms beam pulse of ~ 90 keV deuterons at 3.0 s in TFTR [208]. Also shown are theoretical predictions for various values of diffusion D . (a) Total neutron source strength. (b) On-axis 50 keV passive neutral flux. (c) Off-axis 50 keV neutral flux. (d) Central neutron flux measured by a collimated detector. (e) Off-axis neutron flux. (f) Full width at half-maximum of a Gaussian fit to the neutron profile.

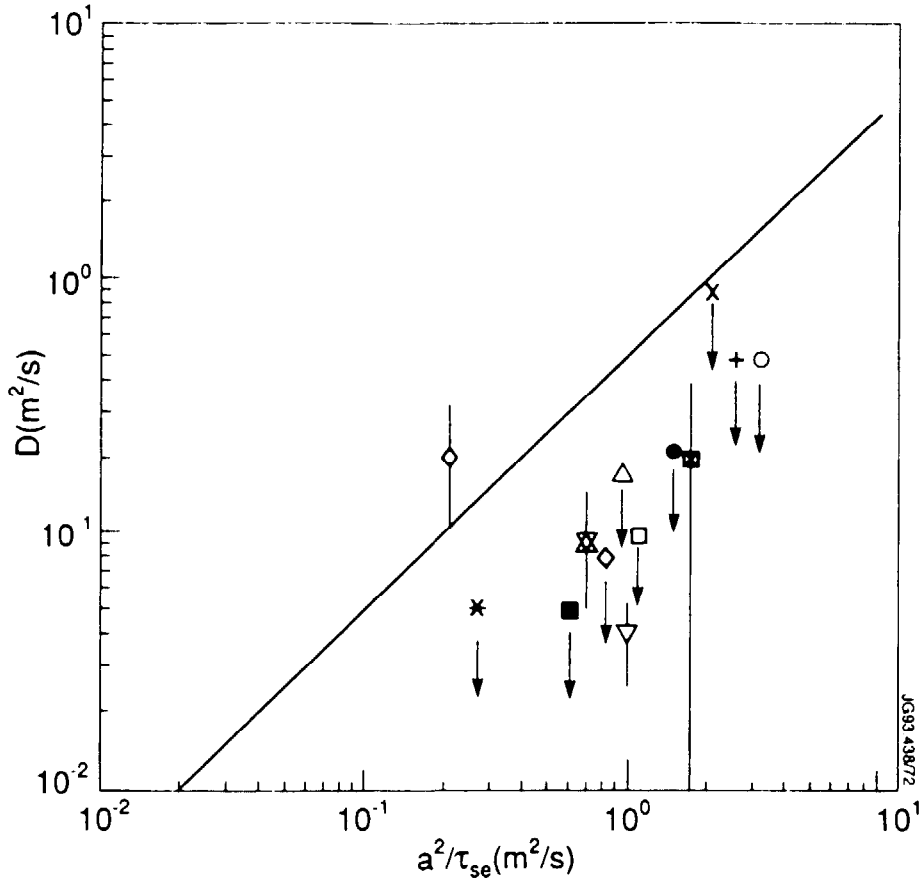


Fig. 48. Reported values of the effective fast-ion diffusion coefficient D plotted versus approximate values of a^2/τ_{se} . [a is the minor radius and τ_{se} is the slowing-down time on electrons (Eq. 10).] Downward-directed arrows indicate that the reported value is an upper bound on the effective diffusion. Appreciable global losses occur for $D \gtrsim a^2/2\tau_{se}$ (diagonal line).

- Isotropic ~ 45 keV deuterium beam ions in PLT deduced from the absolute value of the $d(d,n)^3\text{He}$ emission [203].
- + Trapped ^3He minority tail ions (~ 400 keV) in PLT deduced from 15 MeV proton measurements of the energy of the tail (assuming that the energy gained per pass of the resonance layer is described by the Stix theory) [66].
- Co-circulating ~ 95 keV deuterium beam ions in the outer region ($r > 0.35$ m) of TFTR inferred from passive charge exchange measurements of the spreading of a tangential beam injected off axis [297,231].
- × Isotropic 0.8 MeV ^3He ions in TFTR inferred from the radial profile of the 15 MeV proton emission [209].
- ◇ Isotropic 1.0 MeV tritons in JET inferred from the time evolution of the 14 MeV neutron signal (upper value) in discharges with $\tau_{se} > 2$ s [213,71,329]. The lower value is inferred from the profile of the 14 MeV neutron emission [329,326].
- ☆ Isotropic 1.0 MeV tritons in TFTR inferred from the absolute value of the 14 MeV neutron emission [323].

- ⊗ Isotropic 1.0 MeV tritons in JT-60U inferred from the absolute value of the 14 MeV neutron emission [212].
- △ Trapped proton minority tail ions ($T_{\perp} \sim 5$ MeV) in JET deduced from comparison of the measured perpendicular stored energy with a modified Stix model [124].
- Central counter-passing 3 MeV protons and 1 MeV tritons in TFTR inferred from the time evolution, pitch-angle distribution, gyroradius distribution, and current dependence of edge losses [261].
- * Circulating ~ 95 keV deuterium beam ions in TFTR inferred from the time evolution of neutron and passive charge-exchange signals following a 20 ms beam pulse [208].
- ▽ Trapped ~ 100 keV proton minority tail ions deduced from a scan of the resonance layer past the sightline of a vertically-viewing passive charge-exchange detector in TFTR [121]. The analysis assumes that the proton tail is accelerated in the resonance layer.

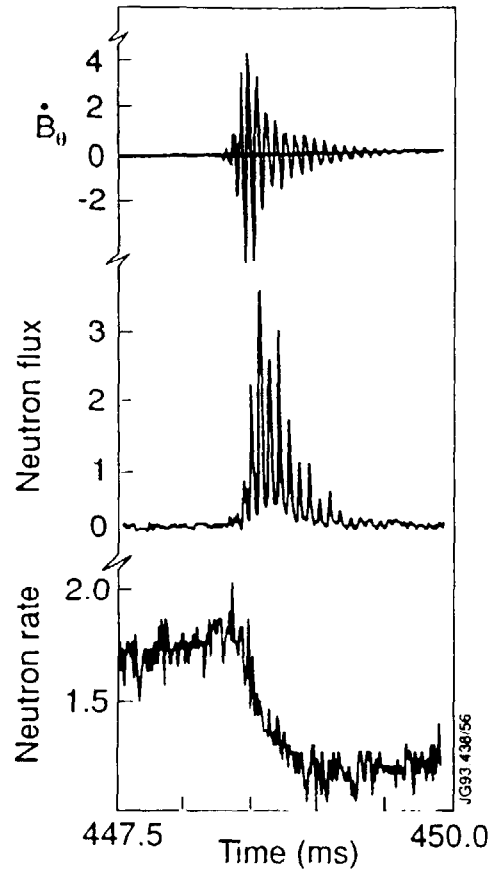


Fig. 49. Signals from a Mirnov coil positioned at the outer midplane, a perpendicular-viewing passive charge-exchange detector tuned to measure ions just below the injection energy, and a $d(d,n)^3\text{He}$ neutron detector during a fishbone instability in PDX [361]. (The units are arbitrary for all three signals.) To excite the instability, perpendicular deuterium beams (~ 45 keV) were injected into a high beta plasma. The large reduction in neutron yield implies that approximately 40% of the beam ions were lost during the burst.

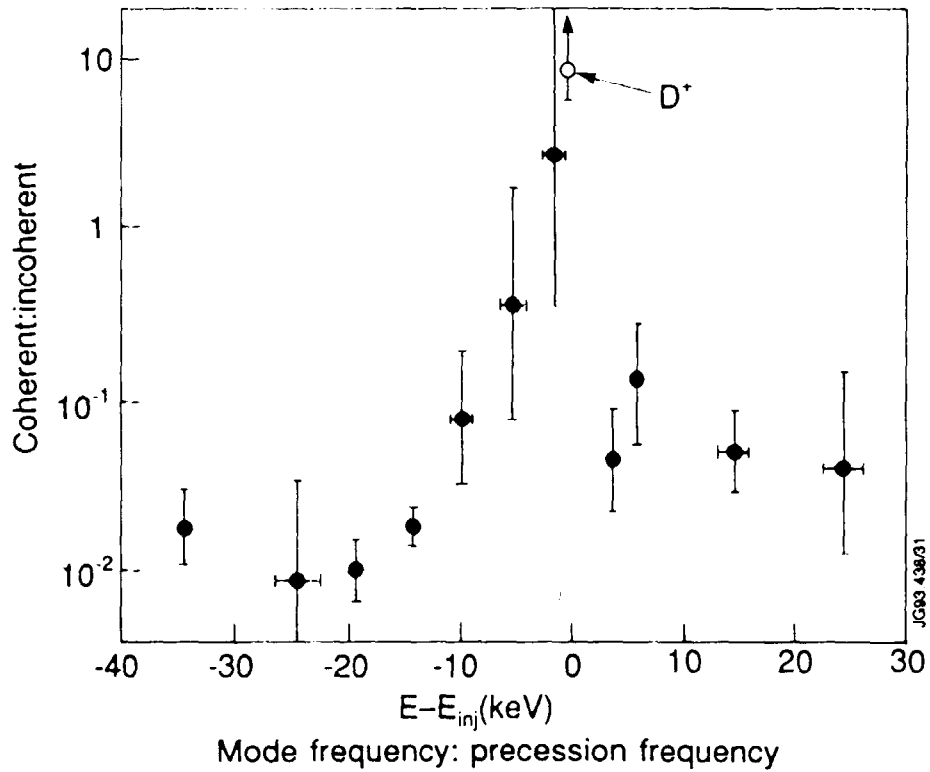


Fig. 50. Modulation of the charge-exchange signal as a function of energy during fishbone bursts in PDX. The data are from a vertically-viewing analyzer that detects trapped particles from the large major radius edge of the plasma [337,338]; E is the analyzer energy and E_{inj} is the beam injection energy (typically 45 keV). The ordinate is the ratio of the flux that is modulated at the fishbone frequency to the unmodulated flux (background subtracted). The error bars indicate the standard deviation of many large fishbone bursts. The open circle represents data from a silicon diode mounted at the top of PDX [343]; this detector integrates over energy.

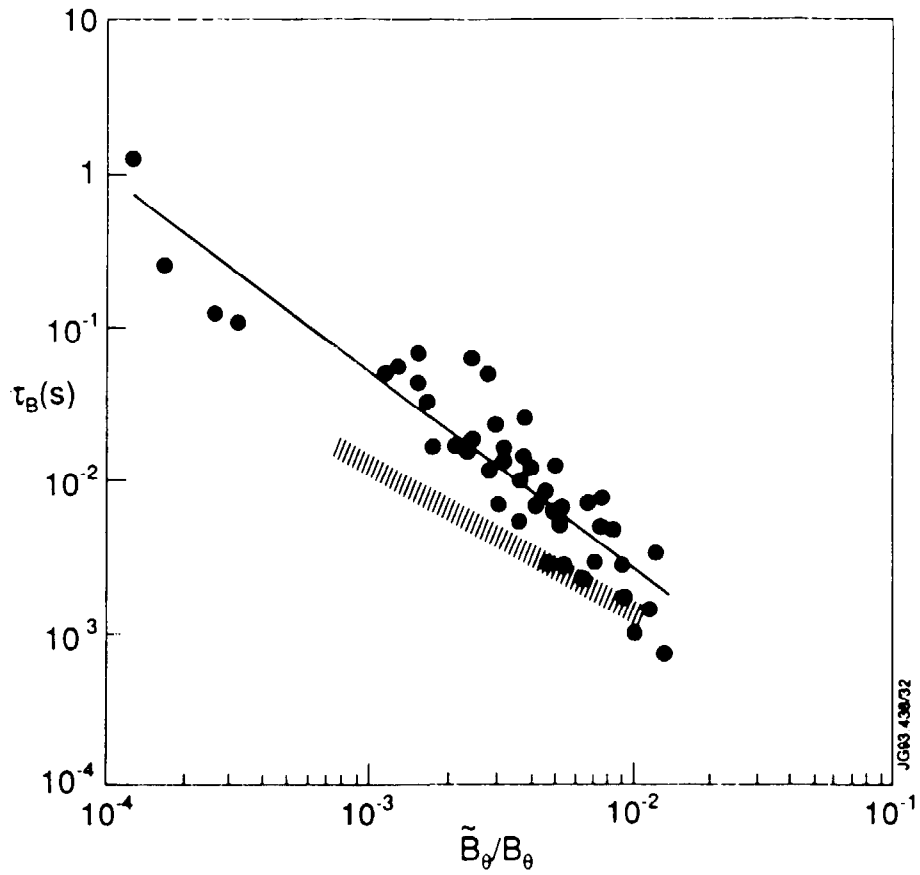


Fig. 51. Effect of fishbone instabilities upon the slope of the neutron emission in PDX [302]. The ordinate is the minimum value of the “energetic ion confinement time”, $\tau_B \simeq S/\dot{S}$ (S is the neutron emission rate) and the abscissa is the maximum amplitude of the magnetic perturbation $\tilde{B}_\theta/B_\theta$ measured by a Mirnov coil at the outer midplane. The hatched region shows the instantaneous values of τ_B as a function of mode amplitude for a single large event. A fit to the data (solid line) indicates $\tau_B \propto (\tilde{B}_\theta/B_\theta)^{-1.36 \pm 0.07}$.

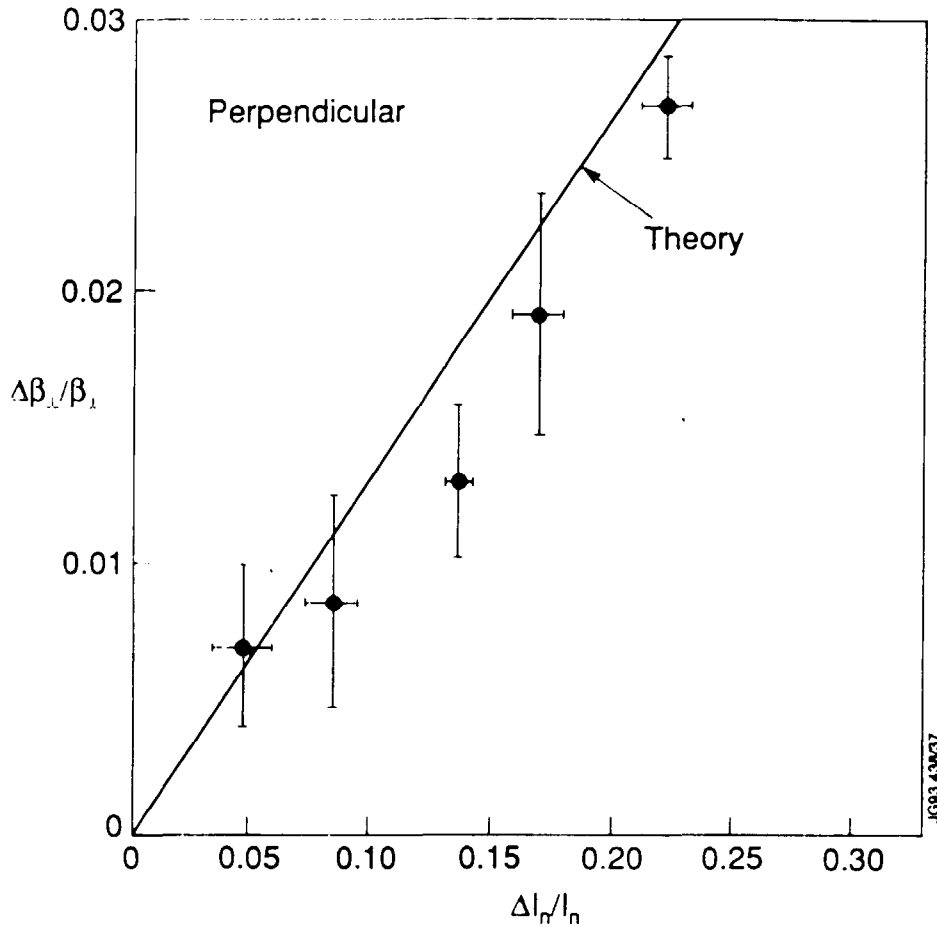


Fig. 52. Fractional reduction in perpendicular beta $\Delta\beta_{\perp}/\beta_{\perp}$ inferred from diamagnetic loop measurements versus fractional reduction in the number of beam ions $\Delta I_n/I_n$ inferred from the neutron emission during fishbone bursts in PBX [344]. Perpendicular $D^0 \rightarrow D^+$ injection (~ 45 keV) was employed. The solid line shows the expected change in β_{\perp} (calculated assuming that the reduction in neutron emission is due to the loss of beam ions with energies between 35-45 keV). The error bars represent the standard deviation of many bursts. The measurements imply that virtually all of the measured drop in β_{\perp} is caused by the loss of beam ions.

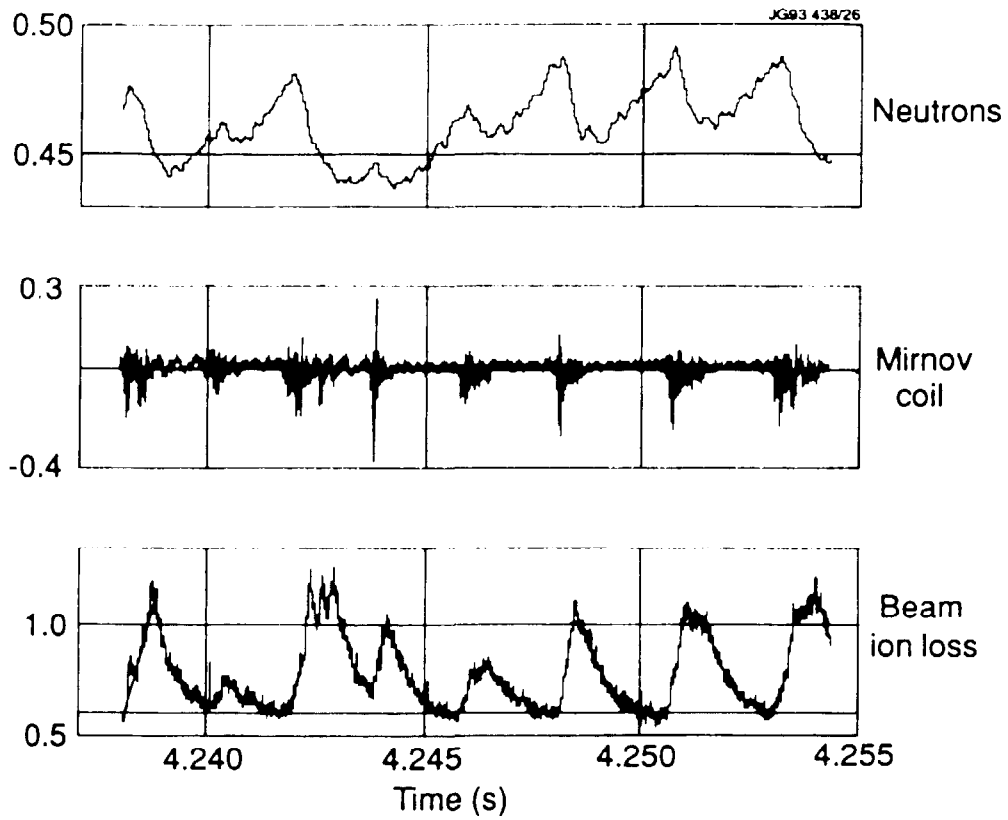


Fig. 53. Signals from a 2.5 MeV neutron detector, a Mirnov coil positioned near the outer midplane, and a scintillator mounted inside the vacuum vessel just below the midplane during tangential injection of ~ 95 keV deuterium beams into TFTR [355]. The magnetic activity detected by the Mirnov coil is in the range 25-50 kHz, somewhat below the expected frequency of TAE modes (Sec. 5.2) for these conditions.

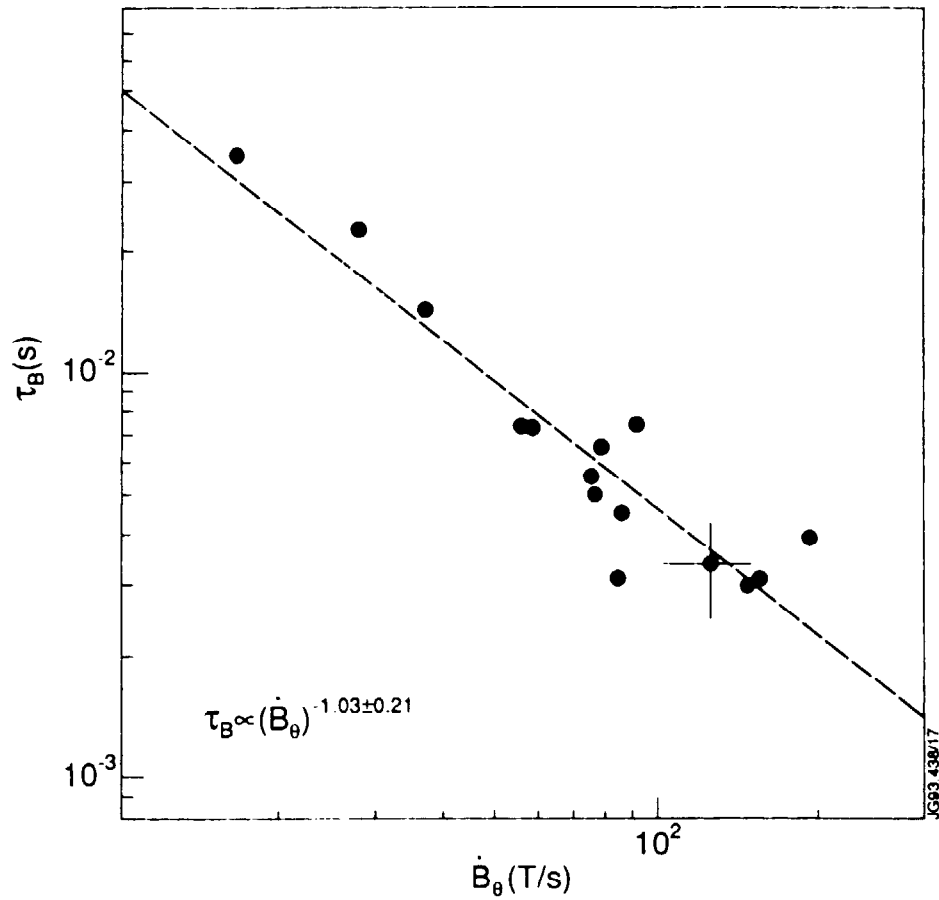


Fig. 54. Effect of a single circulation-frequency instability on the slope of the neutron emission in DIII-D [359]. The ordinate is the instantaneous value of the “energetic ion confinement time”, $\tau_c \simeq S/\dot{S}$ and the abscissa is the instantaneous magnetic perturbation amplitude measured by a Mirnov coil positioned in the outer midplane (normalized to the toroidal field).

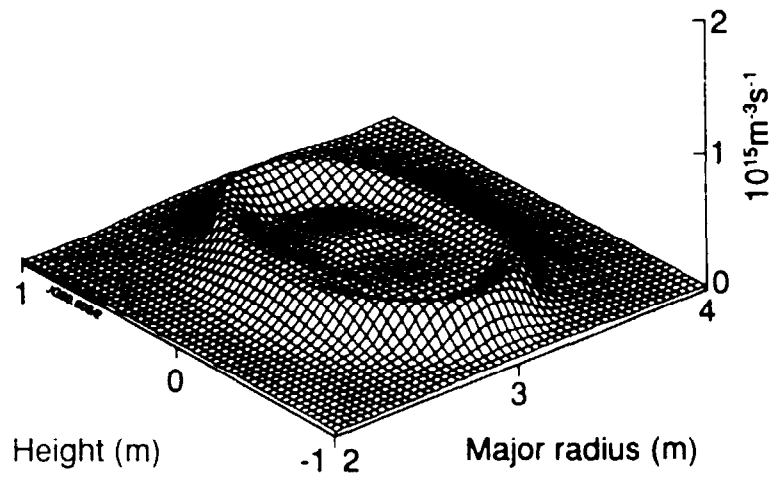
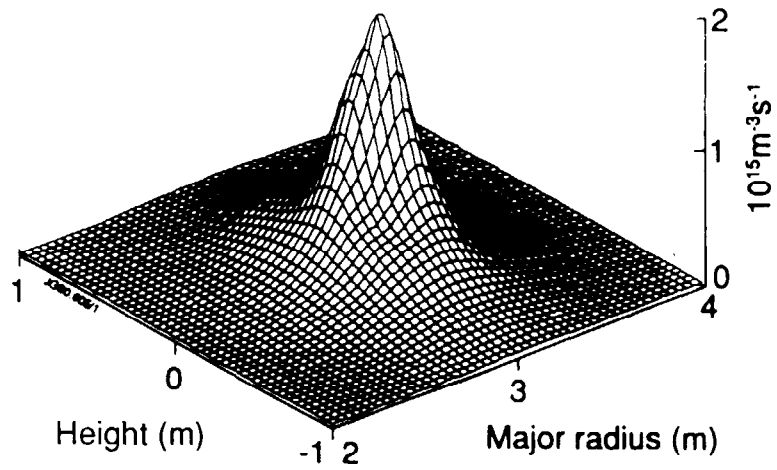


Fig. 55. Neutron emissivity profile just before and just after a sawtooth during deuterium beam injection into JET [363]. The profiles are reconstructed from data obtained by two neutron collimator arrays. The sawtooth caused the total neutron emission to drop by $\sim 1/6$.

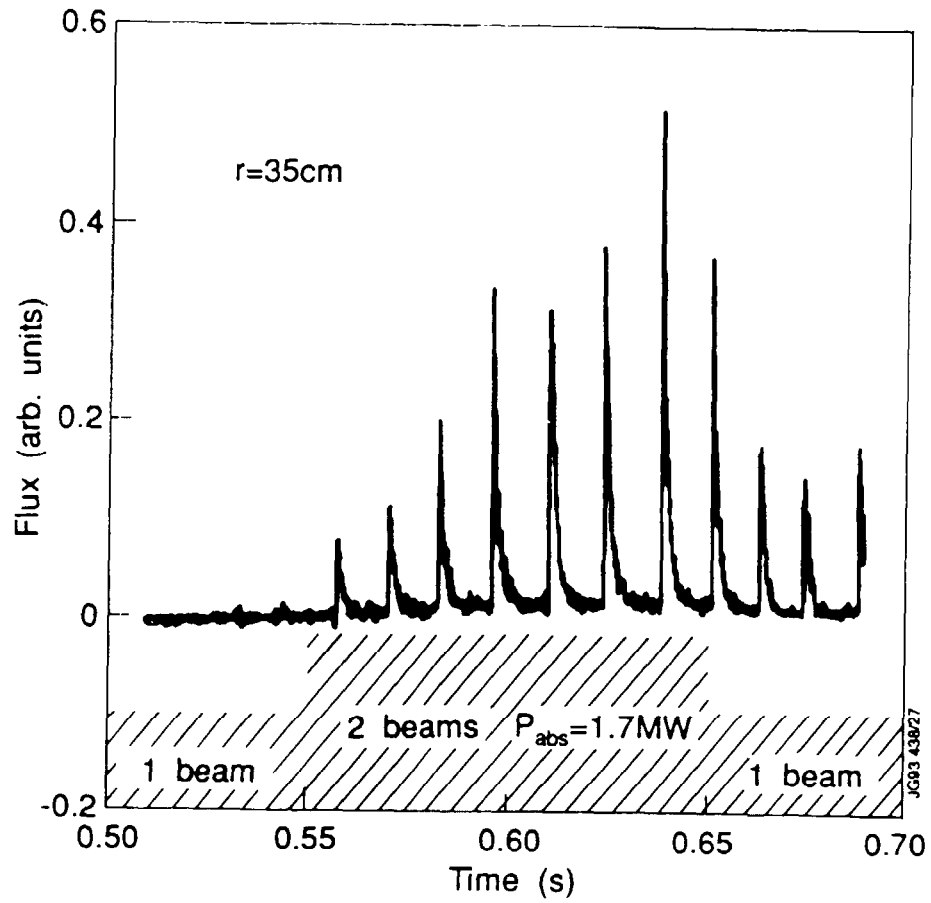


Fig. 56. Active 4.2 keV hydrogen flux from the outside of the plasma ($r = 35 \text{ cm}$, $a = 44 \text{ cm}$) during deuterium neutral beam injection into a hydrogen plasma in PDX [252]. The bursts coincide with sawtooth crashes. $T_i \simeq 2 \text{ keV}$.

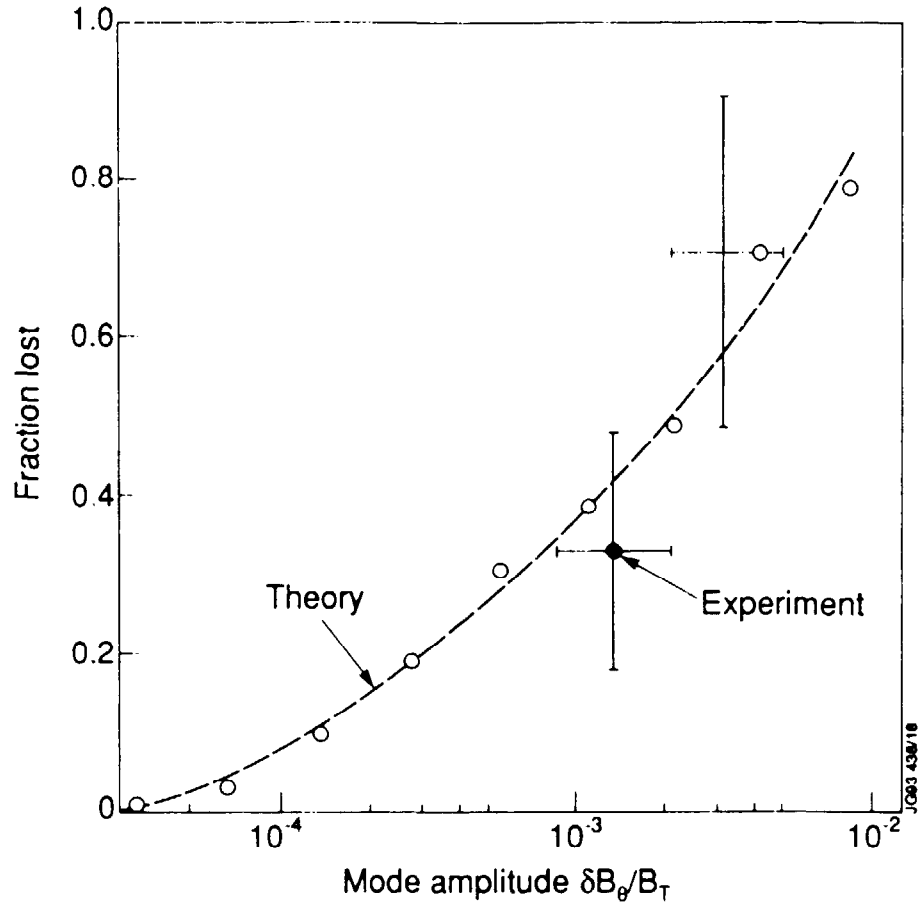


Fig. 57. Fractional loss of 0.8 MeV ^3He ions during fishbone bursts with $n = 1$, $m = 1$ mode amplitudes $\delta B_\theta / B_T$ in PDX [369]. The open points are the results of Hamiltonian Monte Carlo simulations; the curve is a fit to the calculated points. The solid points represent the ^3He losses deduced under the assumption that the measured reduction in ^3He burnup is due to fishbone losses of ^3He ions. The vertical error bars represent the uncertainty in relating the burnup reduction to the losses per fishbone and the horizontal error bars represent uncertainty in the mode amplitude in the plasma.

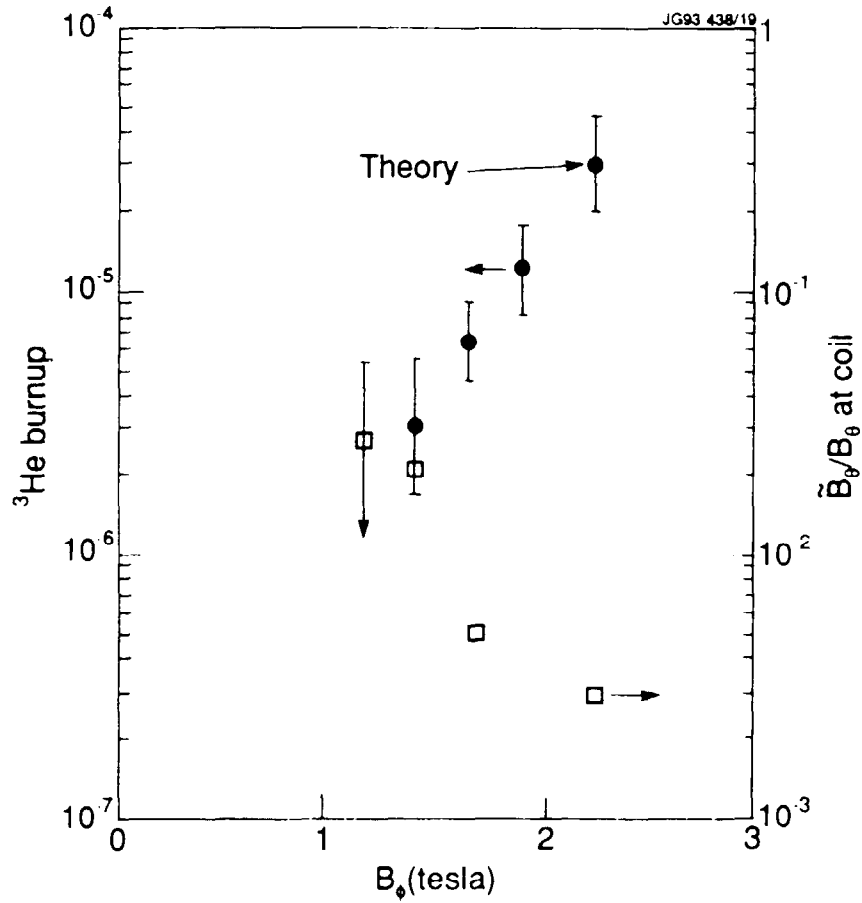


Fig. 58. ^3He burnup versus toroidal field during $\text{D}^0 \rightarrow \text{H}^+$ beam injection into PDX [20]. At 1.1 T, the burnup was below the detectable level of 5×10^{-6} . With the exception of the discharges at 1.1 T, the beam power, electron density, plasma current, and electron temperature were approximately constant throughout the scan. The line represents the classically predicted toroidal field dependence, normalized to the 2.2 T data point. The magnetic field fluctuations \tilde{B}_θ had an $m = 2$, $n = 1$ mode structure.

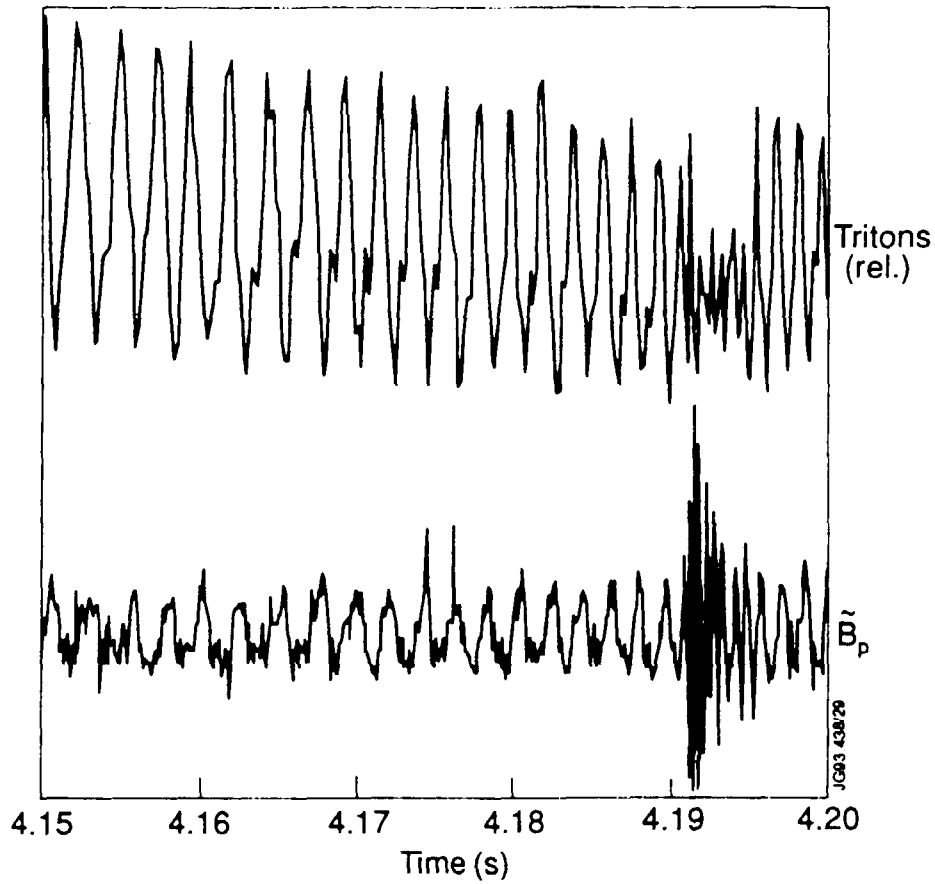


Fig. 59. Signals from a scintillator mounted at the bottom of the TFTR vacuum vessel and from a Mirnov coil (arbitrary units) during $m = 2$ activity [260]. The scintillator measures 1 MeV tritons and 3 MeV protons on orbits that pass near the trapped/passing boundary.

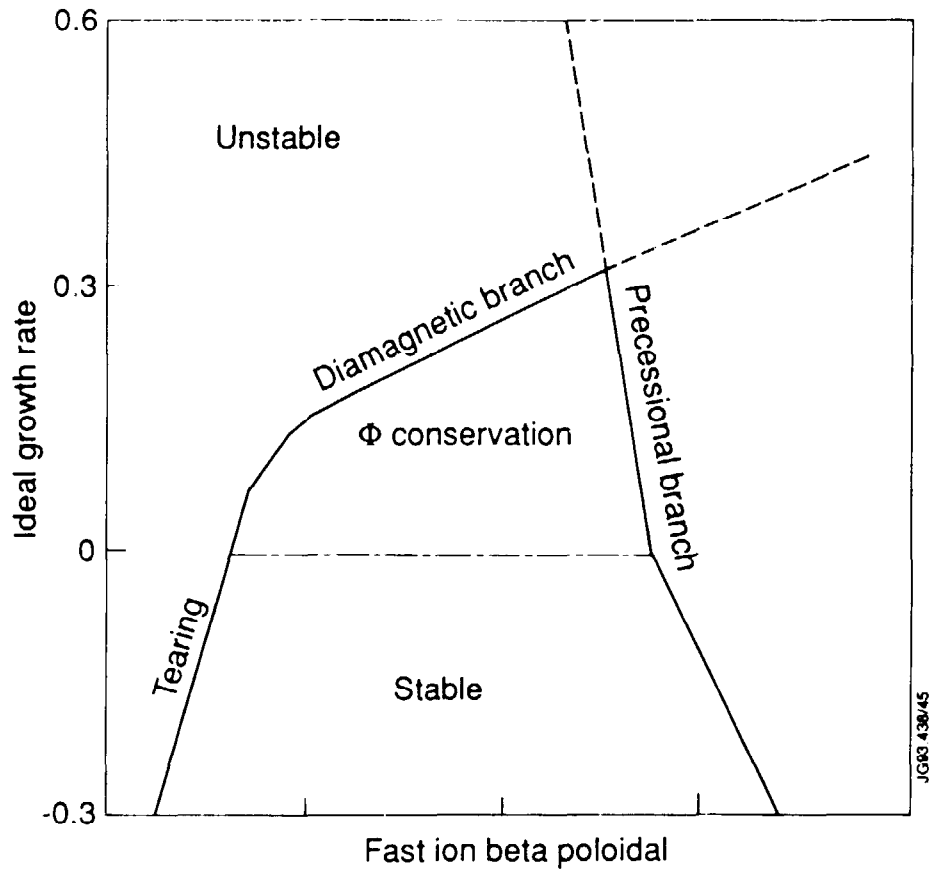


Fig. 60. Schematic stability diagram for the $n = 1$, $m = 1$ internal kink. The ideal MHD growth rate γ_I (normalized to the Alfvén frequency) is plotted along the ordinate and the β_p of the trapped fast ions within the $q = 1$ surface is plotted on the abscissa. Near the origin, resistive effects are important. For modest values of the fast-ion pressure, the adiabatic response of the fast ions can stabilize $m = 1$ oscillations even if $\gamma_I > 0$. The stable region is bounded by the two branches of the fishbone instability, the ω_{*i} branch (associated with resonances between the fast ions and the bulk ions) and the ω_{pre} branch (associated with the resonance between the precessional drift motion of the fast ions and the mode).

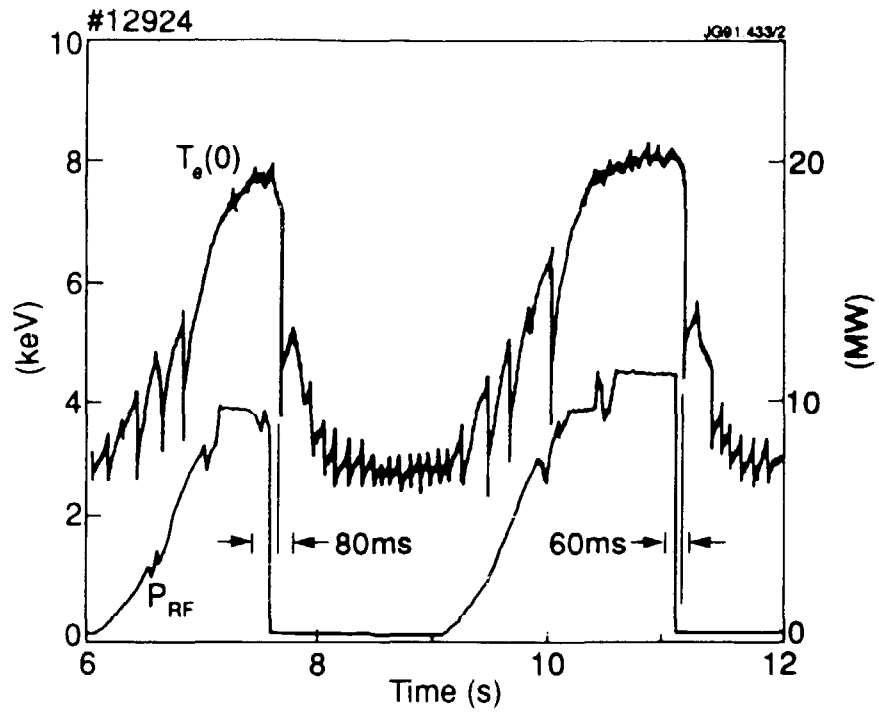


Fig. 61. Sawtooth stabilization during ICRF heating of JET [5]. As the rf power is increased, the amplitude and period of the sawteeth increase leading to full stabilization at ~ 7.0 and 10.0 s. After the rf power is turned off, a “monster” sawtooth crash occurs 80 and 60 ms later.

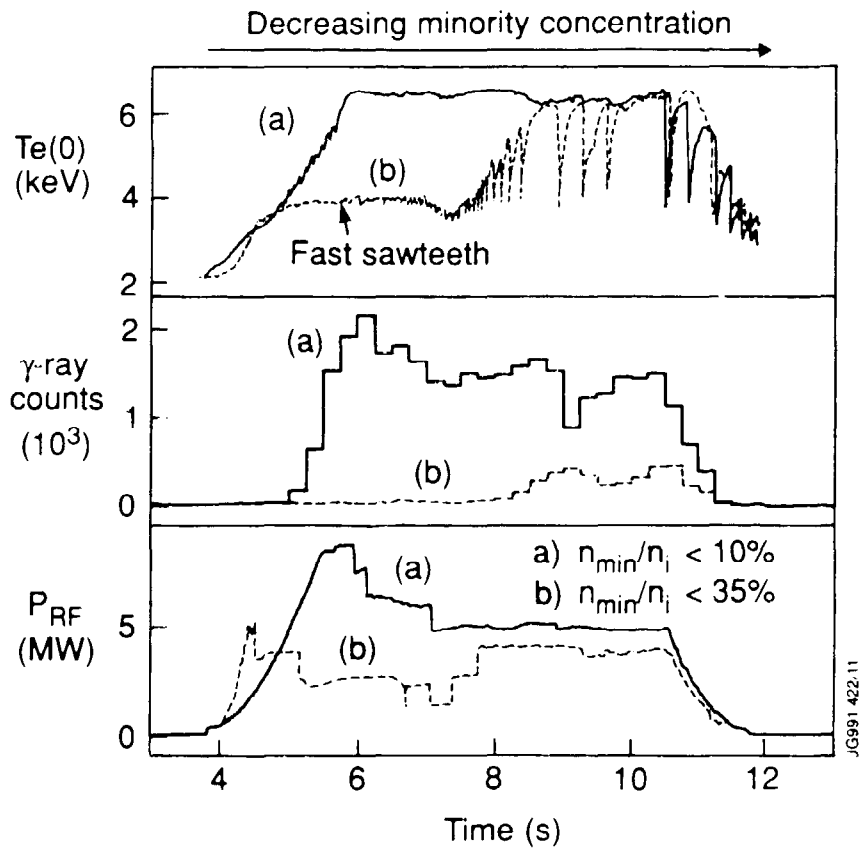


Fig. 62. Time evolution of the electron temperature, the $^{12}\text{C}(^3\text{He},\gamma)$ emission, and the ICRF power during ^3He minority heating in JET [5]. The discharge with low minority concentration (a) had better rf coupling and a more intense gamma ray emission than the discharge with high concentration (b). In both cases, the ^3He concentration probably decreased throughout the discharge. The sawtooth stabilization (T_e trace) correlates with the presence of an intense, energetic minority population (γ trace).

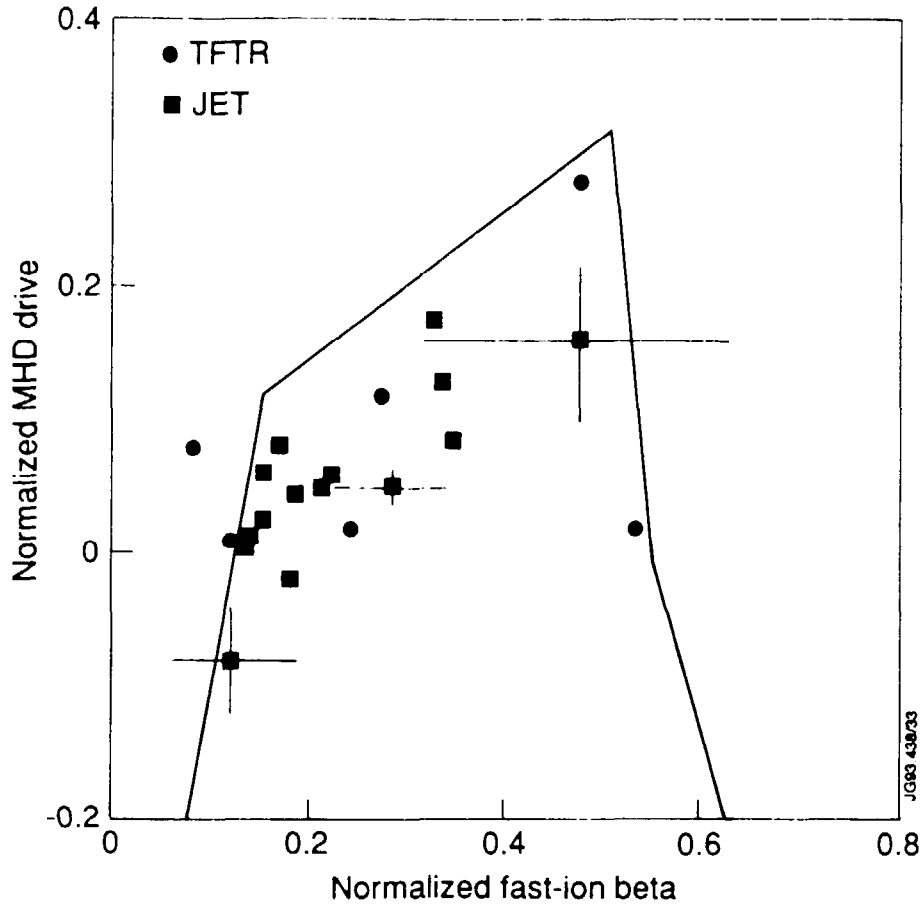


Fig. 63. Conditions for stabilization of sawteeth during minority ICRF heating in TFTR [381] and JET [383]. The ordinate represents γ_I/ω_{pre} and the abscissa represents $r_1 v_A \langle \beta_{ph} \rangle_u / (\sqrt{3} s R^2 \omega_{pre})$, where $\langle \beta_{ph} \rangle_u$ is the poloidal beta of the trapped fast ions within the $q = 1$ surface, s is the shear at the $q = 1$ surface, and R is the major radius. The theoretical curve is a qualitative sketch of the expected stability boundary [383]. Errors for the TFTR data were not quoted but presumably are comparable to the JET error bars.

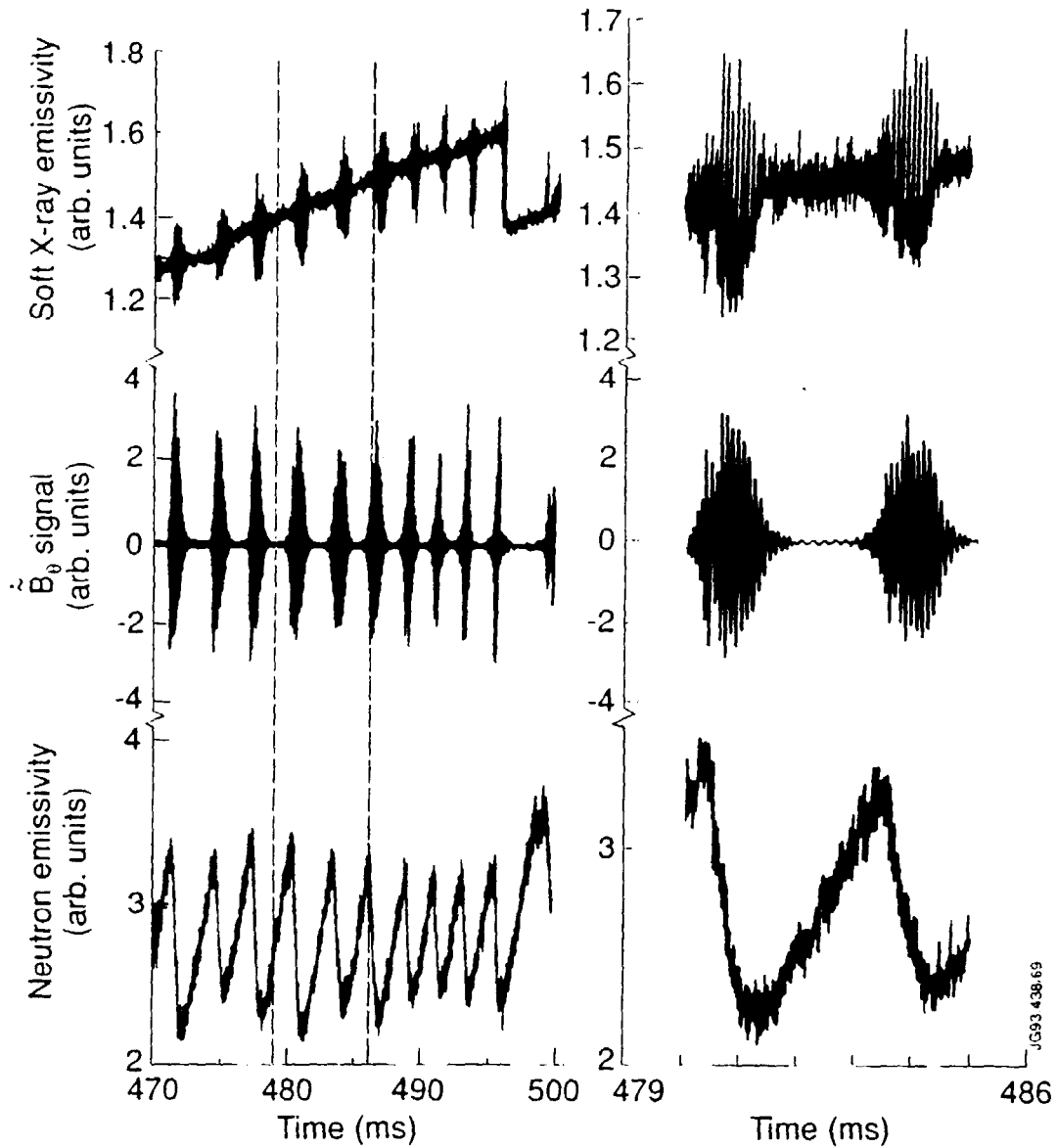


Fig. 64. Strong fishbone bursts as observed during perpendicular deuterium injection into PDX [377]. The bursts on the central soft x-ray channel and Mirnov coil signal are caused by fishbones. Each burst correlates with a reduction in the 2.5 MeV neutron emission (which is primarily due to beam-plasma interactions for these conditions). The event at 496 ms includes a sawtooth crash.

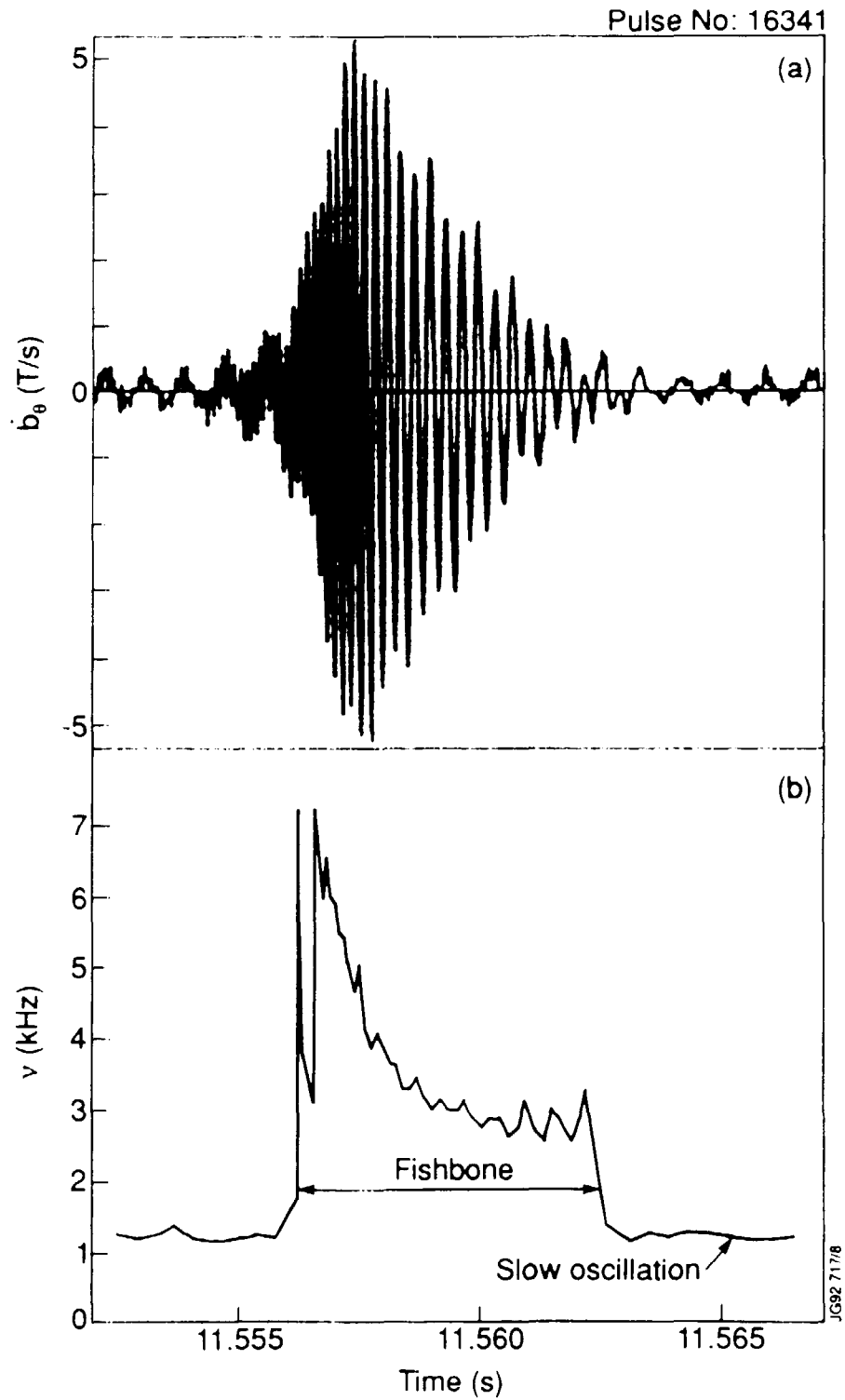


Fig. 65. Raw magnetic signal (a) and oscillation frequency (b) for a fishbone burst during combined neutral beam and ICRF heating in JET [349]. The signal is from an $n = 1$ coil combination measured 45° above the outer midplane. The frequency of the slow oscillation is comparable to the rotation frequency of the bulk plasma.

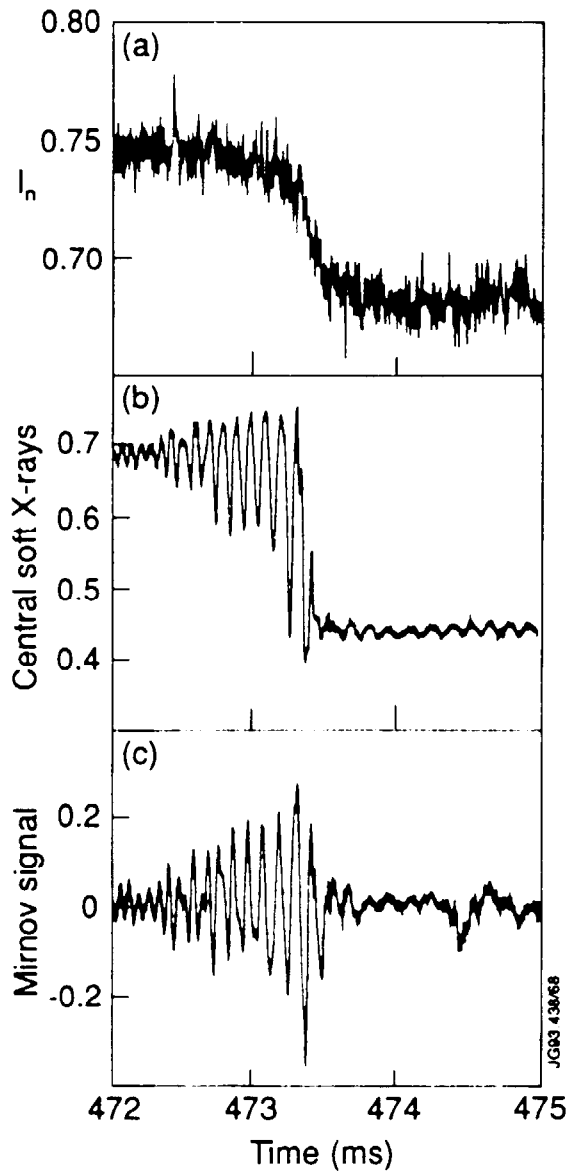


Fig. 66. Neutron emission, central soft x-ray signal, and \dot{B}_0 signal at a sawbone during deuterium injection into PDX [302]. The 2.5 MeV neutron signal is dominated by neutrons from beam-plasma reactions and the Mirnov signal is from a coil located in the outer midplane.

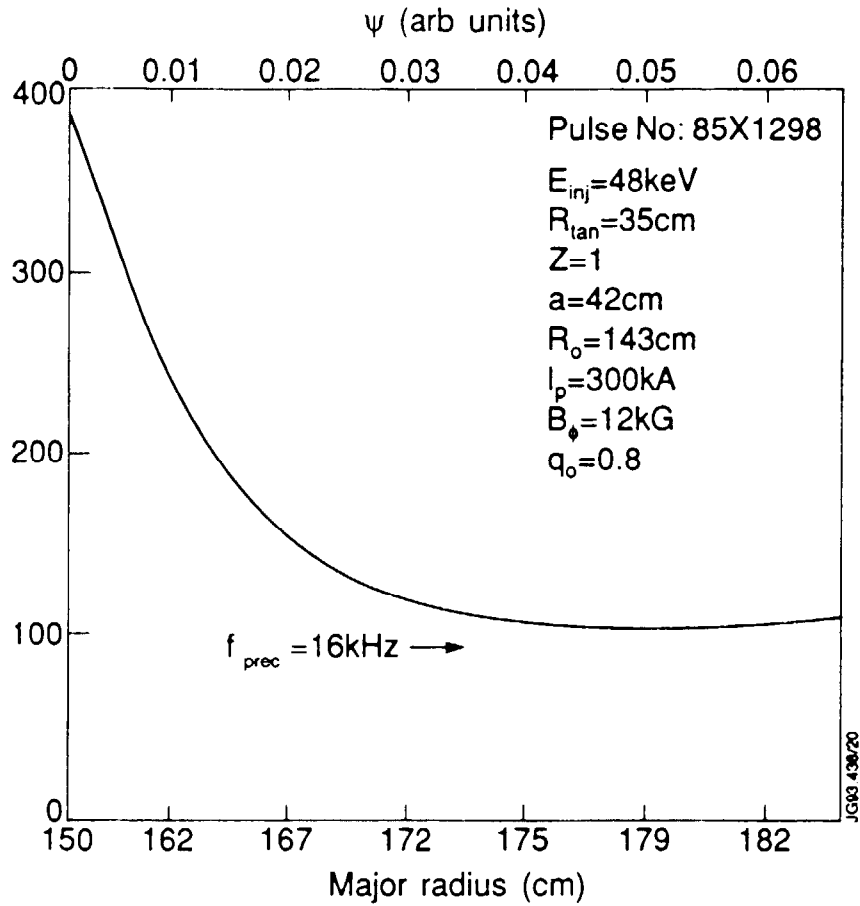


Fig. 67. Calculated toroidal precession frequency versus major radius for perpendicular deuterium beam injection into PDX [342]. The observed fishbone frequency of approximately 16 kHz coincides with the precession frequency in the outer part of the plasma.

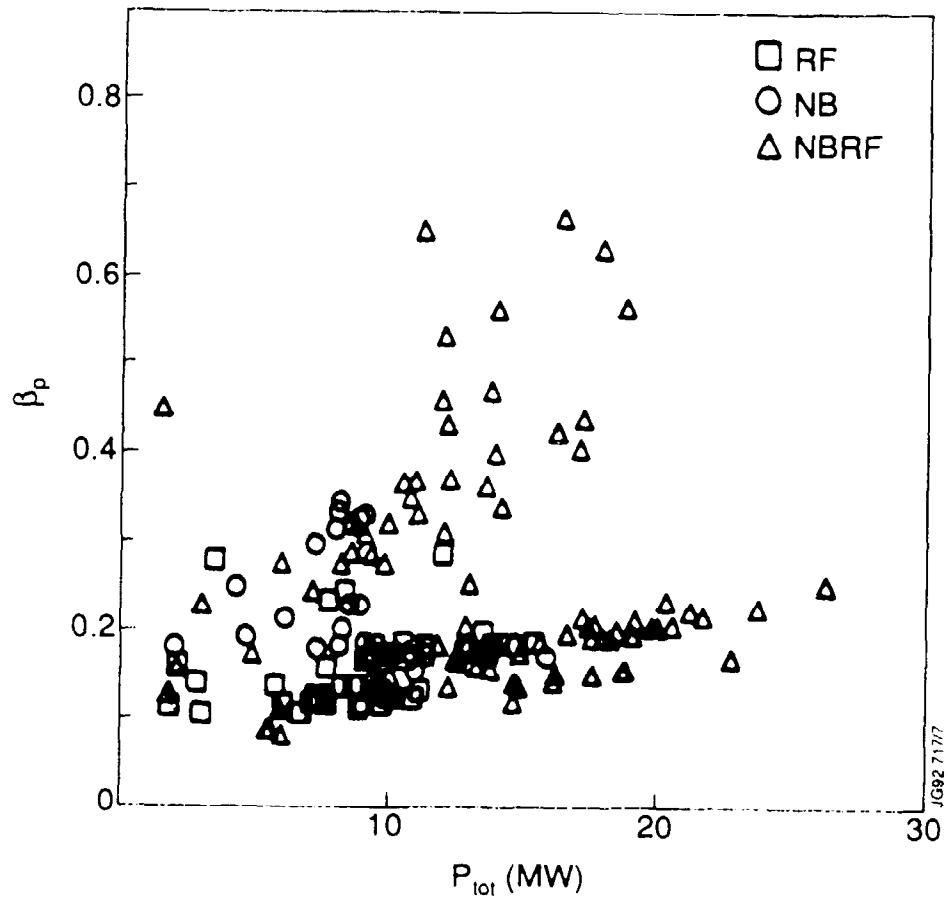


Fig. 68. Poloidal beta versus injected power for JET plasmas with fishbones [349]. The symbols represent ICRF heating alone (\square), neutral-beam heating alone (\circ), and combined ICRF and neutral-beam heating (\triangle). Instability is observed at very low values of β_p .

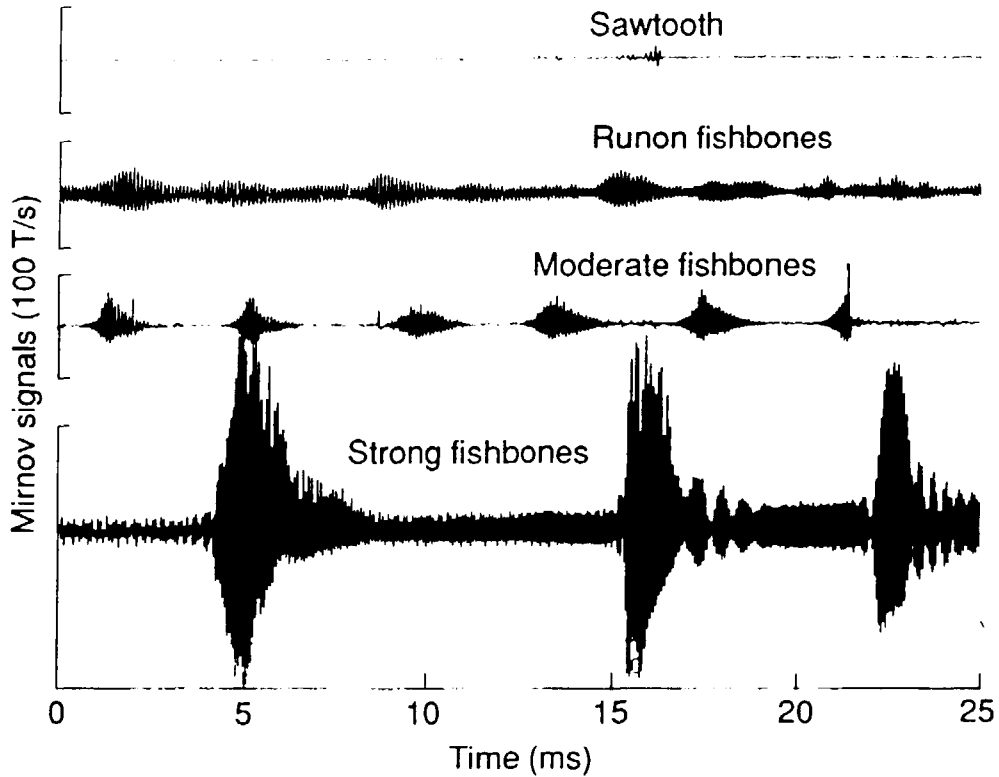


Fig. 69. Typical progression of $n = 1$ MHD activity during beam injection in DIII-D. The traces show the \dot{B}_θ signal from the same coil (located near the outer wall slightly below the midplane) in four different discharges.

Sawtooth $B = 2.1$ T, $I_p = 1.0$ MA, $\bar{n}_e = 4.5 \times 10^{13} \text{ cm}^{-3}$, $P_b \simeq 7$ MW.

Run-on fishbones $B = 0.9$ T, $I_p = 0.53$ MA, $\bar{n}_e = 4.3 \times 10^{13} \text{ cm}^{-3}$, $P_b \simeq 10$ MW.

Moderate fishbones $B = 0.9$ T, $I_p = 0.45$ MA, $\bar{n}_e = 3.5 \times 10^{13} \text{ cm}^{-3}$, $P_b \simeq 10$ MW.

Strong fishbones $B = 0.8$ T, $I_p = 0.7$ MA, $\bar{n}_e = 2.8 \times 10^{13} \text{ cm}^{-3}$, $P_b \simeq 9$ MW.

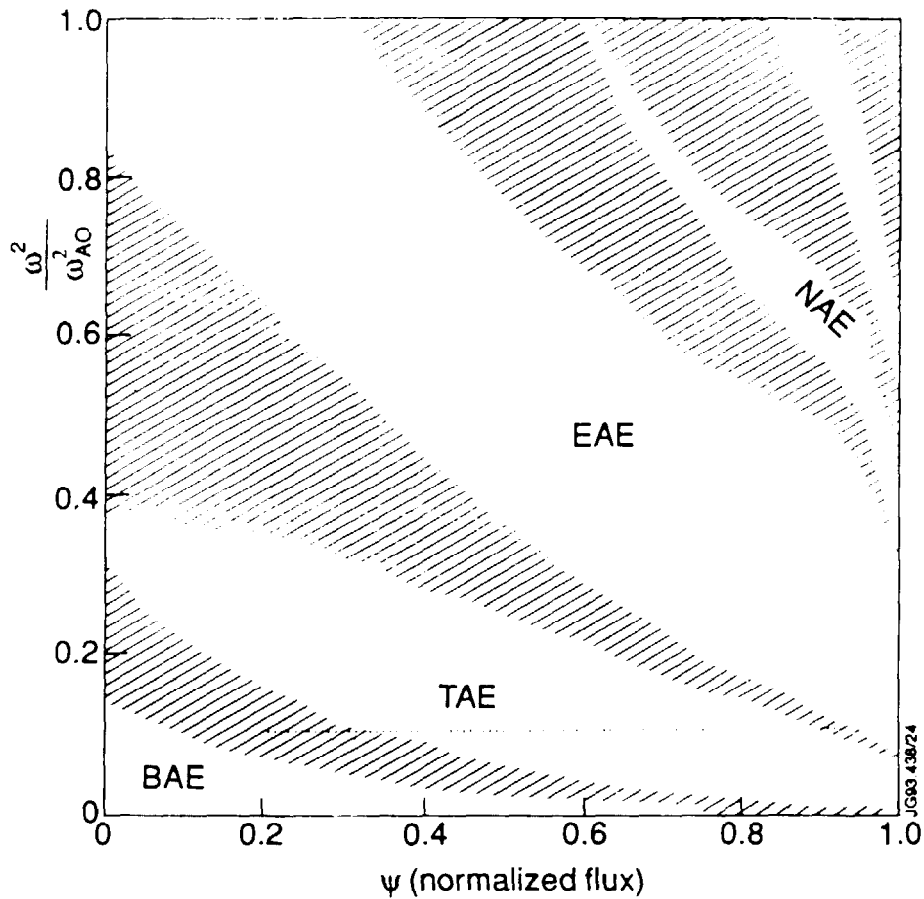


Fig. 70. Continuum shear Alfvén spectrum for $n = 3$ modes in a DIII-D equilibrium [401]. The mode frequency is normalized to ω_A evaluated at the plasma center. The abscissa represents the toroidal flux ψ . The shaded regions are the Alfvén continuum of ideal MHD. Gap modes reside between the continuum bands. The dotted line indicates the frequency and approximate spatial extent of a discrete mode that was numerically predicted and experimentally observed.

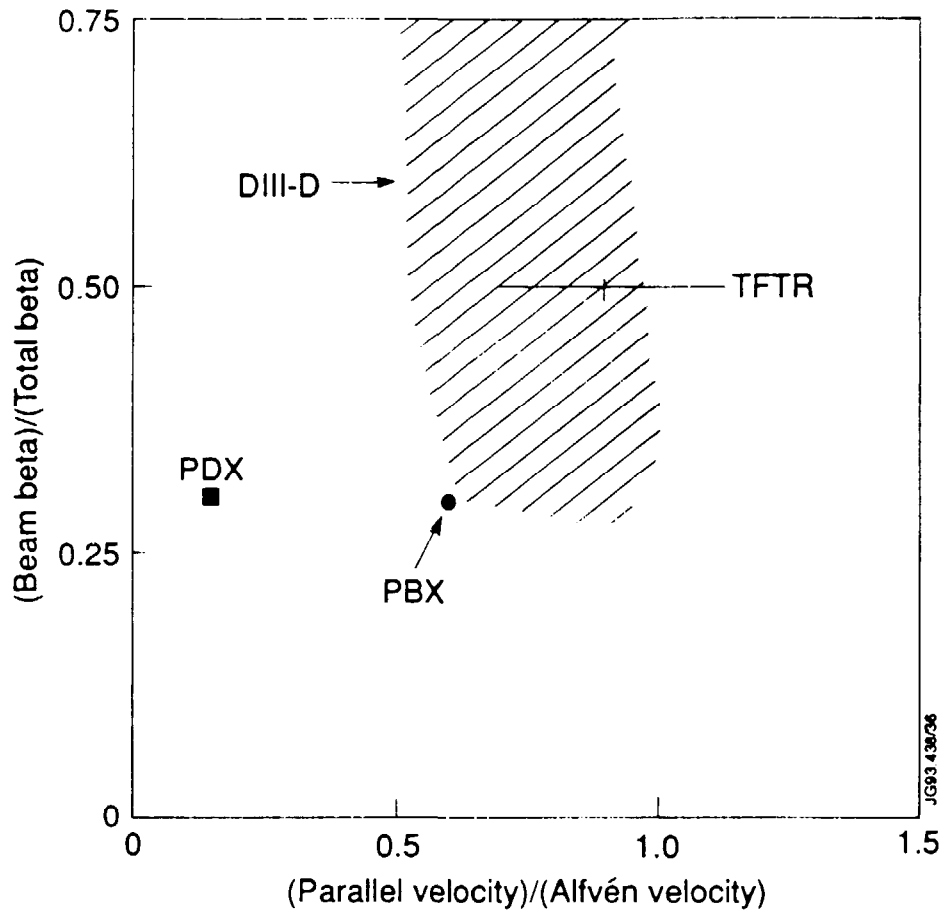


Fig. 71. Volume-averaged β_f/β_t versus v_{\parallel}/v_A for several experiments in which beam-driven instabilities with frequencies of 50-200 kHz were observed. Fast-ion losses reduce the actual beam beta below the classical value quoted here. The parallel velocity is for full-energy beam ions deposited on axis, $v_{\parallel 0} = v(R_{tan}/R)$. The hatched region represents the range of unstable values observed in DIII-D [413], the line indicates the results of the first TFTR experiment [353], and the triangles are typical values from PDX [302] and PBX [362].

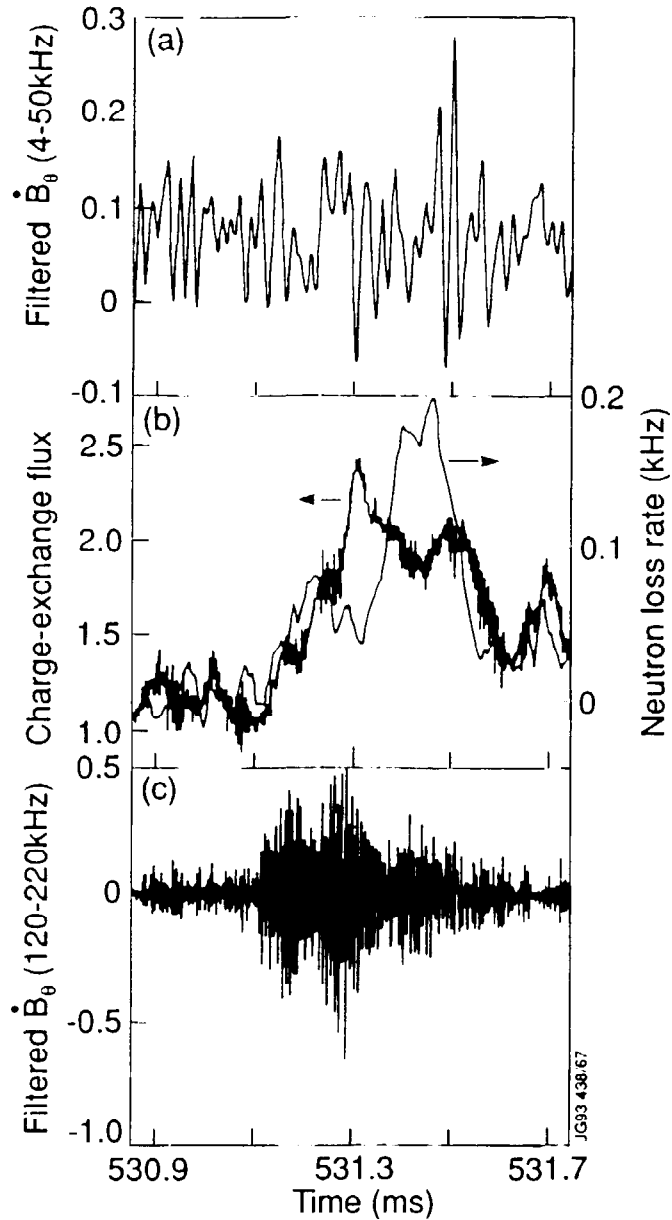


Fig. 72. Isolated TAE-like MHD burst during deuterium beam injection (45 keV) into PBX [344]. (a) Digitally filtered low-pass Mirnov signal from the outer midplane. The amplitude of low-frequency fluctuations is very small. (b) Passive tangential charge-exchange flux (35 keV) and negative derivative of the neutron emission $-S/\dot{S}$. Beam ions are lost during the burst. (c) Digitally filtered high-pass Mirnov signal. The mode grows rapidly until it is stabilized by the loss of fast ions.

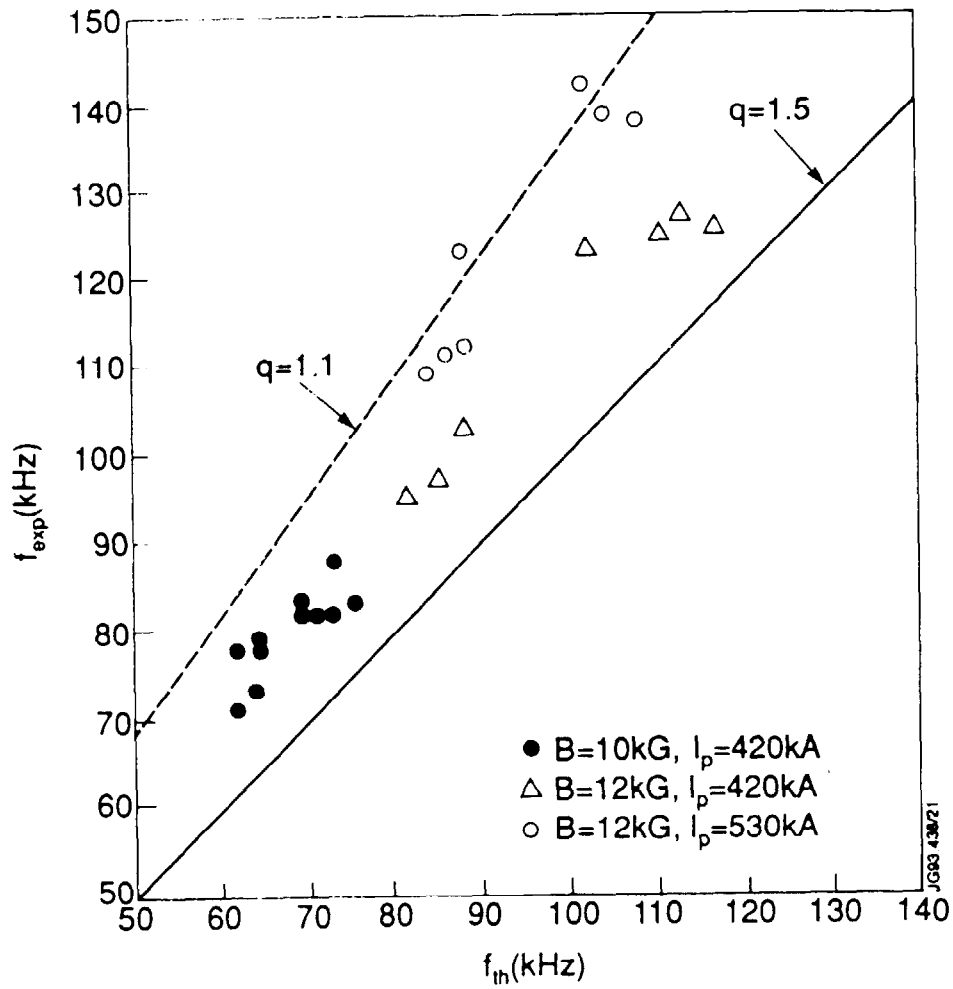


Fig. 73. Measured frequency of MHD bursts versus $f_{TAE} = v_A/4\pi qR$ (assuming $q = 1.5$) for a toroidal field scan in TFTR [353].

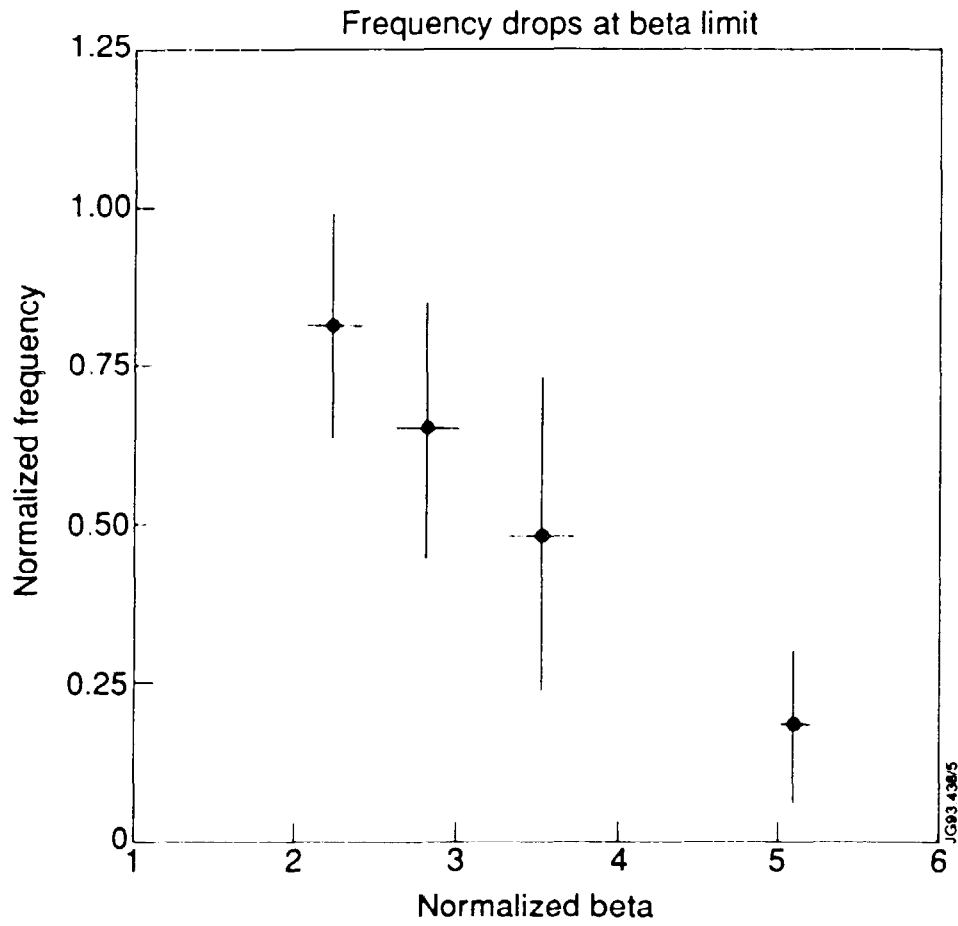


Fig. 74. Measured frequency (after correction for the Doppler shift) divided by the nominal TAE frequency (Eq. 33) as a function of β_N in DIII-D [417]. The frequency drops as the plasma approaches the beta limit at $\beta_N \simeq 3.5$. For the discharges with $\beta_N > 3.5$ current ramping was employed.

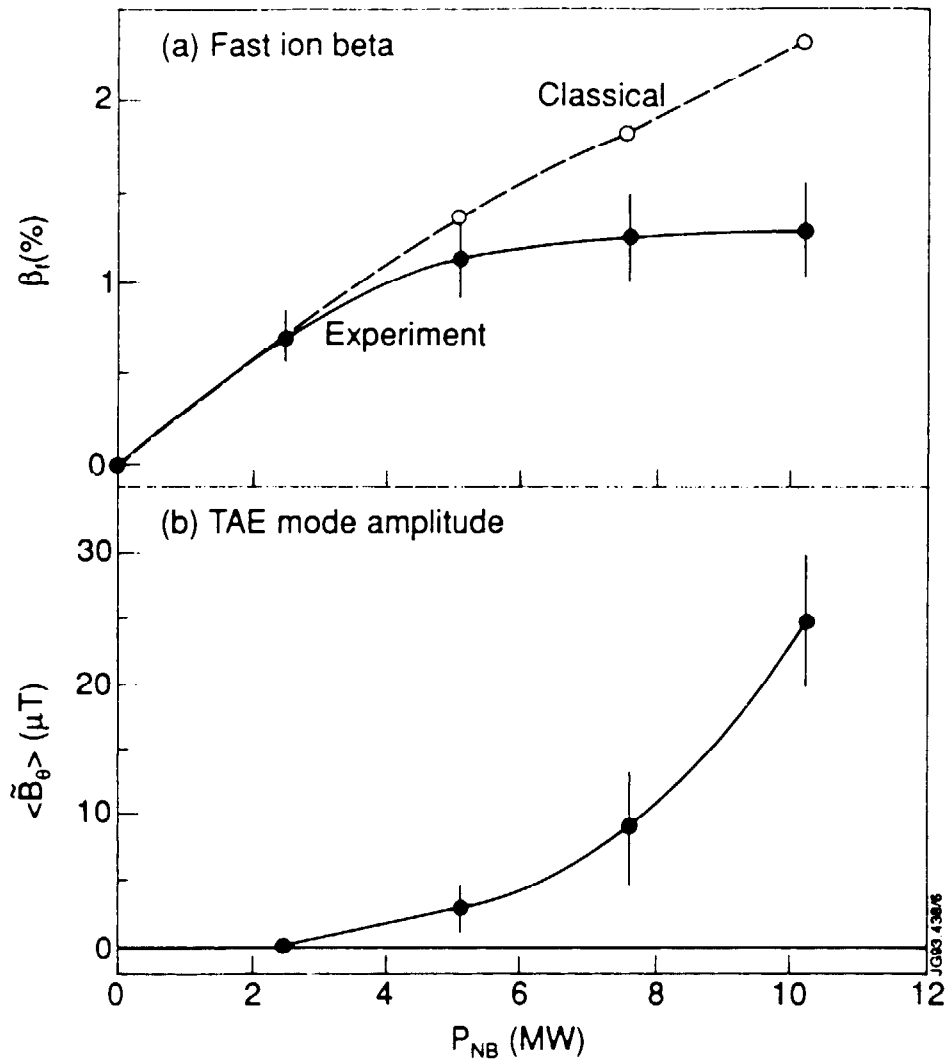


Fig. 75. Saturation of the fast-ion beta with increasing beam power during TAE activity in DIII-D [412]. (a) The beam beta inferred from the neutron emission (solid) and the expected scaling for classical slowing down (open). (b) RMS amplitude of the magnetic fluctuations (caused by TAE activity), $60 < f < 250$ kHz, at the outboard vacuum vessel wall.

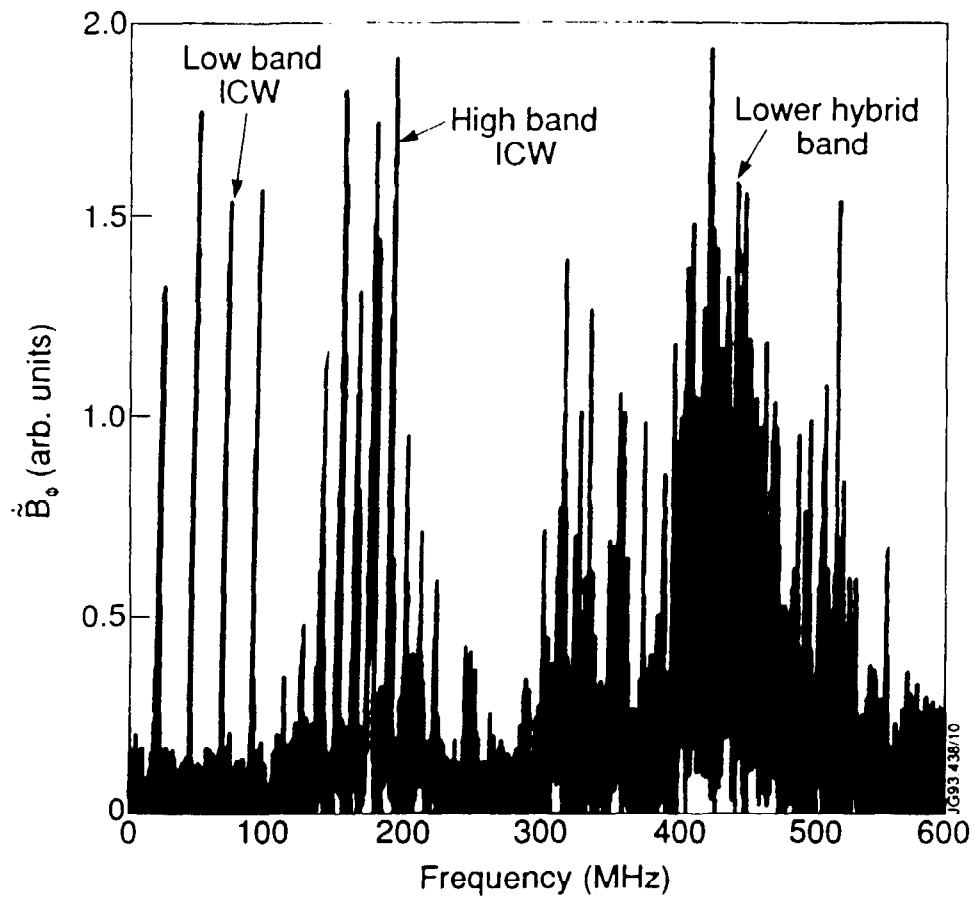


Fig. 76. Uncalibrated spectrum measured with an rf coil on the inside wall during counter-perpendicular ($\sim 99^\circ$) deuterium beam injection (45 keV) into PDX [342]. Narrow emission lines are observed at low even harmonics of the deuterium cyclotron frequency at the outer edge of the plasma (Low Band ICW), broader lines are seen at higher harmonics of the cyclotron frequency (High Band ICW), and a broad band of emission is observed in the lower-hybrid band (which ranged from 230 MHz at the plasma edge to 600 MHz at the plasma center).

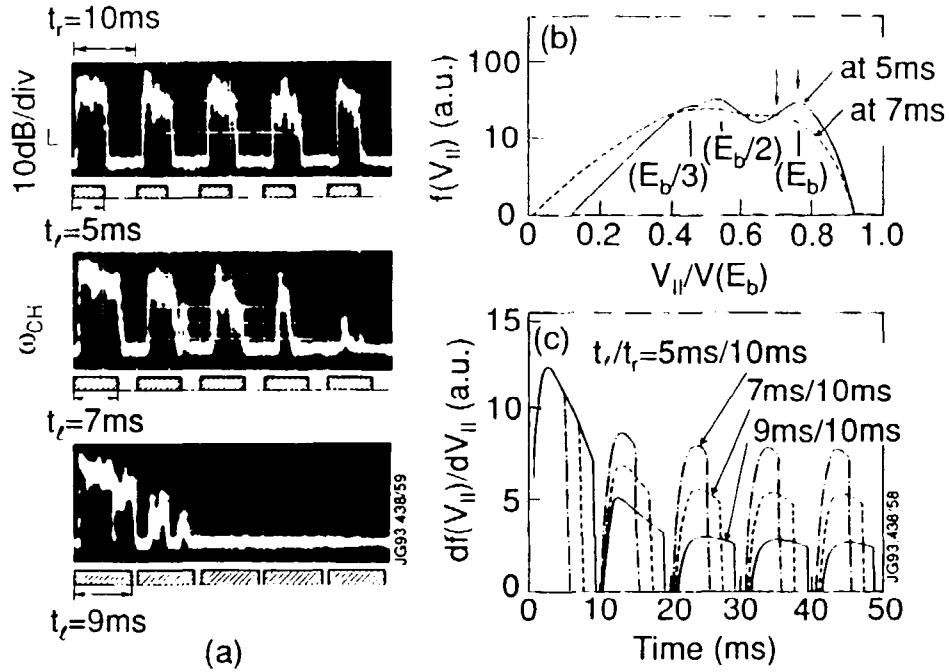


Fig. 77. Study of ion cyclotron emission in JFT-2M using multiple short pulses of hydrogen neutral beams [427]. (a) Neutral beam waveform (sketch) and rf power at the hydrogen fundamental (oscillograms) versus time. The beams (35 keV, co-injection) were injected tangentially and the ion cyclotron emission was measured with electrostatic probes placed in the scrape-off layer in the outer midplane. (b) Calculated distribution function in the center of the plasma for different pulse durations. (c) Calculated time behavior of the slope of the parallel velocity distribution function near the injection energy [between the two arrows in (b)] for various pulse durations.

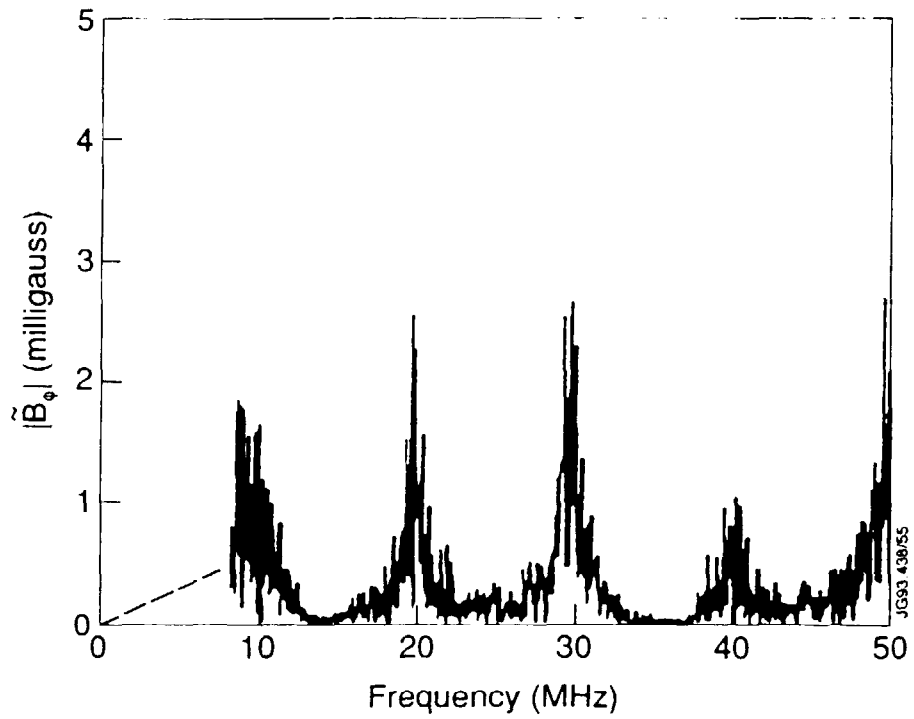


Fig. 78. Spectrum of ICE measured during fishbone activity caused by perpendicular deuterium beam injection (45 keV) into PDX [419]. The emission was measured by a small coil positioned on the inner wall. The peaks occur at harmonics of the deuterium cyclotron frequency at the outer edge of the plasma.

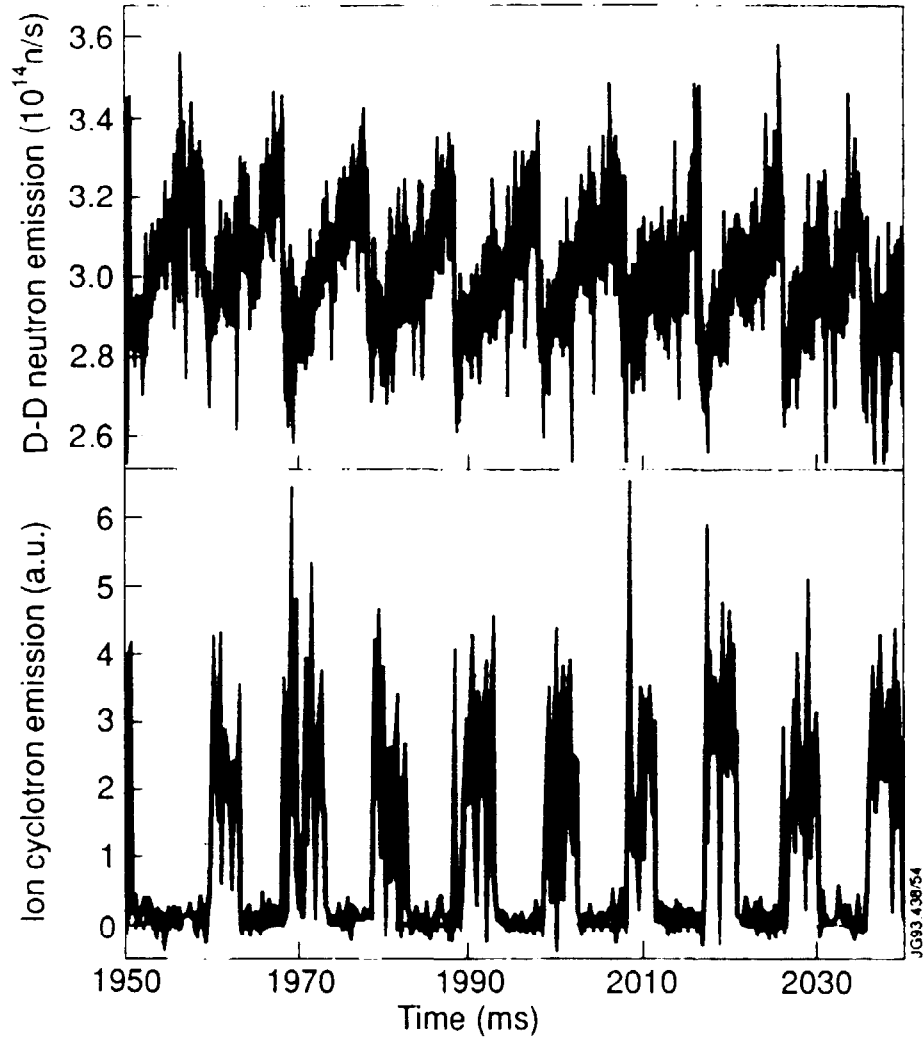


Fig. 79. Time evolution of the 2.5 MeV neutron emission and emission at ~ 20 MHz during combined fishbone and TAE activity driven by deuterium beam injection (75 keV) into DIII-D [359]. The ICE is measured with a small loop positioned on the outer midplane; 20 MHz corresponds to the second harmonic of deuterium at the outer edge of the plasma. The sudden drops in neutron emission are coincident with the MHD instabilities and indicate expulsion of beam ions from the center to the edge of the plasma. The bursts of ICE correlate with the reductions in neutron emission.

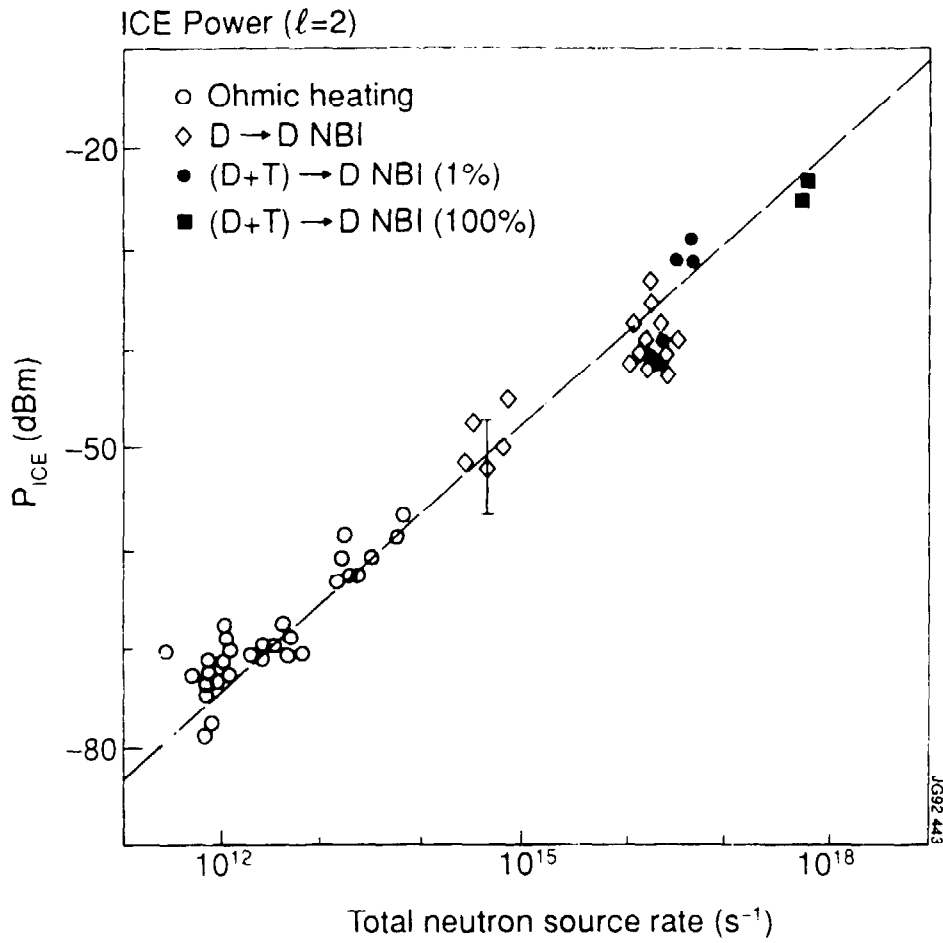


Fig. 80. Power in the second-harmonic ICE peak versus the total neutron yield for JET data [374]. The ICRF heating antenna located on the outer midplane was used to detect the emission. The estimated relative uncertainty between groups of data is ± 6 dB.

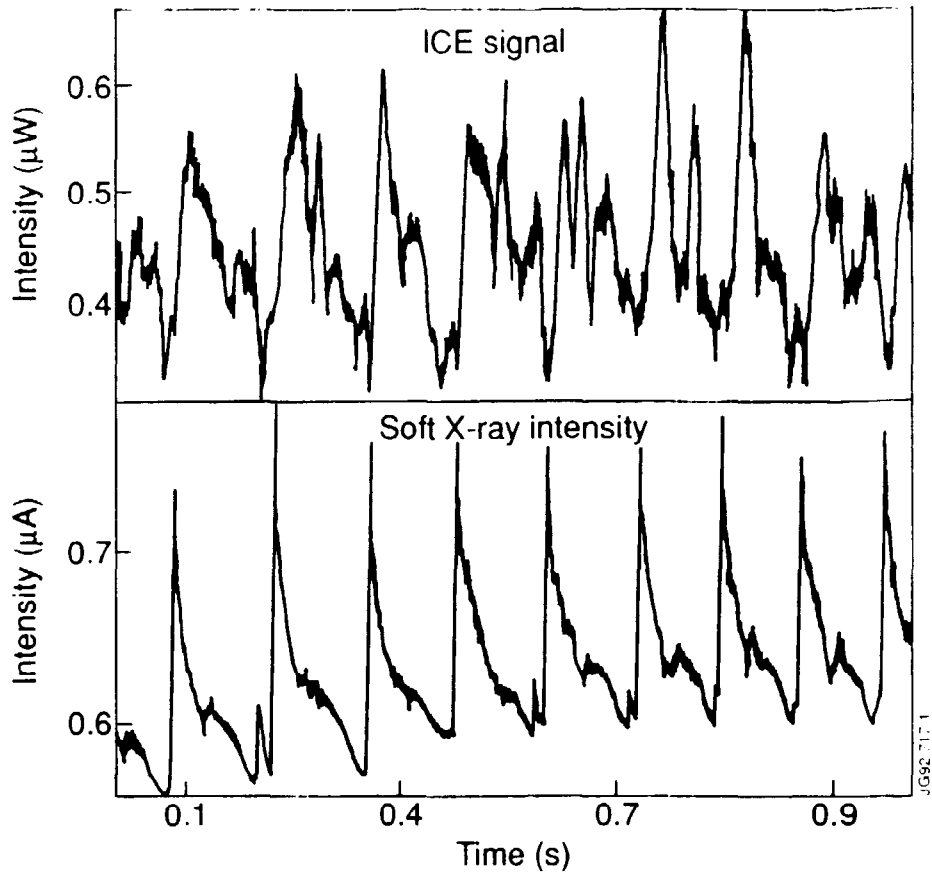


Fig. 81. Time evolution of the 55 MHz spectral peak and of the edge soft X-ray signal during sawtooth activity associated with deuterium ohmic heating in JET [423]. The emission was detected by the ICRF antenna at the outer midplane. The bursts of ICE are delayed ~ 12 ms with respect to the sawtooth crash, and correlate with the arrival of the heat pulse (produced by the sawtooth) at the plasma edge. Although changes in antenna loading may cause part of the modulation in ICE signal [374], this effect cannot account for the full variation.